DOCTOR OF SCIENCES

Synthesis and characterization of vertically aligned metal dichalcogenides for gas sensing application

Sierra Castillo, Ayrton

Award date:
2021

Awarding institution:
University of Namur

University of Namur

Faculty of Science

Ph.D. Thesis

SYNTHESIS AND CHARACTERIZATION OF VERTICALLY ALIGNED METAL DICHALCOGENIDES FOR GAS SENSING APPLICATION

Ayrton Sierra-Castillo

Jury members

Prof. Carmela Aprile (University of Namur, Belgium)

Prof. Luc Henrard (University of Namur, Belgium)

Prof. Marc Debliquy (University of Mons, Belgium)

Prof. Eduard Llobet (Universitat Rovira i Virgili, Spain)

Dr. Carla Bittencourt (University of Mons, Belgium, co-promoter)

Dr. Jean-François Colomer (University of Namur, Belgium, promoter)

October 2021

Acknowledgments

I am very grateful to the University of Namur for supporting this work and for the financial support (UNamur-Ceruna grant).

I thank to the jury members for judging the present doctoral work.

I am extremely thankful with my supervisor Dr. Jean-François Colomer for the opportunity to come here, be part of his group and learn so many new things and live new experiences during these 4 years. I am grateful for the experience acquired. I express my total gratitude to my supervisor in the University of Mons, Dr. Carla Bittencourt for her advices, for all the support during my first arrival in Namur and especially during the PhD study.

Among the people in the University of Namur, I specially thank to Corry Charlier for the training and all the help with the SEM and TEM during these 4 years. An enormous thank to my colleague Dr. Emile Haye for his help and his time in the processing of the XPS results. I also thank to all the collaborators of this work: Dr. Selene Acosta, Dr. Geetanjali Deokar, Prof. Raul Arenal and Prof. Eduard Llobet. We definitely had a very productive collaboration, it was an honor to work with all of you.

Additionally, I want to thank all the experiences, histories, parties, talks, travels and dinners to all my friends in Namur: Adriana, Alessandra, Alexandra, Diana, Laura, Tania, Alex, Anthony, Quentin, Domenico and Nacho; without you, it would not be the same, my little family in Namur.

Finally, special thanks go to my mother, father, sister, brother and Sofía as well as relatives and best friends in Mexico. Without you, I would not achieve what I have now.

Table of Contents

Université de Namur

Faculté des Sciences

61, Rue de Bruxelles, Namur, Belgium

Synthesis and characterization of Vertically Aligned Metal Dichalcogenides Nanosheets for Gas Sensing

Abstract

Following the isolation of graphene in 2004, scientists quickly showed that it possesses remarkable properties. However, as the scientific understanding of graphene matured, it became clear that it also has limitations: for example, graphene does not have a bandgap, making it poorly suited for use in digital logic. This motivated exploration of monolayer materials “beyond graphene”, which could embody functionalities that graphene lacks. In recent years there has been an increased interest in layered materials such as semiconducting Metal Dichalcogenides (MDs). When isolated in their monolayer form, they are essentially a 2D material, with unique properties. The implementation of 2D materials into future electronic devices could be desirable for industry; as their potential applications include cheap, fast and flexible electronic devices. Furthermore, to fully exploit the unique electrical properties of these materials, such as high

electron mobility, new synthesis, manipulation, integration and characterization techniques must be developed.

In this thesis, the synthesis of high quality and crystallinity vertical aligned multilayer MDs by the Chemical Vapor Deposition (CVD) technique is reported. The morphology and the structure, as well as the optical properties, of the so-produced material have been studied using electron microscopies (SEM and TEM), X-ray photoelectron spectroscopy (XPS), Photoluminescence (PL), UV–visible and Raman spectroscopies and X-ray diffraction (XRD). The so-synthesized materials are potentially interesting in various applications where edge accessibility or directionality of the nanosheets play a major role such as gas sensing. For that, the performance of these materials as a gas sensor to detect toxic gases, for example NO_2 and NH_3, were investigated and discussed in this thesis work.

Ph. D thesis in Physical Sciences

October 19th 2021

Promoter : Jean -François Colomer

Université de Namur

Faculté des Sciences

61, Rue de Bruxelles, Namur, Belgium

Synthèse et caractérisation de nanoplaquettes de dichalcogénures métalliques alignés verticalement pour la détection de gaz

Résumé

Après l'isolement du graphène en 2004, les scientifiques ont rapidement montré qu'il possédait des propriétés remarquables. Cependant, à mesure que la compréhension scientifique du graphène a mûri, il est apparu clairement qu'il avait aussi des limites : par exemple, le graphène n'a pas de bande interdite, ce qui le rend peu adapté à une utilisation en logique numérique. Cela a motivé l'exploration de matériaux monocouches "au-delà du graphène", qui pourraient présenter des fonctionnalités dont le graphène est dépourvu. Ces dernières années, les matériaux en couches, tels que les dichalcogénures métalliques (MDs) semi-conducteurs, ont suscité un intérêt croissant. Lorsqu'ils sont isolés sous leur forme monocouche, ils constituent essentiellement un matériau 2D, aux propriétés uniques. La mise en œuvre de matériaux 2D dans les futurs dispositifs électroniques pourrait être souhaitable pour l'industrie, car leurs applications potentielles incluent des dispositifs électroniques bon marché, rapides et flexibles. En outre, pour exploiter pleinement les propriétés électriques uniques de ces matériaux, telles

que la mobilité élevée des électrons, de nouvelles techniques de synthèse, de manipulation, d'intégration et de caractérisation doivent être développées.

Dans cette thèse, la synthèse de MDs multicouches alignés verticalement de haute qualité et cristallinité par la technique de dépôt chimique en phase vapeur (CVD) est rapportée. La morphologie et la structure, ainsi que les propriétés optiques, du matériau ainsi produit ont été étudiées à l'aide de microscopies électroniques (SEM et TEM), de la spectroscopie photoélectronique des rayons X (XPS), de la photoluminescence (PL), des spectroscopies UV-visible et Raman et de la diffraction des rayons X (XRD). Les matériaux ainsi synthétisés sont potentiellement intéressants dans diverses applications où l'accessibilité des bords ou la directionnalité des nanofeuilles jouent un rôle majeur, comme la détection de gaz. Pour cela, les performances de ces matériaux comme capteur de gaz pour détecter les gaz toxiques, par exemple NO_2 et NH_3, ont été étudiées et discutées dans ce travail de thèse.

Thèse de doctorat en Sciences Physiques

Le 19 Octobre 2021

Promoteur : Jean-François Colomer

List of Acronyms

2D	Two Dimensional
MDs	Metal Dichalcogenides
TMDs	Transition Metal Dichalcogenides
TDs	Tin Dichalcogenides
CVD	Chemical Vapor Deposition
MoS_2	Molybdenum Disulfide
WS_2	Tungsten Disulfide
SnS_2	Tin Disulfide
$MoSe_2$	Molybdenum Diselenide
WSe_2	Tungsten Diselenide
$SnSe_2$	Tin Diselenide
NO_2	Nitrogen Dioxide
NH_3	Ammonia
SEM	Scanning Electron Microscopy
TEM	Transmission Electron Microscopy
XPS	X-Ray Photoelectron Spectroscopy
XRD	X-Ray Diffraction
PL	Photoluminescence
UV-vis	Ultra Violet-visible
DOS	Density of States
DFT	Density-functional theory
CBM	Conduction Band Minimum
VBM	Valence Band Maximum
nm	Nanometer
FET	Field-effect transistors
EES	Electrochemical Energy Storage
HDS	Hydro-Desulfurization
HER	Hydrogen Evolution Reaction

MLs	Monolayers
NMP	N-methyl-2-pyrrolidone
IPA	2-propanol
CHP	N-cyclohexyl-2-pyrrolidone
THF	Tetrahydrofuran
CVT	Chemical Vapor Transport
S	Sulfur
Se	Selenium
Mo	Molybdenum
W	Tungsten
Sn	Tin
sccm	Standard cubic centimeters per minute
Ar	Argon
H_2	Hydrogen
AP	Atmospheric Pressure
ppb	part per billion
VA	Vertically-Aligned
NTs	Nanotriangles
NFs	Nanoflakes

Chapter 1

Context

Here, the main scientific questions planted in this work are presented. The fundamental scientific motivations and the potentialities for the development of novel 2D metal dichalcogenides with multilayer nature for gas sensing applications are given. Additionally, the research objectives of this Ph.D. thesis are explained and the experimental methodology employed to accomplish these objectives is described.

1.1 Motivation

An atomically thin two-dimensional (2D) material is defined as a material whose free charges are immobile in one spatial dimension, however mobile in the other two. This property enables 2D materials to have new or superior properties, distinct from traditional bulk materials or thin films [1]. After isolating graphene [2], as the first 2D material in 2004, about 700 others 2D materials have been predicted or reported, some of them are illustrated in the Figure 1.1. In this context, it must be emphasized that today this area of research, 2D materials, represents the largest growing field in materials science, engineering and applications.

Two-dimensional materials offer a platform that allows creation of heterostructures with a variety of electronic, optical and mechanical properties with remarkable potential for technological applications [3]. One atom-thick crystals now comprise a large family of these materials, collectively covering a very broad range of properties [4].

Many 2D materials exist in bulk form as stacks of strongly bonded atoms in layers with weak interlayer interaction, allowing exfoliation into individual, atomically thin layers [5].

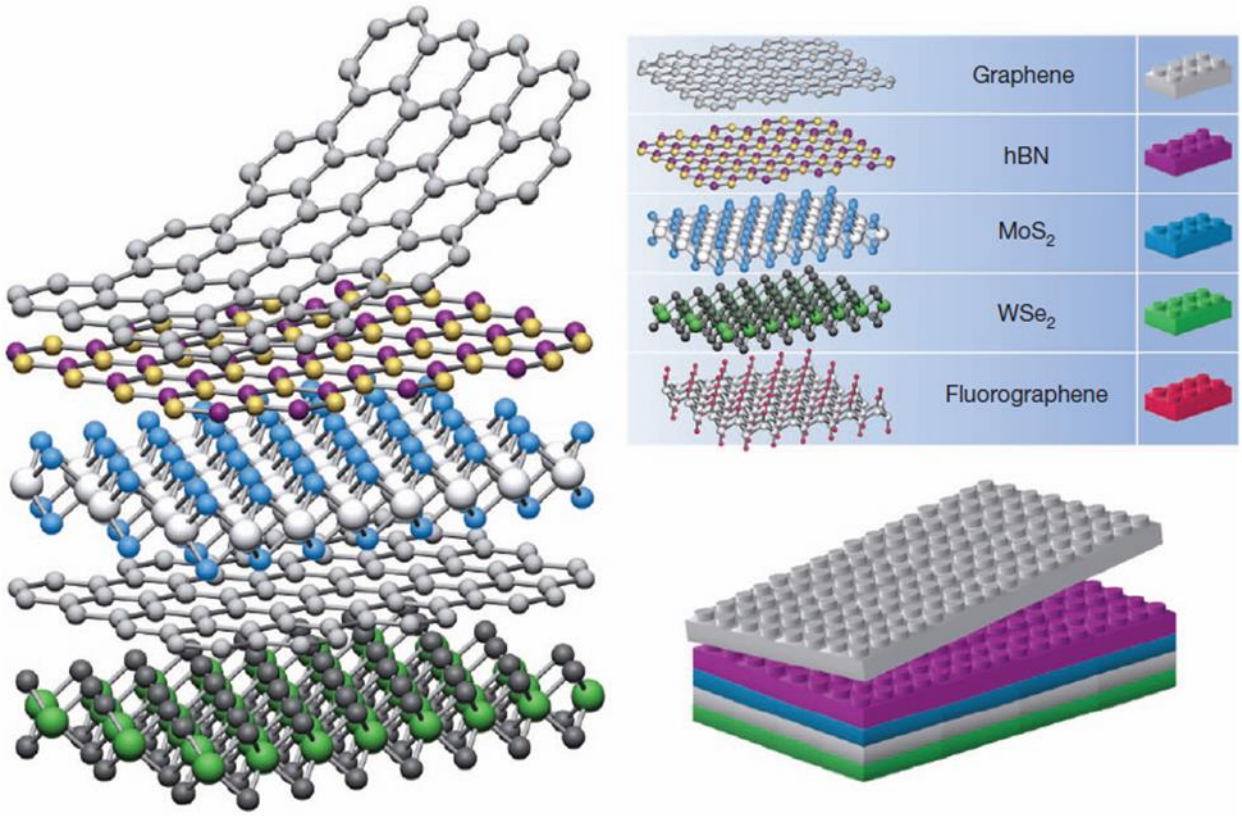

Figure 1.1 Schematic representation of different 2D materials and their assembly in heterostructures [6].

Until recently, the 2D material that had been received more attention of the scientific community was graphene, which name denominates a flat monolayer of carbon atoms tightly packed into a two-dimensional honeycomb lattice. Graphene is the basic building block for several graphitic

materials of different dimensionalities (see Chapter 2). However, in the last decade, graphene-like 2D layered dichalcogenides have been widely studied due to their potential applications in field effect transistors, photodetectors, solar cells and gas sensors.

Semiconducting metal dichalcogenides (MDs), such as MoS_2, WS_2, $MoSe_2$, WSe_2, SnS_2, $SnSe_2$, etc., form a subgroup of 2D materials with attractive optical properties. They have an optical bandgap in the visible and near-infrared light range. Bulk MDs have been known as lubricants and have not attracted interest for optoelectronics for many years [7]. However, the situation has changed with the advent of the mechanical exfoliation method, that allowed to decrease down to a monolayer, revealing the indirect-to-direct bandgap transition in different MDs [8]. For example, monolayer and multilayer MoS_2 are semiconductors with direct/indirect band gap of $\sim$1.2-1.8 eV, respectively [9]. These structural modifications dramatically increase the quantum efficiency of the single-layer sheets by several orders of magnitude relative to that of the few-layer or bulk crystals [10]. To obtain materials with such interesting characteristics, growth methods for MDs have been adapted and they are reviewed in the Chapter 3.

The research area of MDs ultrathin films and structures is quite new and requires detailed investigations and fundamental understanding. For this reason, the goal of this doctoral thesis is to develop a reliable synthesis method for a subset of next generation nanostructured metal dichalcogenides (MDs). Growth was performed by chemical vapor deposition (CVD) and material characterization was accomplished with a variety of tools that include spectroscopy and microscopy. A description of the main results on this topic, applied sample fabrication methods and optical spectroscopy techniques is outlined in this thesis.

1.2 Research objectives

During this work, six nanostructured Metal Dichalcogenides were synthesized vertically-aligned: The Transition Metal Dichalcogenides (TMDs), MoS_2, WS_2, $MoSe_2$ and WSe_2, and the Tin Dichalcogenides (TDs), SnS_2 and $SnSe_2$. Two of these materials were investigated as a chemical sensor to detect hazardous gases (NO_2 and NH_3) in air (WS_2 and WSe_2).

In this perspective, the objectives of this thesis are:

1) *Synthesis and characterization of highly crystalline vertically aligned Metal Dichalcogenides nanosheets.*
2) *Design a novel chemical sensor based on Metal Dichalcogenides to detect hazardous gases in air.*

1.3 Organization of the thesis

Based on the research objectives the manuscript is organized as follows. Chapter 2 reviews the current literature and research status of the 2D materials research area including the applications of MDs (TMDs and TDs). Chapter 3 discusses the growth of 2D crystalline MDs from the planar to the vertical direction via CVD technique. The growth mechanism and key parameters dominating the growth process are studied using an experimental approach. In Chapter 3 we discuss the vertical growth of the MoS_2, WSe_2, $MoSe_2$, SnS_2, $SnSe_2$ and WS_2 using the CVD technique, each material is described as well as its synthesis process and characterization results. Figure 1.2 describes the research strategy employed.

The results reported on chapter 3 are published in:

- **Sierra-Castillo, A.**, Haye, E., Acosta, S., Bittencourt, C., & Colomer, J. F. (2020). Synthesis and Characterization of Highly Crystalline Vertically Aligned WSe_2 Nanosheets. Applied Sciences, 10(3), 874.
- **Sierra-Castillo, A.**, Haye, E., Acosta, S., Arenal, R., Bittencourt, C., & Colomer, J. F (2021). Atmospheric Pressure Chemical Vapor Deposition Growth of vertically aligned SnS_2 and $SnSe_2$ nanosheets. *Submitted*.

Chapter 4 is focused on the experimental work performed for the development of a chemical sensor based on metal dichalcogenides (WS_2 and WSe_2) to detect toxic gases, such as NO_2 and NH_3, the results obtained from each step of this investigation are discussed. Figure 1.3 describes the research strategy employed for this part of the thesis.

The results presented in this chapter are published in:

- Alagh, A., Annanouch, F. E., Umek, P., Bittencourt, C., **Sierra-Castillo, A.**, Haye, E., Colomer, J. F. & Llobet, E. (2021). CVD growth of self-assembled 2D and 1D WS_2 nanomaterials for the ultrasensitive detection of NO_2. Sensors and Actuators B: Chemical, 326, 128813.
- An ultrasensitive two-dimensional WSe_2 nanoflower based gas sensor. (2021). *In preparation*.

Chapter 5 contains the conclusions and perspectives of the thesis work. Finally, in the first appendix section the characterization techniques are described and in the second appendix the scientific contributions are presented.

This thesis is mainly focusing on the synthesis and characterization of the TMDs and LDs materials.

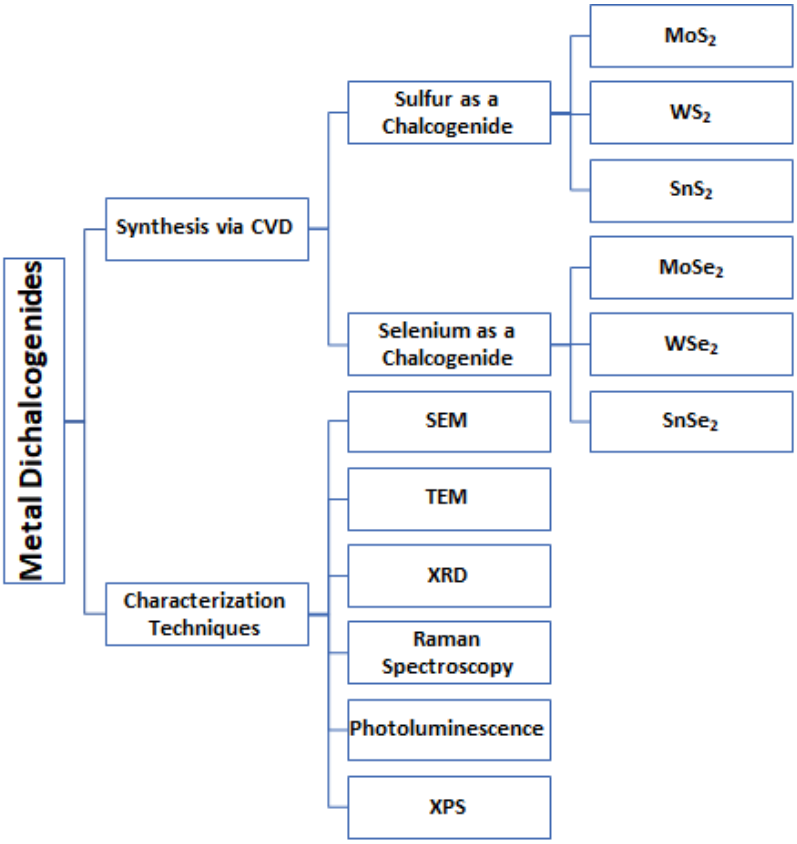

Figure 1.2 Diagram of the research strategy employed in the Chapter 3.

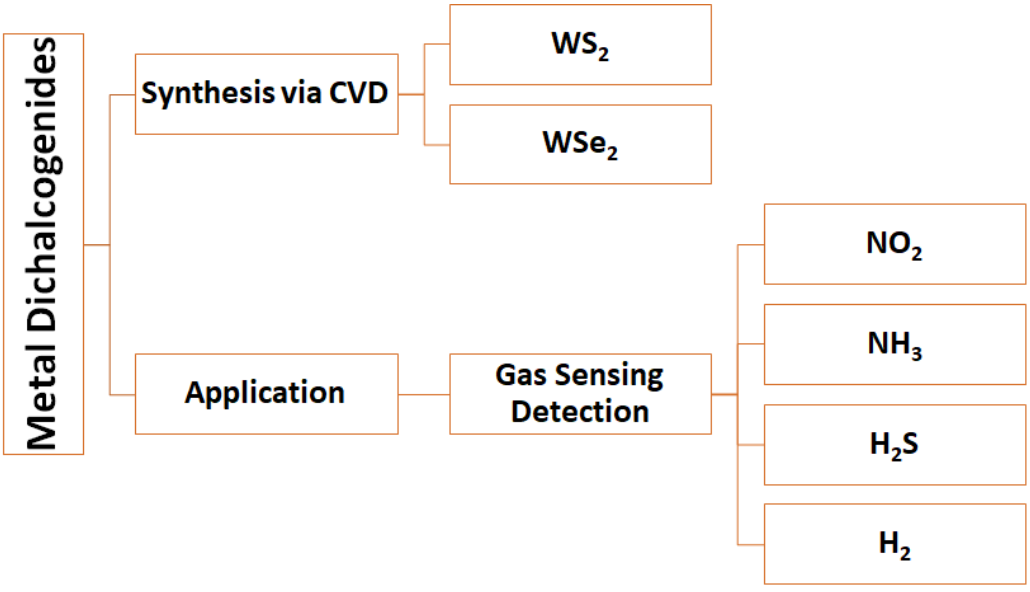

Figure 1.3 Diagram of the research strategy employed in the Chapter 4.

1.4 References

1. Das, S.; Kim, M.; Lee, J.W.; Choi, W. Synthesis, properties, and applications of 2-D materials: A comprehensive review. *Crit. Rev. Solid State Mater. Sci.* **2014**, *39*, 231–252, doi:10.1080/10408436.2013.836075.
2. Geim, A.K.; Novoselov, K.S. The rise of graphene. *Nanosci. Technol. A Collect. Rev. from Nat. Journals* **2009**, 11–19, doi:10.1142/9789814287005_0002.
3. Mannix, A.J.; Kiraly, B.; Hersam, M.C.; Guisinger, N.P. Synthesis and chemistry of elemental 2D materials. *Nat. Rev. Chem.* **2017**, *1*, 1–15, doi:10.1038/s41570-016-0014.
4. Novoselov, K.S.; Mishchenko, A.; Carvalho, A.; Castro Neto, A.H. 2D materials and van der Waals heterostructures. *Science (80-.).* **2016**, *353*, doi:10.1126/science.aac9439.
5. Wang, Q.H.; Kalantar-Zadeh, K.; Kis, A.; Coleman, J.N.; Strano, M.S. Electronics and optoelectronics of two-dimensional transition metal dichalcogenides. *Nat. Nanotechnol.* **2012**, *7*, 699–712, doi:10.1038/nnano.2012.193.
6. Geim, A.K.; Grigorieva, I. V. Van der Waals heterostructures. *Nature* **2013**, *499*, 419–425, doi:10.1038/nature12385.
7. Brudnyi, A.I.; Karmadonov, A.F. Structure of molybdenum disulphide lubricant film. *Wear* **1975**, *33*, 243–249, doi:10.1016/0043-1648(75)90279-3.
8. Mak, K.F.; Lee, C.; Hone, J.; Shan, J.; Heinz, T.F. Atomically thin MoS2: A new direct-gap semiconductor. *Phys. Rev. Lett.* **2010**, *105*, 2–5, doi:10.1103/PhysRevLett.105.136805.
9. Nan, H.; Wang, Z.; Wang, W.; Liang, Z.; Lu, Y.; Chen, Q.; He, D.; Tan, P.; Miao, F.; Wang, X.; et al. Strong photoluminescence enhancement of MoS2 through defect engineering and oxygen bonding. *ACS Nano* **2014**, *8*, 5738–5745, doi:10.1021/nn500532f.

10. Splendiani, A.; Sun, L.; Zhang, Y.; Li, T.; Kim, J.; Chim, C.Y.; Galli, G.; Wang, F. Emerging photoluminescence in monolayer MoS2. *Nano Lett.* **2010**, *10*, 1271–1275, doi:10.1021/nl903868w.

Chapter 2

State of the Art

Nanomaterials are, by definition, natural or artificial materials possessing at least one dimension in nanoscale range. Nanomaterials can be divided in four categories according to their dimensions, including zero-dimensional materials, one-dimensional materials, two-dimensional (2D) materials and three-dimensional materials.

This chapter describes 2D materials, specifically Metal Dichalcogenides (MDs). These materials are classified in this thesis as: Transition Metal Dichalcogenides (TMDs) and Tin Dichalcogenides (TDs). Their structure, properties and applications are discussed.

2.1 The Transition Metal Dichalcogenides

The Transition Metal Dichalcogenides (TMDs) are a family of materials with laminar structures both in three–dimensional (3D, in bulk scale) and two-dimensional (2D, nanometric scale). TMDs are part of a novel group of materials with an increasing interest currently. This is due to the great potential they present in possible applications in various fields of electronics and optoelectronics, as we can see in the section 2.5 in this chapter.

These materials are composed of more than 40 compounds with the generalized formula of MX_2, where M, in the case of TMDs, is a transition metal typically from IV (Ti, Zr, Hf), V (V, Nb, Ta) or VI (Mo, W), and X is a chalcogenide such as S, Se or Te (Figure 2.1) [1]. The transition metal and the chalcogenide are strongly linked by covalent bonds, thus originating sheets based on X-M-X units.

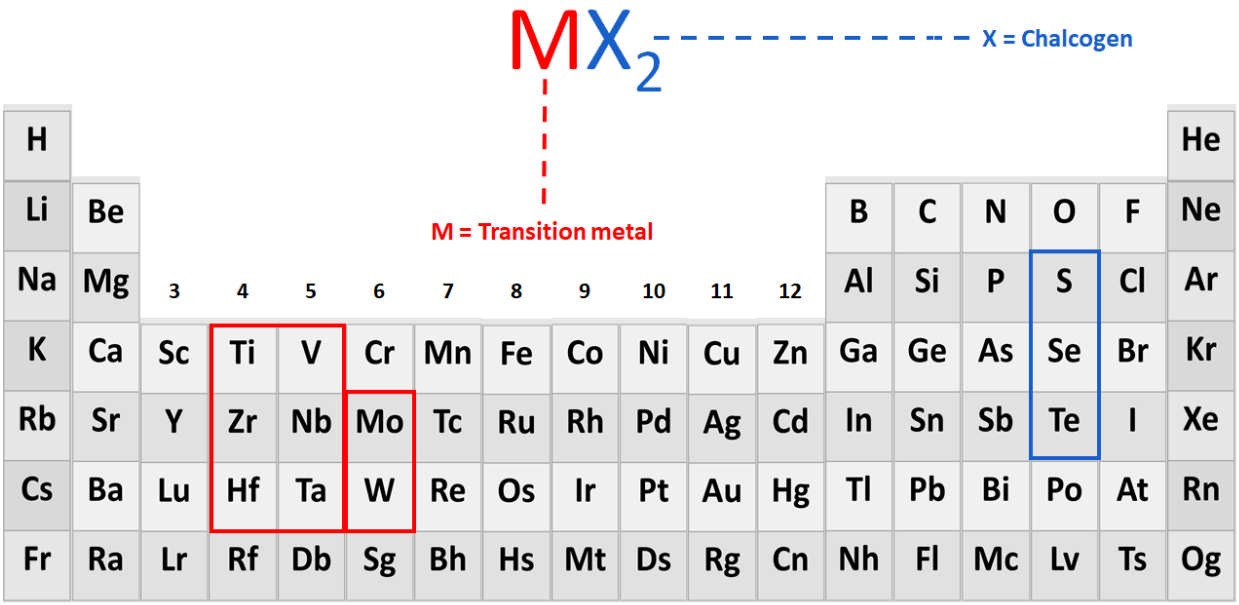

Figure 2.1 A number of possible layered structure TMDs materials exist based on the transition metal (boxed in red) and chalcogenides (boxed in blue).

2.1.1 The Metal Dichalcogenides

Unlike TMDs, Metal dichalcogenides (MDs) are based on a different metal than the transition metals. TMDs can be considered in this category because they present the same structure and some similarities with their properties. Tin (Sn) is presented as a metal and Sulfur or Selenium as the chalcogens. These materials have similar structure as the TMDs, i.e., sheets having the X-Sn-X units (Figure 2.2) [2]. They present optical, electrical, and photoelectric properties suitable to nanoelectronics and optoelectronics devices [3], [4], [5] .

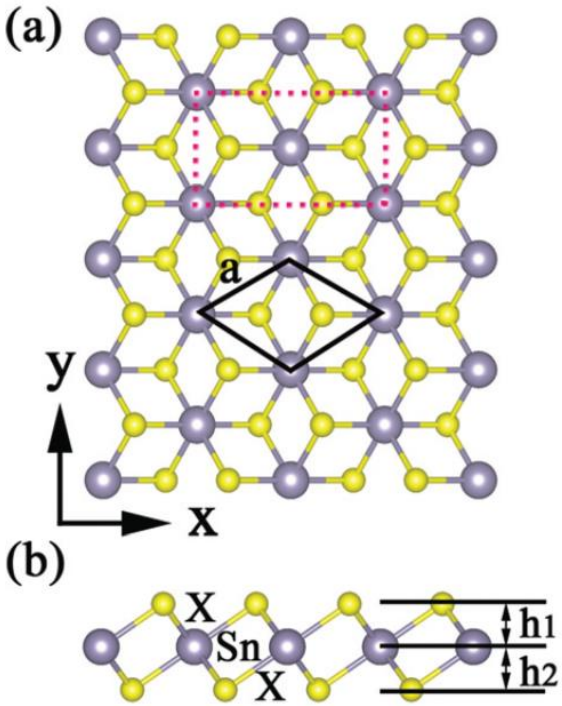

Figure 2.2 Top view (a) and side view (b) of the 2D perfect SnX_2 (X=S, Se, Te) [2].

In addition to the MDs, other 2D materials exist and some of them can be mentioned: Boron Nitride (Hexagonal) [6], Borophene [7], Germanene [8], Phosphorene [9], Silicene [10], etc.

The available research literature is vast on this topic. Although there is a large variety of 2D materials, this work focuses only on MoS_2, WS_2, $MoSe_2$, and WSe_2. The structural, electronic,

optical, and electrical properties of these materials, and some applications are discussed in the following sections of this chapter. In addition, SnS_2 and $SnSe_2$ as TDs are also studied. From now on all materials will be referred to as MDs.

2.2 Structural characteristics of Metal Dichalcogenides

One of the greatest characteristics of the MDs is its polymorphism. Indeed, MDs exist in several structural phases resulting from different possible metal coordination. The two common metal atom coordinations are characterized by either octahedral or trigonal prismatic as shown in Figure 2.3 [11]. The octahedral coordination describes the shape of six atoms symmetrically arranged around a central metal atom, defining the vertices of an octahedron (known as 1T phase) and the trigonal prismatic coordination describes the shape of six atoms arranged around a central metal atom, defining the vertices of a triangular prism (known as 2H phase).

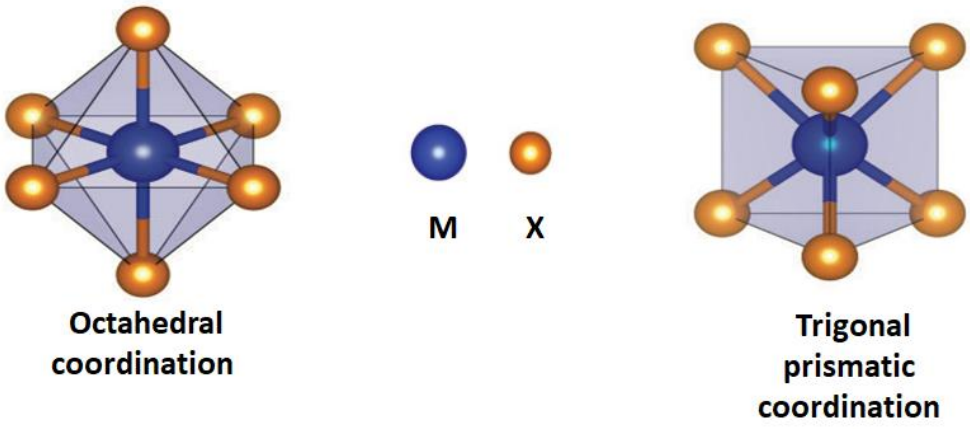

Figure 2.3 Metal Coordination of Metal Dichalcogenides.

The 1T phase is observed in a metastable metallic phase and the 2H phase is in a thermodynamically stable semiconducting phase. Most commonly encountered phases are 1T, 2H, and 3R where the letters stand for trigonal, hexagonal and rhombohedral, respectively [12].

Figure 2.4 shows the possible layered and non-layered structures of MDs materials. Each layer has a thickness of 6-7 Å, which consists of a hexagonally packed layer of metal atoms combined by weak van der Waals forces. The metal atoms provide four electrons to fill the bonding states of the MDs such that the oxidation states of the metal and chalcogen atoms are +4 and −2, respectively. The bonding length of the M-X atom lies between 3.15 Å and 4.03 Å, depending on the size of the metal and chalcogen ions [12]. In X-M-X sandwich layer, the metal (M) is bonded (Covalently) to six nearest neighbor chalcogen atoms.

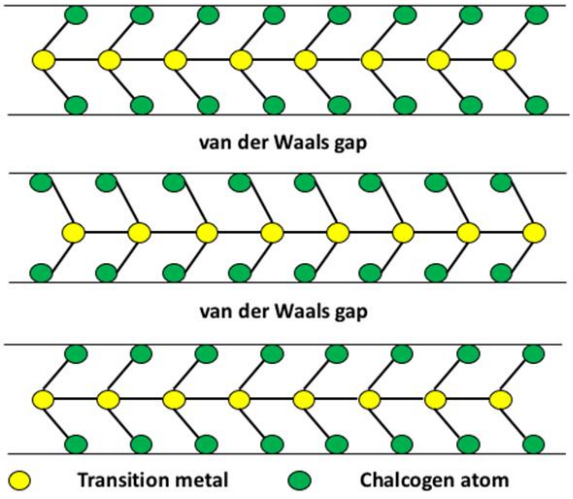

Figure 2.4 Schematic model of MDs layers.

In the next sections the different phases that can be observed are described.

2.2.1 The 1H phase

Firstly, we introduce the 1H phase where a schematic of the atomic configuration can be found in the Figure 2.5. In the 1H phase, the metal and chalcogen atoms are alternating and arranged in a honeycomb like structure (top view), however they are not in the same plane unlike graphene (side view). In 1H-MX_2 the chalcogen atoms are aligned, so viewed from above the underlying

chalcogen atom is hidden. The name 1H is given because is a single layer of the metal dichalcogenides. But, when the material possesses two layers is considered as 2H-phase (see Figure 2.8), which is the most stable phase compared to other phases and presents a semiconducting behavior [13], [14], [15]. The 2H phase is the most studied, abundant and predominant configuration in the family of semiconducting MX_2.

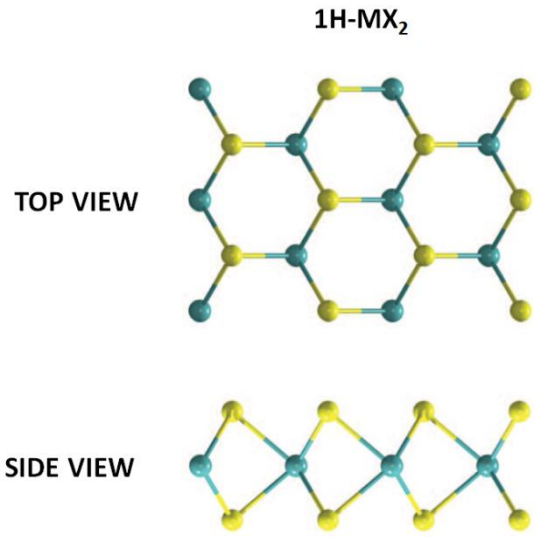

Figure 2.5 1H structure of MX_2 (top and side view) [16].

2.2.2 The 1T phase

The octahedral metal-ion coordinated 1T phase is metallic, this instable crystallographic phase is not found a naturally formed mineral. A schema of the octahedral coordination (1T structure) is represented in the Figure 2.6. In the 1T phase, the top layer of chalcogen atoms is shifted with respect to the bottom layer, exposing all the chalcogen atoms (top view). This phase is very unique due to the change of the metal coordination, affecting the electronic properties inducing metallic properties instead of semiconductor properties as in the 1H phase [17], [18], [19].

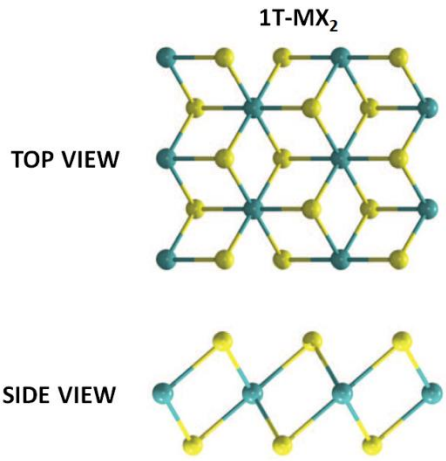

Figure 2.6 1T structure of MX_2 (top and side view) [16].

2.2.3 The 1T' phase

The 1T' configuration is a distorted 1T configuration. A schematic of the 1T' configuration is shown in Figure 2.7. Starting from the 1T phase, if the unit cell is strained on either side, the chalcogen atoms take the inline position. The isolated inline chalcogens are highlighted in red in the top view image of Figure 2.7, its signature is 1T'-MX_2 [20]. This 1T'-structure gives quasi-metallic behavior [21].

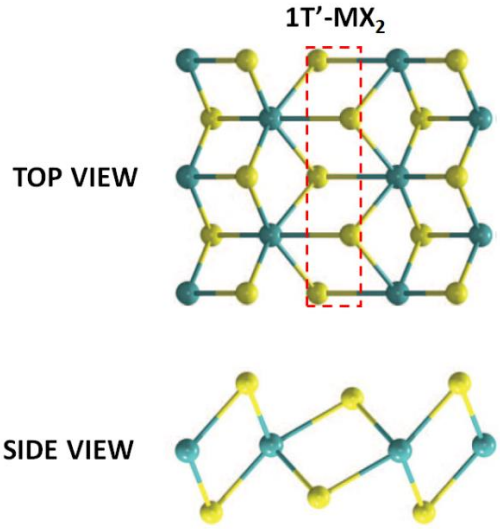

Figure 2.7 1T' structure of MX_2 (top and side view) [16].

2.2.4 The 3R phase

The 3R phase presents the same configuration as 2H-MX_2 and also the semiconducting behavior [22]. The main structural difference between them is that the 2H-phase has two layers per unit cell along the c-axis, whereas for the 3R-type, it possesses three layers per unit cell (Figure 2.8) [23]. Once heated, the 3R-type is easily converted to 2H, indicating that the 2H-type is more stable than the 3R-type.

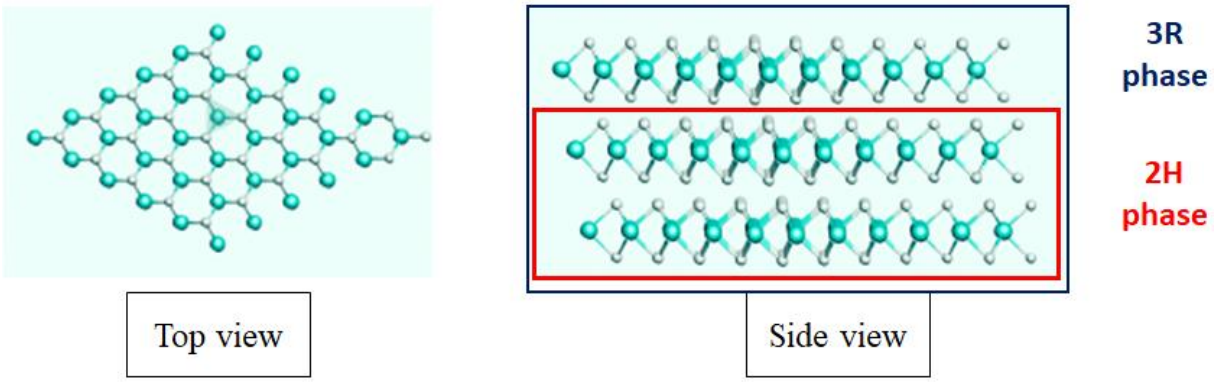

Figure 2.8 3R structure of MX_2 (top and side view) [23].

2.3 Electronic properties of Metal Dichalcogenides

The electronic properties of the MDs are important when considering their potential technological applications. It is expected that variation in the electronic band structure will occur, if the material is presented as monolayer or in the bulk form, this will determinate the electronic properties of MDs [24]. The MDs monolayers are direct bandgap semiconductors while bulk MDs exhibit indirect bandgap [25]. The conduction band and valence band positions change from bulk to few layers to monolayer due to change in electronic band structure because of electron confinement in 2D lattice as shown in Figure 2.9 and Figure 2.10.

The values for indirect and direct bandgap are 1.2 and 1.9 eV respectively for 2H-MoS_2 [26], [27] (Figure 2.9).

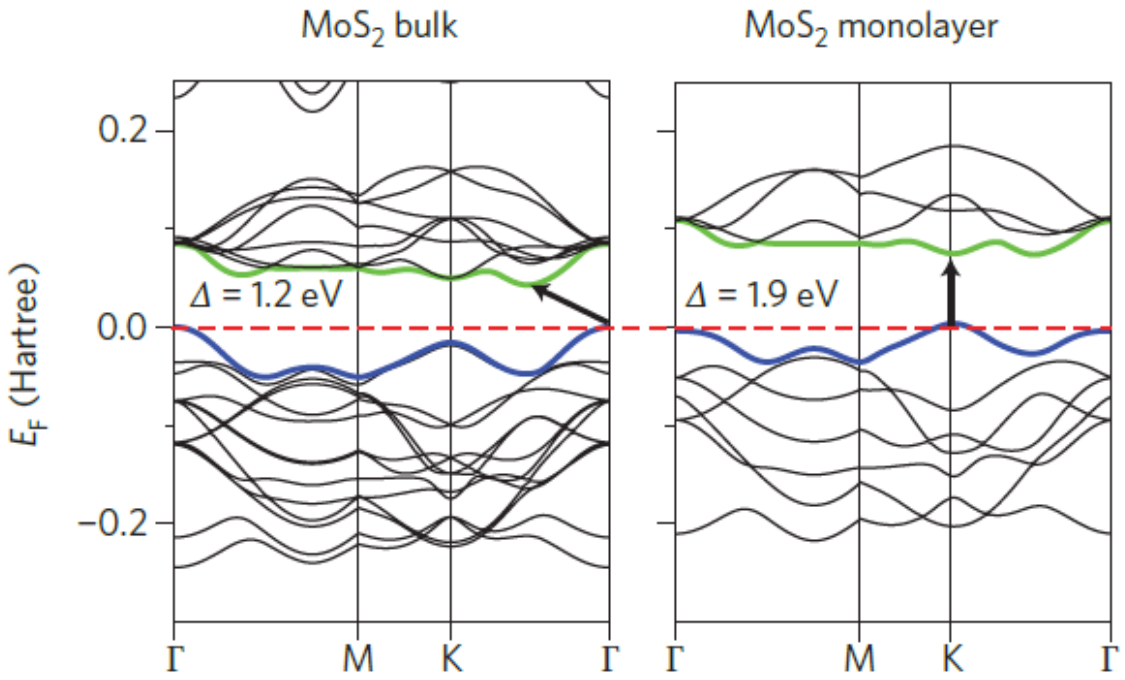

Figure 2.9 Electronic band gap structure of bulk and monolayer MoS_2 [26].

Similarly, for WS_2 the indirect bandgap of 1.3 eV changes to direct bandgap of 2.1 eV form bulk to monolayer [26], [28] (Figure 2.10).

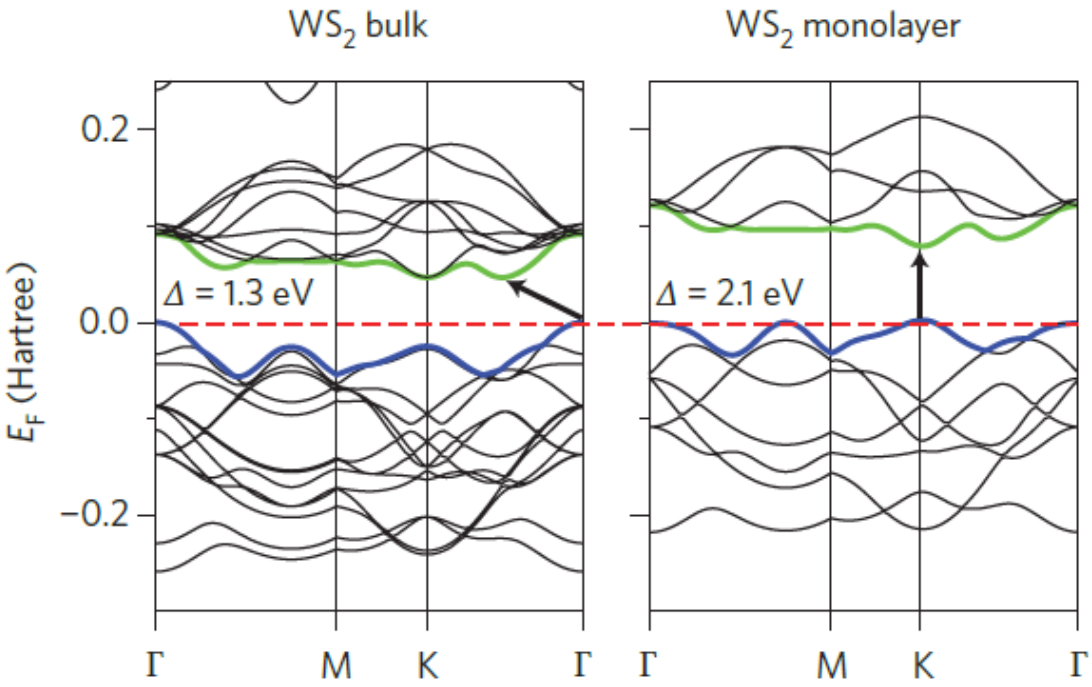

Figure 2.10 Electronic band gap structure of bulk and monolayer WS_2 [26].

The of top valence band and bottom of conduction bands in the monolayer MDs are at the same K point of the wave vector axis, which is the reason they show strong photoluminescence in visible range of electromagnetic spectrum. Therefore, these MDs have strong potential as absorbing materials in solar cells as well as in photovoltaics.

The lack of inversion center also allows high degree of freedom for charge carriers or K-valley index and thus leads to valleytronics. In bulk MDs, the MDs layers are combined with each other, layer by layer, with van der Waals force, and the weak interaction between layers influences the properties of the bulk MDs significantly. MDs can also be combined with other 2D materials to form van der Waals heterostructure devices through the weak van der Waals force.

Semiconducting 2D MDs can be considered as unique building blocks for field effect transistors (FETs), due to the lack of dangling bonds, decent structural stability and mobility comparable to Si [29].

The optical responses of 2D materials reflect their electronic band structures. The unique indirect to direct bandgap transition (when thickness is reduced to monolayer) of MDs makes them promising candidates for optoelectronics [30].

2.4 The Studied Metal Dichalcogenides

MDs are a layered material with one metal atom sandwiched between two chalcogen atoms (X-Mo-X). Strong covalent bond exists between atoms within the crystal and weak Van der Waals forces exist within layers as we can see in Figure 2.11. The six MDs studied in this thesis work are presented below in the following sections with some data that could differentiate between them.

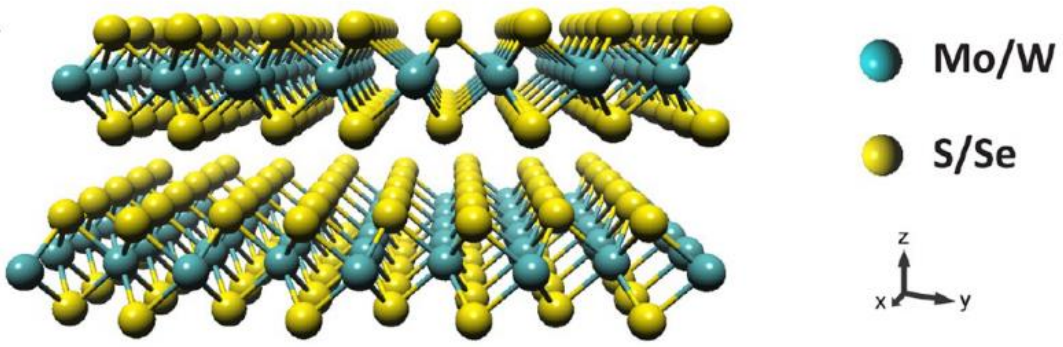

Figure 2.11 Schematic of $MoSe_2$ nanostructures [31].

2.4.1 Molybdenum Disulfide (MoS_2)

Currently, the layered molybdenum disulfide (MoS_2) has been the most studied member of MDs, in the bulk form it has an indirect band gap of 1.2 eV and thinned to monolayer it shows a direct

band gap of 1.9 eV [32]. The MoS_2 electronic properties depend directly on its layer number making them good candidates for diverse applications [33] such as optoelectronics [34]. This configuration defines its application as dry lubricants which are used in aerospace machines [35]. Additionally, single layered MoS_2 displayed properties, which are markedly different from the parent bulk structures. MoS_2 gained popularity as a replacement for graphene in electronics domain, further found applications in various sectors like hydrogen evolution reaction (HER) [36], [37] energy storage and conversion [38], gas sensors [39] and as electrodes in sodium [40] and lithium batteries [41]. The direct band gap in monolayer and ability to produce oscillating piezoelectric voltage and current outputs guaranteed the application in flexible electronics [42] and optoelectronics [34].

2.4.2 Tungsten Disulfide (WS_2)

WS_2 has a particular interest due to its electronic band gap that undergoes a indirect (1.4 eV) to direct (2 eV) transition when its thinned from bulk to monolayer [26]. Ideal materials in solar cells should have a band gap of between 1 and 2 eV, therefore WS_2 has potential to be used in low cost photovoltaic cells [43]. Bulk WS_2 has been used as a high temperature lubricant as well as an intercalation material in rechargeable batteries [44], [45]. Monolayer WS_2 has been demonstrated to possess high mobility, superior chemical robustness, and large spin−valley splitting, which make it a promising candidate for future functional optoelectronic devices [45], [46], [47]. Due to its structural and electronic similarities to MoS_2, WS_2 has received intensive investigation as photoelectrochemical catalysts [48], electrocatalysts [49], field-effect transistors (FET) [50] and hydrogen evolution [51].

2.4.3 Tin Disulfide (SnS_2)

Tin disulfide (SnS_2) is a broadband gap semiconductor with band energy gap of 2.2 eV [52], which is advantageous for suppressing source to drain tunneling in application of short channel MOSFETs [53].

SnS_2 belongs to the family IVa-VIa groups, which are earth-abundant and environment-friendly materials, and due to their low cost, they present a considerable advantage in nanoelectronics and optoelectronics. SnS_2 has exhibited abundant studies on for its optical, electrical, and photoelectric properties [3], [4], [5]. Depending on the structure of the polytype, the width of the bandgap varies over a wide range from 0.81 to 3.38 eV. Also, SnS_2 crystals are rather strongly photosensitive, a fact of considerable interest since the photosensitivity is present in the visible region of the spectrum [5]. In addition, SnS_2 has a higher theoretical capacity due to their superior delivered performance[54]. All these properties make SnS_2 a promising candidate for FETs, integrated logic circuits, photodetectors; energy storage materials and solar cells. Recently, these materials have been employed in several applications including water splitting [55] and gas sensing [56].

2.4.4 Molybdenum diselenide ($MoSe_2$)

Molybdenum diselenide ($MoSe_2$) has attracted noticeable attention due their sizable band gap and unique optical and electronical properties you need to add few properties [57]. $MoSe_2$ has attracted attention due its unique structure and remarkable physical and chemical properties. It has received attention for use as promising electrodes for lithium-ion batteries because the lamellar structure enables facile intercalation of metal ions such as Li+ because of its high capacity

(800 mA h g^{-1}) compared with theoretical capacity of commercial graphite (372 mA h g^{-1}) and MoS_2 (670 mA h g^{-1}) [58]. Other applications include use as a lubricants [59] and catalysts [57]. Reports have suggested that $MoSe_2$ could be superior to MoS_2 for device applications due to its narrower bandgap of 1.5 eV [60], [61]. Such tunable properties of $MoSe_2$ render it an ideal material for various electrical and optical applications. Recently, back-gated field effect transistors were fabricated on ultrathin $MoSe_2$ films, achieving an on/off ratio as high as 106 and an intrinsic mobility up to ~50 cm2 V^{-1} s^{-1} at room temperature, which was shown to increase nearly 4-fold at 78 K. Given such properties, monolayer to few-layers $MoSe_2$ appears to be a tremendous candidate for applications in electrical and optical devices. For electrochemical catalysts, it has been reported that active sites at the edges of $MoSe_2$ sheets have similar properties as in vertically-aligned MoS_2 sheets. The edges are full of dangling bonds and chemically active to manipulate the properties of the layered materials, for example in n-type doping for graphene. In addition, the edges of layered materials are also the active sites for many important catalytic reactions, such as hydrodesulfurization, hydrogen evolution reaction (HER), oxygen reduction reactions and methane conversion [57].

2.4.5 Tungsten Diselenide (WSe_2)

Bulk WSe_2 has attracted increasing attention because of its interesting properties, exemplified by its ultralow thermal conductivity at room temperature (0.05 $W.m^{-1}.K^{-1}$) when considering disordered crystals [62]. This bulk material has also been reported to be efficient in different applications, such as catalysts for hydrogen evolution reactions [31], [63], or in photovoltaic devices [31] because it possesses good stability and resistance to oxidation in humid

environments [64]. Actually, it has been reported that the properties of MDs, such as MoS_2, WS_2, and WSe_2, depend directly on the number of layers in the structure, especially in systems with few layers [65]. Moreover, monolayer WSe_2 possesses a small band-gap (smaller than monolayer MoS_2), and shows an ambipolar transport phenomenon [66]. Several potential optoelectronic applications have been described using monolayer WSe_2, such as photodetectors [67], light-emitting diodes [68], and solar-energy convertors [69].

2.4.6 Tin Diselenide ($SnSe_2$)

$SnSe_2$ has a similar configuration as MoS_2 and as SnS_2, belongs to the family IVa-VIa groups. $SnSe_2$ has a direct band gap of 1.4 eV [54], the layered structure, proper electronic properties and inherent semiconducting characteristics make $SnSe_2$ attractive in for novel nanoelectronics and optoelectronic devices [70].

2.5 Technological Applications of MDs

The electronic, electrical, and optical properties of MDs open avenues for a myriad of potential technological applications. The presence of a direct and indirect bandgaps makes them ideal candidates for optoelectronic devices, field-effect transistors, gas sensing devices, energy storage devices, etc. A few applications of these materials are discussed in this section.

2.5.1 Optoelectronic devices

MDs have diverse optical properties, for example, bandgaps from the IR to the near UV energy range, the direct and indirect transitions depending in the number of layers, and their large excitonic binding energies. Development of novel optical devices based on these materials has been driven by these unique characteristics [71].

For example, MDs, such as MoS_2, are characterized by strong light-matter interaction and photon absorption which are desired characteristics for photodetector devices [72]. Lee *et al.* [73] reported that light detection depends on the number of layers, in the case of MoS_2, green light for mono and bi-layer, and red light for tri-layer structures (Figure 2.12). Such differences were attributed to the thickness-modulated optical gap of nanosheets. According to their photoelectric probing technique on working transistors with the nanosheets, single layer MoS_2 has a significant energy bandgap of 1.82 eV, while those of double- and triple-layer MoS_2 showed 1.65 and 1.35 eV, respectively.

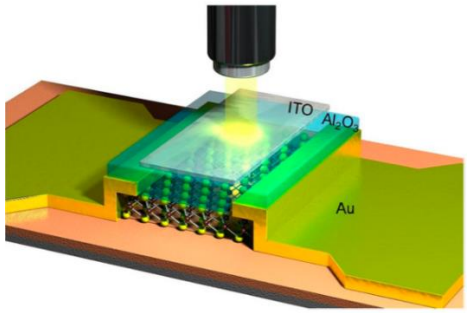

Figure 2.12 Schematic 3D view of single-layer transistor with hexagonal structure MoS_2 nanosheet, 50 nm-thick Al_2O_3 dielectric, and ITO top-gate under monochromatic light [73].

Considering other MDs, Yu *et al.* [74] reported on O_2-plasma-treated SnS_2 photodetectors exhibiting response with excellent photoelectrical conversion abilities. Herein, oxygen plasma treatment is employed to enhance the optoelectronic performance of SnS_2 flakes, which results in artificial sub-bandgap in SnS_2. As a result, the constructed O_2-plasma-treated SnS_2-based device demonstrates a significant improvement in broadband photo sensing from ultraviolet to cover the entire visible light span (300–750 nm).

WSe_2 has been used as potential active layer in photodetector applications, Zheng *et al.* [75] have fabricated a flexible, all-transparent photodetector with excellent transparency of approximately

80% in the visible light range and superior photo response characteristics and an ultra-broadband spectral detection ranges from 370 to 1064 nm (Figure 2.13). In addition, the device photocurrents demonstrate high stability and reversibility, even after the device has been bent into a small radius of 5 mm or placed in the atmosphere for a month.

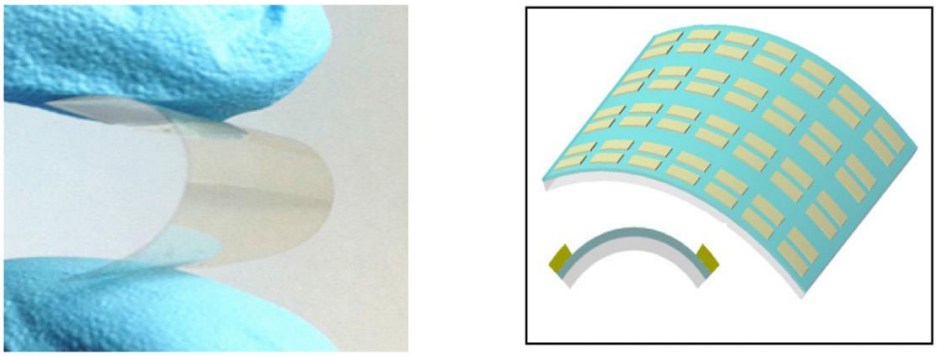

Figure 2.13 a) Optical image and b) schematic illustration of the fabricated WSe_2 photodetectors in a flexible state [75].

2.5.2 Field-effect transistors (FET)

In basic terms, a transistor is a semiconductor electronic device which controls the flow of the electrical charge. Field-effect transistors (FETs) are the particular class of transistors in which a semiconductor material is used as a channel [76].

2D nanomaterials are considered promising channel for FET sensors. They exhibit high potential in miniaturized and low-power consumption transistor due to 2D structure. 2D nanomaterials are also potentially more sensitive in sensing applications due to their 2D nanostructures that have high specific surface area for dense modification of binding sites [77].

Alike other inorganic semiconductors, MDs have drawn attention as they demonstrate high mobility of charge carriers associated to the strong covalent bonding of atoms within the layers. They have a weak van der Waals interlayer bonding, which leads to a low field-effect threshold

due to the low density of surface traps. The MD-based transistors can be used in the electron- and hole-accumulation modes [78].

For these properties, MDs have been used as channel materials in high-performance field-effect transistors (FET) [79]. However, not all of them have demonstrated the same combination of characteristics.

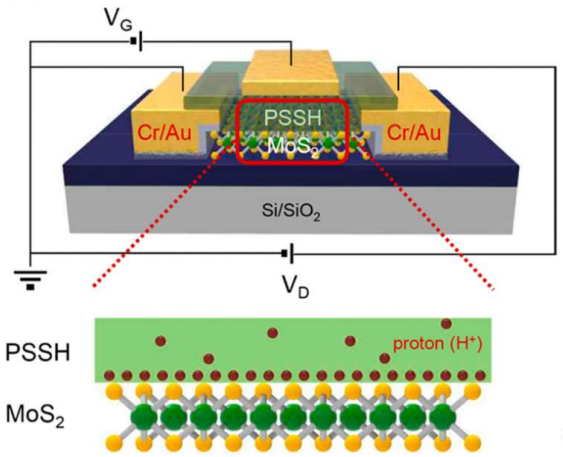

Figure 2.14 Structure diagram of the field effect transistor (FET), choosing PSSH as the proton-conductor-gate [80].

2.5.3 Gas sensing devices

A key problem in the use of different type of gases in diverse areas like domestic, industries, food packaging, laboratories, etc. is the lack of optimal devices for their detection. During the last years, many efforts have been done for developed these devices due its potential applications. The sensing mechanism is based on changes in electrical resistance or conductance of nanomaterials due to chemical interaction in between the gaseous species and the nanomaterials. The resistance of the materials is determinate by the charge transfer process induced by chemical interactions. The resistance decreases in presence of reducing gases such as

Methane, Liquefied Petroleum Gas (LPG), Ammonia Gas (NH_3) when the nanomaterials are n-type and increases if they are p-type [81].

In the past few years, it has been emphasized experimentally and theoretically that semi-conducting MDs are a potential candidate material for gas-sensing applications due to the high surface-to-volume ratio. Several groups demonstrated the applicability of single monolayer and few-layer MoS_2 structures as effective sensors, exhibiting highly selective reactivity to a range of analytes and providing sensitive transduction of transient surface physisorption events to the conductance of the monolayer channel. 2D nanomaterials may present good sensing characteristics such as fast response, commendable selectivity, excellent sensitivity and the lower limit of detection for the gas-sensing [81]. It has been reported that structural defects, including point defects, grain boundaries and edges in MDs play significant roles in sensing applications. There are two advantages in the use of 2D structures in gas-sensing applications: the large specific area rich on active sites, increasing interaction with a large number of gas molecules. And, the control of the electronic properties by controlling the number of layers [82]. An important characteristic of 2D materials is their ability for gas detection at low temperature, therefore low power consumption gas detection systems can be manufactured using simplified processes and operating cost are reduced [83].

New materials often generate entirely new possibilities, pushing the limits of the accepted boundaries of materials properties within which engineers operate. With the increasing demand of highly sensitive, fast and stable sensor, a series of sensing applications of nanoscale MDs-based composites and hybrids have been of growing interest. For example, Pham et al. [84] discuss that Red LED illumination with photon energy matching the direct band gap of the single-layer MoS_2

allowed to use induced photocurrent instead of dark current as a tool for NO_2 gas sensing (Figure 2.15).

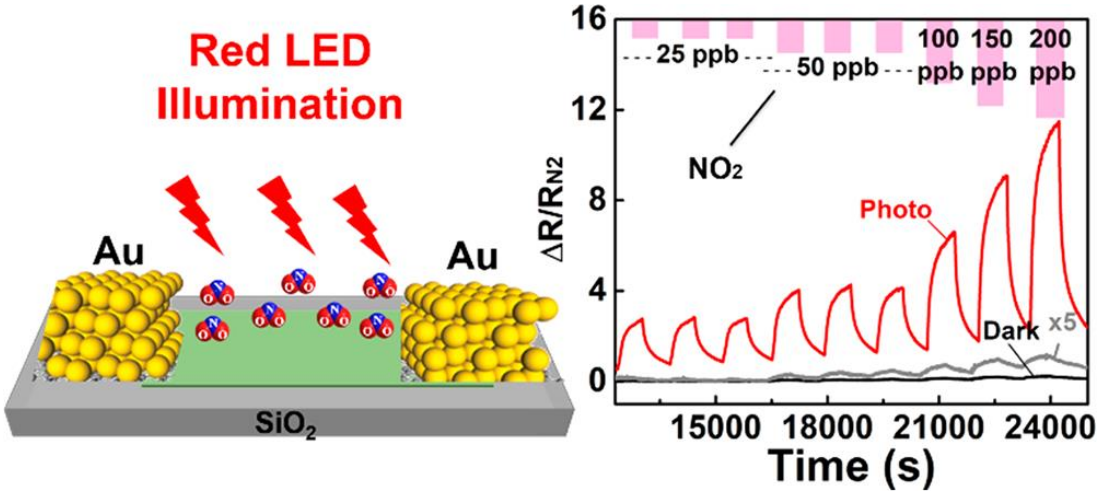

Figure 2.15 Effect of NO_2 gas exposure at concentrations from 25 to 200 ppb on normalized resistance of the Au−MoS_2−Au device in the dark (black line; gray line shows 5-fold magnified data) and under red LED illumination (red curve) [84].

2.5.4 Energy storage devices

Renewable energy, such as solar energy and wind energy are expected to replace the conventional fossil fuels. However, a main drawback for large-scale grid application is the lack of stable generation of electricity due to nonconstant supply of renewable energy [85]. Therefore, it is important to develop efficient electrical energy storage systems to store renewable energy, obtaining stable power output for practical usage. Electrochemical Energy Storage (EES) is an emergent solution, few examples are batteries and supercapacitors, they are able to store electrical energy via the interconversion of chemical and electrical energy [86]. The 2D nature of layered MDs nanomaterials makes them suitable active materials for the EES due to the following aspects:

i) The large specific surface area ensures a large contact area between the active materials and the electrolyte, enabling the fast “Faradaic” and “non-Faradaic” reactions at the surfaces of layered MDs nanomaterials [87].

ii) The under-coordinated edge sites of layered MDs nanomaterials can act as adsorption sites for metal ions and thus contribute to extra metal-ion storage capacities [88].

iii) The adjacent X–M–X layers in layered MDs nanomaterials are coupled by weak van der Waals forces. The interlayer space between layers promotes fast ion diffusion, insertion and extraction, as well as better material utilization during the metal-ion insertion process [88].

iv) The thin and flexible characteristics of 2D MDs nanosheets make them easy to be incorporated into flexible EES devices [89].

MDs nanomaterials are often hybridized with other kind of materials (carbon materials, metal sulfides, metal oxides and conducting polymers) when they are applied in EES systems. Carbon materials are the most frequently used materials for the hybridization because they present important properties such as the high electrical conductivity, which can accelerate the electron transport in layered MDs/carbon hybrids [90]. Additionally, 3D layered MDs-based nanomaterials with hierarchical structures can be constructed by growing layered MDs on the pre-synthesized substrates, which are expected to exhibit excellent electrochemical performance.

2.5.5 Catalytic applications of Metal Dichalcogenides

2D materials have attracted a lot of attention for their potential application in the catalysis of hydrogen evolution, hydrodesulfurization and CO_2 reduction. The edges of their sheets are

reported to provide active sites for various processes [91]. The development of novel and efficient catalysts for renewable hydrogen generation has brought much interest since H_2 is regarded as a superior energy source due to its large energy density and being environmental-friendly.

Early studies have shown that MDs are useful catalysts in hydro-desulfurization (HDS) reactions. MDs possess edges that comprise chalcogen or metal atoms. Edges can also be covered with 0%, 50%, 75%, or 100% of chalcogen atoms, depending on the synthesis conditions and the size of the nanosheets [92]. Vertically aligned MDs nanosheets are also synthesized for catalytic applications due to having a high edge density [93].

Structural engineering through 2H semiconducting to 1T metallic phase transformation of MoS_2 shows a notable electrocatalytic performance, however the metastable nature of 1T phase will end up restacking in 2H semiconducting phase during the hydrogen evolution reaction (HER) [94]. The surface area, in exfoliated MD nanosheets, carries high density of edges which are potential active sites for electrochemical applications in sensing and energy production, in particular for hydrogen evolution reaction (HER). Exfoliated MD nanosheets have generated a great deal of attention as potential electrocatalysts for HER. The HER activity of MDs nanosheets stems from their edges while their basal planes are deemed inert. Efforts are underway to develop MDs with optimized HER abilities comparable to platinum such as by increasing the number of active sites improving electrical conductivity and enhancing the catalytic capacity of the active sites [95].

2.6 References

1. Han, S.A.; Bhatia, R.; Kim, S.W. Synthesis, properties and potential applications of two-dimensional transition metal dichalcogenides. *Nano Converg.* **2015**, *2*,

doi:10.1186/s40580-015-0048-4.

2. Zhang, X.; Cui, Y.; Sun, L.; Li, M.; Du, J.; Huang, Y. Stabilities, and electronic and piezoelectric properties of two-dimensional tin dichalcogenide derived Janus monolayers. *J. Mater. Chem. C* **2019**, *7*, 13203–13210, doi:10.1039/c9tc04461b.

3. Lifshitz, E.; Chen, Z.; Bykov, L. Optical spectroscopy of 1T-SnS2 single crystal. *J. Phys. Chem.* **1993**, *97*, 238–242, doi:10.1021/j100103a041.

4. Dubrovskiĭ, G.B. Crystal structure and electronic spectrum of SnS2. *Phys. Solid State* **1998**, *40*, 1557–1562, doi:10.1134/1.1130598.

5. Dubrovskiĭ, G.B.; Shelykh, A.I. Photoelectric properties of tin disulfide. *Phys. Solid State* **1998**, *40*, 1295–1296, doi:10.1134/1.1130547.

6. Tan, B.; Yang, H.; Hu, Y.; Gao, F.; Wang, L.; Dai, M.; Zhang, S.; Shang, H.; Chen, H.; Hu, P. Synthesis of High-Quality Multilayer Hexagonal Boron Nitride Films on Au Foils for Ultrahigh Rejection Ratio Solar-Blind Photodetection. *ACS Appl. Mater. Interfaces* **2020**, *12*, 28351–28359, doi:10.1021/acsami.0c00449.

7. Khan, K.; Tareen, A.K.; Aslam, M.; Khan, M.F.; Shi, Z.; Ma, C.; Shams, S.S.; Khatoon, R.; mahmood, N.; Zhang, H.; et al. *Synthesis, properties and novel electrocatalytic applications of the 2D-borophene Xenes*; Elsevier Ltd, 2020; Vol. 59; ISBN 0000000272.

8. Li, C.; Kang, J.; Xie, J.; Wang, Y.; Zhou, L.; Hu, H.; Li, X.; He, J.; Wang, B.; Zhang, H. Two-dimensional monoelemental germanene nanosheets: Facile preparation and optoelectronic applications. *J. Mater. Chem. C* **2020**, *8*, 16318–16325, doi:10.1039/d0tc03892j.

9. Khandelwal, A.; Mani, K.; Karigerasi, M.H.; Lahiri, I. Phosphorene – The two-dimensional

black phosphorous: Properties, synthesis and applications. *Mater. Sci. Eng. B Solid-State Mater. Adv. Technol.* **2017**, *221*, 17–34, doi:10.1016/j.mseb.2017.03.011.

10. Vogt, P.; Capiod, P.; Berthe, M.; Resta, A.; De Padova, P.; Bruhn, T.; Le Lay, G.; Grandidier, B. Synthesis and electrical conductivity of multilayer silicene. *Appl. Phys. Lett.* **2014**, *104*, 4–9, doi:10.1063/1.4861857.
11. Manzeli, S.; Ovchinnikov, D.; Pasquier, D.; Yazyev, O. V.; Kis, A. 2D transition metal dichalcogenides. *Nat. Rev. Mater.* **2017**, *2*, doi:10.1038/natrevmats.2017.33.
12. Chhowalla, M.; Shin, H.S.; Eda, G.; Li, L.J.; Loh, K.P.; Zhang, H. The chemistry of two-dimensional layered transition metal dichalcogenide nanosheets. *Nat. Chem.* **2013**, *5*, 263–275, doi:10.1038/nchem.1589.
13. Chhowalla, M.; Voiry, D.; Yang, J.; Shin, H.S.; Loh, K.P. Phase-engineered transition-metal dichalcogenides for energy and electronics. *MRS Bull.* **2015**, *40*, 585–591, doi:10.1557/mrs.2015.142.
14. Joe, J.; Bae, C.; Kim, E.; Ho, T.A.; Yang, H.; Park, J.H.; Shin, H. Mixed-phase (2H and 1T) MoS2 catalyst for a highly efficient and stable si photocathode. *Catalysts* **2018**, *8*, 1–15, doi:10.3390/catal8120580.
15. Lv, R.; Robinson, J.A.; Schaak, R.E.; Sun, D.; Sun, Y.; Mallouk, T.E.; Terrones, M. Transition metal dichalcogenides and beyond: Synthesis, properties, and applications of single- and few-layer nanosheets. *Acc. Chem. Res.* **2015**, *48*, 56–64, doi:10.1021/ar5002846.
16. Xiaofeng Qian, Junwei Liu, Liang Fu, J.L. Quantum spin Hall effect in two-dimensional transition metal dichalcogenides. *Science (80-.).* **2014**, *346*, 1344–1348.
17. Yu, Y.; Nam, G.H.; He, Q.; Wu, X.J.; Zhang, K.; Yang, Z.; Chen, J.; Ma, Q.; Zhao, M.; Liu, Z.; et

al. High phase-purity 1T'-MoS2- and 1T'-MoSe2-layered crystals. *Nat. Chem.* **2018**, *10*, 638–643, doi:10.1038/s41557-018-0035-6.

18. Huang, H.; Cui, Y.; Li, Q.; Dun, C.; Zhou, W.; Huang, W.; Chen, L.; Hewitt, C.A.; Carroll, D.L. Metallic 1T phase MoS2 nanosheets for high-performance thermoelectric energy harvesting. *Nano Energy* **2016**, *26*, 172–179, doi:10.1016/j.nanoen.2016.05.022.

19. Acerce, M.; Voiry, D.; Chhowalla, M. Metallic 1T phase MoS2 nanosheets as supercapacitor electrode materials. *Nat. Nanotechnol.* **2015**, *10*, 313–318, doi:10.1038/nnano.2015.40.

20. Qian, X.; Liu, J.; Fu, L.; Li, J. Quantum spin hall effect in two - Dimensional transition metal dichalcogenides. *Science (80-.).* **2014**, *346*, 1344–1347, doi:10.1126/science.1256815.

21. Tan, S.J.R.; Abdelwahab, I.; Ding, Z.; Zhao, X.; Yang, T.; Loke, G.Z.J.; Lin, H.; Verzhbitskiy, I.; Poh, S.M.; Xu, H.; et al. Chemical Stabilization of 1T' Phase Transition Metal Dichalcogenides with Giant Optical Kerr Nonlinearity. *J. Am. Chem. Soc.* **2017**, *139*, 2504–2511, doi:10.1021/jacs.6b13238.

22. Toh, R.J.; Sofer, Z.; Luxa, J.; Sedmidubský, D.; Pumera, M. 3R phase of MoS2 and WS2 outperforms the corresponding 2H phase for hydrogen evolution. *Chem. Commun.* **2017**, *53*, 3054–3057, doi:10.1039/c6cc09952a.

23. Meng, C.; Chen, X.; Gao, Y.; Zhao, Q.; Kong, D.; Lin, M.; Chen, X.; Li, Y.; Zhou, Y. Recent modification strategies of MoS2 for enhanced electrocatalytic hydrogen evolution. *Molecules* **2020**, *25*, 1–18, doi:10.3390/molecules25051136.

24. Gusakova, J.; Wang, X.; Shiau, L.L.; Krivosheeva, A.; Shaposhnikov, V.; Borisenko, V.; Gusakov, V.; Tay, B.K. Electronic Properties of Bulk and Monolayer TMDs: Theoretical Study Within DFT Framework (GVJ-2e Method). *Phys. Status Solidi Appl. Mater. Sci.* **2017**,

214, 1–7, doi:10.1002/pssa.201700218.

25. Zhou, K.G.; Zhao, M.; Chang, M.J.; Wang, Q.; Wu, X.Z.; Song, Y.; Zhang, H.L. Size-dependent nonlinear optical properties of atomically thin transition metal dichalcogenide nanosheets. *Small* **2015**, *11*, 694–701, doi:10.1002/smll.201400541.
26. Wang, Q.H.; Kalantar-Zadeh, K.; Kis, A.; Coleman, J.N.; Strano, M.S. Electronics and optoelectronics of two-dimensional transition metal dichalcogenides. *Nat. Nanotechnol.* **2012**, *7*, 699–712, doi:10.1038/nnano.2012.193.
27. Yin, Z.; Li, H.; Li, H.; Jiang, L.; Shi, Y.; Sun, Y.; Lu, G.; Zhang, Q.; Chen, X.; Zhang, H. Single-layer MoS 2 phototransistors. *ACS Nano* **2012**, *6*, 74–80, doi:10.1021/nn2024557.
28. Rong, Y.; Fan, Y.; Leen Koh, A.; Robertson, A.W.; He, K.; Wang, S.; Tan, H.; Sinclair, R.; Warner, J.H. Controlling sulphur precursor addition for large single crystal domains of WS2. *Nanoscale* **2014**, *6*, 12096–12103, doi:10.1039/c4nr04091k.
29. Radisavljevic, B.; Radenovic, A.; Brivio, J.; Giacometti, V.; Kis, A. Single-layer MoS2 transistors. *Nat. Nanotechnol.* **2011**, *6*, 147–150, doi:10.1038/nnano.2010.279.
30. Liu, H.L.; Shen, C.C.; Su, S.H.; Hsu, C.L.; Li, M.Y.; Li, L.J. Optical properties of monolayer transition metal dichalcogenides probed by spectroscopic ellipsometry. *Appl. Phys. Lett.* **2014**, *105*, doi:10.1063/1.4901836.
31. Wang, H.; Kong, D.; Johanes, P.; Cha, J.J.; Zheng, G.; Yan, K.; Liu, N.; Cui, Y. MoSe2 and WSe2 nanofilms with vertically aligned molecular layers on curved and rough surfaces. *Nano Lett.* **2013**, *13*, 3426–3433, doi:10.1021/nl401944f.
32. Li, X.; Zhu, H. Two-dimensional MoS2: Properties, preparation, and applications. *J. Mater.* **2015**, *1*, 33–44, doi:10.1016/j.jmat.2015.03.003.

33. Mak, K.F.; Lee, C.; Hone, J.; Shan, J.; Heinz, T.F. Atomically thin MoS2: A new direct-gap semiconductor. *Phys. Rev. Lett.* **2010**, *105*, 2–5, doi:10.1103/PhysRevLett.105.136805.

34. Zhang, X.; Biekert, N.; Choi, S.; Naylor, C.H.; De-Eknamkul, C.; Huang, W.; Zhang, X.; Zheng, X.; Wang, D.; Johnson, A.T.C.; et al. Dynamic Photochemical and Optoelectronic Control of Photonic Fano Resonances via Monolayer MoS2 Trions. *Nano Lett.* **2018**, *18*, 957–963, doi:10.1021/acs.nanolett.7b04355.

35. Colas, G.; Saulot, A.; Regis, E.; Berthier, Y. Investigation of crystalline and amorphous MoS2 based coatings: Towards developing new coatings for space applications. *Wear* **2015**, *330–331*, 448–460, doi:10.1016/j.wear.2015.01.011.

36. Voiry, D.; Salehi, M.; Silva, R.; Fujita, T.; Chen, M.; Asefa, T.; Shenoy, V.B.; Eda, G.; Chhowalla, M. Conducting MoS2 nanosheets as catalysts for hydrogen evolution reaction. *Nano Lett.* **2013**, *13*, 6222–6227, doi:10.1021/nl403661s.

37. Li, Y.; Wang, H.; Xie, L.; Liang, Y.; Hong, G.; Dai, H. MoS2 nanoparticles grown on graphene: An advanced catalyst for the hydrogen evolution reaction. *J. Am. Chem. Soc.* **2011**, *133*, 7296–7299, doi:10.1021/ja201269b.

38. Xue, Y.; Zhang, Q.; Wang, W.; Cao, H.; Yang, Q.; Fu, L. Opening Two-Dimensional Materials for Energy Conversion and Storage: A Concept. *Adv. Energy Mater.* **2017**, *7*, 1–23, doi:10.1002/aenm.201602684.

39. Shokri, A.; Salami, N. Gas sensor based on MoS2 monolayer. *Sensors Actuators, B Chem.* **2016**, *236*, 378–385, doi:10.1016/j.snb.2016.06.033.

40. Xie, X.; Makaryan, T.; Zhao, M.; Van Aken, K.L.; Gogotsi, Y.; Wang, G. MoS2 Nanosheets Vertically Aligned on Carbon Paper: A Freestanding Electrode for Highly Reversible

Sodium-Ion Batteries. *Adv. Energy Mater.* **2016**, *6*, 1–7, doi:10.1002/aenm.201502161.

41. Feng, C.; Ma, J.; Li, H.; Zeng, R.; Guo, Z.; Liu, H. Synthesis of molybdenum disulfide (MoS2) for lithium ion battery applications. *Mater. Res. Bull.* **2009**, *44*, 1811–1815, doi:10.1016/j.materresbull.2009.05.018.

42. Pu, J.; Yomogida, Y.; Liu, K.; Li, L.; Iwasa, Y.; Takenobu, T. Highly Flexible MoS2 Thin-Film Transistors with Ion Gel Dielectrics. *Nano Lett.* **2012**, *13*, 4013–4017.

43. Carmalt, C.J.; Parkin, I.P.; Peters, E.S. Atmospheric pressure chemical vapour deposition of WS2 thin films on glass. *Polyhedron* **2003**, *22*, 1499–1505, doi:10.1016/S0277-5387(03)00194-3.

44. Brown, S.; Musfeldt, J.L.; Mihut, I.; Betts, J.B.; Migliori, A.; Zak, A.; Tenne, R. Bulk vs nanoscale WS2: Finite size effects and solid-state lubrication. *Nano Lett.* **2007**, *7*, 2365–2369, doi:10.1021/nl0710147.

45. Bhandavat, R.; David, L.; Singh, G. Synthesis of surface-functionalized WS 2 nanosheets and performance as li-ion battery anodes. *J. Phys. Chem. Lett.* **2012**, *3*, 1523–1530, doi:10.1021/jz300480w.

46. Lan, F.; Yang, R.; Xu, Y.; Qian, S.; Zhang, S.; Cheng, H.; Zhang, Y. Synthesis of large-scale single-crystalline monolayer WS2 using a semi-sealed method. *Nanomaterials* **2018**, *8*, 1–7, doi:10.3390/nano8020100.

47. Zhang, W.; Huang, Z.; Zhang, W.; Li, Y. Two-dimensional semiconductors with possible high room temperature mobility. *Nano Res.* **2014**, *7*, 1731–1737, doi:10.1007/s12274-014-0532-x.

48. Ho, W.; Yu, J.C.; Lin, J.; Yu, J.; Li, P. Preparation and photocatalytic behavior of MoS2 and

WS 2 nanocluster sensitized TiO2. *Langmuir* **2004**, *20*, 5865–5869, doi:10.1021/la049838g.

49. Holt, C.M.B.; Murphy, S.; Gray, M.R.; Mitlin, D. Electrocatalytic hydrogenation of 2-cyclohexen-1-one in a high sulfur environment using a carbon-supported nanostructured tungsten sulfide catalyst. *Catal. Commun.* **2010**, *12*, 314–317, doi:10.1016/j.catcom.2010.09.028.

50. Georgiou, T.; Jalil, R.; Belle, B.D.; Britnell, L.; Gorbachev, R. V.; Morozov, S. V.; Kim, Y.J.; Gholinia, A.; Haigh, S.J.; Makarovsky, O.; et al. Vertical field-effect transistor based on graphene-WS 2 heterostructures for flexible and transparent electronics. *Nat. Nanotechnol.* **2013**, *8*, 100–103, doi:10.1038/nnano.2012.224.

51. Voiry, D.; Yamaguchi, H.; Li, J.; Silva, R.; Alves, D.C.B.; Fujita, T.; Chen, M.; Asefa, T.; Shenoy, V.B.; Eda, G.; et al. Enhanced catalytic activity in strained chemically exfoliated WS 2 nanosheets for hydrogen evolution. *Nat. Mater.* **2013**, *12*, 850–855, doi:10.1038/nmat3700.

52. Mandalidis, S.; Kalomiros, J.A.; Kambas, K.; Anagnostopoulos, A.N. Optical investigation of SnS2 single crystals. *J. Mater. Sci.* **1996**, *31*, 5975–5978, doi:10.1007/BF01152147.

53. Wang, J.; Lundstrom, M. Does source-to-drain tunneling limit the ultimate scaling of MOSFETs? *Tech. Dig. - Int. Electron Devices Meet.* **2002**, 707–710, doi:10.1109/iedm.2002.1175936.

54. Sun, W.; Rui, X.; Yang, D.; Sun, Z.; Li, B.; Zhang, W.; Zong, Y.; Madhavi, S.; Dou, S.; Yan, Q. Two-Dimensional Tin Disulfide Nanosheets for Enhanced Sodium Storage. *ACS Nano* **2015**, *9*, 11371–11381, doi:10.1021/acsnano.5b05229.

55. Sun, Y.; Cheng, H.; Gao, S.; Sun, Z.; Liu, Q.; Leu, Q.; Lei, F.; Yao, T.; He, J.; Wei, S.; et al.

Freestanding tin disulfide single-layers realizing efficient visible-light water splitting. *Angew. Chemie - Int. Ed.* **2012**, *51*, 8727–8731, doi:10.1002/anie.201204675.

56. Ou, J.Z.; Ge, W.; Carey, B.; Daeneke, T.; Rotbart, A.; Shan, W.; Wang, Y.; Fu, Z.; Chrimes, A.F.; Wlodarski, W.; et al. Physisorption-Based Charge Transfer in Two-Dimensional SnS2 for Selective and Reversible NO2 Gas Sensing. *ACS Nano* **2015**, *9*, 10313–10323, doi:10.1021/acsnano.5b04343.

57. Kong, D.; Wang, H.; Cha, J.J.; Pasta, M.; Koski, K.J.; Yao, J.; Cui, Y. Synthesis of MoS2 and MoSe2 films with vertically aligned layers. *Nano Lett.* **2013**, *13*, 1341–1347, doi:10.1021/nl400258t.

58. Liu, N.; Choi, W.; Kim, H.; Jung, C.; Kim, J.; Choo, S.H.; Kwon, Y.; An, B.S.; Hong, S.; So, S.; et al. Rapid and mass-producible synthesis of high-crystallinity MoSe2 nanosheets by ampoule-loaded chemical vapor deposition. *Nanoscale* **2020**, *12*, 6991–6999, doi:10.1039/c9nr10418f.

59. Bergmann, E.; Melet, G.; Müller, C.; Simon-Vermot, A. Friction properties of sputtered dichalcogenide layers. *Tribol. Int.* **1981**, *14*, 329–332, doi:10.1016/0301-679X(81)90100-6.

60. O'Brien, M.; Mcevoy, N.; Hanlon, D.; Lee, K.; Gatensby, R.; Coleman, J.N.; Duesberg, G.S. Low wavenumber Raman spectroscopy of highly crystalline MoSe2 grown by chemical vapor deposition. *Phys. Status Solidi Basic Res.* **2015**, *252*, 2385–2389, doi:10.1002/pssb.201552225.

61. Wu, C.T.; Hu, S.Y.; Tiong, K.K.; Lee, Y.C. Anisotropic effects in the Raman scattering of Re-doped 2H-MoSe2 layered semiconductors. *Results Phys.* **2017**, *7*, 4096–4100, doi:10.1016/j.rinp.2017.10.033.

62. Costescu, R.M.; Cahill, D.G.; Fabreguette, F.H.; Sechrist, Z.A.; George, S.M. Ultra-Low Thermal Conductivity in W/Al2O3 Nanolaminates. *Science (80-.).* **2004**, *303*, 989–990, doi:10.1126/science.1093711.

63. Velazquez, J.M.; Saadi, F.H.; Pieterick, A.P.; Spurgeon, J.M.; Soriaga, M.P.; Brunschwig, B.S.; Lewis, N.S. Synthesis and hydrogen-evolution activity of tungsten selenide thin films deposited on tungsten foils. *J. Electroanal. Chem.* **2014**, *716*, 45–48, doi:10.1016/j.jelechem.2013.11.030.

64. Liu, W.; Kang, J.; Sarkar, D.; Khatami, Y.; Jena, D.; Banerjee, K. Role of metal contacts in designing high-performance monolayer n-type WSe2 field effect transistors. *Nano Lett.* **2013**, *13*, 1983–1990, doi:10.1021/nl304777e.

65. Jana, M.K.; Rao, C.N.R. Two-dimensional inorganic analogues of graphene: Transition metal dichalcogenides. *Philos. Trans. R. Soc. A Math. Phys. Eng. Sci.* **2016**, *374*, doi:10.1098/rsta.2015.0318.

66. Fang, H.; Chuang, S.; Chang, T.C.; Takei, K.; Takahashi, T.; Javey, A. High-performance single layered WSe 2 p-FETs with chemically doped contacts. *Nano Lett.* **2012**, *12*, 3788–3792, doi:10.1021/nl301702r.

67. Baugher, B.W.H.; Churchill, H.O.H.; Yang, Y.; Jarillo-Herrero, P. Optoelectronic devices based on electrically tunable p-n diodes in a monolayer dichalcogenide. *Nat. Nanotechnol.* **2014**, *9*, 262–267, doi:10.1038/nnano.2014.25.

68. Ross, J.S.; Klement, P.; Jones, A.M.; Ghimire, N.J.; Yan, J.; Mandrus, D.G.; Taniguchi, T.; Watanabe, K.; Kitamura, K.; Yao, W.; et al. Electrically tunable excitonic light-emitting diodes based on monolayer WSe2 p-n junctions. *Nat. Nanotechnol.* **2014**, *9*, 268–272,

doi:10.1038/nnano.2014.26.

69. Pospischil, A.; Furchi, M.M.; Mueller, T. Solar-energy conversion and light emission in an atomic monolayer p-n diode. *Nat. Nanotechnol.* **2014**, *9*, 257–261, doi:10.1038/nnano.2014.14.

70. Chen, M.; Li, Z.; Li, W.; Shan, C.; Li, W.; Li, K.; Gu, G.; Feng, Y.; Zhong, G.; Wei, L.; et al. Large-scale synthesis of single-crystalline self-standing SnSe2 nanoplate arrays for wearable gas sensors. *Nanotechnology* **2018**, *29*, doi:10.1088/1361-6528/aade32.

71. Tian, H.; Chin, M.L.; Najmaei, S.; Guo, Q.; Xia, F.; Wang, H.; Dubey, M. Optoelectronic devices based on two-dimensional transition metal dichalcogenides. *Nano Res.* **2016**, *9*, 1543–1560, doi:10.1007/s12274-016-1034-9.

72. Choi, W.; Cho, M.Y.; Konar, A.; Lee, J.H.; Cha, G.B.; Hong, S.C.; Kim, S.; Kim, J.; Jena, D.; Joo, J.; et al. High-detectivity multilayer MoS2 phototransistors with spectral response from ultraviolet to infrared. *Adv. Mater.* **2012**, *24*, 5832–5836, doi:10.1002/adma.201201909.

73. Lee, H.S.; Min, S.W.; Chang, Y.G.; Park, M.K.; Nam, T.; Kim, H.; Kim, J.H.; Ryu, S.; Im, S. MoS 2 nanosheet phototransistors with thickness-modulated optical energy gap. *Nano Lett.* **2012**, *12*, 3695–3700, doi:10.1021/nl301485q.

74. Yu, J.; Suleiman, A.A.; Zheng, Z.; Zhou, X.; Zhai, T. Giant-Enhanced SnS2 Photodetectors with Broadband Response through Oxygen Plasma Treatment. *Adv. Funct. Mater.* **2020**, *30*, 1–8, doi:10.1002/adfm.202001650.

75. Zheng, Z.; Zhang, T.; Yao, J.; Zhang, Y.; Xu, J.; Yang, G. Flexible, transparent and ultra-broadband photodetector based on large-area WSe2 film for wearable devices. *Nanotechnology* **2016**, *27*, doi:10.1088/0957-4484/27/22/225501.

76. Ahmed, S.; Yi, J. Two-dimensional transition metal dichalcogenides and their charge carrier mobilities in field-effect transistors. *Nano-Micro Lett.* **2017**, *9*, 1–23, doi:10.1007/s40820-017-0152-6.

77. Chen, X.; Liu, C.; Mao, S. Environmental Analysis with 2D Transition-Metal Dichalcogenide-Based Field-Effect Transistors. *Nano-Micro Lett.* **2020**, *12*, doi:10.1007/s40820-020-00438-w.

78. Podzorov, V.; Gershenson, M.E.; Kloc, C.; Zeis, R.; Bucher, E. High-mobility field-effect transistors based on transition metal dichalcogenides. *Appl. Phys. Lett.* **2004**, *84*, 3301–3303, doi:10.1063/1.1723695.

79. Cho, A.J.; Park, K.C.; Kwon, J.Y. A high-performance complementary inverter based on transition metal dichalcogenide field-effect transistors. *Nanoscale Res. Lett.* **2015**, *10*, 1–6, doi:10.1186/s11671-015-0827-1.

80. Wu, M.; Xiao, Y.; Zeng, Y.; Zhou, Y.; Zeng, X.; Zhang, L.; Liao, W. *Synthesis of two-dimensional transition metal dichalcogenides for electronics and optoelectronics*; 2021; Vol. 3; ISBN 2018050718170.

81. Donarelli, M.; Ottaviano, L. 2d materials for gas sensing applications: A review on graphene oxide, mos2, ws2 and phosphorene. *Sensors (Switzerland)* **2018**, *18*, doi:10.3390/s18113638.

82. Cho, S.Y.; Lee, Y.; Koh, H.J.; Jung, H.; Kim, J.S.; Yoo, H.W.; Kim, J.; Jung, H.T. Superior Chemical Sensing Performance of Black Phosphorus: Comparison with MoS2and Graphene. *Adv. Mater.* **2016**, *28*, 7020–7028, doi:10.1002/adma.201601167.

83. Liu, L.; Ikram, M.; Ma, L.; Zhang, X.; Lv, H.; Ullah, M.; Khan, M.; Yu, H.; Shi, K. Edge-exposed

MoS2 nanospheres assembled with SnS2 nanosheet to boost NO2 gas sensing at room temperature. *J. Hazard. Mater.* **2020**, *393*, 1–10, doi:10.1016/j.jhazmat.2020.122325.

84. Pham, T.; Li, G.; Bekyarova, E.; Itkis, M.E.; Mulchandani, A. MoS 2 -Based Optoelectronic Gas Sensor with Sub-parts-per-billion Limit of NO 2 Gas Detection. *ACS Nano* **2019**, *13*, 3196–3205, doi:10.1021/acsnano.8b08778.

85. Liu, C.; Li, F.; Lai-Peng, M.; Cheng, H.M. Advanced materials for energy storage. *Adv. Mater.* **2010**, *22*, 28–62, doi:10.1002/adma.200903328.

86. Choi, N.S.; Chen, Z.; Freunberger, S.A.; Ji, X.; Sun, Y.K.; Amine, K.; Yushin, G.; Nazar, L.F.; Cho, J.; Bruce, P.G. Challenges facing lithium batteries and electrical double-layer capacitors. *Angew. Chemie - Int. Ed.* **2012**, *51*, 9994–10024, doi:10.1002/anie.201201429.

87. Lin, L.; Lei, W.; Zhang, S.; Liu, Y.; Wallace, G.G.; Chen, J. Two-dimensional transition metal dichalcogenides in supercapacitors and secondary batteries. *Energy Storage Mater.* **2019**, *19*, 408–423, doi:10.1016/j.ensm.2019.02.023.

88. Stephenson, T.; Li, Z.; Olsen, B.; Mitlin, D. Lithium ion battery applications of molybdenum disulfide (MoS2) nanocomposites. *Energy Environ. Sci.* **2014**, *7*, 209–231, doi:10.1039/c3ee42591f.

89. Bonaccorso, F.; Colombo, L.; Yu, G.; Stoller, M.; Tozzini, V.; Ferrari, A.C.; Ruoff, R.S.; Pellegrini, V. Graphene, related two-dimensional crystals, and hybrid systems for energy conversion and storage. *Science (80-.).* **2015**, *347*, doi:10.1126/science.1246501.

90. Deng, Z.; Jiang, H.; Li, C. 2D Metal Chalcogenides Incorporated into Carbon and their Assembly for Energy Storage Applications. *Small* **2018**, *14*, 1–9, doi:10.1002/smll.201800148.

91. Tedstone, A.A.; Lewis, D.J.; O'Brien, P. Synthesis, Properties, and Applications of Transition Metal-Doped Layered Transition Metal Dichalcogenides. *Chem. Mater.* **2016**, *28*, 1965–1974, doi:10.1021/acs.chemmater.6b00430.

92. Zhou, W.; Zou, X.; Najmaei, S.; Liu, Z.; Shi, Y.; Kong, J.; Lou, J. Intrinsic structural defects in monolayer MoS2. *Nano Lett.* **2013**.

93. Eichfeld, S.M.; Hossain, L.; Lin, Y.C.; Piasecki, A.F.; Kupp, B.; Birdwell, A.G.; Burke, R.A.; Lu, N.; Peng, X.; Li, J.; et al. Highly scalable, atomically thin WSe2grown via metal-organic chemical vapor deposition. *ACS Nano* **2015**, *9*, 2080–2087, doi:10.1021/nn5073286.

94. Marzari, N.; Sanchez, O.L.; Kung, Y.; Krasnozhon, D.; Chen, M.; Bertolazzi, S.; Gillet, P.; Fontcuberta, A.; Radenovic, A.; Kis, A. Large-Area Epitaxial Monolayer MoS 2. *ACS Nano* **2015**, *4*, 4611–4620.

95. Chia, X.; Ambrosi, A.; Sofer, Z.; Luxa, J.; Pumera, M. Catalytic and charge transfer properties of transition metal dichalcogenides arising from electrochemical pretreatment. *ACS Nano* **2015**, *9*, 5164–5179, doi:10.1021/acsnano.5b00501.

Chapter 3

Synthesis techniques of Metal Dichalcogenides

MDs materials can be synthesized using top-down techniques, where the bulk forms are exfoliated into monolayers (MLs), and bottom-up techniques where precursors are used to growth MDs on different substrates or to crystals.

3.1 The top-down technique

The top-down technique can produce high-quality monolayer samples at low cost and are very convenient for fundamental research and for the realization of proof-of-concept devices. There are basically two top down strategies adopted: mechanical exfoliation, where the Scotch-tape technique is the most known method, and the liquid exfoliation technique.

3.1.1 Mechanical exfoliation method

Mechanical exfoliation is the most common method for reducing bulk material down to the monolayer form [1]. The “scotch tape method” was first reported by Andre Geim and Konstantin Novoselov (Nobel prize for Physics in 2010) at the University of Manchester in 2004, these authors used a piece of tape to successfully isolate graphene. Despite its simplicity and crude procedure, the as-cleaved materials provide crystalline samples with extraordinary mechanical and electrical properties. Mechanical exfoliation became highly popular for synthesizing 2D materials, due to its versatility for the study of countless materials in the monolayer and few layers form and also for its low cost [2].

In a typical mechanical exfoliation process, appropriate thin MDs crystals are first peeled off from their bulk crystals several times to separate the layers of the material from their weak van der Waals interaction by using adhesive Scotch tape (Figure 2.10). The tape is then pressed on the substrate and gently heated to release the material from the tape onto the substrate. The tape is then removed and the substrate is studied under an optical microscope. Small regions of monolayer material can be observed on the substrate in the Figure 3.1. The isolated monolayer region is of very high quality however very small. This method is exceptional for basic

characterization and study of novel nanomaterials; however, the sparse monolayer region makes this process non-scalable for any future application [1].

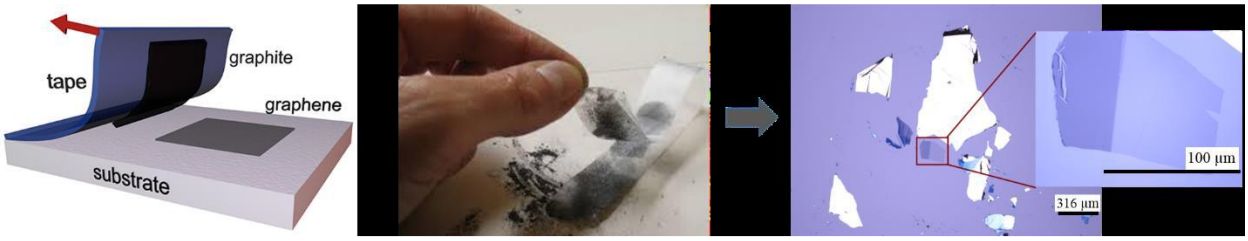

Figure 3.1 Schematic representation of the mechanical exfoliation process for graphene production [3].

Mechanical exfoliation is a low-cost method of 2D materials production, and is extremely convenient for fundamental research. However, scalable production of 2D flakes is highly challenging at this time. Additionally, several other factors (stoichiometry and stacking orders) play a key role in successful fabrication of monolayer MX_2 nanostructures by the mechanical exfoliation. Since most MDs, and in particular MoS_2, $MoSe_2$, WS_2 and WSe_2, are available in bulk form, single layers can be exfoliated using the Scotch tape method.

3.1.2 Liquid exfoliation method

Liquid exfoliation methods are likely to be better suited for fundamental and proof-of-concept demonstrations in applications where large quantities of materials are required, such as electrochemical energy storage, catalysis, sensing or fillers for composites [4]. In liquid exfoliation a bulk material is inserted into a solvent such as N-methyl-2-pyrrolidone (NMP), 2-propanol (IPA) and N-cyclohexyl-2-pyrrolidone (CHP) or Tetrahydrofuran (THF) [5], [6]. Then, the solvent intercalates in the layers of the bulk material and through ultra-sonication, the solvent separates the layers (Figure 3.2) [7].

The shearing of the layers in the bulk material results in the abundance of monolayer and few layers in the solvent. A droplet of the solution is deposited onto the substrate and large amounts of monolayer material can be found (Figure 2.11). This method offers large amounts of monolayer material; however, the monolayers often have degraded due to surface contamination and structural distortion.

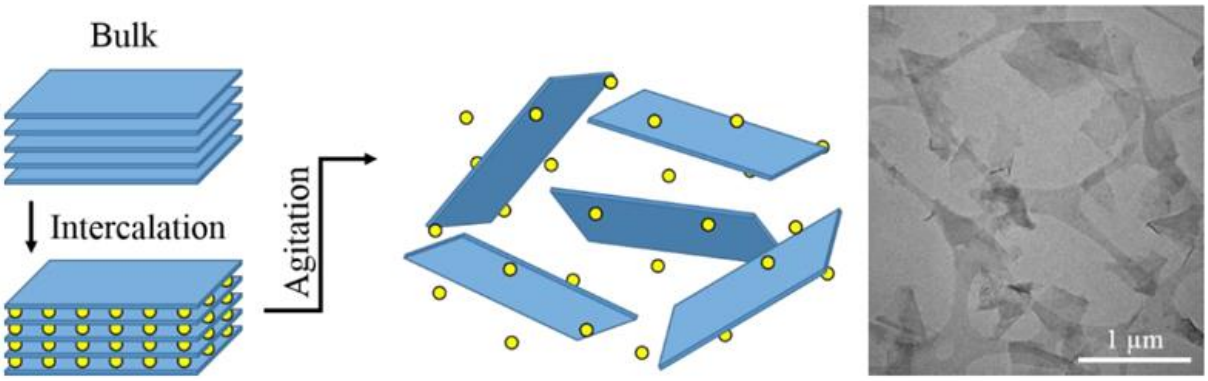

Figure 3.2 Liquid exfoliation. Example of few layers graphene by shear exfoliation in liquids [4]**.**

3.2 Bottom-up technique

It is mandatory to obtain a good control of synthesis in terms of number of layers, crystal quality, lateral dimension of sheets and scalability to large area substrates if we want to integrate MDs in existing electronics and to design novel devices. Top down methods, even if they permit to produce very high-quality material, in the case of the Mechanical Exfoliation method, they do not cover most of the requirements. For this reason, several techniques were developed with a bottom up approach, starting from MD constituent elements to controllably synthesize nanosheets over a given substrate.

One method that is considered as a promising route, owing to its advantages of environment friendly, simple fabrication process and high product purity is the Hydrothermal synthesis, where

the surfactants play a significant role in the growth of various morphologies [8]. In the other hand, most of the reported bottom-up methods utilize one or two of the MDs constituent elements (metal and chalcogen) in vapor form, transporting the selected species over the substrate with a carrier gas [9]. This permits, in principle, to achieve a good control over the gas composition and, through flow dynamic optimizations obtained with chamber/tube design, to deliver the precursors in a homogeneous way over all the substrate area: large area scalability, uniformity and thickness control are routinely achieved for thin films deposited by Atomic Layer Deposition (ALD) or Chemical Vapor Deposition (CVD) and can be used to obtain monolayer MDs [10].

3.2.1 Hydrothermal Synthesis

The hydrothermal technique is historically rooted in the geological sciences. In the mid-19th century, the term “hydrothermal” was first used by the British Geologist Sir Roderick Murchison to describe the formation of minerals by hot water solutions rising from cooling magma. Since then, extensive study has been performed to study the synthesis of new materials, the development of new hydrothermal methods, and the understanding of reaction mechanism[11]. Hydrothermal synthesis is a unique method for crystallizing substances from high-temperature aqueous solutions at high vapor pressures; also termed “hydrothermal method.'' The term “hydrothermal” is of geologic origin.

Hydrothermal synthesis can be defined as a method of synthesis of single crystals that depends on the solubility of minerals in hot water under high pressure. The crystal growth is performed in an apparatus consisting of a steel pressure vessel called an autoclave, in which a nutrient is supplied along with water. A temperature gradient is maintained between the opposite ends of

the growth chamber. At the hotter end the nutrient solute dissolves, while at the cooler end it is deposited on a seed crystal, growing the desired crystal [12].

Traditional fabrication of MX_2 films usually adopt physical methods that cannot be easily scaled up for commercial production. Generally, these methods, either involve a high temperature procedure or a complicated manipulation, which may result in the cost increase and further limit the potential applications [8]. By example, chemical vapor deposition is intensively used for the growth of two-dimensional MX_2 thin sheet, requiring higher temperature synthesis. That is why, various chemical approaches were introduced for fabrication of MX_2 thin films. Hydrothermal method is one of them and is considered a promising process due to its simplicity and high purity production.

For example, Wen *et al.* [13] reported a hydrothermal strategy developed to synthesize high-quality WSe_2 films on a quartz substrate. N, N-dimethylformamide (DMF) and deionized water are used as double solvent, and low-cost selenium powder and sodium tungstate dehydrate are used as the Se and W sources, respectively. WSe_2 films were in hexagonal phase, composed of almost vertically arranged WSe_2 nanolayer, as we can see in the Figure 3.3.

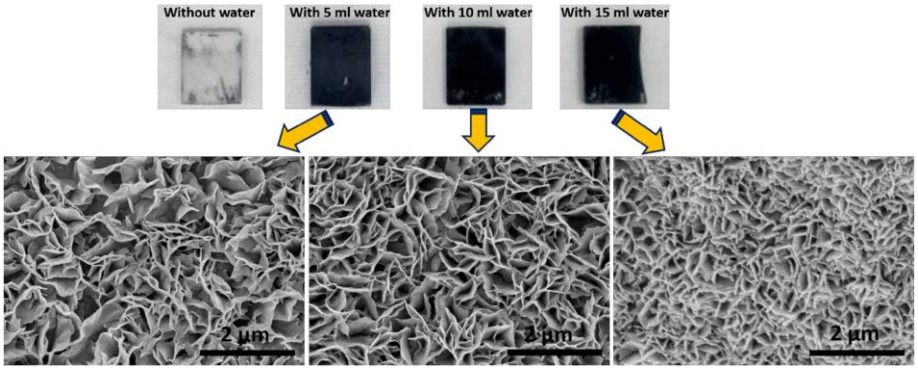

Figure 3.3 Photographs and SEM images of product on quartz with the reaction of different volumes of deionized water [13].

3.2.2 Atomic Layer Deposition (ALD)

ALD is a technique in which the two precursors are delivered separately in the growth chamber. It was invented by T. Suntola in 1974 and was originally used to deposit ZnS film for electroluminescent devices. ALD is nowadays very common for oxides growth and for conformal deposition on nanostructures, patterned substrates, high aspect ratio structures such as trenches or pillars, etc, and it is largely used for the deposition of high-k oxides [14].

A single ALD growth cycle consists in: injection of precursor 1, purge with inert gas, injection of precursor 2, purge with inert gas (Figure 3.4). Excess reactants and reaction by-products are evacuated during purge cycles and the surface reactions during precursors supply are self-limited: if the substrate surface is sufficiently reactive to the precursor and if the precursor does not bond with itself, one ALD growth cycle should in principle deposit a single monolayer of the selected specie: uniform films with excellent conformality can be thus deposited even onto complex-shaped large area substrates. For this reason, ALD should be considered as one of the most promising technique for the deposition of MDs, because theoretically it would permit to tailor the number of deposited layers by defining the number of cycles. Despite its potential, ALD is still not so widespread for MDs, mainly because of a lack of suitable chemistry. Nevertheless, several groups used ALD also for the deposition of metals or metal oxides of controlled thickness to be further sulfurized or selenized by other techniques [15].

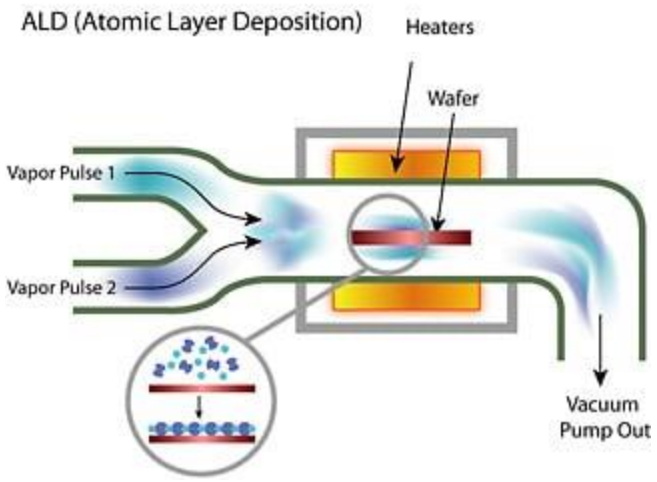

Figure 3.4 Schematic representation of ALD technique.

3.2.3 Chemical Vapor Deposition (CVD)

The term of CVD includes different routes for the synthesis of MDs such as Thin-Film Conversion [16], Chemical Vapor Transport (CVT) [17], Powder Vaporization [18] or the most general, Chemical Vapor Deposition (CVD) [19], etc. These routes will be explained better in the section 3.2.3.1 of this chapter. All of them follow the same principle, however slight changes will determine the name of the technique. Once when we know these techniques and the characteristics that differentiate them, we can have a better understanding of the synthesis route used to obtain MDs nanostructures in this thesis.

The different CVD routes are widely used in materials science and the semiconductor industry. Far from being limited to thin film growth, which is the focus in this work, CVD can also be used for the synthesis of nanoparticles, nanotubes, and bulk powders. It is formally defined as the formation of a solid film on a substrate by the reaction of vapor phase chemicals that contain the required constituents. These vapor phase chemicals react on the substrate surface to produce the desired material, while by-products are removed from the CVD chamber by gas flow. The

final form of the material deposited relies on a number of parameters, including deposition temperature, pressure, gas flow and he growth substrate. The advantage of CVD over other thin film technologies, such as evaporation, molecular beam epitaxy, sputter coating or electroplating, is the high purity and control over film growth that can be obtained at a relatively economical cost. This has led to the application of CVD for the growth of epitaxial layers on crystalline substrates or films, and metallic, semiconducting and insulating layers in the microelectronics industry. Disadvantages of CVD include the possible by-products that can be formed during reactions, which could be potentially hazardous, or contaminate the final product [20]. Another major disadvantage is that CVD is generally carried out at high temperatures, restricting the substrates on which growth can occur. This could necessitate post-growth transfer of films to other substrates, which can cause damage and degradation [20].

3.2.3.1 Different routes of Chemical Vapor Deposition (CVD)

As we mentioned in the previous section, there are several methods under the denomination of Chemical Vapor Deposition. Here we focus in the most used ones and they are presented in the next sections with their characteristics that differentiate between them.

3.2.3.1.1 Thin-Film Conversion

Thin films of MDs were first synthesized in the 70's [21]. The primary, uniform and scalable synthesis method was the conversion of a deposited metal (Mo, W, Sn, etc.) or oxide (MoO_3, WO_3, etc.) layer into MX_2 in a chalcogen (S (g), Se (g), etc.) vapor environment or solid chalcogen precursors, this method was called Thin-Film Conversion (Figure 3.5). Recent refinement of this methods has led to high quality multilayer structures [17] and vertically aligned nanosheets [11]. While this technique is quite successful at achieving continuous films of MDs, it often results in

nanocrystalline structures, though recent works indicate that this can be overcome to achieve high-quality multilayer films with good management of parameters such as temperature and gas flow.

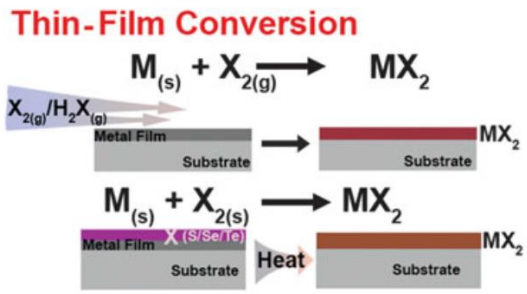

Figure 3.5 Schematic representation of Thin-Film Conversion.

3.2.3.1.2 Chemical Vapor Transport (CVT)

Today most MD bulk crystals are synthesized via chemical vapor transport (CVT, Figure 3.6) [18], this method consists of mixing stoichiometric amounts of the metal with the chalcogen and a transport agent in a sealed vacuum tube. This system is then placed in a high-temperature furnace (700–1000 °C), where a temperature gradient across the sealed tube provides a driving force for transport of the elemental materials to the cool end, forming crystals of MX_2.

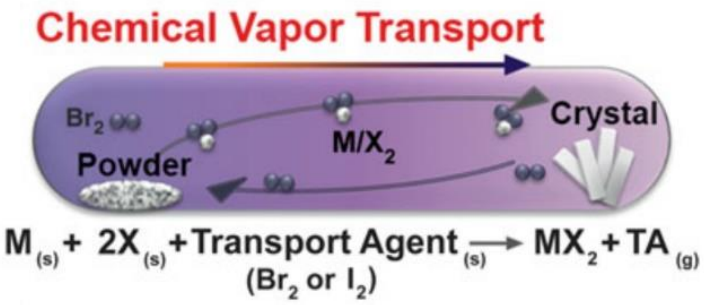

Figure 3.6 Schematic representation of Chemical Vapor Transport (CVT).

3.2.3.1.3 Powder Vaporization

Another widely utilized synthesis method is powder vaporization, basically there is a direct sulfurization or selenization of the transition metal oxide in a tube furnace where the two precursors are all in powder form. Most studies utilizing this method focus on vaporization of metal oxide (MoO_3, WO_3, etc.) and chalcogen (S, Se) powders in a horizontal tube furnace, where the chalcogen powder is placed upstream from the hot zone and just outside the tube furnace. Upon heating, the metal oxide and chalcogen powders are vaporized and transported downstream in the furnace, coating the substrate material and forming MX_2 (Figure 3.7) [19].

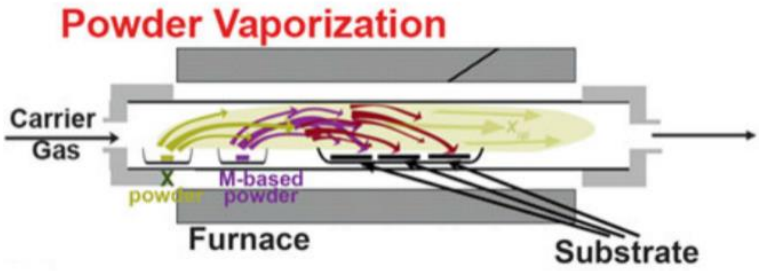

Figure 3.7 Schematic representation of Powder Vaporization.

3.2.3.1.4 Chemical Vapor Deposition (CVD)

Finally, another vapor phase growth method, the chemical vapor deposition (CVD). The precursors in CVD are typically outside of the reactor tube and involve at least one gas phase precursor that thermally decomposes to deposit the final product (Figure 3.8).

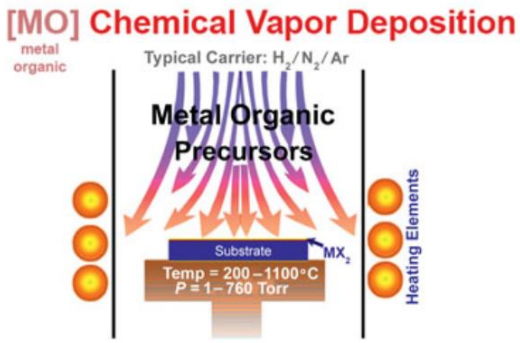

Figure 3.8 Schematic representation of Chemical Vapor Deposition.

To reach the objectives of this thesis a metallic thin-film was deposited on sapphire and SiO_2 substrates and a chalcogen powder was used for vaporization. Though this thesis we use the term CVD instead of CVD-powder vaporization/Thin film conversion for simplicity.

In 2012, for the first time, Lain-Jong Li's group [22] reported a CVD method to synthesis large-area, monolayer MoS_2 films on silicon dioxide (SiO_2) substrate. Molybdenum trioxide (MoO_3) and sulfur (S) powders acted as solid reactants (Figure 3.9).

In addition to MoS_2 monolayer, there are also multilayers. For example, Zhan *et al.* [23] reported CVD synthesis of MoS_2 by direct sulfurization of Mo metal film to get large area, few layers film. Transition metal oxide precursor-based methods were reported by Lee et al. wherein, few-layer MoS_2 was synthesized using CVD [24]. The examples presented focus on MoS_2 because it is the most studied within this family of materials but there are also studies about monolayers of WS_2 [25] for example or multilayers of WSe_2 [26].

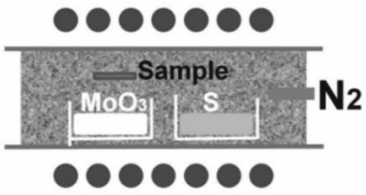

Figure 3.9 Schematic illustration for the experimental set-up [22].

Recently there have been significant advances using CVD to produce high-quality MDs monolayer single crystals [22], [27]. CVD of MDs typically uses solid precursors, which are evaporated before the reaction and growth takes place. This is in contrast to gaseous precursors that are generally used for CVD growth of thin films, and may be responsible for some of the limitations in MDs growth which have recently been realized. The solid precursors are evaporated and carried downstream to the growth substrate in the gaseous phase, where they react and deposit on the substrate. Depending on the particular setup, the gas flow can be carefully controlled through the chamber design and a good flow dynamic optimization can, in principle, guarantee an efficient transport of species, good homogeneity, easily scale up to large area and excellent reproducibility. For these reasons, CVD is one of the most promising techniques to synthesize monolayers MDs on large area with controlled thickness, good crystallographic quality and excellent electronic properties. In addition, many reports of MDs production via CVD require excess amounts of oxide precursors, which can result in oxysulfide and other contaminants [22], [28].

The application of MDs materials to real devices, their large-scale growth is essential. The chemical vapor deposition (CVD) method is the most effective way to generate high-quality MDs layers with a scalable size, controllable thickness and excellent electronic properties. The obtained MDs monolayers or films can be used as the active components for nanoelectronics as the building blocks for constructing layered heterostructures (Figure 3.10) [29].

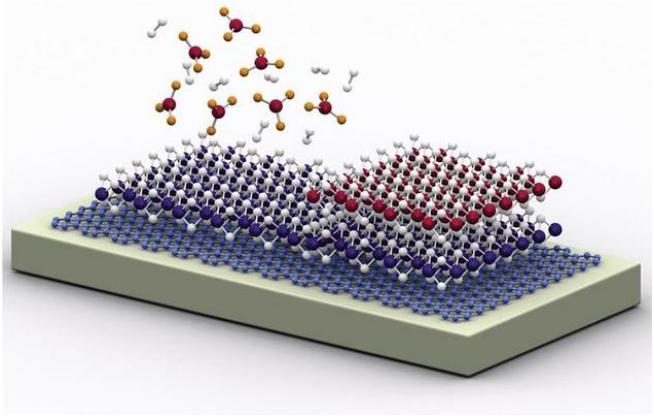

Figure 3.10 Large-scale of growth of 2D materials by CVD [30].

3.2.3.2 Vertical growth of MDs

The majority of recent studies are focused on the synthesis of 2D MX_2, with domains of different morphology, crystallinity (phase), crystal size, etc. The MDs monolayer are a direct gap semiconductors [31] due to the 2D confinement. The difference in the electronic structure of monolayer MX_2 in comparison with its bulk counterpart offers many opportunities for diverse applications such as solar cells [32], light-emitting devices [33] and ultrasensitive photodetectors [34]. The thesis focus on the synthesis of thin films, particularly with MDs layers with vertical orientation, this morphology is attractive because of the predominately exposed edges exhibit a high surface energy and are reported to be metastable which may serve for diverse catalytic reaction [19] [29], [35]. Vertically grown MDs, with exposed edge sites have also been reported for hydrogen evolution reaction (HER) [36] and gas sensing applications [37]. The control of the morphology, orientation and crystallography depend on the growth method and parameters used. The used CVD strategy for the synthesis of vertically-aligned nanosheets is based on the co-evaporation of two precursors one for the metal, the other for the chalcogenide. The formation of the vertically aligned MDs layers is proposed to be driven by kinetic process, where at a high

temperature the transition metal thin film coverts to sulfide/selenide much faster than the diffusion of sulfur/selenium. Thus, the sulfur/selenium diffusion limits the growth process. On the other hand, the anisotropic structure of MDs layers makes it much faster for sulfur/selenium diffusion along the van der Waals gaps. Therefore, the MDs layers naturally orient perpendicular to the film, exposing van der Waals gaps for fast reaction.

Table 3.1 Comparison of the different parameters using CVD method for vertically aligned MDs synthesis using S as a chalcogen.

Material	Morphology	Parameters	Method	Application	Reference
MoS_2	Hexagonal-shaped nanoplates (HNPs) of MoS_2	850 °C, 60 min, 50 nm of Mo, S powder, Ar flow	CVD	Gas sensing	[37]
MoS_2	Vertical aligned MoS_2 flakes	850 °C, 60 min, MoO_3 powder, S powder, Ar flow	CVD	Gas sensing	[38], [39]
WS_2	WS_2 nanosheets	500 °C, 20 min, WO_3 powder, S powder, Ar flow, H_2 flow	CVD	Photoelectrochemical water splitting	[40]
WS_2	WS_2 nanosheets	0.25 mmol of $(NH_4)_6H_2W_{12}O_{40}\cdot xH_2O$, 10 mmol thiourea, 30 ml of deionized water	Hydrothermal	Thermoelectric	[41]
SnS_2	SnS_2 nanosheets	700 °C, 5 min, SnI_2 powder, S powder, Ar flow, H_2 flow	CVD	Phototransistors	[42]
SnS_2	SnS_2 nanosheets	450 °C, $SnCl_4\cdot 5H2O$, S powder, Ar flow, H_2 flow	CVD	Photoelectrochemical water splitting	[43]

Table 3.2 Comparison of the different parameters using CVD method for vertically aligned MDs synthesis using Se as a chalcogen.

Material	Morphology	Parameters	Method	Application	Reference
$MoSe_2$	$MoSe_2$ nanoflowers	850 ° C, 25 min, MoO_3 powder, Se pellets, Ar flow, H_2 flow	CVD	HER	[38],[44]
WSe_2	WSe_2 films	800 ° C, 25 min, W film, Se pellets, Ar flow, H_2 flow	CVD	Field-effect transistors	[45]
WSe_2	WSe_2 films	0.20 g (NaBH4), 9.2 mmol selenium powder, 4 mmol sodium tungstate dehydrate ($Na_2WO_4 \cdot 2H_2O$), 60 ml DMF.	Hydrothermal	Photodetector	[13]
$SnSe_2$	$SnSe_2$ nanosheets	700 °C, 20 min, SnI_2 powder, Se powder, Ar flow, H_2 flow	CVD	Photodetector	[46]

Tables 3.1 and 3.2 summarize reported results of state-of-the-art growth methods and applications. MoS_2 is the most studied material and there are several publications about the synthesis of this material, including the vertical orientation. In this table, the different parameters used for the synthesis of vertically-aligned MDs are presented and can be compared with the methodology report in the Chapter 4. From these results it is clear that there are different ways to synthesize MDs, however it is always important find the fastest, low-cost, most scalable and reproducible routes. Compared with CVD routes, the hydrothermal method presents advantages such as low-cost and large area of production. However, the low solubility of elemental chalcogen and metal salt seems to be a problem as it limits the choice of organic solvents. An incomplete

dissolving of the reagent leads to low chemical reaction rate, which retards the formation of MX_2 films [13].

Preliminary results on vertically aligned growth by our group were reported in [37], [47–49]. This thesis extends these studies to increase the knowledge in the growth of different vertically aligned MDs using vapor powder deposition and application in gas sensing.

3.3 References

1. Li, H.; Wu, J.; Yin, Z.; Zhang, H. Preparation and applications of mechanically exfoliated single-layer and multilayer MoS2 and WSe2 nanosheets. *Acc. Chem. Res.* **2014**, *47*, 1067–1075, doi:10.1021/ar4002312.
2. Das, S.; Kim, M.; Lee, J.W.; Choi, W. Synthesis, properties, and applications of 2-D materials: A comprehensive review. *Crit. Rev. Solid State Mater. Sci.* **2014**, *39*, 231–252, doi:10.1080/10408436.2013.836075.
3. Zan, R.; M., Q.; Jalil, R.; Bangert, U. Atomic Structure of Graphene and h-BN Layers and Their Interactions with Metals. *Adv. Graphene Sci.* **2013**, 3–30, doi:10.5772/56640.
4. Nicolosi, V.; Chhowalla, M.; Kanatzidis, M.G.; Strano, M.S.; Coleman, J.N. Liquid exfoliation of layered materials. *Science (80-.).* **2013**, *340*, 72–75, doi:10.1126/science.1226419.
5. Backes, C.; Berner, N.C.; Chen, X.; Lafargue, P.; LaPlace, P.; Freeley, M.; Duesberg, G.S.; Coleman, J.N.; McDonald, A.R. Functionalization of liquid-exfoliated two-dimensional 2H-MoS2. *Angew. Chemie - Int. Ed.* **2015**, *54*, 2638–2642, doi:10.1002/anie.201409412.
6. Jawaid, A.; Nepal, D.; Park, K.; Jespersen, M.; Qualley, A.; Mirau, P.; Drummy, L.F.; Vaia, R.A. Mechanism for Liquid Phase Exfoliation of MoS2. *Chem. Mater.* **2016**, *28*, 337–348, doi:10.1021/acs.chemmater.5b04224.

7. Coleman, J.N.; Lotya, M.; O'neill, A.; Bergin, S.D.; King, P.J.; Khan, U.; Young, K.; Gaucher, A.; De, S.; Smith, R.J.; et al. Two-Dimensional Nanosheets Produced by Liquid Exfoliation of Layered Materials. *Science (80-.).* **2011**, *331*, 568–571.

8. Cao, S.; Liu, T.; Hussain, S.; Zeng, W.; Peng, X.; Pan, F. Hydrothermal synthesis of variety low dimensional WS2 nanostructures. *Mater. Lett.* **2014**, *129*, 205–208, doi:10.1016/j.matlet.2014.05.013.

9. Zhang, Y.; Yao, Y.; Sendeku, M.G.; Yin, L.; Zhan, X.; Wang, F.; Wang, Z.; He, J. Recent Progress in CVD Growth of 2D Transition Metal Dichalcogenides and Related Heterostructures. *Adv. Mater.* **2019**, *31*, 1–30, doi:10.1002/adma.201901694.

10. Bosi, M. Growth and synthesis of mono and few-layers transition metal dichalcogenides by vapour techniques: A review. *RSC Adv.* **2015**, *5*, 75500–75518, doi:10.1039/c5ra09356b.

11. Feng, S.H.; Li, G.H. *Hydrothermal and Solvothermal Syntheses*; 2017; ISBN 9780444635914.

12. Kafle, B.P. *Introduction to nanomaterials and application of UV–Visible spectroscopy for their characterization*; 2020; ISBN 9780128148662.

13. Wen, R.; Wei, A.; Tao, L.; Luo, D.; Liu, J.; Yang, Y.; Xiao, Z.; Liu, Z.; Zhao, Y. Hydrothermal synthesis of WSe2 films and their application in high-performance photodetectors. *Appl. Phys. A Mater. Sci. Process.* **2018**, *124*, 1–8, doi:10.1007/s00339-018-2059-6.

14. Wang, C.; Hu, L.; Lin, Y.; Poeppelmeier, K.; Stair, P.; Marks, L. Controllable ALD synthesis of platinum nanoparticles by tuning different synthesis parameters. *J. Phys. D. Appl. Phys.* **2017**, *50*, doi:10.1088/1361-6463/aa8709.

15. Drozd, V.E.; Nikiforova, I.O.; Bogevolnov, V.B.; Yafyasov, A.M.; Filatova, E.O.; Papazoglou, D. ALD synthesis of SnSe layers and nanostructures. *J. Phys. D. Appl. Phys.* **2009**, *42*,

doi:10.1088/0022-3727/42/12/125306.

16. Vogel, E.M.; Robinson, J.A.; Materials, T.; Solids, W. WSe 2 thin-film realization by synthesis and by tarnishing. *J. Phys. Condens. Matter* **1994**, *6*, 8527.

17. Liu, Y.; Ang, R.; Lu, W.J.; Song, W.H.; Li, L.J.; Sun, Y.P. Superconductivity induced by Se-doping in layered charge-density-wave system 1T-TaS2-xSex. *Appl. Phys. Lett.* **2013**, *102*, doi:10.1063/1.4805003.

18. Elías, A.L.; Perea-López, N.; Castro-Beltrán, A.; Berkdemir, A.; Lv, R.; Feng, S.; Long, A.D.; Hayashi, T.; Kim, Y.A.; Endo, M.; et al. Controlled synthesis and transfer of large-area WS2 sheets: From single layer to few layers. *ACS Nano* **2013**, *7*, 5235–5242, doi:10.1021/nn400971k.

19. Eichfeld, S.M.; Hossain, L.; Lin, Y.C.; Piasecki, A.F.; Kupp, B.; Birdwell, A.G.; Burke, R.A.; Lu, N.; Peng, X.; Li, J.; et al. Highly scalable, atomically thin WSe2grown via metal-organic chemical vapor deposition. *ACS Nano* **2015**, *9*, 2080–2087, doi:10.1021/nn5073286.

20. Creighton, J.R.; Ho, P. Introduction to Chemical Vapor Deposition (CVD). *Chem. Vap. Depos.* **2001**, 1–13.

21. Vogel, E.M.; Robinson, J.A. Two-dimensional layered transition-metal dichalcogenides for versatile properties and applications. *MRS Bull.* **2015**, *40*, 558–563, doi:10.1557/mrs.2015.120.

22. Lee, Y.H.; Zhang, X.Q.; Zhang, W.; Chang, M.T.; Lin, C. Te; Chang, K. Di; Yu, Y.C.; Wang, J.T.W.; Chang, C.S.; Li, L.J.; et al. Synthesis of large-area MoS 2 atomic layers with chemical vapor deposition. *Adv. Mater.* **2012**, *24*, 2320–2325, doi:10.1002/adma.201104798.

23. Gatensby, R.; McEvoy, N.; Lee, K.; Hallam, T.; Berner, N.C.; Rezvani, E.; Winters, S.; O'Brien,

M.; Duesberg, G.S. Controlled synthesis of transition metal dichalcogenide thin films for electronic applications. *Appl. Surf. Sci.* **2014**, *297*, 139–146, doi:10.1016/j.apsusc.2014.01.103.

24. Yim, C.; O'Brien, M.; McEvoy, N.; Riazimehr, S.; Schäfer-Eberwein, H.; Bablich, A.; Pawar, R.; Iannaccone, G.; Downing, C.; Fiori, G.; et al. Heterojunction hybrid devices from vapor phase grown MoS 2. *Sci. Rep.* **2014**, *4*, 4–10, doi:10.1038/srep05458.

25. McCreary, K.M.; Hanbicki, A.T.; Jernigan, G.G.; Culbertson, J.C.; Jonker, B.T. Synthesis of Large-Area WS 2 monolayers with Exceptional Photoluminescence. *Sci. Rep.* **2016**, *6*, 1–7, doi:10.1038/srep19159.

26. Salitra, G.; Hodes, G.; Klein, E.; Tenne, R. Highly oriented WSe2 thin films prepared by selenization of evaporated WO3. *Thin Solid Films* **1994**, *245*, 180–185, doi:10.1016/0040-6090(94)90896-6.

27. Kang, K.; Xie, S.; Huang, L.; Han, Y.; Huang, P.Y.; Mak, K.F.; Kim, C.J.; Muller, D.; Park, J. High-mobility three-atom-thick semiconducting films with wafer-scale homogeneity. *Nature* **2015**, *520*, 656–660, doi:10.1038/nature14417.

28. Najmaei, S.; Liu, Z.; Zhou, W.; Zou, X.; Shi, G.; Lei, S.; Yakobson, B.I.; Idrobo, J.C.; Ajayan, P.M.; Lou, J. Vapour phase growth and grain boundary structure of molybdenum disulphide atomic layers. *Nat. Mater.* **2013**, *12*, 754–759, doi:10.1038/nmat3673.

29. Shi, Y.; Li, H.; Li, L.J. Recent advances in controlled synthesis of two-dimensional transition metal dichalcogenides via vapour deposition techniques. *Chem. Soc. Rev.* **2015**, *44*, 2744–2756, doi:10.1039/c4cs00256c.

30. Novoselov, K.S.; Mishchenko, A.; Carvalho, A.; Castro Neto, A.H. 2D materials and van der

Waals heterostructures. *Science (80-.).* **2016**, *353*, doi:10.1126/science.aac9439.

31. Marzari, N.; Sanchez, O.L.; Kung, Y.; Krasnozhon, D.; Chen, M.; Bertolazzi, S.; Gillet, P.; Fontcuberta, A.; Radenovic, A.; Kis, A. Large-Area Epitaxial Monolayer MoS 2. *ACS Nano* **2015**, *4*, 4611–4620.

32. Wei, Z.; Li, B.; Xia, C.; Cui, Y.; He, J.; Xia, J.B.; Li, J. Various Structures of 2D Transition-Metal Dichalcogenides and Their Applications. *Small Methods* **2018**, *2*, 1–19, doi:10.1002/smtd.201800094.

33. Pu, J.; Takenobu, T. Monolayer Transition Metal Dichalcogenides as Light Sources. *Adv. Mater.* **2018**, *30*, 1–22, doi:10.1002/adma.201707627.

34. Wang, F.; Wang, Z.; Yin, L.; Cheng, R.; Wang, J.; Wen, Y.; Shifa, T.A.; Wang, F.; Zhang, Y.; Zhan, X.; et al. 2D library beyond graphene and transition metal dichalcogenides: A focus on photodetection. *Chem. Soc. Rev.* **2018**, *47*, 6296–6341, doi:10.1039/c8cs00255j.

35. Kong, D.; Wang, H.; Cha, J.J.; Pasta, M.; Koski, K.J.; Yao, J.; Cui, Y. Synthesis of MoS2 and MoSe2 films with vertically aligned layers. *Nano Lett.* **2013**, *13*, 1341–1347, doi:10.1021/nl400258t.

36. Chia, X.; Ambrosi, A.; Sofer, Z.; Luxa, J.; Pumera, M. Catalytic and charge transfer properties of transition metal dichalcogenides arising from electrochemical pretreatment. *ACS Nano* **2015**, *9*, 5164–5179, doi:10.1021/acsnano.5b00501.

37. Deokar, G.; Vancsó, P.; Arenal, R.; Ravaux, F.; Casanova-Cháfer, J.; Llobet, E.; Makarova, A.; Vyalikh, D.; Struzzi, C.; Lambin, P.; et al. MoS2–Carbon Nanotube Hybrid Material Growth and Gas Sensing. *Adv. Mater. Interfaces* **2017**, *4*, 1–10, doi:10.1002/admi.201700801.

38. Kong, D.; Wang, H.; Cha, J.J.; Pasta, M.; Koski, K.J.; Yao, J.; Cui, Y. Synthesis of MoS2 and

MoSe2 films with vertically aligned layers. *Nano Lett.* **2013**, *13*, 1341–1347, doi:10.1021/nl400258t.

39. Rahul Kumar, Pawan K. Kulriya, Monu Mishra, Fouran Singh, G.G. and M.K. Highly selective and reversible NO2 gas sensor using vertically aligned MoS2 flake networks. *Nanotechnology* **2018**, *29*, 464001.

40. Ahmadi, A.; Zargar Shoushtari, M. Enhancing the photoelectrochemical water splitting performance of WS2 nanosheets by doping titanium and molybdenum via a low temperature CVD method. *J. Electroanal. Chem.* **2019**, *849*, 113361, doi:10.1016/j.jelechem.2019.113361.

41. Piao, M.; Chu, J.; Wang, X.; Chi, Y.; Zhang, H.; Li, C.; Shi, H.; Joo, M.K. Hydrothermal synthesis of stable metallic 1T phase WS2 nanosheets for thermoelectric application. *Nanotechnology* **2018**, *29*, doi:10.1088/1361-6528/aa9bfe.

42. Zhou, X.; Zhang, Q.; Gan, L.; Li, H.; Zhai, T. Large-Size Growth of Ultrathin SnS2 Nanosheets and High Performance for Phototransistors. *Adv. Funct. Mater.* **2016**, *26*, 4405–4413, doi:10.1002/adfm.201600318.

43. Liu, G.; Li, Z.; Hasan, T.; Chen, X.; Zheng, W.; Feng, W.; Jia, D.; Zhou, Y.; Hu, P.A. Vertically aligned two-dimensional SnS2 nanosheets with a strong photon capturing capability for efficient photoelectrochemical water splitting. *J. Mater. Chem. A* **2017**, *5*, 1989–1995, doi:10.1039/c6ta08327g.

44. Masurkar, N.; Thangavel, N.K.; Arava, L.M.R. CVD-Grown MoSe2 Nanoflowers with Dual Active Sites for Efficient Electrochemical Hydrogen Evolution Reaction. *ACS Appl. Mater. Interfaces* **2018**, *10*, 27771–27779, doi:10.1021/acsami.8b07489.

45. Campbell, P.M.; Tarasov, A.; Joiner, C.A.; Tsai, M.Y.; Pavlidis, G.; Graham, S.; Ready, W.J.; Vogel, E.M. Field-effect transistors based on wafer-scale, highly uniform few-layer p-type WSe2. *Nanoscale* **2016**, *8*, 2268–2276, doi:10.1039/c5nr06180f.

46. Zhou, X.; Zhou, N.; Li, C.; Song, H.; Zhang, Q.; Hu, X.; Gan, L.; Li, H.; Lü, J.; Luo, J.; et al. Vertical heterostructures based on SnSe2/MoS2 for high performance photodetectors. *2D Mater.* **2017**, *4*, doi:10.1088/2053-1583/aa6422.

47. Deokar, G.; Vignaud, D.; Arenal, R.; Louette, P.; Colomer, J. Synthesis and characterization of MoS 2 nanosheets. *Nanotechnology* **2016**, *27*, 075604.

48. Deokar, G.; Rajput, N.S.; Vancsó, P.; Ravaux, F.; Jouiad, M.; Vignaud, D.; Cecchet, F.; Colomer, J.F. Large area growth of vertically aligned luminescent MoS2 nanosheets. *Nanoscale* **2017**, *9*, 277–287, doi:10.1039/c6nr07965b.

49. Deokar, G.; Rajput, N.S.; Li, J.; Deepak, F.L.; Ou-Yang, W.; Reckinger, N.; Bittencourt, C.; Colomer, J.F.; Jouiad, M. Toward the use of CVD-grown MoS2 nanosheets as field-emission source. *Beilstein J. Nanotechnol.* **2018**, *9*, 1686–1694, doi:10.3762/bjnano.9.160.

Chapter 4

Synthesis and Characterization of Metal Dichalcogenides

The controllable growth of MDs is the first for step for the optimal integration in devices. The goal is to have a reproductible control of the material characteristics, which includes the number of layers, the crystallographic phase composition, or/and film morphology. Previous studies have already demonstrated that these 2D materials can prepared using mechanical and chemical exfoliation [1], [2], and chemical vapor deposition (CVD) [3–5]. CVD has proven to be an effective method for synthesizing MDs with control of the number of layers and morphology of the material, opening up new applications. This thesis focusses on the synthesis of vertically-aligned MDs, for potential application in gas sensing. The choice of vertically aligned nanosheets is due to the presence of a high number of exposed sheet edges.

This chapter is divided in three sections: a discussion on the synthesis of metal dichalcogenides, a discussion on the synthesis and characterizations of MDs based on Sulfur (MoS_2, WS_2 and SnS_2) and on MDs based on Selenium ($MoSe_2$, WSe_2 and $SnSe_2$). Possible applications of each synthesized material are also discussed. The characteristics and specifications of the characterization techniques can be found in the Appendix I.

4.1 Synthesis of Metal Dichalcogenides

Once the materials of interest and the techniques used to synthesize them have been introduced as mentioned in the previous chapters, the next step is to synthesize the MDs. The synthesis of metal dichalcogenides were performed at the University of Namur, Belgium, under the supervision of Dr. Jean-François Colomer. The MDs nanosheets were grown using an Atmospheric Pressure (AP)-CVD technique (Figure 4.1). We choose APCVD due to it is the most general type of CVD reactors and has a low operating cost since no vacuum needed.

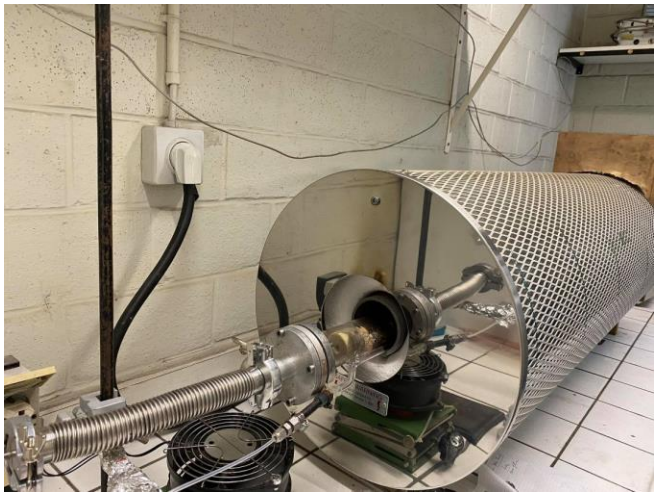

Figure 4.1 AP-CVD set-up used for the growth of MDs at the University of Namur.

A schematic representation is showed in the Figure 4.2 in order to give a better idea of the synthesis process. Figure 4.2 a) shows the synthesis scheme for the TMDs, where “M” is the metal film, “C” the chalcogen, “T” the temperature in °C. In the Figure 4.2 b) we can see the representation of the TDs synthesis. The parameters of all the synthesis are presented in the Table 4.2.

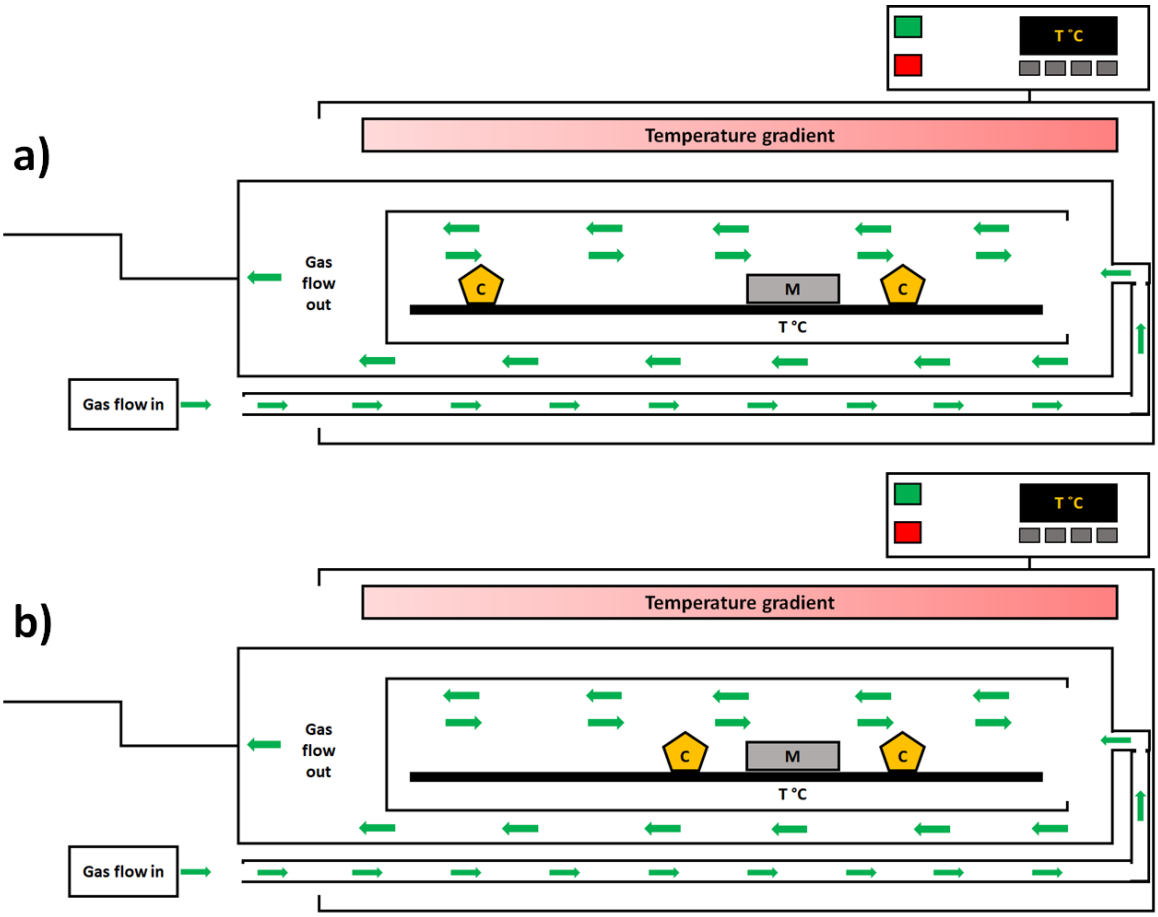

Figure 4.2 Schematic representation of the synthesis of a) TMDs and b) TDs.

In order to prepare the samples for the synthesis, Molybdenum, Tungsten and Tin were deposited by sputtering process and more specific by magnetron sputtering. The sputtering process begins when a substrate to be coated is placed in a vacuum chamber containing an inert gas (usually Argon) and a negative charge is applied to a target source material that will be deposited onto the substrate causing the plasma to glow. Free electrons flow from the negatively charged target source material in the plasma environment, colliding with the outer electronic shell of the Argon gas atoms driving these electrons off due to their like charge. The inert gas atoms become positively charged ions attracted to the negatively

charged target material at a very high velocity that “Sputters off” atomic size particles from the target source material due to the momentum of the collisions. These particles cross the vacuum deposition chamber of the sputter coater and are deposited as a thin film of material on the surface of the substrate to be coated (Figure 4.3 a). A 50-nm thick metal film (Mo, W or Sn) was deposited on different substrates (sapphire or SiO_2) by direct current magnetron sputtering (sputter current 100 mA), using a commercial sputter deposition system (Quorum Q15T/ES) in an Argon (99.9995%) atmosphere (Figure 4.3 b).

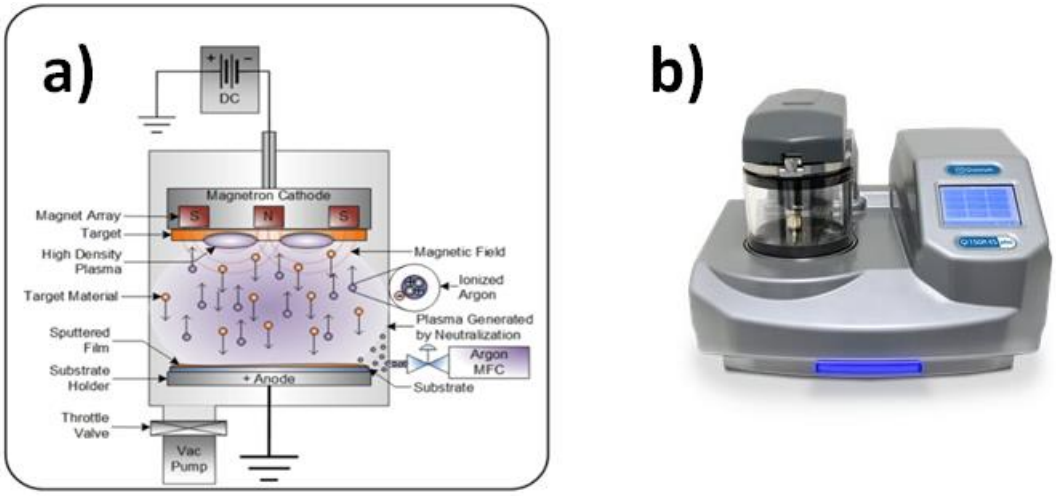

Figure 4.3 a) Diagram of the DC Magnetron Sputtering Process and b) Quorum Q150T/ES.

A pure metal target (Mo, Sn and W) with a 57 mm diameter was used, and the substrates were placed on a rotating holder with a 90 mm target (Figure 4.4). The pressure of the argon in the deposition chamber was 1×10^{-3} mbar. The metal film thickness was monitored using a quartz microbalance mounted in the deposition system.

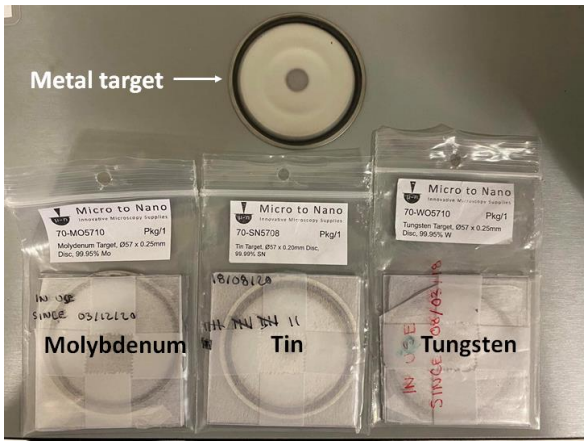

Figure 4.4 Metal targets used for magnetron sputtering.

When the metal films were deposited on the substrates for the synthesis of TMDs (Figure 4.5 a) and the TDs (Figure 4.5 b), they were placed on the 49 centimeters of the quartz boat used as a support for the samples before the synthesis. For TMDs synthesis the chalcogen powder is placed at 3 cm and 51 cm, this is because the chalcogen in the case of TMDs will be placed at the ends because it is necessary a two-step reaction (each of 30 min) where in the first step the chalcogen closest to the sample is placed in the part of the reactor with the ideal temperature and the second chalcogen remains in a zone where it does not interfere until the second step when it is placed inside the reactor. While for TDs (Figure 4.5 b), only one step is necessary and the chalcogen is placed in centimeters 47 and 51. Tin has a lower melting point in comparison with Mo and W and for that, the reaction time is smaller compared to with the TMDs reaction. The positions have been optimized and will change depending in the temperature and the reaction used.

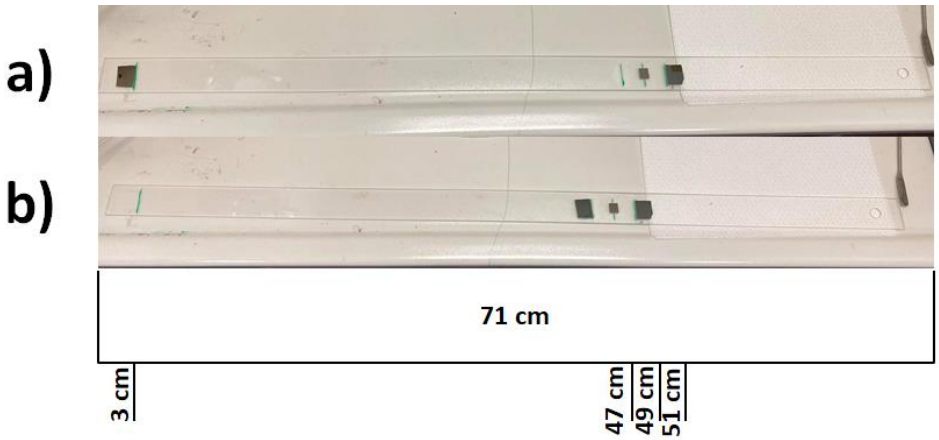

Figure 4.5 Quartz stand used as a support for the samples during the reaction of a) TMDs and b) TDs.

Then, the quartz boat is placed inside of the quartz tube that is close at the end in order to concentrate the vapor phase of the chalcogen powder and help with the diffusion in the metal film as we can see in the Figure 4.6 a) with its schematic representation in Figure 4.6 b). The gas diffusion inside the tube goes from the open inlet to the bottom and back. In the case of the MD synthesis chalcogen powders are used. The parameters (presented in the Table 4.2 in this chapter) were varied to determine the optimal conditions for the growth of the vertically aligned nanosheets.

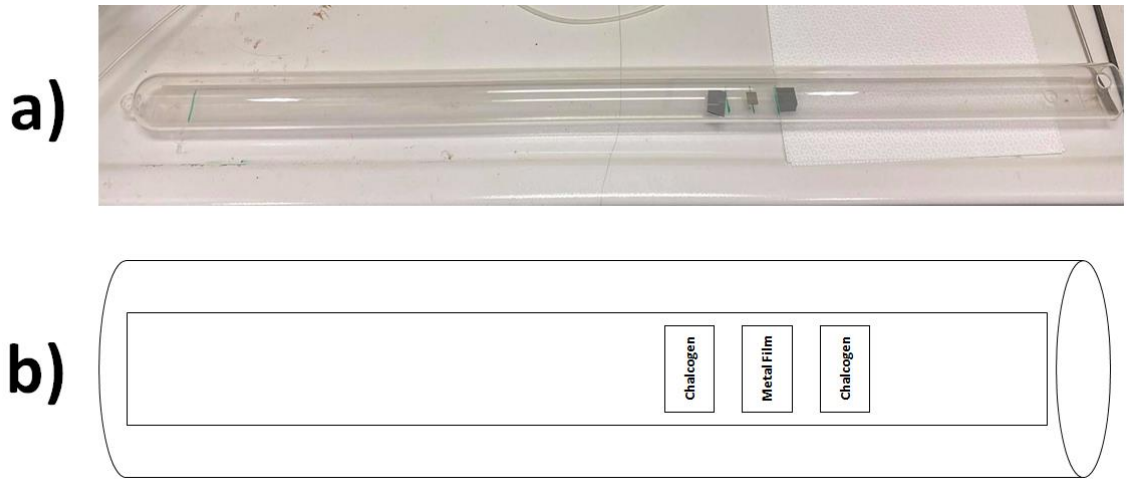

Figure 4.6 a) Quartz tube used during the MDs synthesis and b) schematic representation of the quartz tube.

Finally, the quartz tube is placed inside the reactor, which is compose of a quartz tube with 5 cm diameter, a special closing system to prevent gas leaks is connected to a hose where the waste comes out in vapor form (Figure 4.7)

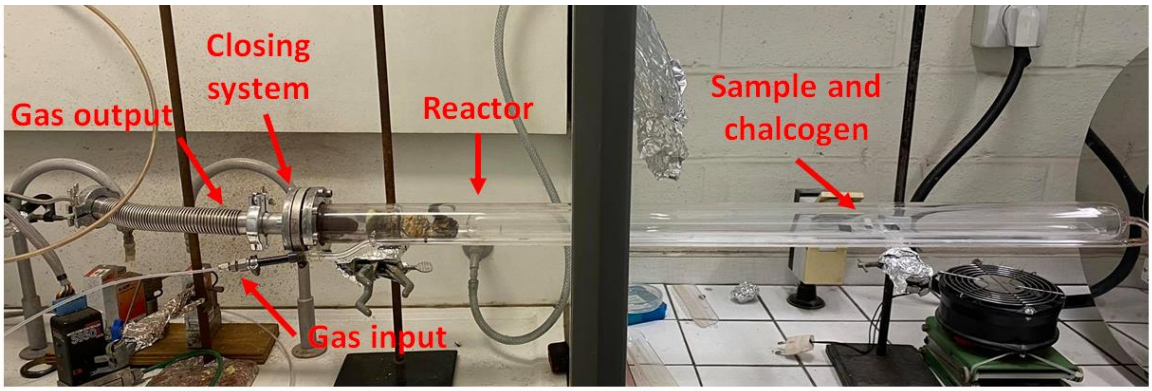

Figure 4.7 MDs system employed for synthesis reaction.

During the synthesis the temperature in the reactor can be varied from 25 to 1100 °C and it will be controlled by a temperature control purchased from Carbolite (Figure 4.8).

Figure 4.8 Temperature control system purchased from Carbolite.

The zones in the reactor where the temperature can be considered as optimal for the synthesis were determined by previous reports in the synthesis of MoS_2 nanosheets [3]. These optimal temperature zones for the reaction are shown the Figure 4.9 b). The zone one at 850 °C is where the reaction happens and the zone 2 at 400 °C is where the second chalcogen is keep before the second step without interaction with the synthesis in the first step. These temperature zones are used for the synthesis of TMDs. The zone one at 550 and 450 °C are used for the synthesis of TDs (SnS_2 and $SnSe_2$, respectively). The temperature of the zone 2 decreases with the change of temperature for the TDs synthesis however, this zone is not used because only one step is employed as we presented in Figure 4.5 b).

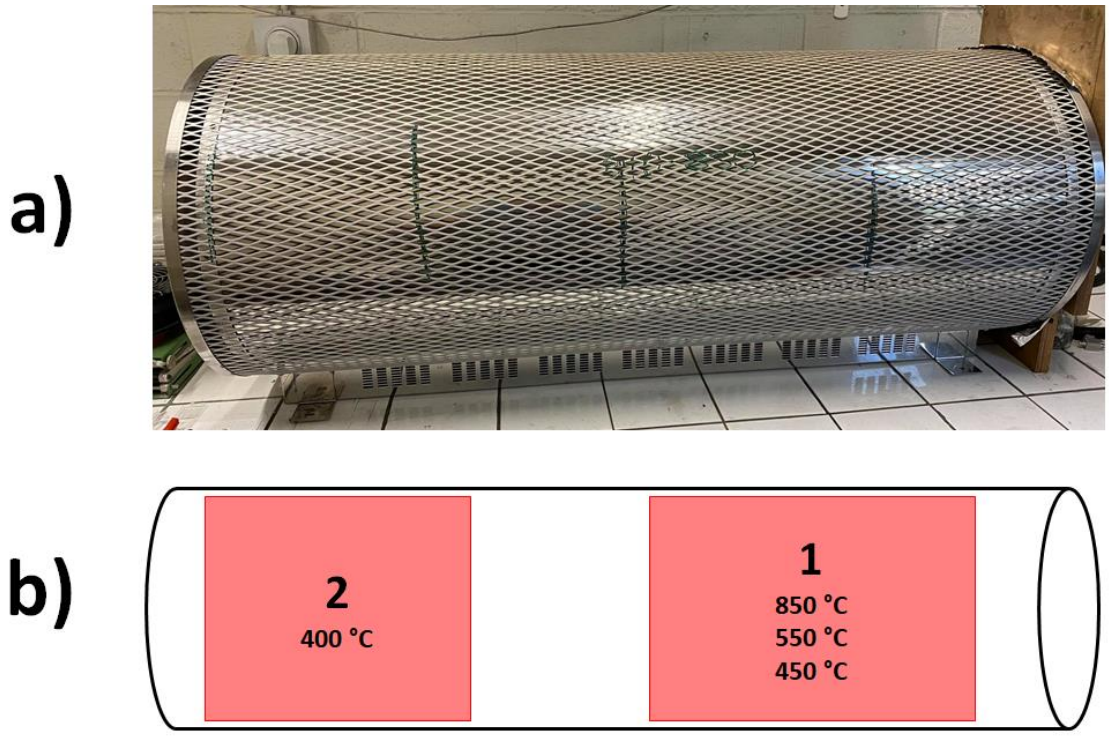

Figure 4.9 a) CVD system and b) Schematic representation of the CVD temperature zones used during MDs synthesis.

Prior to the sulfurization or the selenization the reactor is flushed for one hour to remove (reduce) oxygen, using a 0.745 L min^{-1} argon flow. After that, the reactor is inserted in the furnace. In the Figure 4.10 a) we present how does it like when we introduce the reactor into the furnace for the first step of the TMDs synthesis and the only step for the TDs synthesis. In the case of TMDs, a second step is performed and Figure 4.10 b) shows the final position of the reactor. After the reaction, the quartz tube was removed from the reactor and was cooled with the argon flow for 1 h.

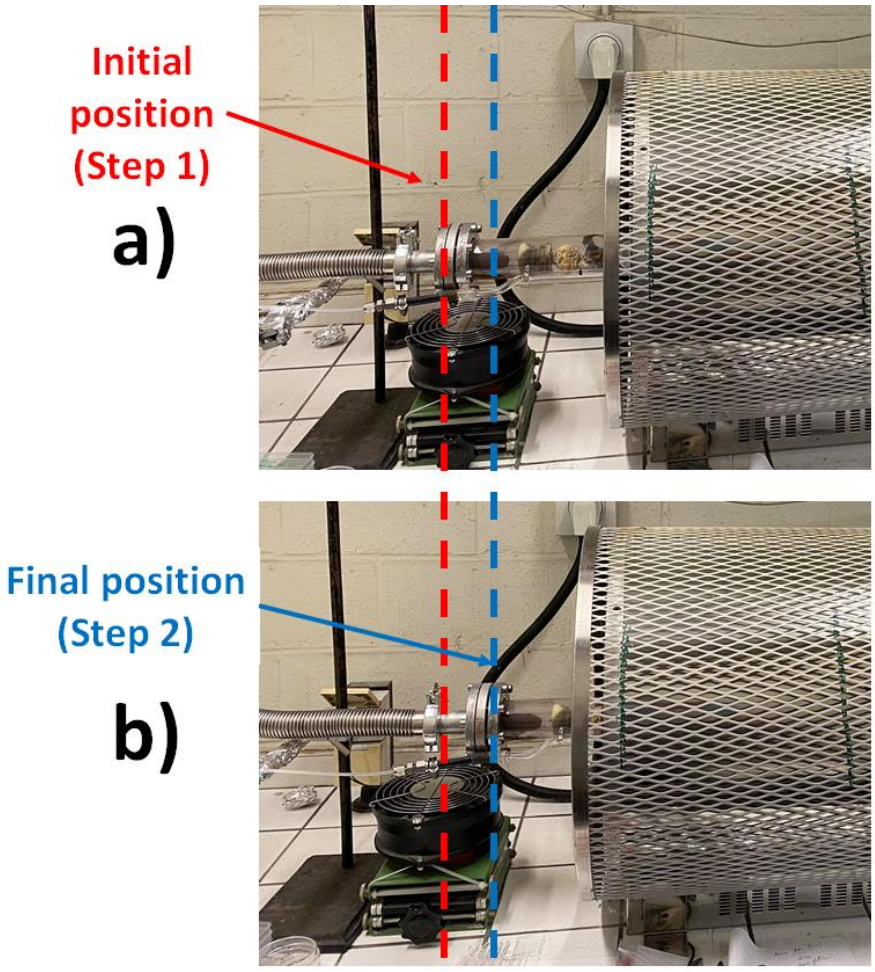

Figure 4.10 a) Illustration of the first step of the MDs synthesis and b) second step. The position of the quartz tube changes 7 cm between a) and b).

In 2015, in our lab group, J-F Colomer reported a CVD method to synthesize vertically aligned MoS_2 nanosheets (Figure 4.11) on Si substrates at atmospheric pressure [3]. This process was improved in 2016 replacing MoO_3 with sputter-deposited Mo film on a Si (001). The Mo film samples were subject to sulfurization at 850 °C for 30 min under a constant Ar flow at atmospheric pressure [6].

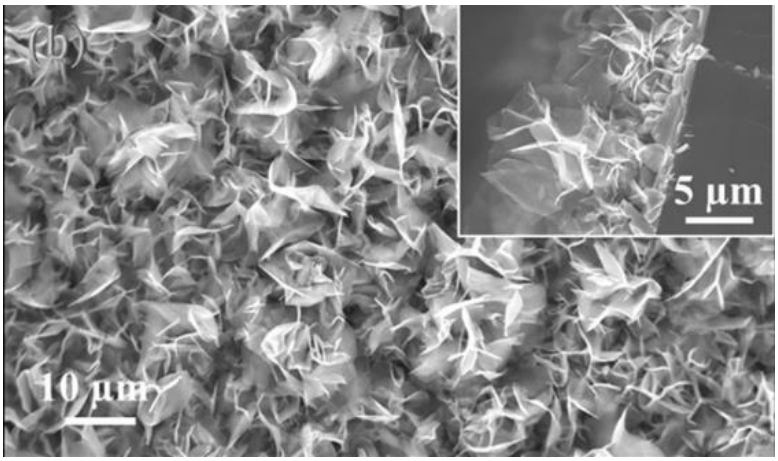

Figure 4.11 SEM images of MoS_2 nanosheets grown [3].

The reaction routes for the synthesis of MoS_2 this experiment using powders for the metal oxide and chalcogen could be expressed as follows (where, s = solid, and g = gas):

$$S_{(s)} \rightarrow S_{(g)} \dots\dots @450\ ^{\circ}C$$

$$MoO_{3_{(s)}} \rightarrow MoO_{3_{(g)}} \dots\dots @850\ ^{\circ}C$$

$$MoO_{3_{(g)}} + 4S_{(g)} \rightarrow 2MoS_{2_{(s)}} + 3O_{2_{(g)}} \dots\dots @850\ ^{\circ}C$$

As the reaction proceeds, further adsorption of incoming species occurs at the already nucleated sites. This leads to the formation of MoS_2 nanosheets on the substrate surface. A very fast reduction of MoO_3 by S might have an important role in the formation of vertically aligned layered MoS_2 nanosheets [3]. These results are the starting parameter to find the good conditions for the synthesis of other MDs and they will be discussed in the Discussions sections of this chapter.

4.1.1 Influence of the metal thin film on the morphology of the MDs

Depending on the growth method, the metal precursor can be metal oxide powders, vaporized liquids or pre-deposited thin metallic or metal-oxide layer on a substrate. The direct deposition of the metal film (Mo, W and Sn) onto the substrate SiO_2 or sapphire is the best way to control the thickness of these materials for the sulfurization or selenization. It is often reported that the synthesis of mono or few-layers MDs depends on the thickness and homogeneity of the initial metal deposition. The thickness control is not studied in this thesis, for all samples the starting metallic film was 50 nm.

4.1.2 Effect of the Oxidation on the morphology of the MDs

The sputtering deposition of the metal film onto the substrate, was performed extra-situ therefore the films were exposed to air and oxidation occurred. This oxidation plays an important role during the synthesis process. In the case of the TMDs for example, Mo and W when exposed to air will be oxidized and form Mo or W oxides. During the high-temperature procedure, the metal oxide aggregation and the sulfurization or selenization reaction will take place simultaneously. This oxidation helps for the vertical growth of the nanosheets and we will talk about it in the final discussion of this chapter. For the Tin, the Sn thin film is exposed to air, however oxidation by air exposition is not enough to favorize the formation of vertically-aligned nanosheets. For that the Sn thin film after deposition is oxidized in air at 300 °C and before the synthesis reaction. In the Figure 4.12 a), we can observe the morphology of the starting material exposed only to air and in Figure 4.12 b) the morphology changes when it is oxidized at 300 °C before sulfurization. Comparing these

two figures we can observe clearly how the oxidation of the starting material changes the morphology of Sn and some aggregates are presented in the starting material (Sn in this case), forming valleys in the film where the chalcogen in vapor phase can be internalized in these valleys, the diffusion of this is favorized for the formation of the vertically-aligned nanosheets.

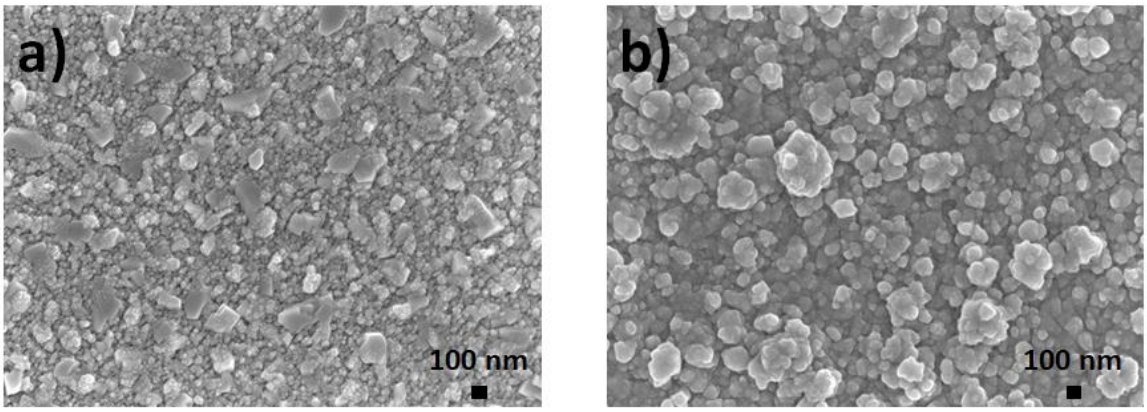

Figure 4.12 SEM images of a) 50 nm of Sn exposed to air and b) 50 nm of Sn oxidized in air at 300 °C.

Find the correct temperature for the oxidation is also an important step because it may change the morphology of the MDs nanomaterial. In the Figure 4.13 we can observe two SnS_2 synthesized samples using the same parameters however with different morphologies due to the oxidation temperature. For oxidation at 200 °C, sphere-like nanostructures are formed (Figure 4.13 a) however, if the temperature increases to 300 °C the formation of vertically-aligned nanosheets (Figure 4.13 b) is favorized.

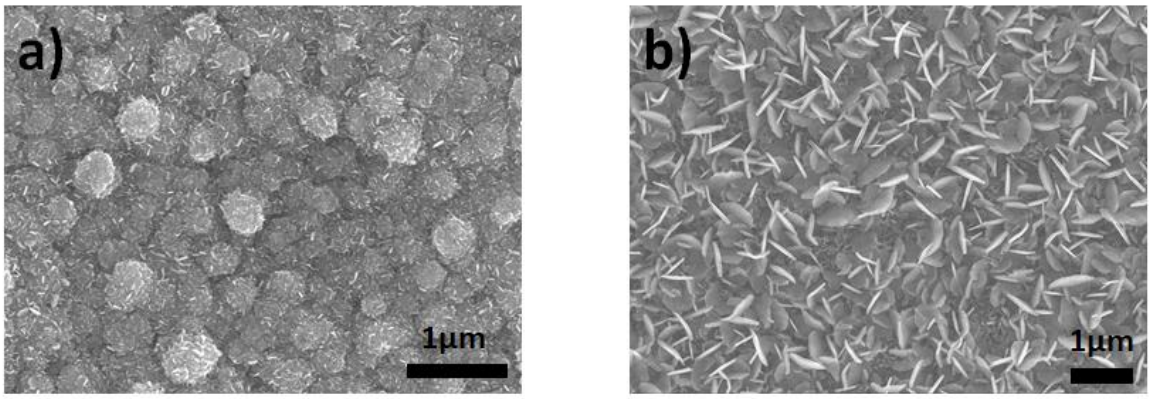

Figure 4.13 SEM images of SnS_2 with different morphologies, a) spheres and b) vertically-aligned nanosheets.

Both Mo and W films (50 nm) air oxidized at room temperature were used as a starting material for the synthesis of TMDs. While Sn films (50 nm) air oxidized at 300 °C were used for the synthesis of TDs.

4.1.3 Effect of the Temperature during the MDs synthesis

During the synthesis different parameters such as temperature, gas flow (Argon and Hydrogen), quantity of chalcogen and thickness of the metal film were varied. Stablish optimal synthesis parameters is crucial because they will strongly affect properties of the materials such as purity, crystallinity, as well as morphology. Here we evaluate the effect of the reaction temperature.

The reaction temperature will be different depending on the melting point of the metal film. For comparison, we refer to results reported to MoS_2 [6]. For example, when temperature was varied from 850 °C to 500 °C vertically-aligned nanosheets were not formed (Figure 4.14), even if we kept all the parameters (gas flow, thickness of the metal film and quantity

of chalcogen) fixed as reported in [3]. The result was an oxidized Mo film without the presence of nanosheets of any type (vertical or horizontal way).

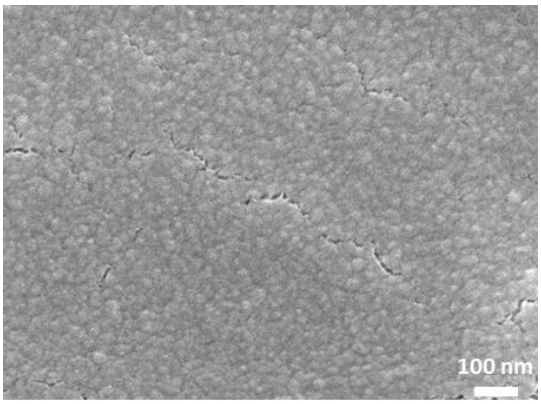

Figure 4.14 SEM image of the MoS_2 synthesis at 500 °C.

The melting temperatures and evaporating temperatures of the used materials are presented in the Table 4.1.

Material	Melting temperature (°C)	Evaporation temperature (°C)
Mo	2623	4639
MoO_3	795	1155
W	3410	5930
WO_3	1473	1700
Sn	232	2602
SnO_2	1630	1800
S	115	445
Se	221	685

Table 4.1 Melting temperatures and evaporating temperatures of the used materials.

For TDs due to lower melting temperature of Tin, low reaction temperatures were used for the synthesis of SnS_2. In figure 4.15 we can observe that increasing the reaction temperature the formation of sheets occurs, the number and size of the sheets increased until 600 °C above this temperature the material is damaged. The final temperatures of all the materials are presented in the Table 4.2. It is important to mentioned that these temperatures were not selected for the final parameters.

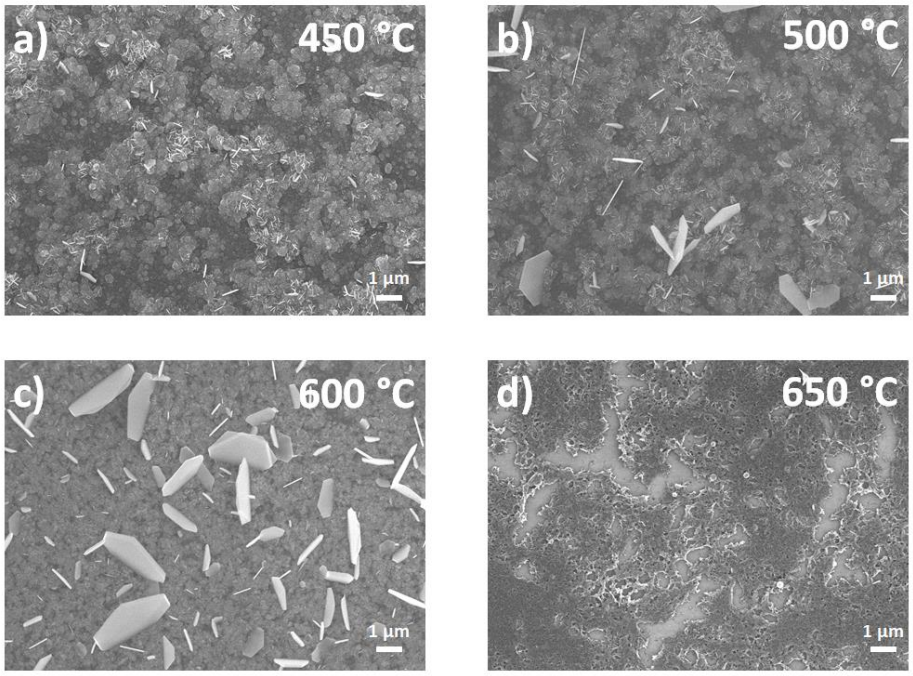

Figure 4.15 SEM images of the SnS_2 synthesis at different temperatures a) 450 °C, b) 500 °C, c) 600 °C and d) 650 °C.

4.1.4 Effect of the Gas Flow in the MD's morphology

Another parameter to considered is the gas flow, Argon in the case of the metal disulfides and Argon/Hydrogen for the metal diselenides (Figure 4.16 a). The gas flow determines the interaction time (residence time) of the chalcogen atoms with the surface of the metal film.

This is a very important parameter for the synthesis of aligned sheets. All the gases were introduced in the furnace via a mass flow controller (Figure 4.16 b), therefore the chalcogen concentration during the vapor phase was determinate by the gas flow.

Figure 4.16 a) Bottoms of Argon (Ar) and Hydrogen (H_2) utilized during this thesis work and b) gas controllers.

The SEM micrographs in Figure 4.17 show the morphology of the obtained SnS_2 samples synthesized using different gas flow that were not selected as a final parameter. Decreasing the gas flow the amount of nanosheets decreased, however their size increased due to the high concentration of chalcogen and because the velocity of the reaction was going slow. Further results will be discussed in the next sections.

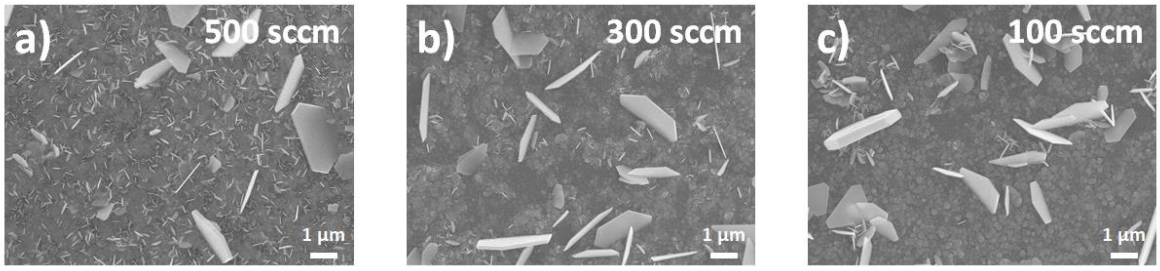

Figure 4.17 SEM images of the SnS_2 synthesis at different gas flows a) 500 sccm, b) 300 sccm and c) 100 sccm.

For metal diselenides, the gas flow changes now with the addition of H_2. The presence of a strong reducer is indeed mandatory for the selenization reaction, compared with the sulfurization reaction [4], [7], [8].

That said, finding the optimal conditions for gas flow in the case of metal diselenides is very important because you also have to find the ideal conditions for the H_2 to help with the reduction of the Se part. In the Figure 4.18 we can observed the differences in morphology, size and formation of nanosheets between the gas's concentration but also how the final product change when the reducer is increased.

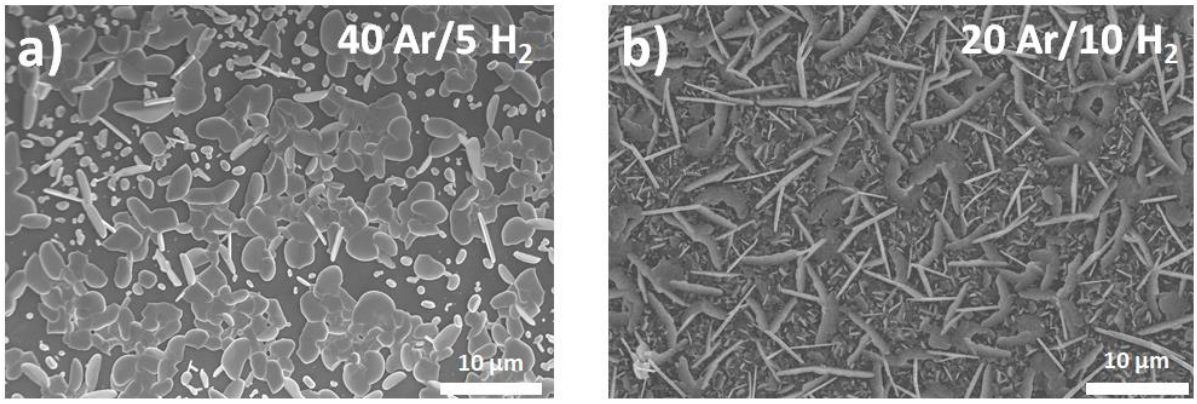

Figure 4.18 SEM images of the $SnSe_2$ synthesis at different gas flows a) 40 Ar/5 H_2 and b) 20 Ar/10 H_2.

The final parameters presented in this thesis work are shown in the Table 4.2.

Sample	*Temperature (°C)*	*Gas Flow (sccm)*	*Time (min)/steps*	*Metal film (nm)*	*Chalcogen (g)*	*Reference*
MoS_2	850	745 Ar	30/2	50 nm of Mo	0.420 g of Sulfur	[6]
WS_2	850	745 Ar	30/2	50 nm of W	0.420 g of Sulfur	[9]
SnS_2	550	70 Ar	30/1	50 nm of Sn	0.420 g of Sulfur	Article Submitted
$MoSe_2$	900	600 Ar 60 H_2	30/2	50 nm of Mo	0.700 g of Selenium	
WSe_2	850	475 Ar 150 H_2	30/2	50 nm of W	0.700 g of Selenium	[4]
$SnSe_2$	450	10 Ar 10 H_2	30/1	50 nm of Sn	0.700 g of Selenium	Article Submitted

Table 4.2 Parameters used for the synthesis of MDs vertically-aligned nanosheets.

4.2 Characterization techniques

The results discussed in the next section were obtained using the following equipment:

- Scanning electron microscopy (SEM) analyses were conducted on a JEOL 7500F microscope operating at 15 kV.

- Transmission electron microscopy studies were carried out on a TECNAI T20 microscope working under 200 kV for bright-field images and electron diffraction and on an aberration-corrected FEI Titan Low-base microscope for scanning TEM. This STEM instrument was operated at 80 kV.

- The structure of the sample has been investigated by X-ray diffraction (XRD) using a Panalytical X'Pert PRO diffractometer (Cu Kα radiation, Bragg–Brentano geometry).

- The MDs nanosheets were examined using a micro-Raman system (Senterra Bruker Optik GmbH) with a 3 cm^{-1} resolution, using a laser excitation laser source (532 nm wavelength), and a laser power of 2 and 5 mW, respectively.

- The chemistry of the MDs nanosheets was studied with X-ray photoelectron spectroscopy (XPS) using an Escalab 250i Thermo Fisher ScientificTM instrument (consisting of a monochromatic Al Kα X-ray source and a hemispherical deflector analyzer working at a constant pass energy).

METAL DICHALCOGENIDES WITH SULFUR AS A CHALCOGEN

4.3 Synthesis results of Metal Dichalcogenides using Sulfur as a Chalcogen

The study of MX_2 samples synthesized by sulfurization of 50 nm of metal film deposited on a sapphire or SiO_2 substrate are presented in the next sections (Parameters used in Table 4.2).

4.4 Molybdenum Disulfide (MoS_2)

4.4.1 Electron microscopies of MoS_2 nanosheets

SEM images show the morphology of the MoS_2 samples, the low-magnification images in Figure 4.19 a) reveals a large amount of MoS_2 nanosheets with vertical orientation that are uniformly distributed on the sapphire substrate. The high magnification image in Figure 4.19 b) shows that the MoS_2 nanosheets, with a thickness around 20 nm and a length between 70-100 nm, these have a well-defined shape with sharp edges. The optimized double sulfurization step leads to a homogeneous distribution of MoS_2 nanosheets over the entire substrate surface without forming any aggregated crystals, as previous reported by us [10]. In addition, we observed a good synthesis reproducibility.

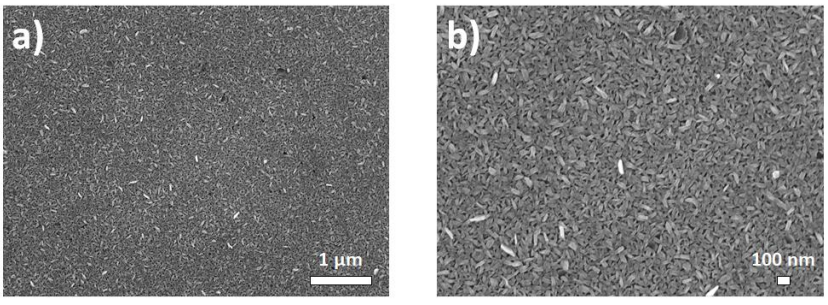

Figure 4.19 SEM images of synthesized products for a) and b) vertically aligned MoS_2 nanosheets.

These structures were further characterized using transmission electron microscopy (TEM). The nanosheets were removed from the substrate by scratching, and were collected on a holey-carbon copper grid. As can be seen in Figure 4.20 , the MoS_2 layers are well stacked with an interlayer distance of 0.64 nm, corresponding to the (002) plane of bulk MoS_2 [3], [6], further detailed analysis in the same region of the sample, shows a lattice d spacing of 0.24 nm, which corresponds to (100) lattice plane of hexagonal MoS_2 phase (2H phase) [11].

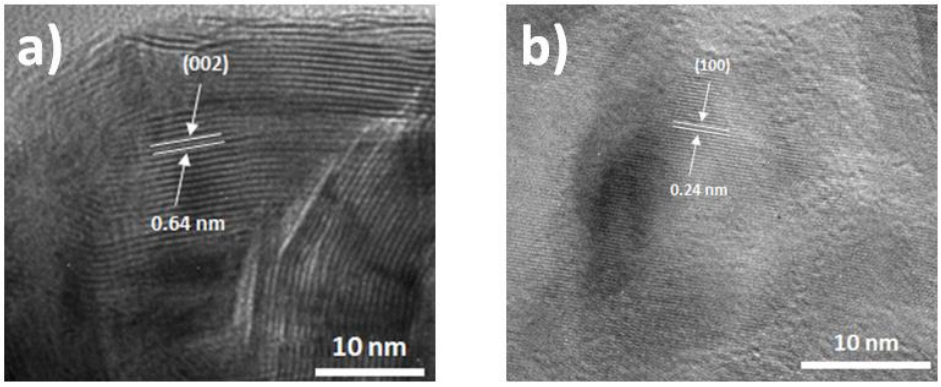

Figure 4.20 High resolution TEM image of the MoS_2 crystals, showing the (002) and (100) crystal planes.

4.4.2 X-Ray diffraction analysis of MoS_2 nanosheets

Based on the microscopy studies, the conclusions that can be drawn is that the MoS_2 nanosheets are crystallized in the hexagonal structure. This has been checked using XRD. Typical XRD spectra of the MoS_2 nanosheets obtained by CVD are shown in Figure 4.21. The diffraction peaks appearing at 14.26°, 33.8°, 39.67°, 45.38° and 58.4° can be assigned to the (002), (100), (103), (006) and (110) family lattice planes of hexagonal MoS_2, which correspond to the reported data (JCPDS card no.77-1716) for the hexagonal 2H phase [12–

14] with the unit cell parameters a = b = 0.315 nm, c = 1.229 nm. In well agreement with TEM analysis.

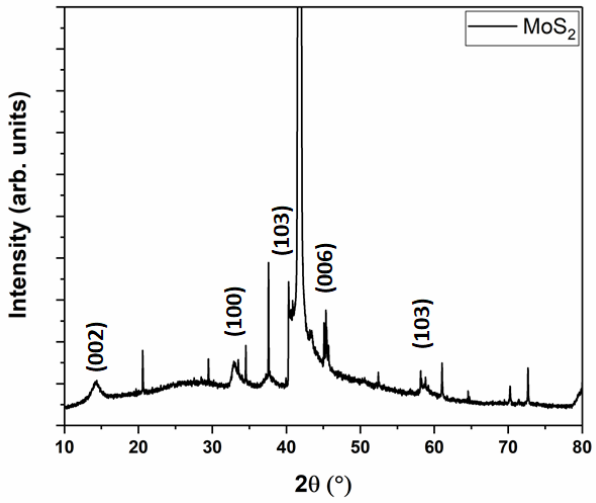

Figure 4.21 XRD pattern of MoS_2 nanosheets.

4.4.3 Raman spectroscopy of MoS_2 nanosheets

Raman spectroscopy was performed to study the signature of vibrational modes to confirm the formation of the MX_2 nanosheets for all the materials in this chapter. A typical Raman spectrum of the as-synthesized MoS_2 nanosheets is shown in Figure 4.22. We found that MoS_2 exhibits two intense peaks at 383.1 and 408.3 cm^{-1}, assigned to MoS_2 phonon modes. The most intense peak at 408.3 cm^{-1} corresponds to the out-of-plane A_{1g} vibration mode. The in-plane E^1_{2g} vibration mode corresponds to the peak at 383.1 cm^{-1} [10], [15]. Lee et al., [16] reported that E^1_{2g} vibration softens (red shifts), while the A_{1g} vibration stiffens (blue shifts) with increasing sample thickness. For samples of four or more layers, the frequencies of both modes converge to the bulk values. Monolayer MoS_2 exhibits a strong E^1_{2g} vibration mode at 384 cm^{-1} and A_{1g} vibration mode near 400 cm^{-1}. Our values are closer with the

values reported for the bulk phase (383 and 408 cm^{-1} for E^1_{2g} and A_{1g}, respectively) [17]. The position with these peaks agrees with our Raman analysis and we can conclude the multilayer nature of our sample.

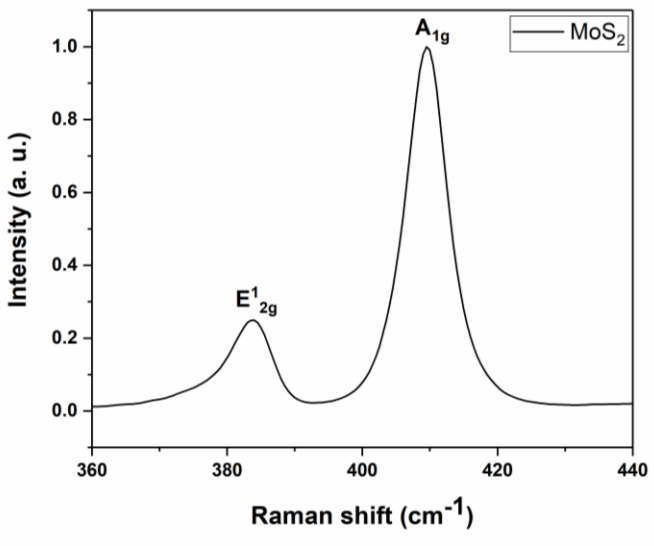

Figure 4.22 Raman spectrum with 532 nm excitation laser of MoS_2 nanosheets.

4.4.4 Photoluminescence of MoS_2 nanosheets

Photoluminescence is an effective technique to evaluate the optical properties of luminescent materials. Photoluminescence in semiconductors quantifies the recombination efficiency of photogenerated charges.

All the samples were studied at the excitation wavelength of 532 nm. In Figure 4.23 the first peak at 580 nm could be attributed to the direct allowed transitions in MoS_2, value close to ones given in the literature, which is in agreement with the values of monolayer samples and can be due to the presence of some nanosheets with monolayer nature [6], [18]. For monolayer the valence band maxima and conduction band minima are both at high-

symmetric K-point revealing direct band gap semiconductor as can be seen in Figure 2.10 in Chapter 2 [19]. The PL peak observed at 799 nm (1.35 eV) correspond to an increased band-gap of the as-grown MoS_2 nanosheets. In this case, the signature of the substrate can also be found in the low intensity peak at 871 nm (1.42 eV). Here, SiO_2 was used as substrate due to the strong transitions of sapphire made impossible to see the answer of the materials, the transitions from substrate are visible. A similar photoluminescence has been previously reported for few-layer MoS_2 [20], [21]. In bulk MoS_2, the photoluminescence is not observable because it is an indirect band gap (1.29 eV) semiconductor [21]. Due to the vertical orientation of the nanosheets, the morphology of the sample can influence the results obtained in PL. The edges of these nanosheets are exposed and it has been demonstrated an increase of photoluminescence in this region because of the S vacancies [22], [23]. The TEM analysis was not oriented to find imperfections and it cannot confirm these vacancies.

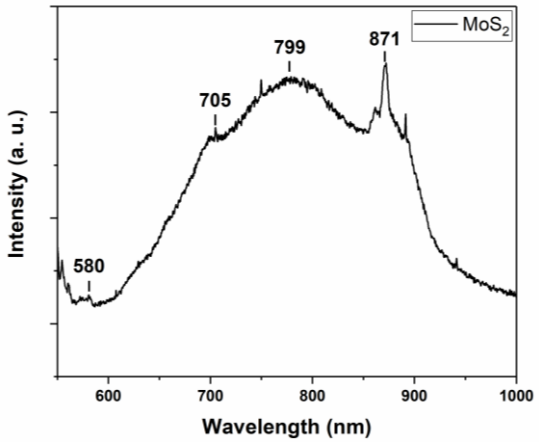

Figure 4.23 a) PL spectra of MoS_2 nanosheets.

4.4.5 Chemical analysis of MoS_2 nanosheets

The MoS_2 nanosheets were analyzed by X-Ray photoelectron spectroscopy to obtain their atomic relative concentration and chemical configuration. Figure 4.24 shows the survey spectrum of MoS_2 nanosheets after the synthesis. The presence of the Sulfur XPS signal indicates that synthesis of MoS_2 was successful. the peaks belonging to O1s, C1s, Mo3d and S2p are marked in the spectrum. The relative atomic concentration of the sample was oxygen 11.15 at. %, carbon 23.13 at. %, molybdenum at 23.91 % and sulfur 41.81 at. % with a S/Mo ratio of 1.74. This ratio is given as an indication (and will be for the other materials in the following paragraphs). It depends on many factors, including the XPS analysis parameters and of course the sample. Thus, in our studies, we focused on the regions of interest (Mo3d, W4f, S2p, Se 3d, etc...) in high resolution, and the survey spectra were taken only to observe the elements present, with low energy resolution and low number of scans. Another information is the depth of analysis, the first nanometers of the surface, which gives in fact in the case of our samples an idea an information on the edges exposed mostly on the surface, due to the nanosheets alignment. The theoretical value of this ratio is of course 2. A value less than 2 could indicate that there are some S vacancies and these vacancies are located at the edges of the sample.

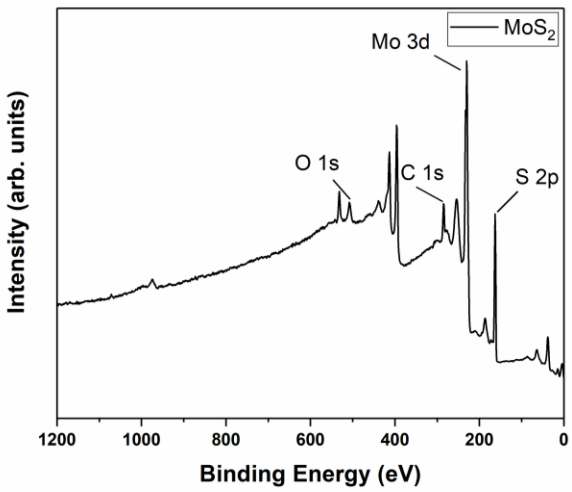

Figure 4.24 Survey spectrum of MoS_2 nanosheets. The peaks from O1s, C1s, Mo3d and S2p are observed.

The chemical state of the as-grown samples was investigated by X-ray photoelectron spectroscopy (XPS). The XPS spectra recorded on the Mo 3d and S 2p areas are shown figures 4.25 a) and b), respectively. In the Figure 4.25 a), the Mo 3d region exhibits two characteristic emission peaks at 232.1 and 229.0 eV attributed to the doublets Mo $3d_{3/2}$ and Mo $3d_{5/2}$. These binding energy values are consistent with electrons of Mo^{4+} corresponding to MoS_2 [24], [25]. Additionally, in this region, the S 2s peak at a binding energy of 226.2 eV corresponding to MoS_2 is also observed [25]. Besides the main MoS_2 component, there is a small contribution of the Mo 3d doublet at binding energies 235.7 and 232.8 eV attributed to the presence of MoO_3 [26]. Figure 4.25 b), shows two main peaks, S $2p_{1/2}$, and S $2p_{3/2}$ at 163 and 161.8 eV, respectively, with a spin–orbit energy separation of 1.2 eV corresponding to MoS_2 (S^{2-} oxidation state) [27]. One should note that no sulfur oxide peak was observed between 168 and 170 eV, which indicates that no oxidation of sulfur atoms occurred in this

sample. All these results are consistent with the reported values for the 2H-phase of the MoS_2 nanosheets [3].

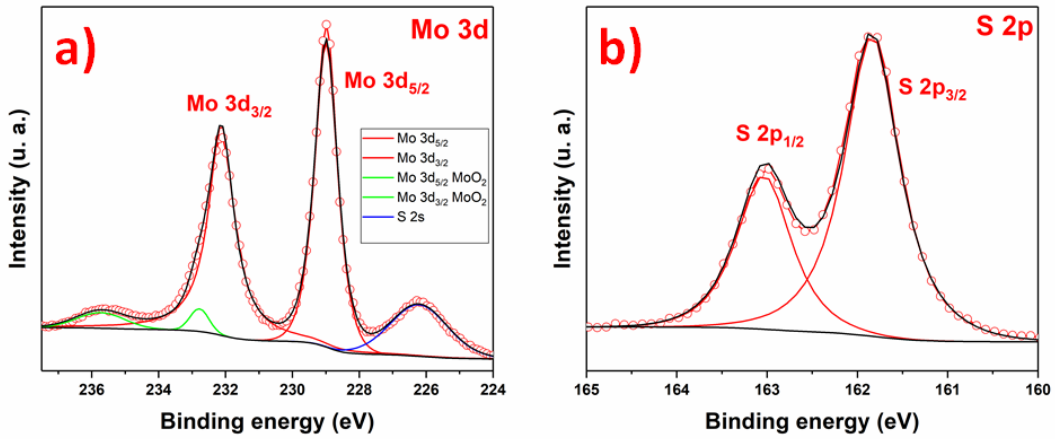

Figure 4.25 XPS spectra of the MoS_2 nanosheets (a) Mo 3d and b) S 2p.

4.4.6 Conclusions

Highly crystalline vertically-aligned MoS_2 nanosheets on sapphire substrate have been synthesized by CVD method. The TEM, XRD and Raman spectroscopy characterization of the nanosheets give us information about the presence of the 2H phase and with the SEM images we observe the thickness and size of this nanosheets (around 20 and 100 nm, respectively). PL presents the multilayer nature of this sample and also the S vacancies in the exposed edges and which is also confirmed with the ratio in the XPS analysis.

4.5 Tungsten Disulfide (WS_2)

4.5.1 Electron microscopies of WS_2 Nanosheets

The morphology of the as-synthesized WS_2 sample was characterized by SEM. The low-magnification images in Figure 4.26 a) reveal a large amount of WS_2 nanosheets with a vertical orientation that are uniformly distributed on the sapphire substrate. The nanosheets present thickness between 10 and 20 nm, length around 30 nm and have a well-defined shape with sharp edges. The synthesized samples are homogeneous without formation of crystal aggregates.

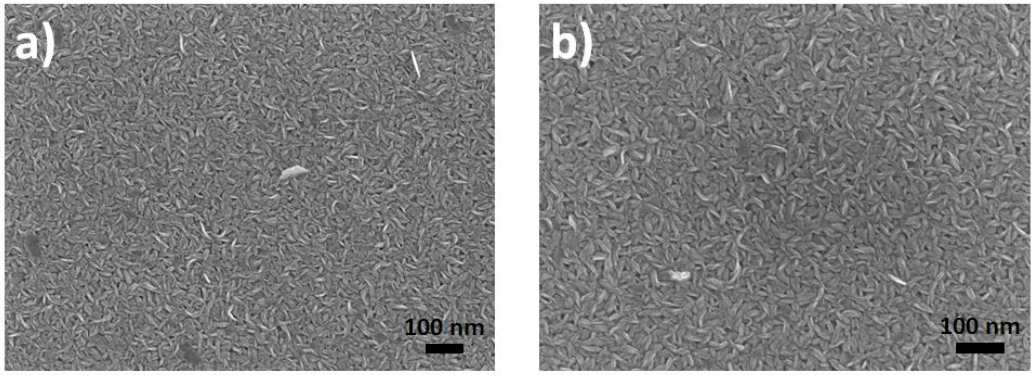

Figure 4.26 SEM images of synthesized products for a) and b) vertically aligned WS_2 nanosheets.

Individual WS_2 nanosheets were analyzed using the Transmission Electron Microscopy (TEM). The TEM image in the Figure 4.27 a) reveals the stacking of WS_2 (002) layers with an interplanar spacing of 0.62 nm and a lattice spacing of 0.33 nm, which is corresponds to (100) lattice plane of hexagonal WS_2 phase (Figure 4.27 b) [28], [29].

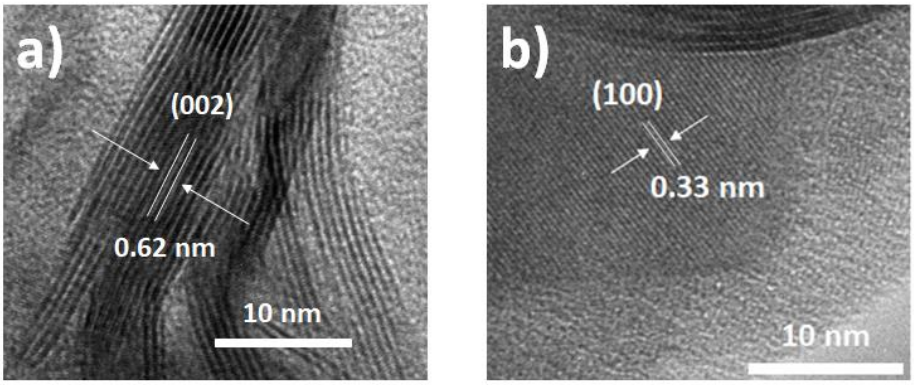

Figure 4.27 High resolution TEM image of the crystal showing the a) (002) and b) (100) crystal planes.

WS_2 samples were also examined by Energy-dispersive X-ray spectroscopy (EDS) using Scanning Transmission Electron Microscopy/High-Angle Annular Dark-Field imaging (STEM/HAADF) in the EMAT's group at the University of Antwerp. Figure 4.28 a) shows a cross-section of a WS_2/SiO_2 the vertical orientation of the nanosheets can be clearly seem. In the EDS spectrum the W and S are observed, demonstrating the chemical composition of our sample (Figure 4.28 b and c), indicating that these elements are uniformly distributed along the nanosheets.

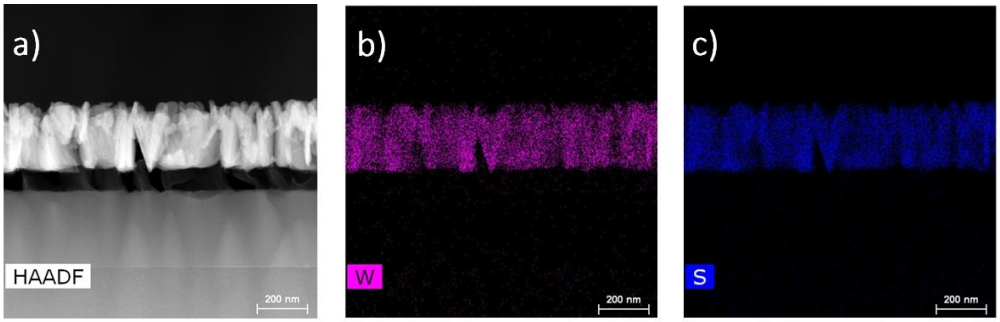

Figure 4.28 a) STEM/HAADF of vertically aligned WS_2 nanosheets and EDS spectrum of b) W and c) S.

4.5.2 X-Ray diffraction analysis of WS_2 Nanosheets

XRD was used to examine the crystal structure of the WS_2 nanosheets. Figure 4.29 presents the XRD patterns of the sample. The diffraction peaks at 14.16°, 33.1°, 38.5°, 45.28°, 58.5° and 69.2° can be referred to the crystal planes (002), (100), (103), (006), (110) and (108) of WS_2 [30]. All the peaks can be attributed to the 2H phase (JCPDS no. 08-0237), indicating its high purity [31] with the unit cell parameters a = b = 0.315 nm, c = 1.227 nm. The (002) diffraction peak of the WS_2 nanosheets is observed at 14.16°, indicating their well-stacked layered structure. Zheng *et al*. [32] reported that the intensity of the diffraction peak (002) is directly proportional with the crystal size and the number of layers of the sample. When the material is close to the bulk phase, the intensity of the peak is higher than the monolayer phase. Therefore, the main difference is the intensity of the (002) diffraction peak, where in the case of MoS_2 is higher than in the XRD pattern of WS_2. For that, we can say that MoS_2 presents more layers in its structure than WS_2.

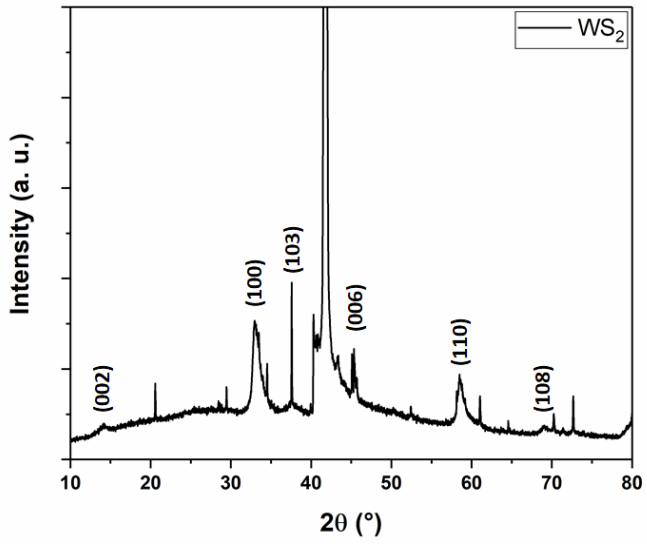

Figure 4.29 XRD pattern of WS_2 nanosheets.

4.5.3 Raman spectroscopy of WS_2 Nanosheets

Figure 4.30 shows the Raman spectrum of WS_2 nanosheets with the two main peaks at 353.9 and 420 cm^{-1}, assigned to the phonon modes. as in the case of MoS_2 [33]. In a monolayer sample, the two peaks are observed at 350 and 420 cm^{-1} corresponding to the E^1_{2g} and A_{1g} vibration modes, respectively. The frequency difference is thickness dependent and can be used to determine the number of layers as we explained in the Raman analysis of MoS_2. Zeng *et al*. [5] reported a frequency difference between E^1_{2g} and A_{1g} modes of 65.5 cm^{-1} for monolayer, while for bulk phase the value is around 70 cm^{-1}. The red-shifting of E^2_{g1} mode and blue-shifting of A_{1g} mode could be observed with increasing layer number [34], [35]. The frequency difference is our sample is 66.1 cm^{-1} which indicates that our material is multilayer because its frequency is between the monolayer and bulk phase.

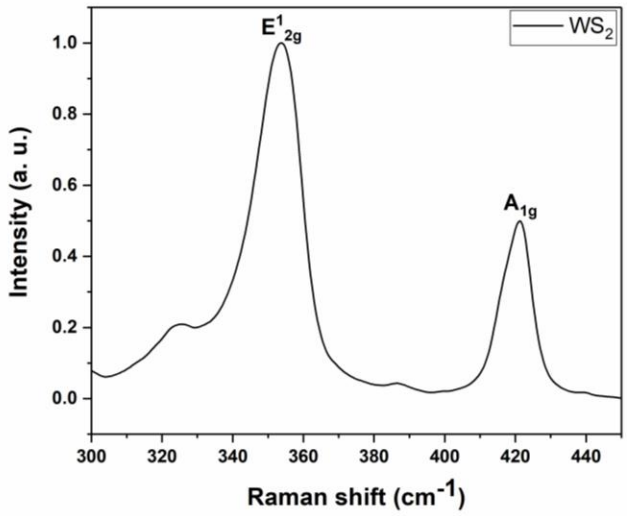

Figure 4.30 Raman spectrum with 532 nm excitation laser of WS_2 nanosheets.

4.5.4 Photoluminescence of WS_2 Nanosheets

Photoluminescence shows that WS_2 exhibits a transition from indirect band-gap semiconductor in the form of bulk and multilayers to direct band-gap one in monolayers [34]. The Figure 4.31 presents the PL spectrum of the WS_2 sample. The first peak at 580 nm could be attributed to the direct allowed transitions in WS_2, value close to ones given in the literature [36], which agrees with the values of monolayer samples and similar to MoS_2 cases [18] (see Figure 2.11 in Chapter 2). The PL peak observed at 799 nm (1.35 eV) correspond to an increased band-gap of the as-grown WS_2 nanosheets. In our sample, the maximum PL intensity may be attributed to the nanosheets edges. In this context, Peimyoo *et al.* [22] have demonstrated larger monosulfur vacancies concentration near the edges in comparison with the interior of the nanosheets, explaining the features observed in our PL spectrum.

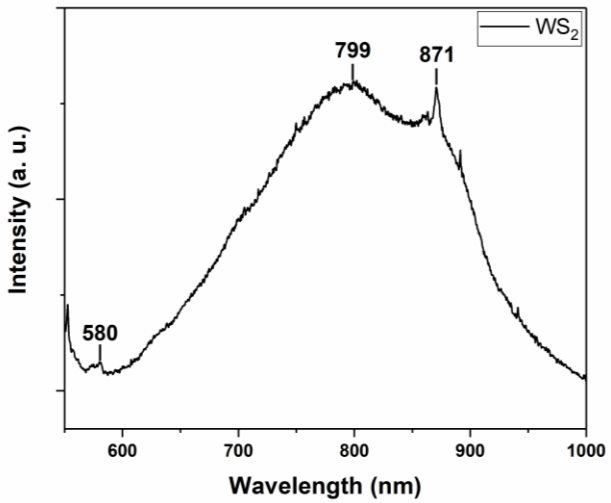

Figure 4.31 PL spectra of WS_2 nanosheets.

4.5.5 Chemical analysis of WS_2 Nanosheets

The WS_2 nanosheets were analyzed by X-Ray photoelectron spectroscopy to obtain their atomic relative concentration and chemical configuration. Figure 4.32 shows the survey spectrum of WS_2 nanosheets after the synthesis. The presence of the Sulfur and W XPS signal indicates the bond between these two elements is present. The peaks belonging to O1s, C1s, S2p and W4f are marked in the spectrum. The relative atomic concentration of the sample was oxygen 9.62 at. %, carbon 29.62 at. %, sulfur 40.8 at. % and tungsten 19.96 at. % with a S/W ratio of 2.04. The value is close to the theoretical one and can be considered but with the precautions explained previously in the section 4.4.5.

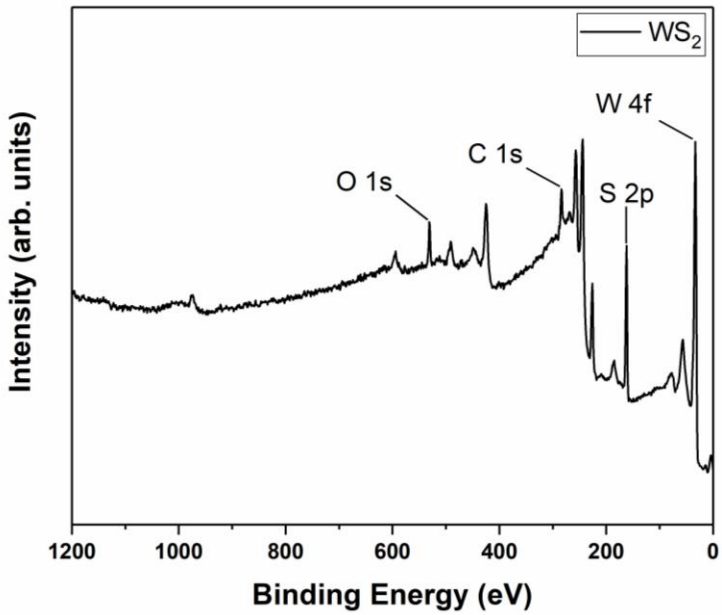

Figure 4.32 Survey spectrum of WS_2 nanosheets. The peaks from O1s, C1s, S2p and W4f are observed.

The WS_2 nanosheets were investigated by X-ray photoelectron spectroscopy (XPS). The XPS spectra recorded on the W 4f and S 2p binding energy regions are shown in Figure 4.33. Figure 4.33 a) shows W $4f_{3/2}$ and W $4f_{7/2}$ peaks at 34.8 and 32.7 eV, respectively, which confirms the presence of W with a valence of +4 [37] of the semiconducting 2H phase [38]. As for the doublet at 38.3 and 36 eV in Figure 4.33 a), we assign them to the W-O bond, indicating that some of the starting material (WO_3) is not reacting and remains so in the final product [29]. Similarly, Figure 4.33 b) shows deconvoluted peaks corresponding to S $2p_{1/2}$ and S $2p_{3/2}$ at 163.5 and 162.3 eV. These values are coherent to the previously reported values of WS_2 nanosheets. Doublet peaks of S $2p_{1/2}$ and S $2p_{3/2}$ are characteristic of S^{2-} in WS_2 [39]. The XPS results indicate that the W film is transformed into WS_2 nanosheets after the sulfurization process [39]. During sulfurization the metal oxide film may not react completely during the synthesis process.

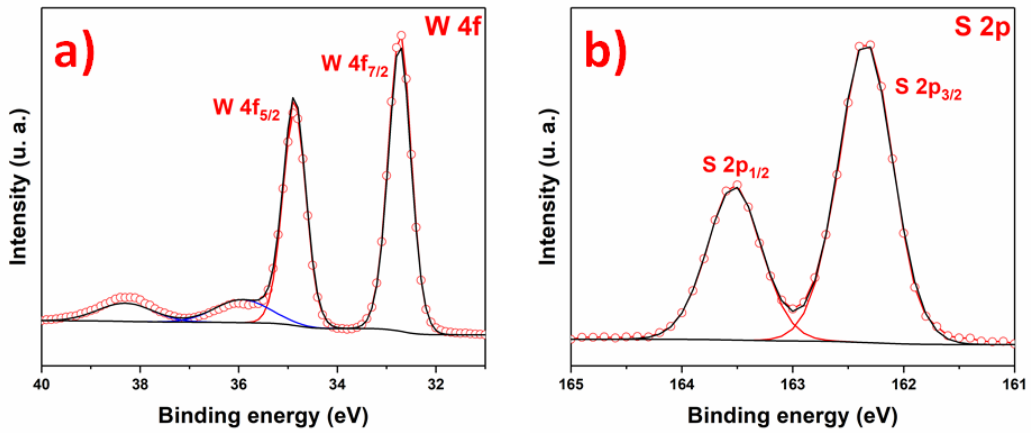

Figure 4.33 XPS spectra of the WS_2 nanosheets (a) W 4f and 5p and b) S 2p.

4.5.6 Conclusions

Highly crystalline vertically-aligned WS_2 nanosheets on sapphire and SiO_2 substrates have been synthesized by the proposed CVD route. The length and thickness of the nanosheets are around 30 and 20 nm, respectively. In accordance, TEM, XRD and Raman spectroscopy characterization indicate the presence of the 2H phase. The PL spectrum suggest the presence of few monolayers in the sample, however the majority of the nanosheets are multilayers. An intense peak associated to S vacancies at the exposed edges was observed. Finally, the XPS analysis shows that the sulfurization reaction was almost complete.

4.6 Tin Disulfide (SnS_2)

4.6.1 Electron microscopies of SnS_2 nanosheets

SEM images in Figure 4.34 show the morphology after the sulfurization of Sn deposited (50 nm) on a sapphire substrate for the SnS_2 nanosheets. The low-magnification images in Fig. 4.34 a) and b) reveal a large amount of SnS_2 nanosheets that are uniformly distributed on the sapphire substrate. The high magnification image (Figure 4.34 c) shows SnS_2 nanosheets, with an average length of 500-600 nm and a thickness of 30-35 nm, have a well-defined shape with sharp edges. The difference between these three images is the magnification. The homogeneity of the sample (Figure 4.34 a) can be observed (Figures 4.34 b and c). Figure 4.34 d) shows the cross section of the sample. The image was taken at till angle of 62°, the presence of SnS_2 nanosheets with vertical orientation can be observed.

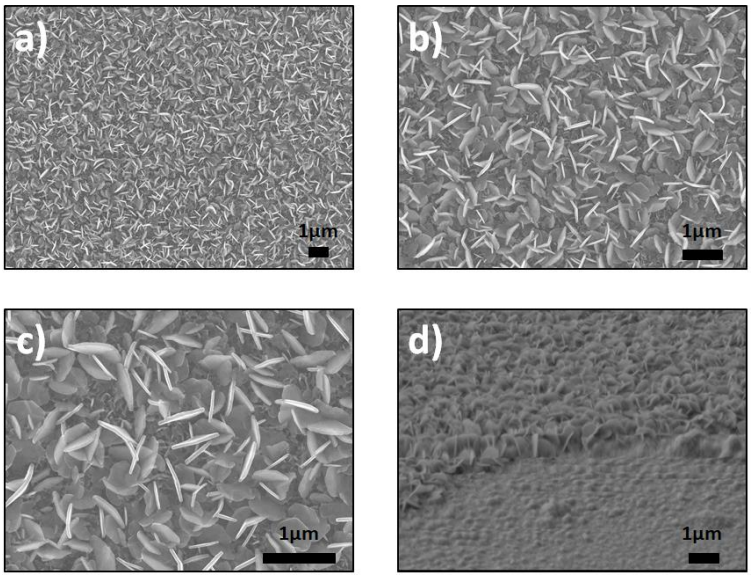

Figure 4.34 SEM images of synthesized products for vertically aligned SnS_2 nanosheets, a-c) top view and d) cross section (62°).

The morphology of the as-synthesized SnS_2 nanosheets has been characterized using TEM (Figure 4.35 and 4.36). The Figure 4.35 a) and b) shows representative images of nanosheets exhibiting the layered structure with a typical interlayer distance of 0.59 nm corresponding to the (001) crystal planes. Figure 4.35 c) shows a low magnification image of a single nanosheet with the corresponding selected area diffraction (SAED) pattern in the inset. This SAED pattern exhibits well-defined and sharp spots in a hexagonal geometry, indicating a hexagonal crystal structure and the single-crystal nature of the observed nanosheet. A magnified region of this nanosheet is given in Figure 4.35 d) where appears clearly lattice fringes with spacing to 0.32 nm relating to the (100) crystal planes. This distance confirms also the hexagonal phase of the nanosheets [40], [41].

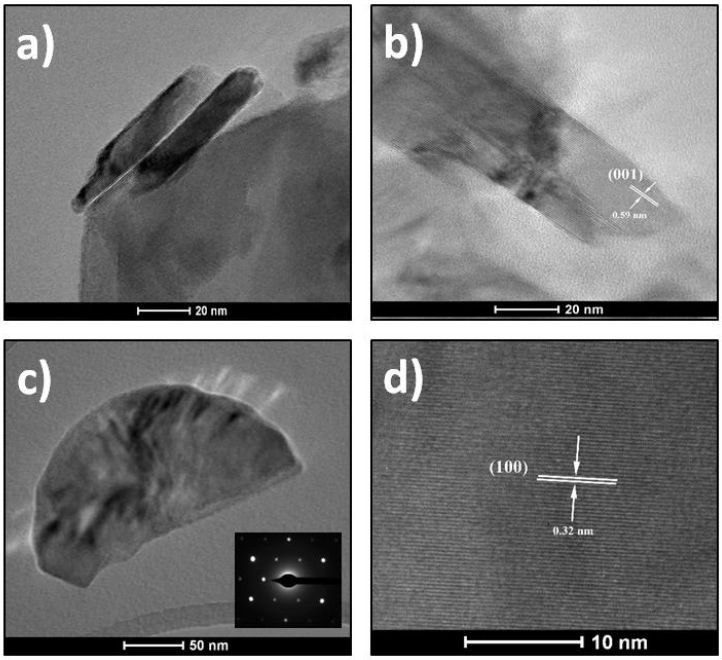

Figure 4.35 a) and b) TEM images of layered structures of nanosheets, c) Low magnification image of a single nanosheet with SAED pattern in inset and d) high resolution image of the crystal showing the (001) crystal planes.

Fig. 4.36 a and b show two high-angle annular dark-field (HAADF) STEM micrographs of two different SnS_2 nanosheets, revealing the high crystallinity of these flakes. EDS analyses performed on these materials confirm the high purity of these flakes with the good ratio S/Sn of 2, see Fig. 4.36 c. The TEM grid is made of Cu and that explain its presence in the spectra.

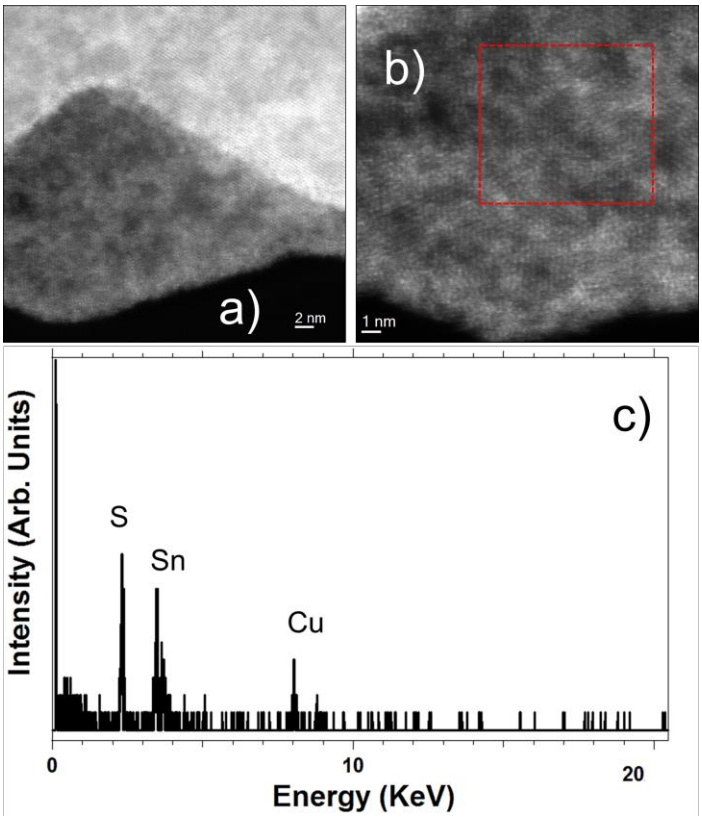

Figure 4.36 STEM images in HAADF mode of SnS_2 nanosheets.

4.6.2 X-Ray diffraction analysis of SnS_2 nanosheets

Based on the microscopy studies, the conclusions that can be drawn is that the SnS_2 nanosheets are crystallized in a hexagonal structure. This has been checked using XRD. Indeed, in Figure 4.37, a typical XRD pattern of the as-prepared SnS_2 nanosheets is shown. The diffraction peaks appearing at 14.5°, 28.6°, 32.3°, 50.2° and 52.1° are distinctly indexed to the (001), (100), (101), (110) and (102) planes of the hexagonal SnS_2 phase, which are very close to the reported data (JCPDS card 23-0677) for the hexagonal 2H phase [42] with the unit cell parameters a = b = 0.364 nm, c = 0.589 nm. The intensity of the (001) diffraction

peak can be because of the lager nanosheets and for the multilayer nature of the sample (more layers if we compare it with MoS_2 and WS_2).

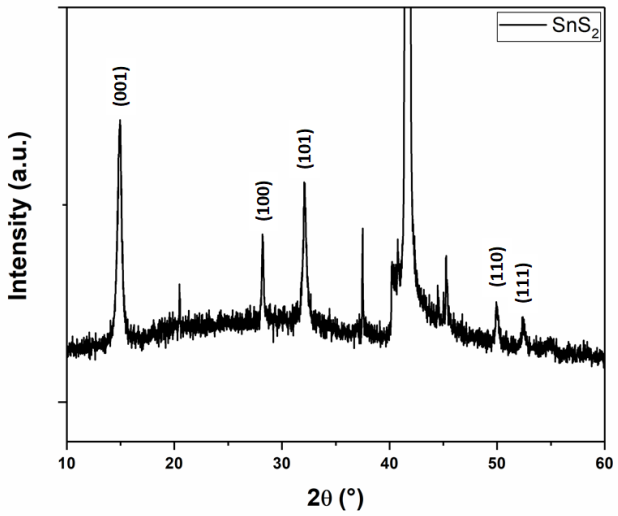

Figure 4.37 XRD pattern of SnS_2 nanosheets.

4.6.3 Raman spectroscopy of SnS_2 nanosheets

Figure 4.38 a) shows the Raman spectrum of SnS_2 nanosheets, the two main peaks of 205 and 315 cm^{-1}, assigned to the phonon modes. The most intense peak at 315 cm^{-1} is assigned as A_{1g} mode corresponding to vertical out-of-plane vibration between S-S. In the Figure 4.38 b) the Eg correspond to non-degenerate in-plane vibration mode with a single band at 205 cm^{-1} [43], [44]. The low intensity of the Eg peak is explained by the low thickness of the nanosheets, reducing the in-plane scattering centers as already reported [45]. The Raman signature of the SnS_2 material agrees with the previous results and confirms the crystallization into hexagonal 2H structure.

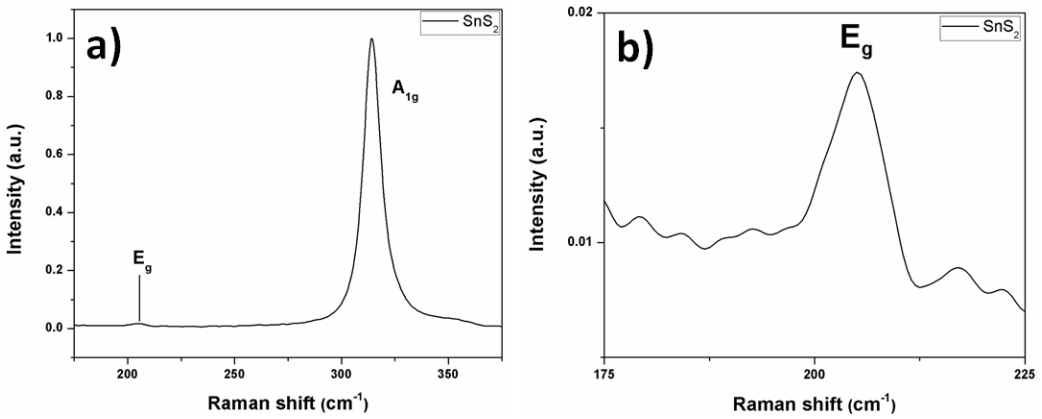

Figure 4.38 Raman spectrum with 532 nm excitation laser of SnS_2 nanosheets (a) and (b).

4.6.4 Photoluminescence of SnS_2 nanosheets

The PL spectrum of the SnS_2 sample exhibits different features: a low intensity sharp peak at 580 nm (2.14 eV) that is attributed to recombination at the indirect bandgap of thin SnS_2 film [46], [47] and an intense broad peak located at 730 nm (1.70 eV) whose origin can be associated to different recombination according to the literature: the presence of another stoichiometry such as SnS material, giving rise to a PL transition at this energy could be the explanation despite the fact that previous discussed characterization results indicate the sole presence of 2H-SnS_2. However the energy does not correspond to the band gap of SnS around 825 nm (1.5 eV) and the broad of the peak does not argue for a single and well-defined energy transition [48]. A report on 2D flakes of SnS_2 synthesized by wet chemistry, show similar features on the PL spectrum (at 532 nm) with a sharp peak at about 580 nm (indirect excitonic peak as previously assigned) and a broader peak centered here at about 660 nm [43]. This was explained by the author as indirect exciton recombination of 4H phase of SnS_2 present in the sample, rejecting the other possibilities due to the high quality of the

synthetized SnS_2 flakes (without impurities, without sulfur vacancies, etc.). In our SnS_2 material, 4H phase is not present, which makes it impossible to reach the same conclusion. However, such broad peak can be also ascribed as effect of crystalline defects/impurities or effect of interface strain between film and substrate, generating bound excitons recombination [46], [49]. A good example is the PL comparison (at 532 nm) between bulk and exfoliated material showing a broad peak centered at 680 nm dramatically increased for the exfoliated material, explained by electron-phonon interaction caused by the large amount of sulfur vacancies [50]. Considering our material, the structural and chemical characterizations demonstrates that high crystalline nanosheets of SnS_2 have been successfully synthetized and the presence of impurities or S vacancies were not shown. However, it was reported for transition metal dichalcogenide materials that bulk characterization techniques such as XRD cannot give a perfect overview of the quality of the synthesized material, which techniques such as Raman and PL spectroscopy do [51]. The possibility of having vacancies/defects in the samples cannot be excluded, as the TEM analyses were not focused on finding these imperfections. Another fact that could also influence the results obtained in PL is the morphology of the samples. Indeed, the nanosheets are oriented vertically with respect to the substrate, exposing their edges. Indeed, it has been shown that there is an increase in photoluminescence at the edges and also at the grain boundaries of triangular WS_2 monolayers, explained by the different structure and composition of these regions compared with the center [52], [53]. Another related study demonstrates a larger monosulfur vacancies concentration near the edges in comparison with the interior, explaining the features observed in PL [23]. A last study,

concerning MoS_2, has shown that he exposed edges of the nanosheets due to the vertical orientation enhanced the PL emissions [6]. The last peak observed in the Fig. 4.39 at 987 nm (1.26 eV) it may be attribute to the emission signal of the SiO_2 substrate.

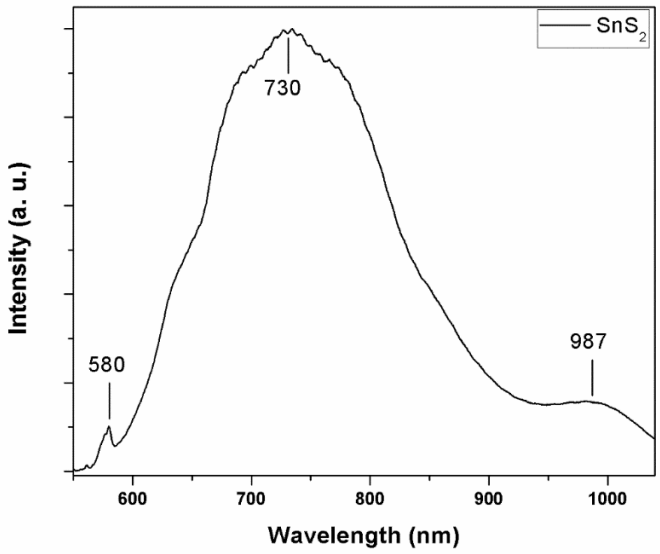

Figure 4.39 PL spectra of SnS_2 nanosheets.

4.6.5 Chemical analysis of SnS_2 nanosheets

The SnS_2 nanosheets were analyzed by X-Ray photoelectron spectroscopy to obtain their atomic relative concentration and chemical configuration. Figure 4.40 shows the survey spectrum of SnS_2 nanosheets after the synthesis. The presence of the Sulfur XPS signal indicates that synthesis of SnS_2 was successful. the peaks belonging to O1s, Sn3d, C1s and S2p are marked in the spectrum. The relative atomic concentration of the sample was oxygen 15.71 at. %, tin 24.84 at. %, carbon 22.92 at. % and sulfur 37.07 at. % with a S/Sn ratio of 1.49.

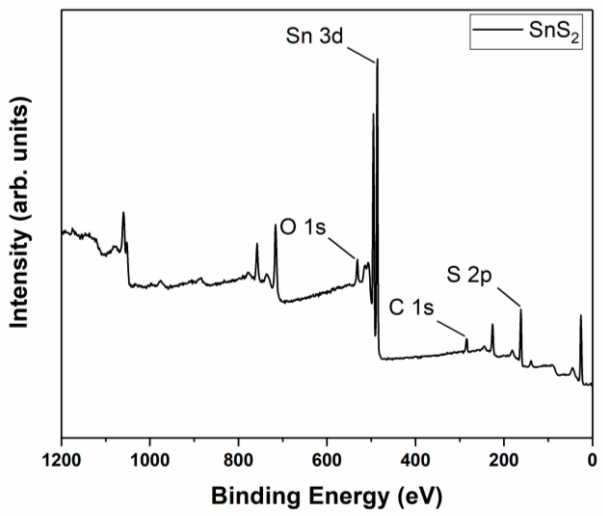

Figure 4.40 Survey spectrum of SnS_2 nanosheets. The peaks from O1s, Sn3d, C1s and S2p are observed.

The chemistry of the as-prepared products was further investigated by XPS as shown in Figure 4.41. Figure 4.41 a) and b) present the Sn 3d and S 2p core level of SnS_2 samples. The Sn 3d signal is composed of one doublet, with contributions centered at 487.1 and 495.6 eV, attributed to Sn $3d_{5/2}$ and Sn $3d_{3/2}$ of Sn^{4+} in SnS_2, respectively [54], [55]. No other contribution is observed [56]. The S 2p spectrum (Figure 4.41 b) is composed of a one doublet, with S $2p_{3/2}$ and S $2p_{1/2}$ signal centered at 161.8 and 162.7 eV respectively, attributed to S^{2-} species in SnS_2 [48]. Both Sn 3p and S 2p confirms the successful formation of SnS_2 phase, without another phase.

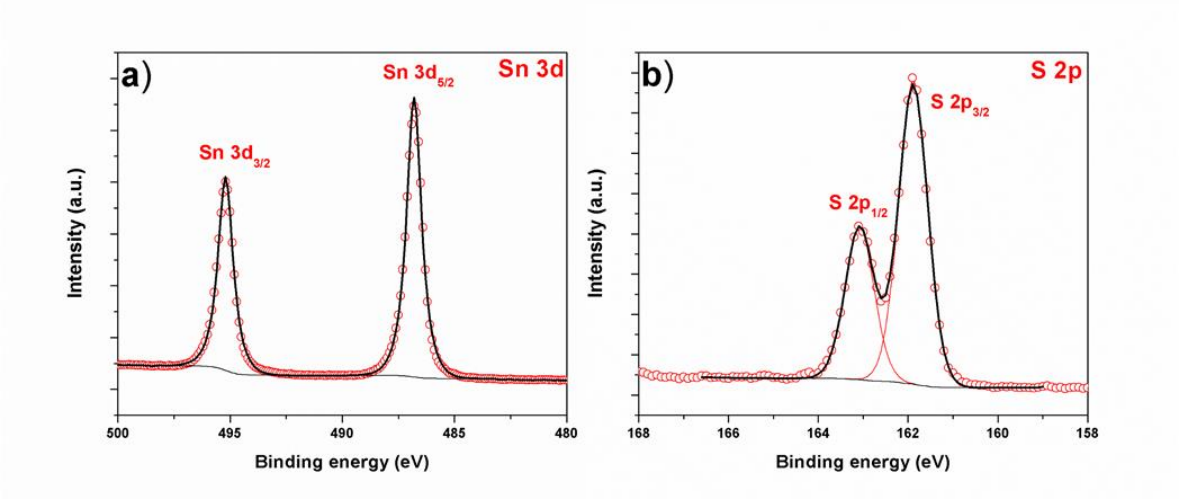

Figure 4.41 XPS spectra of the SnS_2 nanosheets a) Sn 3d and b) S 2p.

4.6.6 Conclusions

It is demonstrated the synthesis of vertically aligned SnS_2 nanosheets using a simple one-step CVD technique by direct sulfurization of a pre-oxidized tin film. We evidenced the quality of the as-synthesized materials by employing XRD, Raman spectroscopy, XPS and electron microscopies. Vertical and homogeneous alignment of well-crystalline 2H-phase SnS_2 nanosheets have been demonstrated, the nanosheets, however, having structural defects at their edges.

4.7 Discussions

With the results discussed in this Chapter, a possible growth model for the XS_2 a, where "X" can be Mo, W, or Sn, aligned nanosheets prepared by sulfurization, respectively, of pre-deposited 50 nm X films via magnetron sputtering is proposed. It is important to mention that the importance of the film thickness was not studied because we used 50 nm as a standard metal film for all the synthesis cases with different metals.

In the first part of the chapter the materials obtained by sulfurization reaction were described. We separated the discussions in this section for the TMDs and TDs results because they present some differences during the preparation and synthesis of the materials. For TMDs, in the case of MoS_2 and WS_2, we proposed a two-step nanosheet growth mechanism by rapid sulfurization, as we explained in the section 4.1 of this chapter. The preparation of the precursor film is the key parameter because it has been shown that the magnetron sputtering parameters play an essential role in the morphology of the deposited films, especially the argon pressure [57]. It has been reported that in tungsten deposition, a lower argon pressure results in a denser film structure than with a higher pressure where the film has a porous structure with cracks. Here, the film deposition has been made at 1×10^{-3} mbar at room temperature that is a lower value than ones reported. During the nanosheet synthesis, the temperature of the sample was maintained at a sufficiently higher temperature (850 °C) favoring the formation of the nanosheets. The S powder was kept at a higher temperature (400 °C) than its boiling point (350 °C). The X (Mo or W) film was oxidized in air and form metal oxides. During the high-temperature growth procedure, the metal oxide segregation and the sulfurization take place simultaneously. If the background sulfur is sufficient, the sulfurization reaction is the dominant mechanism. Most of the surface Mo oxides will be transformed into XS_2 in a short time. The XS_2 film formed on the sample surface will prevent the presence of metal oxide segregation and coalescence. Under a sulfur deficient condition, since there is no sufficient sulfur, only limited numbers of XS_2 will form at the substrate surface. In this case, Mo oxide segregation and coalescence will be the dominant mechanism at the initial stage of the sulfurization

procedure. Small Mo oxide clusters are then formed on the sapphire substrates. The thick metal oxide clusters will prevent complete transformation of the metal oxides into XS_2 [58].

For SnS_2 the chemistry of the film is different, tin instead of molybdenum or tungsten, the results obtained seem not to follow the same trend as vertical alignment of the nanosheets is not observed with direct reaction on the film, certainly due to the film density. We proposed a single-step nanosheet growth mechanism by rapid sulfurization at lower temperature (550 °C). The effect of the pressure on the sputtering tin films has been not studied. To overcome this problem, the solution found was to oxidize the tin film as of homogeneity is promoted. Indeed, the sputtered film is metallic but when it is transferred on air after the deposition a partial oxidation occurs due to the thickness of the film. For a homogeneous oxidation of the whole film, an oxidation step is performed. Depending on the level of oxidation, the surface will change determining the diffusion of the S, which is very important for the vertically growth. Indeed, we observed that the morphology of the nanostructures strongly depends on the oxidation level before sulfurization. As an example, for sulfurization: (i) the vertical alignment of SnS_2 nanosheets was not observed on tin film as sputtered (with partial oxidation in air); (ii) samples synthesized on tin film oxidized at 200°C for 2 hours with air flow presents a flower-like morphology with short nanosheets grouped in the form of spheres without any preferential alignment (Figure 4.13); and (iii) samples synthesized on tin film oxidized at 300°C for 2 hours with air flow shows a vertical orientation of the nanosheets with uniformly distribution in all the surface (Figure 4.13). Therefore, it can be postulated that depending on the level of oxidation, different thickness of the film will be oxidized and this will determine the diffusion of S, a very important factor

for vertical growth of nanosheets. Indeed, it has been reported that the diffusion of S through the film is necessary and that this process is the limiting factor for the orientation of the nanosheets [59]. According to our experimental data, the Sulfur diffusion expands (increases with the thickness of) the oxidized layer, it seems that S interacts just with Sn near the film surface for case(ii) and short nanosheets are formed, while for case (iii) due to the higher temperature the Sn diffuses deeper leading to a pronounced change of the surface morphology. Another parameter reported in the literature playing an important role in the final product characteristics is the composition of the reactive atmosphere near the film, more or less rich in S [58]. Indeed, it has been shown for MoS_2 that in order to have a complete reaction with the oxidized film, it is necessary to have an atmosphere rich in S for this to be the dominant mechanism, instead of having an atmosphere deficient in S, as in this case the modification of the surface occurs due to the dominant mechanism of oxide segregation/coalescence [58]. The effect of the sulfur concentration during the synthesis was not evaluated, however we can assume that the atmosphere is rich enough in S for the sulfurization reaction to occur. Therefore, the Sn oxide film is reduced by sulfur and we obtained SnS_2 in a short synthesis time. A very fast reduction of Sn oxides by S might have an important role in the formation of vertically aligned layered nanosheets. The growth of nanosheets occurs along two directions ([001] and [100]), with higher growth velocity along [001] leading to the formation of sheet-like structures. The vertical alignment of nanosheets formation is possibly favored by its anisotropic atomic bonding nature.

METAL DICHALCOGENIDES WITH SELENIUM

AS A CHALCOGEN

4.8 Synthesis Results of Metal Dichalcogenides using Selenium as a Chalcogen

The study of MX_2 samples synthesized by selenization of 50 nm of metal film deposited on a sapphire or SiO_2 substrate are presented in the next sections (Parameters used in Table 4.2).

4.9 Molybdenum diselenide ($MoSe_2$)

4.9.1 Electron microscopies of $MoSe_2$ Nanosheets

The SEM images in figure 4.42 show the morphology of $MoSe_2$ sample obtained by the selenization of 50 nm of Mo deposited on a sapphire substrate. The low-magnification images (Figure 4.42 a and b) reveal the large amounts of $MoSe_2$ nanosheets with a vertical orientation that are uniformly distributed on the sapphire substrate. The high magnification image in Figure 4.42 c) shows $MoSe_2$ nanosheets with well-defined shape, with a thickness of 70-80 nm, which is larger than MoS_2 (around 20 nm) and a length around 400 nm. The $MoSe_2$ sample is not homogeneous as the MoS_2 sample because the nanosheets have different orientations (vertical and horizontal). This can be attributed to the use Se instead of S as a chalcogen, which is not strong enough to perform the reduction alone and for that H_2 is used during the synthesis.

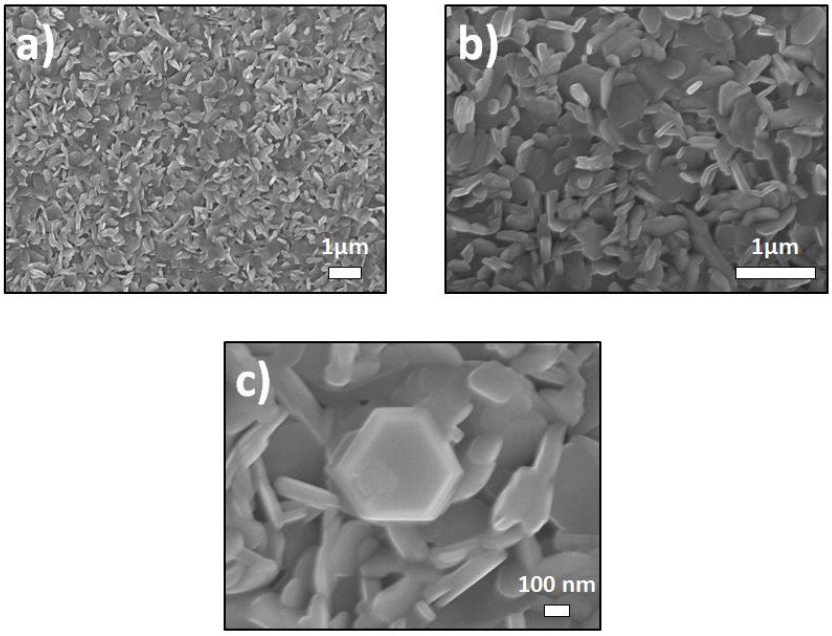

Figure 4.42 SEM images of vertically aligned $MoSe_2$ nanosheets with different magnifications (a-c).

The morphology of the nanosheets was investigated using TEM. A TEM image of a nanosheet with a large edge is shown in Figure 4.43 a), which exhibits the (002) plane with an interlayer spacing of 0.61 nm. The measured lattice distance corresponds to the 2H phase $MoSe_2$ [60]. TEM was performed to further analyze the $MoSe_2$ nanosheets crystal structure. HRTEM (Figure 4.43 b) image reveals hexagonal lattice fringes with a lattice spacing of 0.26nm, which is consistent with the lattice spacing of $MoSe_2$ (100) planes [61].

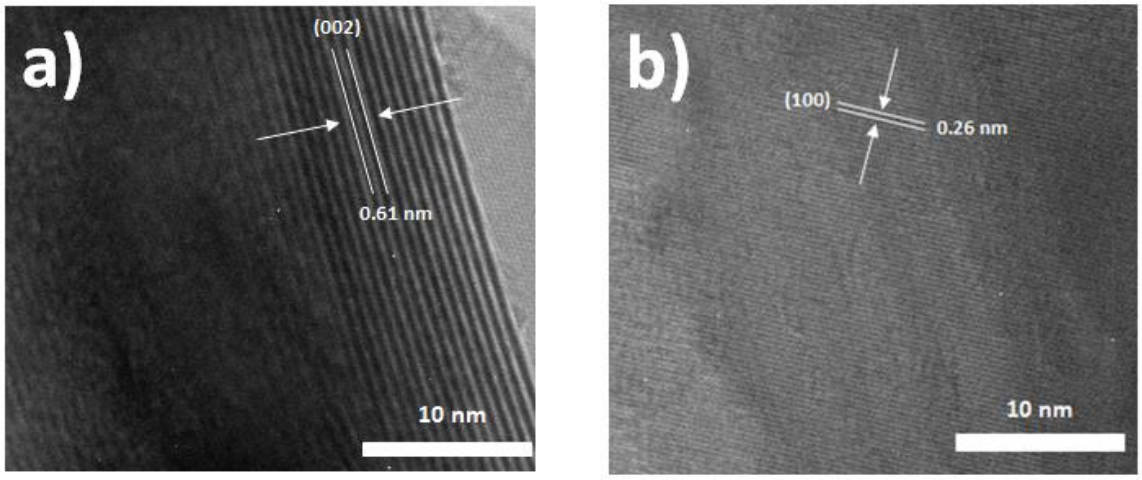

Figure 4.43 High resolution TEM image of the crystal showing the a) (002) and b) (100) crystal planes.

4.9.2 X-Ray diffraction analysis of $MoSe_2$ Nanosheets

The $MoSe_2$ crystallographic phase composition was investigated by XRD. Figure 4.44 shows the recorded XRD pattern, the diffraction peaks appearing at 13.8°, 27.7° and 57.0° are distinctly indexed to the (002), (004) and (008) planes of the hexagonal $MoSe_2$ phase, which correspond to the reported data (JCPDS card 65-3481) [62], [63] with the unit cell parameters a = b = 0.329 nm, c = 1.289 nm. The peaks observed indicate the high purity and crystallinity of the products and agree with the TEM analysis. The well-defined and intense peaks are characteristics when the material is in the bulk phase or close to this phase.

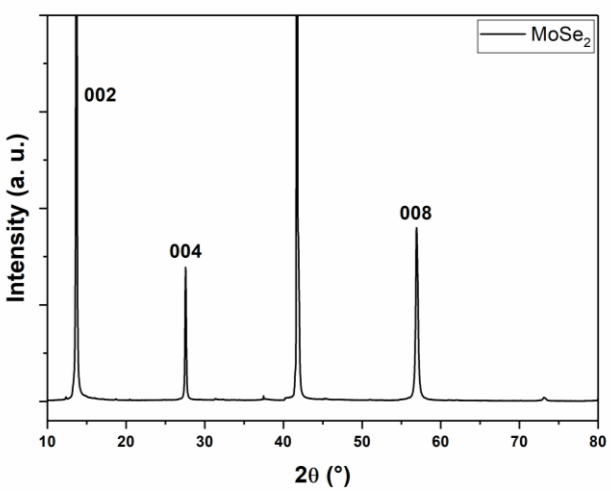

Figure 4.44 XRD pattern of $MoSe_2$**.**

4.9.3 Raman spectroscopy of $MoSe_2$ Nanosheets

The Raman spectrum of the $MoSe_2$ nanosheets is shown in Figure 4.45. Two main peaks located near 169 cm^{-1} and 243 cm^{-1} in the Raman spectra can be assigned to the E_{1g} (corresponding to the in-plane vibration of the Se and Mo atoms) and A_{1g} (out of plane vibration) modes, respectively [63], [64], which is characteristic of the 2H phase. Two low intensity modes also appear, the E^1_{2g} (corresponding to the in-plane vibration of the Se and Mo atoms) and B^1_{2g} (belonging to bulk $MoSe_2$), close to 286 cm^{-1} and 352 cm^{-1}, respectively [5], [62]. Combining Raman and XRD results we can say that the $MoSe_2$ sample is composed of multilayers.

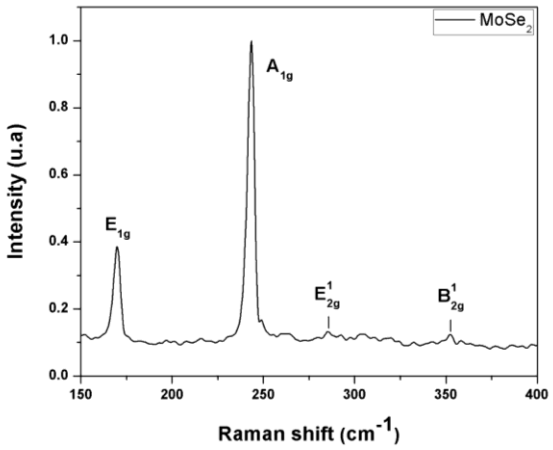

Figure 4.45 Raman spectrum with 532 nm excitation laser of $MoSe_2$ nanosheets.

4.9.4 Photoluminescence of $MoSe_2$ Nanosheets

Monolayer $MoSe_2$ presents a strong direct transition (DT) emission of around 840 nm, due to its direct band gap [5]. When increasing the number of layers of the $MoSe_2$, indirect transitions (IT) emissions also appear at a lower energy. The peak of the IT does not appear in the monolayer PL spectrum (Figure 4.46 a) [4].

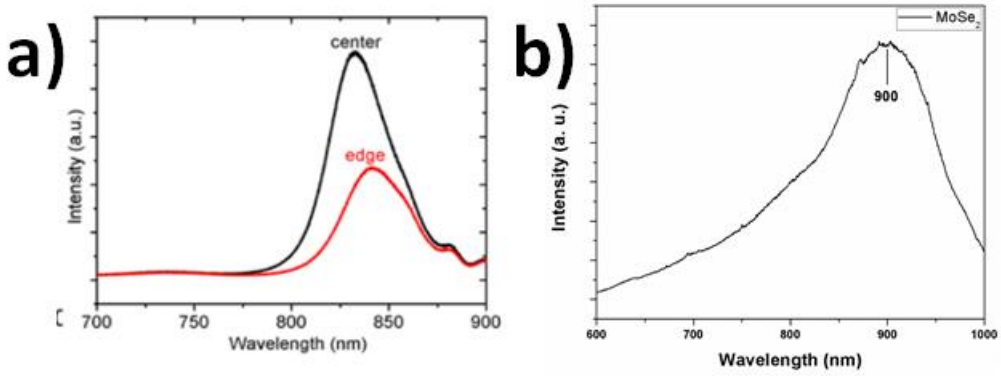

Figure 4.46 PL spectra at the center (black) and edge (red) of monolayer $MoSe_2$ [5] and b) PL spectra of $MoSe_2$ nanosheets.

The PL spectrum of $MoSe_2$ is shown in the Figure 4.46 b). We can observe a main peak at 900 nm wavelength, which corresponds to a red-shift from 840 to 900 nm, indicating the indirect nature of the transitions [65]. This is because as the number of layer increases, their energy band structures experience an obvious transformation. The valence-band maximum (VBM) transfers from the K point to Γ to Γ-K point, while the conduction-band minimum (CBM) transfers from the K point to Γ-K point. In the case of monolayer, both VBM and CBM are located at K point in Brillouin zone as we can see in the Figure 4.47 [66] (The Figure is presented to show the band gap transitions, depending in the calculation the values will be different. For that, these values are not considered and only the ones reported in the Figure 4.46 because they agree with our results). Furthermore, this feature—the presence of IT emissions with important wavelength shifts—demonstrates a multilayer nature, according to the literature. The value of this shift can be considered as a layer number indicator [4]. The shift of the peak in the PL spectrum can by cause by defect, which are more common around the edges. That defects, in particular Se deficiencies, are responsible for the red-shift of the PL peak position and associated apparent reduction of the bandgap at the edges [5].

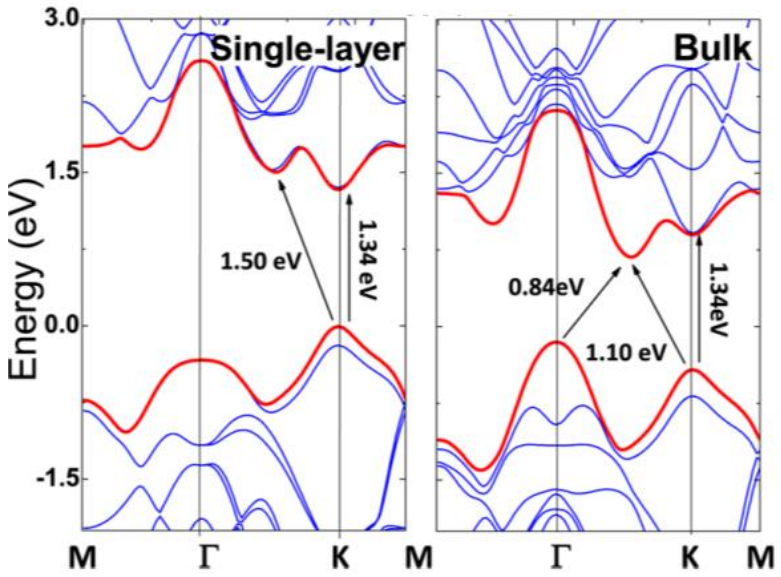

Figure 4.47 Calculated band structure of single-layer and bulk $MoSe_2$ [66]**.**

4.9.5 Uv-vis spectroscopy of $MoSe_2$ Nanosheets

The UV-Vis spectroscopy technique can be employed as an alternative method to unambiguously determine the number of layers [67]. The reflectance spectrum is shown in Figure 4.48. The excitonic peaks are labeled as A, B and C. The peak A originates from the absorption transitions at the K point of the Brillouin zone from the upper valance band to the lowest conduction band. This peak exhibits a red-shift as the layer number increases from monolayer to multilayer, as we can see in the Figure 4.49. It corresponds to the dominant peak in photoluminescence (PL) spectra [68], [69]. The peak B centered at slightly lower wavelength originates from the transitions of the split lower valance band to the conduction band (Figure 4.47).

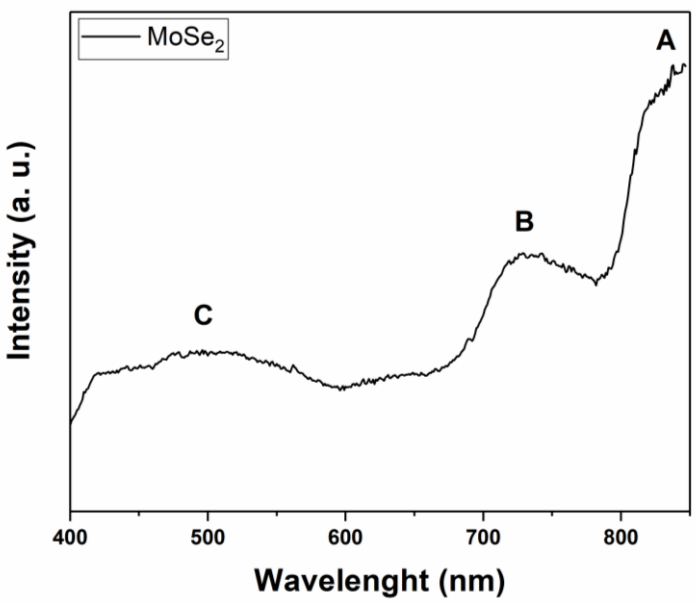

Figure 4.48 UV–VIS spectrum of $MoSe_2$.

For monolayer TMDs, the origin of this higher energy transition at the K point was related to the splitting of the valence band, due to the spin-orbit interaction. For multilayer systems, the splitting of the valence band is driven by a combination of spin-orbit and interlayer interaction [67] (Figure 4.49). Other than the A and B peaks, a broader spectroscopic at the lower wavelength, is referred as C exciton peak. The strong light-matter interaction has been attributed to the transitions of multiple nearly degenerate states between the Γ and K points of the Brillouin zone, where the conduction and valence bands are parallel to each other. The electron-phonon interaction further contributed to the broadened resonance [67], [68].

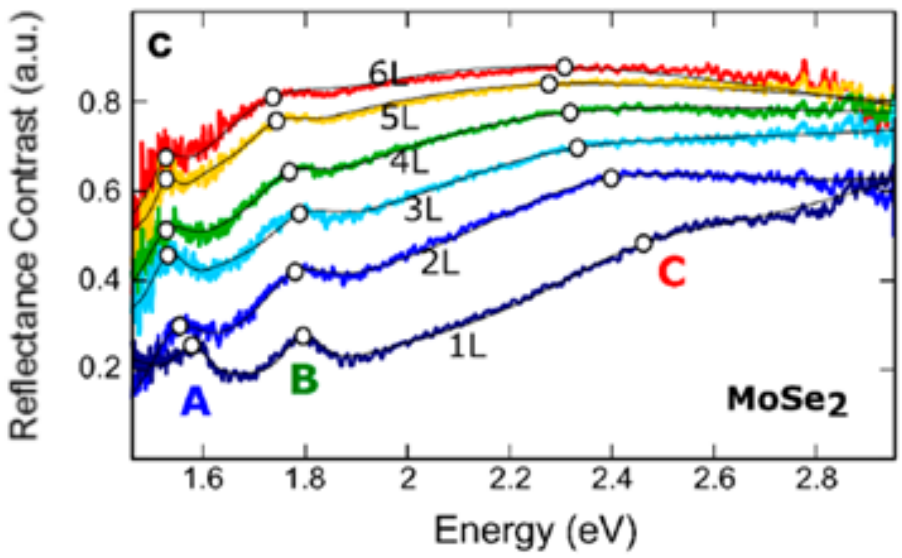

Figure 4.49 Reflectance spectra of $MoSe_2$ measured as a function of the number of layers [67].

4.9.6 Chemical analysis of $MoSe_2$ Nanosheets

The $MoSe_2$ nanosheets were analyzed by X-Ray photoelectron spectroscopy to obtain their atomic relative concentration and chemical configuration. Figure 4.50 shows the survey spectrum of $MoSe_2$ nanosheets after the synthesis. The presence of the Selenium XPS signal indicates that synthesis of $MoSe_2$ was successful. The peaks belonging to O1s, C1s, Mo3d and Se3d are marked in the spectrum. The relative atomic concentration of the sample was oxygen 12.09 at. %, carbon 49.34 at. %, molybdenum 11 at. % and selenium 27.57 at. % with a Se/Mo ratio of 2.5.

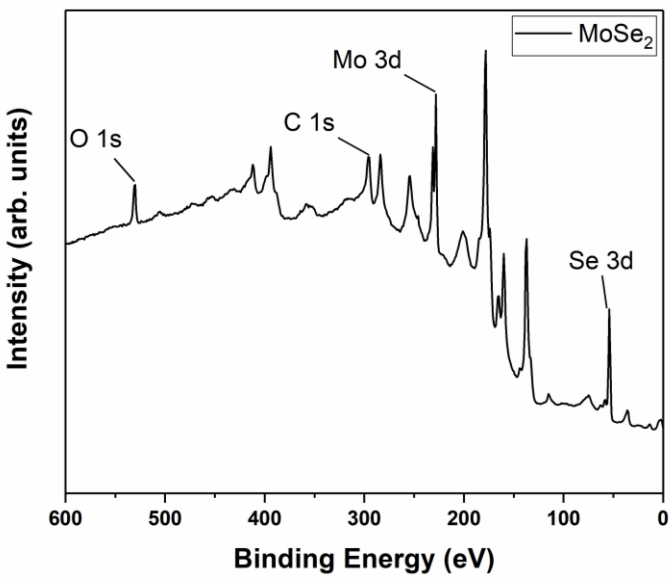

Figure 4.50 Survey spectrum of $MoSe_2$ nanosheets. The peaks from O1s, C1s, Mo3d and Se3d are observed.

X-ray photoelectron spectroscopy was used to investigate the chemical composition of the CVD-grown $MoSe_2$ nanosheets. Figure 4.51 a) show the Mo 3d spectra is composed of four sets of peaks corresponding to Mo^{4+} 3d ($MoSe_2$, red lines) at 228.78 and 231.92 eV, Mo^{6+} 3d (MoO_3, blue lines) at 232.59 and 235.84 eV, Mo^{4+} 3d (MoO_2, green lines) at 229.70 and 233.05 eV and Mo^{2+} 3d (elemental Mo, pink lines) at 228.18 and 231.26 eV [[62], [70]]. It can also be observed one extra peak at 230.74 corresponding to Se 3s ($MoSe_2$). In addition, Figure 4.51 b) shows two peaks at 54.41 and 55.21 corresponding to Se^{2-} 3d [71], [72]. These results indicate the formation of the $MoSe_2$ and different oxidation states of Mo. Liu *et al.* [62] suggests that MoO_3 is reduced to Mo_4O_{11} and MoO_2 during the initial 20 min of growth. After 30 min, most of MoOx is transformed into $MoSe_2$, and the transformation continues with the growth time. That is why some by-products are observed in the Mo 3d spectra,

however the main contribution is the $MoSe_2$ phase because the reaction takes place in 60 min. Therefore, although the selenization reactions occurs it is incomplete.

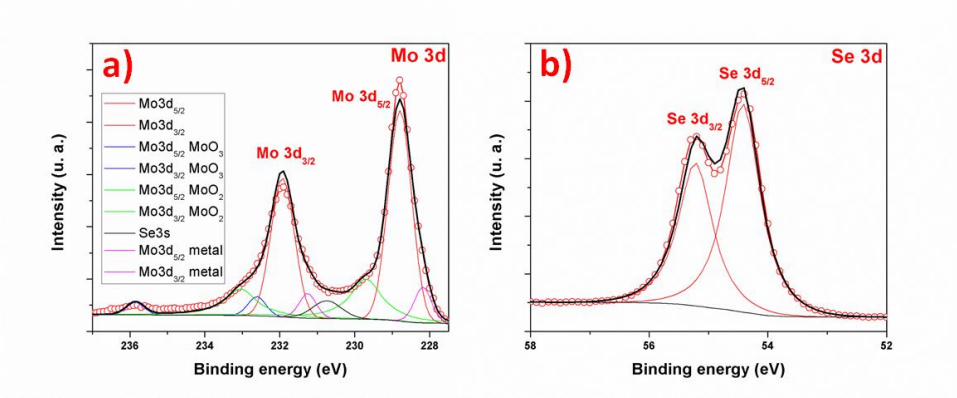

Figure 4.51 XPS spectra of the $MoSe_2$ nanosheets (a) Mo 3d and b) Se 3d).

4.9.7Conclusions

We have demonstrated the synthesis of vertically aligned $MoSe_2$ nanosheets but also some nanosheets are aligned randomly. This was achieved using a two-step CVD technique by direct selenization. Vertically-aligned 2H-phase $MoSe_2$ nanosheets have been demonstrated. However, the presence of Mo-O in the XPS spectrum indicates that the reaction was incomplete and there is some starting material in the final product. Raman spectroscopy and XRD show the presence of the 2H phase and many layers in the synthesized material.

4.10 Tungsten Diselenide (WSe_2)

4.10.1 Electron microscopies of WSe_2 nanosheets

The sample morphology, resulting from the selenization of W film deposited on the sapphire substrate, was examined by SEM (Figure 4.52). The observations show that the sample is less homogeneous than the WS_2 sample, previously discussed, its present platelets over the entire substrate surfaces. These platelets are nanosheets with a well-defined shape exhibiting sharp edges. The low magnification SEM images show two main contrasts, light and dark, can be observed in the lower magnification image (Figure 4.52 a), and can be related to the two orientations of nanosheets to the substrate, perpendicular or parallel, respectively. The higher magnification image (Figure 4.52 b, magnification of a lighter contrast area) indicates that the WSe_2 nanosheets with a thickness between 40–50 nm is preferably grown vertically (perpendicularly to the substrate) and a length around 500 nm.

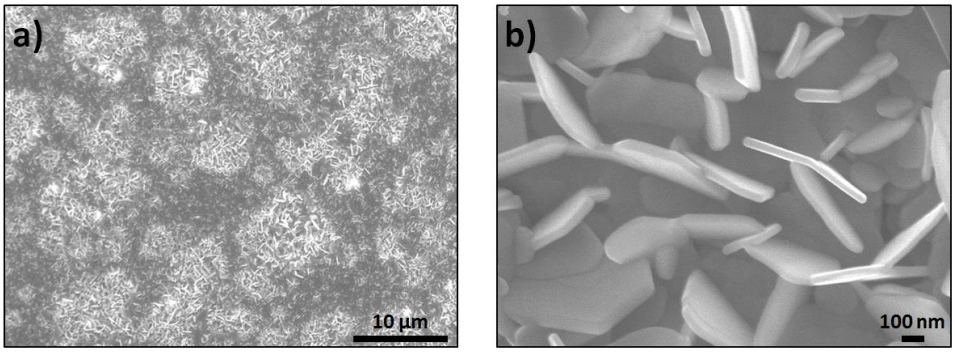

Figure 4.52 SEM images of tungsten diselenide (WSe_2) with a) low and b) high magnification.

The morphology of the nanosheets was investigated using TEM. The nanosheets were removed from the substrate by scratching, and were collected on a holey-carbon copper grid. The TEM analyses confirm the SEM observations above. A TEM image of a nanosheet with a large edge is shown in Figure 4.53 a), which exhibits the (002) plane with an interlayer spacing of 0.62 nm, valued according to the theoretical spacing of 0.648 nm [4], [73]. To get more insight into the crystal structure of WSe_2 nanosheets synthesized in our method, the TEM images were further analyzed as in Figure 4.53 b). The lattice d spacing is estimated to be 0.26 nm, which is corresponds to (100) lattice plane of hexagonal WSe_2 phase.

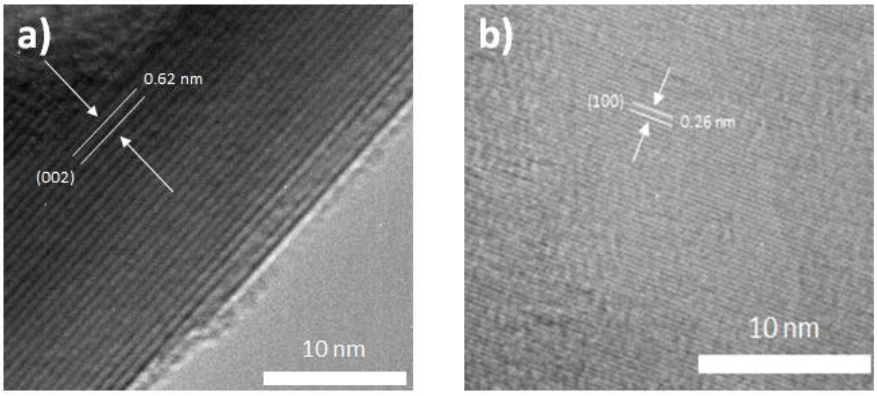

Figure 4.53 High resolution TEM image of the crystal showing the a) (002) and b) (100) crystal planes.

4.10.2 X-Ray diffraction analysis of WSe_2 nanosheets

The XRD pattern of the WSe_2 sample prepared on sapphire (Figure 4.54) reveals the presence of very intense peaks at 13.6°, 27.5°, 31.4°, 37.5°, 56.7° and 78.8°, in agreement with the (002), (004), (100), (103), (008) and (0010) diffraction planes of the hexagonal WSe_2, respectively (space group P63/mmc, Joint Committee on Power Diffractions

Standards (JCPDS) card (no. 38-1388)) with the unit cell parameters a = b = 0.328 nm, c = 1.298 nm. The strong peak intensities with a narrow full width at half maximum (FWHM) indicate that the sample is highly crystalline (the crystallite size was estimated to be higher than 400 nm using the Debye–Scherrer equation, namely, out of the range where this equation remains valid), and that the nanosheets with van der Waals planes perpendicular to the substrate surface (with a C-axis parallel to the surface) are present corroborating the observations made by SEM [57], [74].

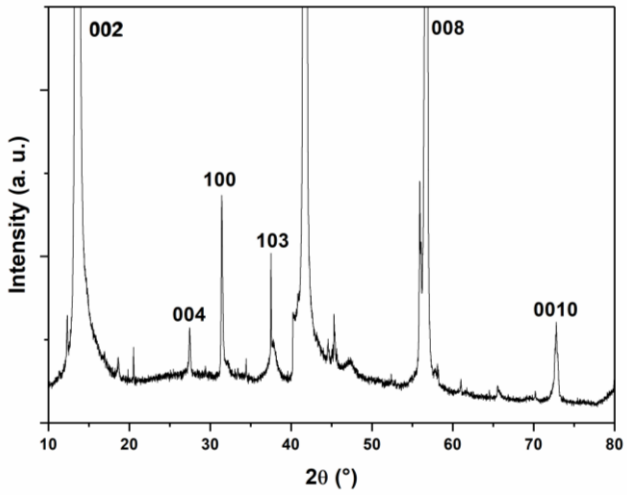

Figure 4.54 XRD pattern of WSe_2.

4.10.3 Raman spectroscopy of WSe_2 nanosheets

The typical Raman spectrum of WSe_2 nanosheets is shown in Figure 4.55, two unresolved peaks at 251 and 257.6 cm^{-1} are well-visible [75]. The observed peak at 251 cm^{-1} corresponds to the E^2_{g1} mode (in-plane vibrational mode). The shoulder peak observed at 257.6 cm^{-1}, associated with the out-of-plane mode, is the A_{1g} mode, indicating that a substantial vibration along the vertical layer direction exists (bond vibration between W and

Se) [75]. The presence of a Raman peak at 306 cm^{-1} (B^2_{g1} mode) has been reported to be related to the interlayer interaction [76], [77]. The Raman signature of the as-grown WSe_2 indicates that its structure is a multilayer 2H type.

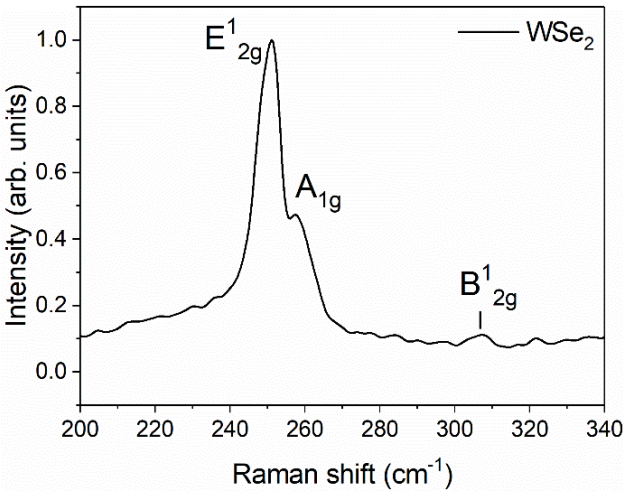

Figure 4.55 Raman spectrum of WSe_2.

4.10.4 Photoluminescence of WSe_2 nanosheets

The PL spectrum of WSe_2 is shown in Figure 4.56. Because of the semiconductor character of the monolayer WSe_2, the PL spectrum exhibits a strong direct transition (DT) emission centered at 760 nm, due to its direct band gap [35] (Figure 4.56 a). When increasing the WSe_2 number of layers, indirect transitions (IT) emissions also appear at a lower energy.

The IT peak the does not appear in the monolayer PL spectrum. Figure 4.56 b) shows a main peak centered at 860 nm wavelength, which corresponds to a red-shift from 760 to 860 nm, indicating the indirect nature of the transitions. Furthermore, the presence of IT emissions with important wavelength shifts demonstrates a multilayer nature, according to the literature. The value of this shift can be considered as a layer number indicator [35]. For

monolayer WSe_2, both valence-band maximum (VBM) and conduction-band minimum (CBM) are located at the K point in Brillouin zone. As the layer number of WSe_2 increases, their energy band structures experience an obvious transformation. The VBM transfers from the K point to Γ point, while the CBM transfers from the K point to Λ point (See Figure 4.57 b) [35].

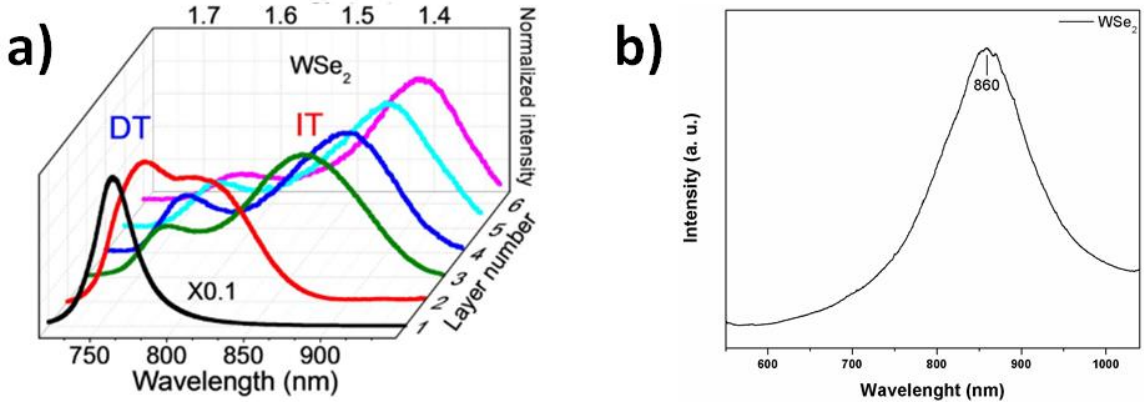

Figure 4.56 Photoluminescence spectrum of WSe_2.

4.10.5 Uv-vis spectroscopy of WSe_2 nanosheets

The absorption spectrum is shown in Figure 4.57 a), the excitonic absorption peaks A and B are located at wavelengths of 785 and 651 nm, respectively. These peaks are related to direct transitions gap of point K. The presence of excitonic transition, red-shifted from the monolayer transition [78], demonstrates the multilayer characteristic of the synthesized nanosheets, according to the PL results. As a result of the superpositions of the Se p-orbitals with W d-orbitals, as well as the adjacent layers, the WSe_2 spectrum shows other absorption peaks of A' and B', in agreement with the PL spectra that shows the multilayer nature. The excitonic nature of these peaks could come from the splitting of the ground and the excited

states of the two transitions of A and B, because the d-electron band is perturbed at the level of the inter- and intra-layer by the Se p-orbitals [78], [79] (Figure 4.61 b).

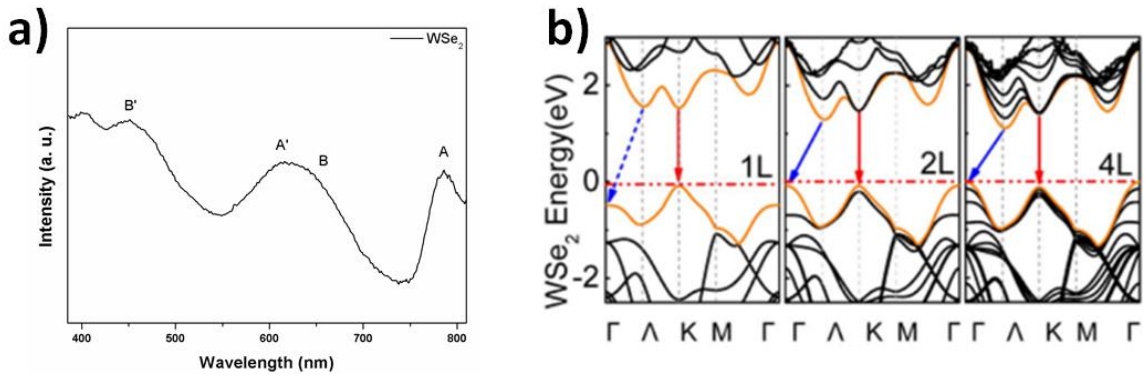

Figure 4.57 a) UV–VIS spectrum of WSe_2 and b) the DFT calculated band gap structures of 1L, 2L and 4L WSe2 obtained from [35].

4.10.6 Chemical analysis of WSe_2 nanosheets

The WSe_2 nanosheets were analyzed by X-Ray photoelectron spectroscopy to obtain their atomic relative concentration and chemical configuration. Figure 4.58 shows the survey spectrum of WSe_2 nanosheets after the synthesis. The presence of the Selenium XPS signal indicates that synthesis of WSe_2 was successful. The peaks belonging to O1s, C1s, Se3d and W4f are marked in the spectrum. The relative atomic concentration of the sample was oxygen 2.93 at. %, carbon 53.64 at. %, selenium 35.9 at. % and tungsten 7.53 at. % with a Se/W ratio of 4.76.

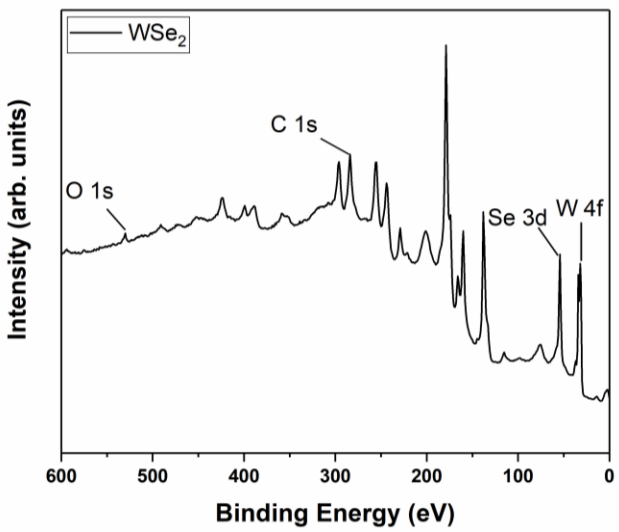

Figure 4.58 Survey spectrum of WSe_2 nanosheets. The peaks from O1s, C1s, Se3d and W4f are observed.

The XPS spectra recorded on the W 4f and Se 3d binding energy regions are shown in Figure 4.59. Considering the W 4f spectrum (Figure 4.59 a), the following three main peaks can be observed: two main contributions centered at 32.5 and 34.6 eV are attributed to the doublets W $4f_{7/2}$ and W $4f_{5/2}$, respectively, and a wide and low intensity centered at 37.8 eV is attributed to the W $5p_{3/2}$. The main contribution can be fitted with two doublets centered at 31.9 and 32.5 eV on a W $4f_{7/2}$ signal, attributed to the 1T' [80] or 1T [81] phase and 2H phase, respectively. The 2H contribution (centered at 32.5 eV) corresponds to 75.0% of the total area, indicating that the sample mainly has a 2H phase. Another additional low intensity contribution is observed at 35.5 eV, due to the W 4f loss.

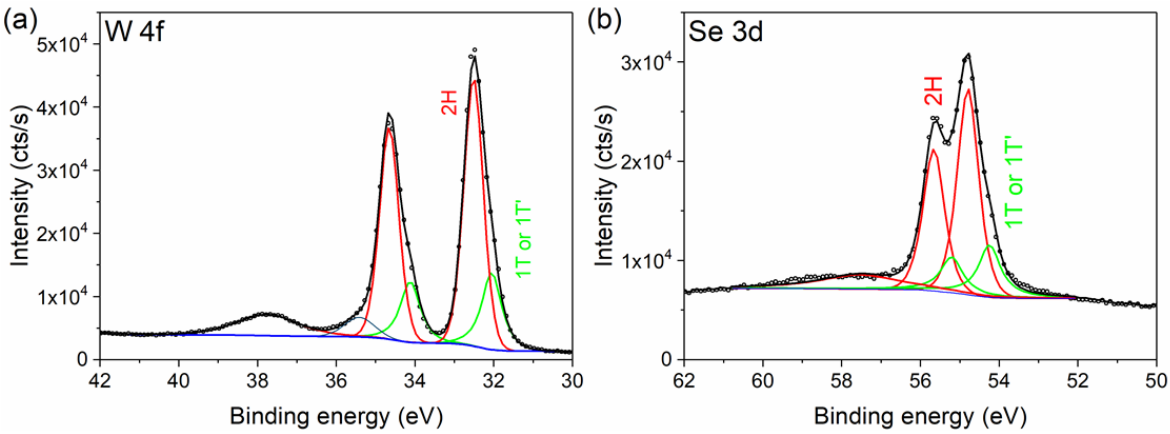

Figure 4.63 XPS spectra of the (a) W 4f and (b) Se 3d of the WSe_2 nanosheets.

The formation of two phases is further confirmed on the Se 3d core level spectra (Figure 4.59 b). The spectrum shows the presence of two main peaks, Se $3d_{5/2}$ and Se $3d_{3/2}$ doublets, centered at 54.8 and 55.6 eV, respectively. Each doublet can be fitted with two components—one at 54.8 eV, corresponding to the 2H-WSe_2 phase, and one corresponding to the other phase (1T or 1T'), centered at 54.3 eV. Here, again, the 2H phase represents nearly 75% of the total area (Table 4.3), verifying the conclusions obtained about the W 4f region. Similar results have been reported in the literature regarding WSe_2 crystals [80], [81], with a major 2H phase and a minor other phase assigned to the 1T' [80] or 1T [81] phases, respectively.

	W 4f Core Level		**Se 3d Core Level**	
	2H Phase	**1T or 1T' Phase**	**2H Phase**	**1T or 1T' Phase**
% Area	74.3	25.7	75.0	25.0

Table 4.3 Relative amount of different crystallographic phases in the WSe_2 nanosheets.

4.10.7 Conclusions

Synthesis of the WSe_2 nanostructures was achieved using an atmospheric pressure CVD route. We have shown that the synthesized nanostructures are crystalline vertically but also horizontal aligned nanosheets. The presence of two crystallographic phases has been shown, and could open a new route to tune the physical properties by phase engineering, as has already been done for similar materials, such as $MoTe_2$. The underlying growth mechanism must be further studied in order to establish the best parameters so as to control the synthesis of the WSe_2 film with different phases. Further studies will be performed aiming at the evaluation of this material active layer in different applications, such as gas sensing and hydrogen evolution reaction catalysis. In comparison, MoS_2 and WS_2 are more homogeneous than $MoSe_2$ and WSe_2. This can be for the change of chalcogen, Se instead of S, because Se is less reactive during the synthesis process.

4.11 Tin Diselenide ($SnSe_2$)

4.11.1 Electron microscopies of $SnSe_2$ nanosheets

SEM images (Figure 4.60) show the $SnSe_2$ nanosheets morphology obtained by selenization of 50 nm of Sn deposited on a sapphire substrate. Figures 4.60 a) and b) show the $SnSe_2$ nanosheets with different orientations (vertical and horizontal). In addition, these nanosheets present a variety of sizes and shapes. This is not the case for the SnS_2 samples, which are more homogeneous. The high magnification of Figure 4.60 c) reveals the average length of the $SnSe_2$ nanosheets (~ 2.5 µm) as well as their thickness (ranging between 50

and 100 nm). The cross section of the sample at till angle of 45° confirms the different orientations of the $SnSe_2$ nanosheets (Fig. 4.60 d).

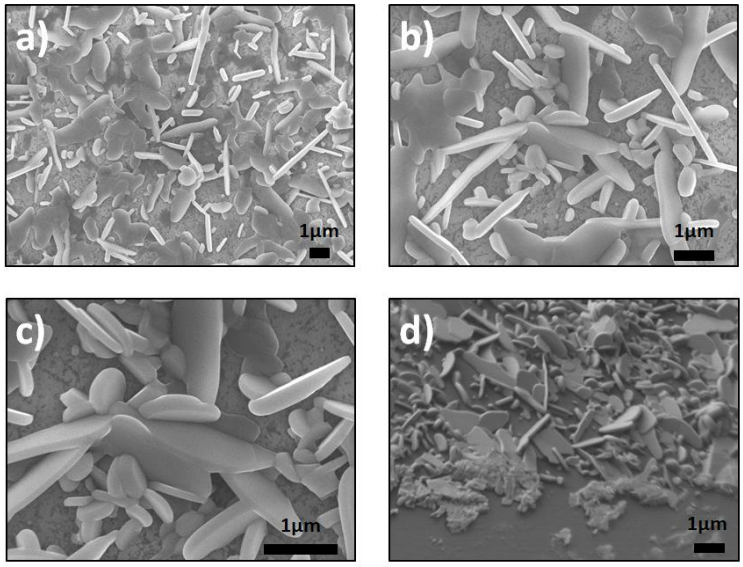

Figure 4.60 SEM images of synthesized products for vertically aligned $SnSe_2$ nanosheets, a-c) top view and d) cross section (45°).

The morphology of the as-synthesized $SnSe_2$ nanosheets was characterized using TEM (Figure 4.61 and 4.62). The layered structure of nanosheets can be observed in Figure 4.61 a) with an interlayer spacing of 0.61 nm, matches to the lattice spacing of (001) planes of hexagonal $SnSe_2$ [82] (the corresponding SAED pattern is in inset). Figure 4.61 b) presents a high-resolution TEM image of nanosheet with well visible lattice fringes with a spacing of 0.33 nm that can be assigned to the (100) planes of the $SnSe_2$. The SAED pattern is in inset of a single nanosheet in the (001) direction confirms the formation of the hexagonal phase of $SnSe_2$ and the crystal structure [83].

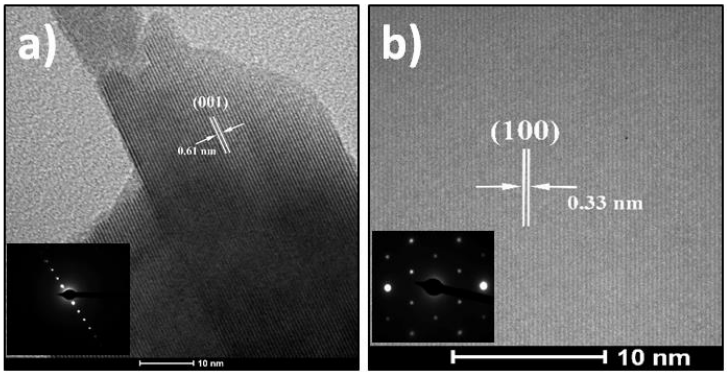

Figure 4.61 a) TEM image of layered structures of nanosheet with the corresponding SAED pattern in inset and b) high resolution image of the crystal showing the (001) crystal planes with in inset a SAED pattern of single nanosheet showing hexagonal spot symmetry.

STEM imaging, bright-field and in HAADF modes (see Fig. 4.62), verifies the high crystallinity of these $SnSe_2$ nanosheets and their hexagonal structure. EDS (Fig. 4.62 c) also confirms the $SnSe_2$ chemical composition (Se/Sn ratio of 2) of those flakes with the presence of Cu due to the TEM grid as we explained before.

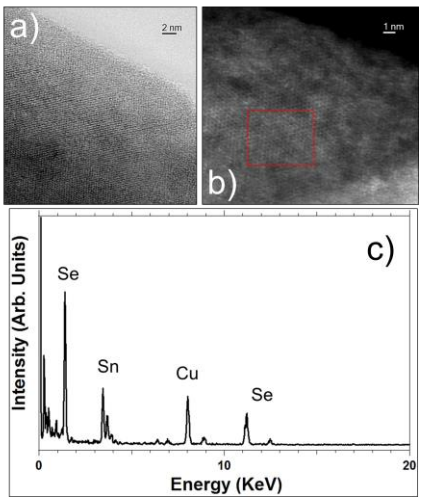

Figure 4.62 STEM images in Bright-Field mode a) and in HAADF mode b) of $SnSe_2$ nanosheets. c) EDS spectrum recorded in the red highlighted area of Fig. 4.62 b).

4.11.2 X-Ray diffraction analysis of $SnSe_2$ nanosheets

Based on the microscopy studies, the conclusions that can be drawn is that the $SnSe_2$ nanosheets are crystallized in a hexagonal structure. This was checked using XRD. The typical XRD pattern of the so-prepared $SnSe_2$ nanosheets in Figure 4.63 show that are crystalline with a good match with the reported pattern for the hexagonal $SnSe_2$ phase (JCPDS card 023-0602) [84] with the unit cell parameters a = b = 0.381 nm, c = 0.614 nm. Indeed, the diffraction peaks appearing at 14.5°, 29.05°, 30.7°, 41.67°, 44.3° and 60.3° are distinctly indexed to the (001), (002), (101), (102), (003) and (004) planes. The peaks observed indicate the high purity and crystallinity of the products.

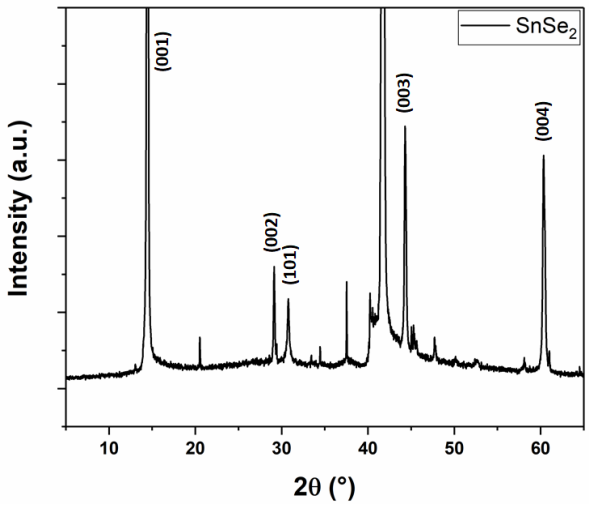

Figure 4.63 XRD pattern of $SnSe_2$.

4.11.3 Raman spectroscopy of $SnSe_2$ nanosheets

In the Figure 4.64 a), the Raman spectrum shows an intense peak that is assigned to the A_{1g} mode at 184 cm^{-1} and another very weak peak corresponding to E_g mode at 117 cm^{-1},

signature of the $SnSe_2$ material [85], [86]. The magnification of the Eg peak region surprisingly shows two low intensity additional peaks at 70 cm^{-1} and 108 cm^{-1}. These peaks cannot be definitively attributed to SnO_2, as a study of the sputtering of thermally oxidized tin metal shows localized Raman modes at different positions (typically at 112 cm^{-1} and 210 cm^{-1} for oxidation temperatures up to 400°C with the appearance of further peaks at higher temperatures) [87]. Alternatively it can be suggested the presence of SnSe, which gives four intense peaks in the region considered, localized at about 70, 108, 130 and 149 cm^{-1}, related to A_g^1, B_{3g}, A_g^2 and A_g^3, respectively [88], [89]. Here, only two low intensity peaks are visible that could be attributed to the A_g^1 and B_{3g} modes to the SnSe material. Finally, the broad peak located at 255 cm^{-1} may be associated with the presence of amorphous Se [90]. This had already been reported and explained by a condensation phenomenon of Se during cooling [91].

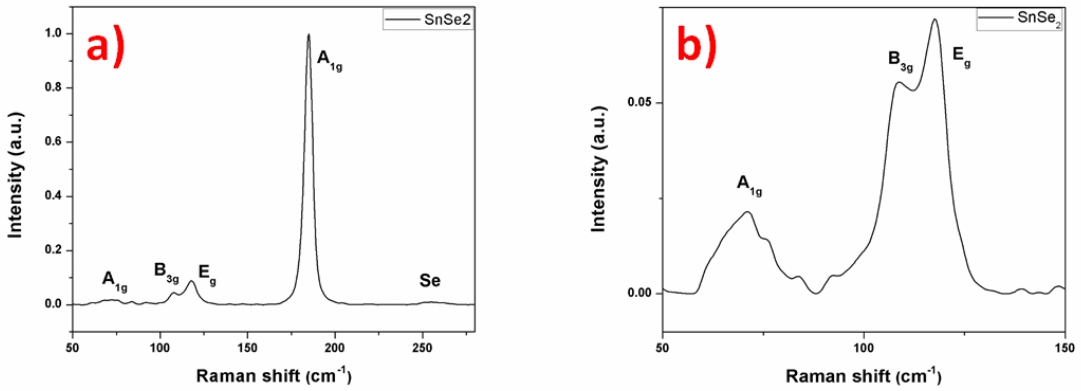

Figure 4.64 Raman spectrum with 532 nm excitation laser of $SnSe_2$ nanosheets (a) and (b).

4.11.4 Photoluminescence of $SnSe_2$ nanosheets

The photoluminescence of the $SnSe_2$ nanosheets is presented in the Figure 4.65. The first peak at 579 nm (2.15 eV) could be attributed to the direct allowed transition in $SnSe_2$, value close to ones given in the literature [92]. This value is close to reported to a monolayer and it is in agreement with one reported for $SnSe_2$ 50 nm thick film [93]. The second broad and more intense peak located at 783nm (1.58 eV) presents a well-defined shoulder at 847 nm (1.46 eV). For this material, few results have been reported on photoluminescence studies. However, due to the similarity of the results with the SnS_2, similar conclusion could be drawn to explain the PL spectrum with the possible presence of defects/vacancies and the edges effect due to the vertical orientation of the nanosheets. A notable difference is the presence of a shoulder located at 847 cm^{-1} that could be explained by another phase, already detected in Raman spectroscopy. Indeed, the formation of polycrystalline thin films of SnSe and $SnSe_2$ has been studied to show that for low selenization temperature (<470°C), hexagonal $SnSe_2$ is formed and for higher temperature (<530°C) orthorhombic SnSe become the preferential material PL [91]. The authors showed for the material synthesized at 470°C made of $SnSe_2$, the presence of SnSe phase with a bandgap value of 1.43 eV [91] that is the close value found in our case with 1.46 eV. Surprisingly, this value does not correspond to a gap value for orthorhombic SnSe but rather to that of cubic SnSe [94]. Then, the other intense peak observed at 987 nm (1.26 eV) can be attribute, as previously shown for SnS_2, to the photoluminescence emissions of the substrate. In this case, the signature of the substrate can also be found in the low intensity peak at 871 nm (1.42 eV) in the shoulder

of the more intense and broader. This is due to the fact that the $SnSe_2$ sample is less homogeneous than SnS_2 sample and the transitions of the substrate are more visible.

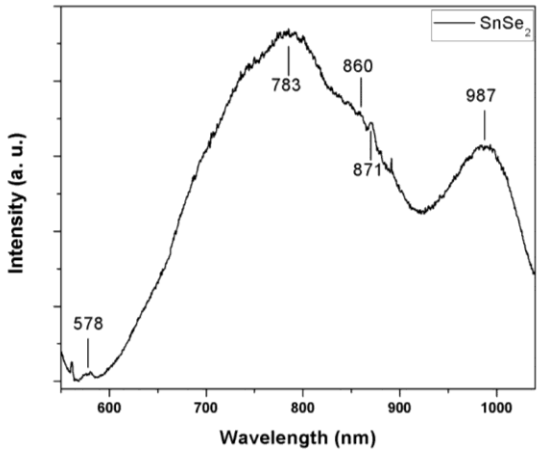

Figure 4.65 Photoluminescence spectrum of $SnSe_2$.

4.11.5 Chemical analysis of $SnSe_2$ nanosheets

Figure 4.66 shows the survey spectrum of $SnSe_2$ nanosheets after the synthesis. The presence of the Selenium XPS signal indicates that synthesis of $SnSe_2$ was successful. The peaks belonging to O1s, Sn3d, C1s and Se3d are marked in the spectrum. The relative atomic concentration of the sample was oxygen 46.89 at. %, tin 18.67 at. % and selenium 34.44 at. % with a Se/Sn ratio of 1.84. The concentration of C1s is not presented because the analysis was made after a cluster cleaning.

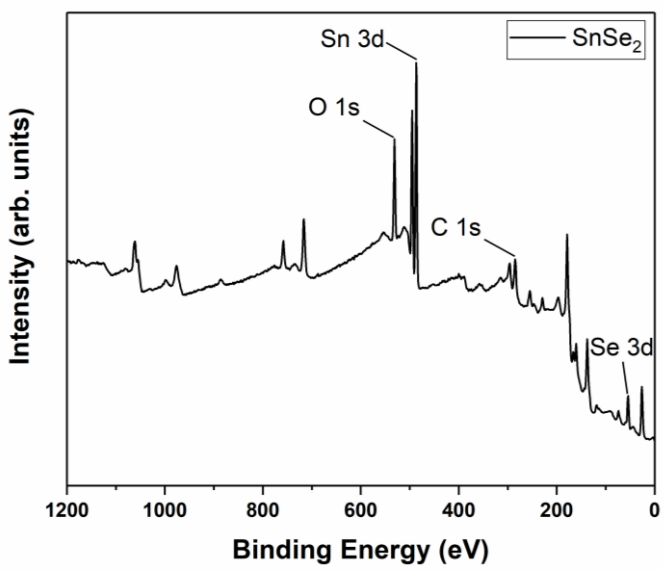

Figure 4.66 Survey spectrum of $SnSe_2$ nanosheets. The peaks from O1s, Sn3d, C1s and Se3d are observed.

The chemistry of the as-prepared product was further investigated by XPS as shown in Figure 4.67. The Figure 4.67 a) and b) shows Sn 3d and Se 2p signal of $SnSe_2$ sample. The Sn 3d is composed of a first doublet, with contributions centered at 486.3 eV and 494.7 eV, attributed to Sn $3d_{5/2}$ and Sn $3d_{3/2}$ states of Sn^{4+} in $SnSe_2$. A second doublet is observed, with contributions at 487.2 and 495.6 eV. The Se 3d spectrum is composed of a first doublet with contributions centered at 53.7 eV and 54.5 eV attributed to Se $3d_{5/2}$ and Se $3d_{3/2}$ of $SnSe_2$ phase [85]. Here too, a second doublet is observed, with Se $3d_{5/2}$ and Se $3d_{3/2}$ contributions centered at 54.8 eV and 55.5 eV respectively. The interpretation of selenium XPS signal is complex and the literature about XPS of $SnSe_x$ reports contradictory and wrong interpretation of Se and Sn signals. One can cite the absence of Se $3d_{5/2}$ contribution in SnSe in [95] or an area of $3d_{3/2}$ contribution higher than the $3d_{5/2}$ in [96], which is physical nonsense. Here, the contribution Sn 3d at 487.2 is attributed to Sn oxide. In reference

paper, SnO_2 is reported at 487.8 in [97], 486.8 in [98] and 486.3 eV [99]. The observation of Sn oxide contribution is consistent with previous results: tin oxide is formed prior to the selenization (and sulfurization), and SEM pictures show that some area are not covered by the nanosheet, namely the XPS probes this surface. For SnS_2, the covering is much better, preventing the tin oxide observation by XPS. Concerning the second contribution in Se signal, at 54.8eV, this contribution is not fully understood in the literature. If this contribution could be attributed to SnSe phase but it cannot be observed because the binding energy is close to the $SnSe_2$ phase , in agreement with [100], one should also see a contribution in the Sn signal, at lower binding energy (shifted by ≈ -0.7eV). The Se contribution cannot be attributed to SeO_2, as this contribution is centered at much higher binding energy, around 59.5 eV [97], [101]. Another option would lie in the formation of $SnSe_{2-x}$ metastable phase. Indeed, D'Olimpio *et al.* [97] did a careful investigation of $SnSe_2$ chemistry when exposed to different environment. However, this would imply also a contribution on the Sn signal, and this contribution would be between $SnSe_2$ and SnSe, i.e. at a lower binding energy of 483.3 eV for the Sn $3d_{5/2}$ contribution of this metastable phase. The most probable explanation would lie in the presence of metallic selenium (Se^0). The Se $3d_{5/2}$ signal of metallic selenium is reported in higher binding energies than tin selenide materials at 56.0 eV for Lee *et al.* [102] and at 54.7 eV by Vishwanath *et al.* [103], this latter value is in good agreement with our data and would confirm the Raman analysis.

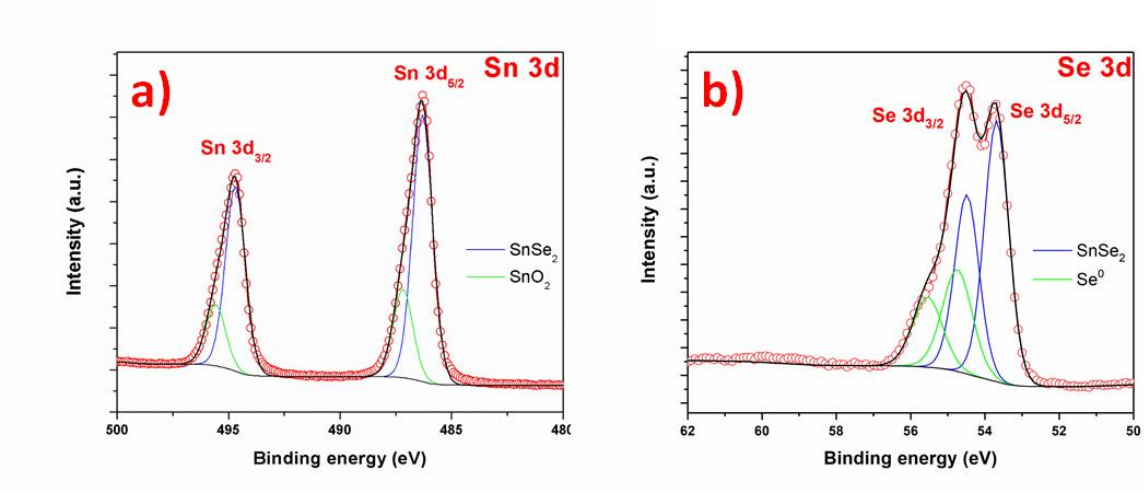

Figure 4.67 XPS spectra of the $SnSe_2$ nanosheets a) Sn 3d and b) Se 3d.

4.11.6 Conclusions

We have demonstrated the synthesis of vertically aligned $SnSe_2$ nanosheets. This was achieved using a simple one-step CVD route by direct selenization of a pre-oxidized tin film. We evidenced the quality of the as-synthesized materials by XRD, Raman spectroscopy, XPS and electron microscopies. The $SnSe_2$ nanomaterial has similar morphology as the SnS_2 nanomaterial, i.e. vertical alignment and well-crystalline 2H phase with also structural defects at their edges, the differences observed were: the nanosheets are larger, they present less homogeneity and the presence of different stoichiometry such as SnSe as well as unreacted selenium.

4.12 Discussions

For the last materials we focused in the use of Se as a chalcogen and a possible growth model for the XSe_2 aligned nanosheets prepared by selenization is proposed. Certainly, Se chemical reactivity is much lower than S one and a suitable reducer agent is required [104].

For that, it is necessary the addition of H_2 to promote the formation of H_2Se (as we can see in the reaction 5.1) which in turn provides atomic Se for the formation of XSe_2 [91], because without H_2 the growth of XSe_2 does not occur. Furthermore, the presence of hydrogen can also lead to the reduction of the oxidized metal film, which is not the goal. However, by optimizing the amount of hydrogen introduced, the selenization reaction occurs to produce vertically aligned layered XSe_2 nanosheets.

$$Se^{0}_{(s)} + H^{0}_{2\,(g)} \rightarrow H^{I}_{2}Se^{-II}_{(g)} \quad 5.1$$

$$Se^{0} + 2e^{-} \rightarrow Se^{-II}\ (Reduction) \quad 5.2$$

$$2H^{0} - 2e^{-} \rightarrow 2H^{I}\ (Oxidation) \quad 5.3$$

In the case of $MoSe_2$ and WSe_2 nanosheets, the parameters of the reaction were similar if we talk about the reaction temperature and the two-steps reaction comparing with MoS_2 and WS_2, the principal differences were the change of chalcogen (Se instead of S) and the addition of H_2. Once H_2Se is obtained the metal oxide segregation and selenization will take place simultaneously as in the synthesis of MoS_2 or WS_2 in high temperatures (850 °C). Same as S, Se has to be sufficient for the selenization to prevent the W oxide segregation and coalescence will be the dominant mechanism. For the last material, $SnSe_2$, the preparation of the Tin film before the synthesis was the same as in the case of the SnS_2 nanosheets. Also, we proposed a succeeded single-step nanosheet growth mechanism by rapid selenization at lower temperature (450 °C°). We perceived that while during the synthesis of $SnSe_2$, SnSe was formed. This can be explained by the thermodynamic conditions of the reaction. The presence of hydrogen is necessary as described above to obtain the correct

selenium reactive species, allowing the formation of the different selenium materials. A last parameter to consider is the temperature. It has been shown that temperature plays a major role in phase selection between SnSe and $SnSe_2$ [91], [100] a lower selenization temperature allows the formation of a dominant $SnSe_2$ phase, whereas a higher temperature leads to the formation of the SnSe phase (this is also dependent on other parameters such as the gases in the reaction chamber). With an intermediate temperature, a mixture of the two phases can be observed [91]. Our reaction occurs at 450 °C, which is a relatively low selenization temperature in the range of temperatures reported for the synthesis of the $SnSe_2$ phase, therefore explaining the observation of a mix of both phases, as we reported in this work. This temperature is not far from the intermediate temperature between the $SnSe_2$ and SnSe formation temperatures, which explains the fact that domains of the other SnSe phase can be found in a product composed mainly of $SnSe_2$. This fact has been already reported in [91] for a selenization temperature of 470°C. Finally, for such syntheses, the temperature is relatively low compared to the formation temperatures of other metal dichalcogenides, which may also explain the presence of structural defects (vacancies).

The control of the size and the thickness of the final products was not the goal of this thesis work because they were always different depending in the metal film and chalcogen used.

Metal Dichalcogenides for gas sensing application

4.13 WS_2 and WSe_2 nanosheets for gas sensing application

For practicality reasons for the application of gas sensors the group of Prof. Eduard Llobet from Spain gave us a new substrate (Alumina substrates with interdigitated platinum electrodes purchased from Ceram Tech GmbH) with a WO_3 film previously deposited using Aerosol Assisted CVD (AACVD). We applied the parameters previously described for the synthesis of WS_2 and WSe_2 nanosheets and the results are shown in the following sections.

4.13.1 Characterization of MDs

The characterization of the sensor active layer before and after sulfurization or selenization of WO_3 deposited on Alumina substrate with interdigitated platinum electrodes is presented in the following sections using SEM and XPS.

4.13.1.1 Electron microscopy of MDs

The sensors active layers are made of WS_2 and WSe_2 using WO_3 film as a starting material. The WO_3 thin film (thickness between 5-20 µm) was deposited on Alumina substrate with interdigitated platinum electrodes. The starting material was prepared using Aerosol-Assited CVD (AACVD) at the University Rovira i Virgili of Tarragona, in Spain by the MINOS group. This starting material presents two different morphologies, nanorods and nanoneedles, by changing the nitrogen flow during the AACVD deposition as can be seen in Figure 4.68. The nanorods present a flower like-tip morphology, while in the nanoneedles this morphology is absent.(Figure 4.68 b). The synthesis conditions reported in this chapter by the CVD method were used for the synthesis of WS_2 and WSe_2 nanosheets (Table 4.2).

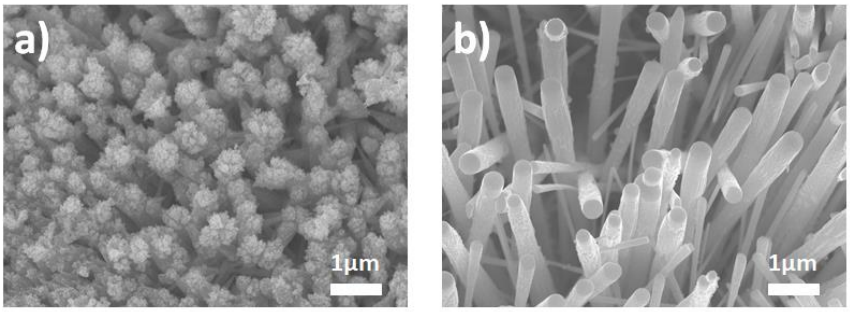

Figure 4.68 SEM images of a) WO_3 nanorods and b) WO_3 nanoneedles as a starting material.

Figure 4.69 shows the different morphologies of the MDs final product depending in the starting material (W or WO_3). In Figure 4.69 a) the results obtained in the section 4.5 of this chapter are presented, where the starting material is a 50 nm W film deposited on sapphire and the final product is presented in the Figure 4.69 b) with the presence of the vertically-aligned nanosheets previously reported. For the materials used in this chapter, the same methodology of the WS_2 synthesis was applied. The main difference is the starting material. As we said, WO_3 deposited on alumina substrate with interdigitated platinum electrodes was used instead of W film deposited on sapphire substrate. As we can see, two WO_3 morphologies were employed, nanorods (Figure 4.69 c) and nanoneedles (Figure 4.69 e and Fig. 4.69 g). When the nanorods were used for the synthesis the result was the WS_2 nanoflakes product. Finally, the nanoneedles were used and we observe two different results, nanotriangles (Figure 4.69 f) for the case of S as a chalcogen and nanoflowers (Figure 4.69 g) when the S is changed for Se and the parameters for the synthesis of WSe_2 nanosheets from the section 4.10 of this chapter are applied. It can be seen that WO_3 nanoneedles were transformed to a 3D assembly of 2D WSe_2, like flower structures with multilayered sheets as petals. With this, we can conclude that the final morphology strongly

depends in the starting material morphology and as we will see below, it will be decisive for the application of gas sensors.

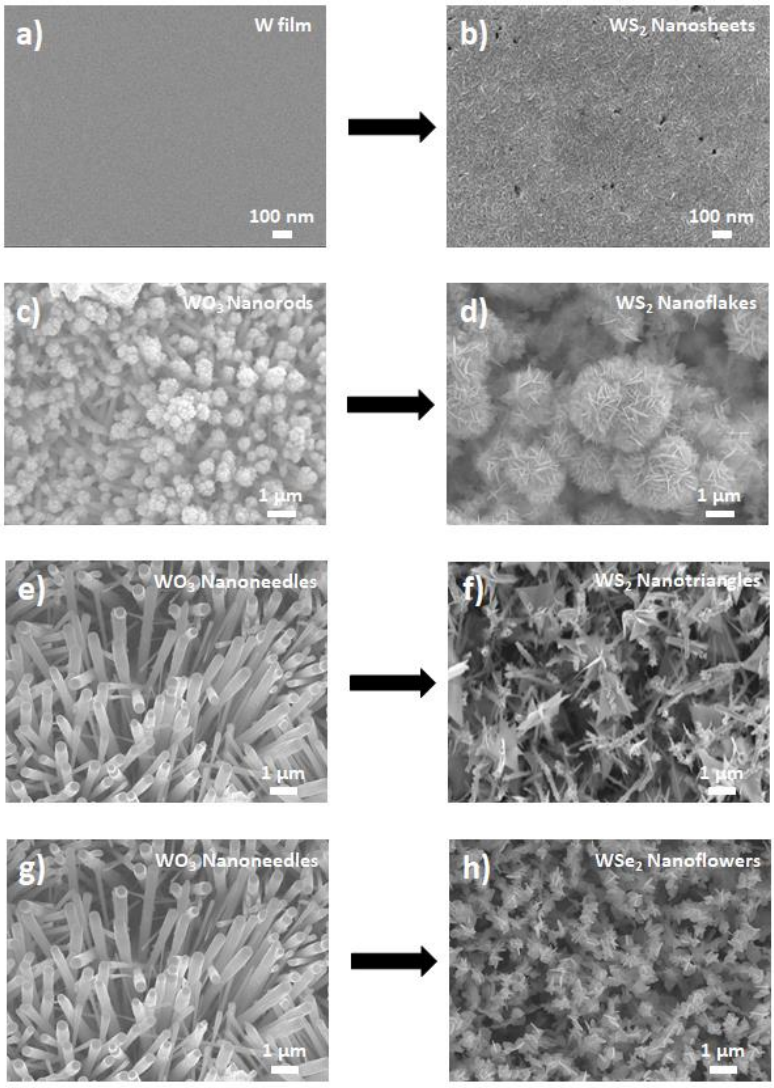

Figure 4.69 SEM images of starting material (a, c, e and g) and final product after sulfurization or selenization (b, d, f and h).

Furthermore, a color change in the deposited film is observed, which clearly indicates the formation of homogeneous and uniform film of WS_2 and WSe_2. The change in morphology

will be important for gas detection because the exposed edges play an important role during gas absorption into the material. In the Chapter 5 the results will be presented depending on the morphology of the synthesized product.

4.13.2.2 Chemical analysis of MDs

The chemical state of the as-grown samples' active layer surface was investigated by X-ray photoelectron spectroscopy (XPS). The Figure 4.70 a-c) shows the typical W 4f, S 2p and O 1s core level spectra recorded on the WO_3 and WS_2 samples. For nanoflakes and nanotriangles the XPS analysis was the same and for that, they are presented as one. Considering the W 4f spectrum of WO_3 (Figure 4.70 a), three components are observed that are associated to the W $4f_{7/2}$ and W $4f_{5/2}$ spin orbit doublet, and a low intensity peak originating from the W $5p_{3/2}$ core level. For the WO_3, the W 4f doublet is centered at 35.4 eV and 37.5 eV and the W 5p weak peak around 41 eV. The W 4f spectrum can be properly fitted by a doublet, confirming the nature of WO_3 material with W only present in the six-valent state [105]. Moreover, one can note the presence of oxygen and the absence of sulfur on this material. Concerning the WS_2, the same features that are observed in the WO_3 can be observed with a binding energy shift of the different components. Here, the W 4f doublet is centered at 32.7 eV and 34.8 eV and the W 5p weak peak around 38.2 eV. The perfect fitting of the spectra for WS_2 by a doublet confirms the presence of WS_2 with values in good agreement with those found in the WS_2 synthesis section in the section 4.5, without the presence of oxide. This is otherwise correlated with the quasi absence of oxygen and the presence of sulfur [105]. Indeed, in the S 2p spectrum, the known doublet peaks, S $2p_{1/2}$

and S $2p_{3/2}$ at 163.4 and 162.2 eV, respectively, can be seen in Figure 4.70 b). The experimental shape is well reproduced by a doublet demonstrating the presence of the unique phase WS_2. Considering the O 1s region (Figure 4.70 c), the difference between the two materials is well visible, with a lower intensity peak of oxygen in the WS_2 material around 533 eV, most likely related to physically adsorbed oxygen molecules. This can be compared to O 1s core level spectrum of WO_3 material with a main peak at 530.8 eV related to the WO_3. Based on the XPS analysis, the complete conversion of WO_3 to WS_2 is demonstrated. The Figure 4.70 d-f) presents the XPS analysis of the sample before and after selenization, and confirm the full conversion of the tungsten oxide. Before selenization, the W 4f signal (Figure 4.70 d) is composed of a doublet centered at 35.5 and 37.7eV, corresponding to W $4f_{7/2}$ and W4 $f_{5/2}$ and an additional contribution at 41.2eV, attributed to W $5p_{3/2}$ level. These positions agree with WO_3 formation [106]. As expected, no selenium is present before the selenization steps (Figure 4.70 e). After selenization, the W 4f signal shift to lower binding energy, and exhibit a unique doublet contribution centered at 32.2 and 34.3 eV, in agreement with WSe_2 2H phase formation, where literature reports binding energy in the range 32.0 to 32.4 eV, and up to 32.7eV for large oxygen-free tungsten diselenide flakes [81], [107]. The Se 3d signal is composed of a unique doublet contribution centered at 54.4 and 55.26 eV due to the Se $3d_{5/2}$ and Se $3d_{3/2}$ levels respectively, in accordance with WSe_2 2H phase formation [4]. No significant oxygen presence is reported after selenization. The oxide formation is also confirmed on the O 1s level (Figure 4.70 f) with an intense contribution at 530.3eV, corresponding to WO_3. Two additional peaks are

observed at 531.9 and 533.5 eV, attributed to organic oxygen (C-O, C=O), probably coming from the synthesis. The complete conversion of WSe_2 from WO_3 is confirmed with XPS.

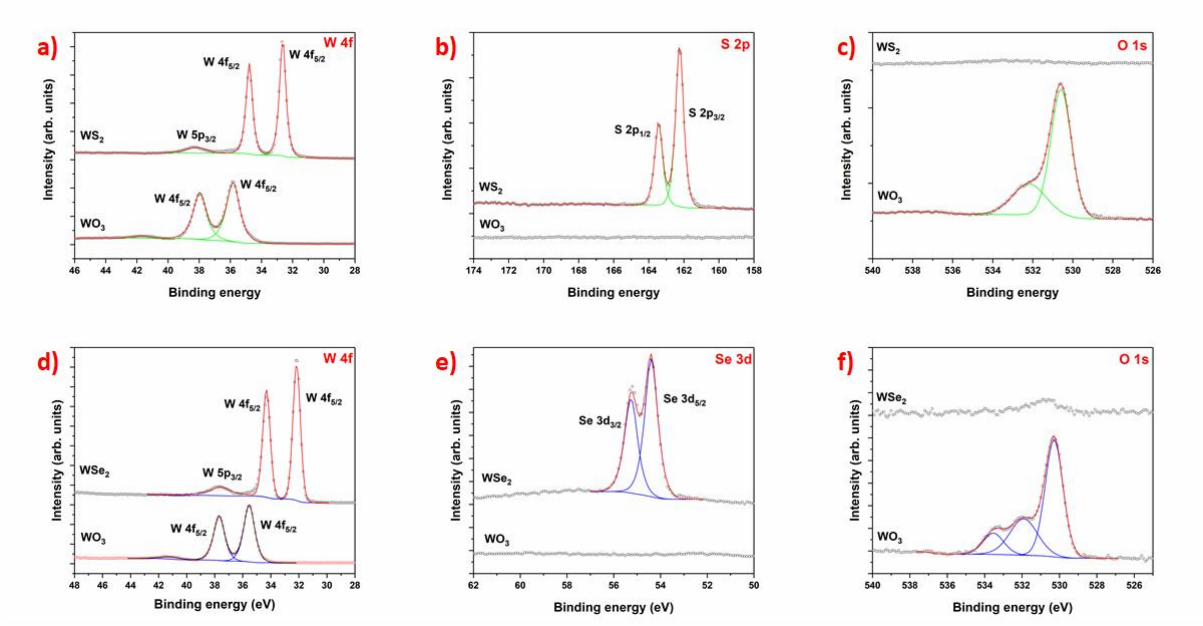

Figure 4.70 XPS spectra of the W 4f a), S 2p b) and O 1s c) core levels for WO_3 and WS_2 and of the W 4f a), Se 3d b) and O 1s c) core levels for WO_3 and WSe_2.

4.13.2.3 Conclusions

We have demonstrated an efficient route to synthesize high quality, multi-layered WS_2 and WSe_2 nanosheets with exposed edges on Alumina substrate with interdigitated platinum electrodes following the synthesis parameters previously reported in this chapter (sections 4.5 and 4.10). The nanomaterials are directly grown onto standard ceramic application transducers for developing chemoresistive gas sensors, using a double step CVD technique. It can be concluded that the final morphology of the films heavily depends on that of pre-

deposited WO_3 layers, which is easily scalable and controllable, making it possible to meet the demands for different applications.

4.14 References

1. Li, H.; Lu, G.; Wang, Y.; Yin, Z.; Cong, C.; He, Q.; Wang, L.; Ding, F.; Yu, T.; Zhang, H. Mechanical exfoliation and characterization of single- and few-layer nanosheets of WSe2, TaS2, and TaSe2. *Small* **2013**, *9*, 1974–1981, doi:10.1002/smll.201202919.

2. Magda, G.Z.; Petõ, J.; Dobrik, G.; Hwang, C.; Biró, L.P.; Tapasztó, L. Exfoliation of large-area transition metal chalcogenide single layers. *Sci. Rep.* **2015**, *5*, 3–7, doi:10.1038/srep14714.

3. Deokar, G.; Vignaud, D.; Arenal, R.; Louette, P.; Colomer, J. Synthesis and characterization of MoS 2 nanosheets. *Nanotechnology* **2016**, *27*, 075604.

4. Sierra-Castillo, A.; Haye, E.; Acosta, S.; Bittencourt, C.; Colomer, J.F. Synthesis and characterization of highly crystalline vertically aligned WSe2 nanosheets. *Appl. Sci.* **2020**, *10*, 874, doi:10.3390/app10030874.

5. XingliWang, Yongji Gong, Gang Shi, Wai Leong Chow, Kunttal Keyshar, GonglanYe, Robert Vajtai, Jun Lou, Zheng Liu, Emilie Ringe, Beng Kang Tay, and P.M.A. Chemical Vapor Deposition Growth of Crystalline Monolayer MoSe2. *ACS Nano* **2014**, *8*, 5125–5131, doi:10.1007/BF02892363.

6. Deokar, G.; Rajput, N.S.; Vancsó, P.; Ravaux, F.; Jouiad, M.; Vignaud, D.; Cecchet, F.; Colomer, J.F. Large area growth of vertically aligned luminescent MoS2 nanosheets.

Nanoscale **2017**, *9*, 277–287, doi:10.1039/c6nr07965b.

7. Li, Y.; Zhang, K.; Wang, F.; Feng, Y.; Li, Y.; Han, Y.; Tang, D.; Zhang, B. Scalable Synthesis of Highly Crystalline MoSe2 and Its Ambipolar Behavior. *ACS Appl. Mater. Interfaces* **2017**, *9*, 36009–36016, doi:10.1021/acsami.7b10693.

8. Li, Y.; Wang, F.; Tang, D.; Wei, J.; Li, Y.; Xing, Y.; Zhang, K. Controlled synthesis of highly crystalline CVD-derived monolayer MoSe2 and shape evolution mechanism. *Mater. Lett.* **2018**, *216*, 261–264, doi:10.1016/j.matlet.2018.01.102.

9. Alagh, A.; Annanouch, F.E.; Umek, P.; Bittencourt, C.; Sierra-Castillo, A.; Haye, E.; Colomer, J.F.; Llobet, E. CVD growth of self-assembled 2D and 1D WS2 nanomaterials for the ultrasensitive detection of NO2. *Sensors Actuators, B Chem.* **2021**, *326*, 128813, doi:10.1016/j.snb.2020.128813.

10. Deokar, G.; Rajput, N.S.; Li, J.; Deepak, F.L.; Ou-Yang, W.; Reckinger, N.; Bittencourt, C.; Colomer, J.F.; Jouiad, M. Toward the use of CVD-grown MoS2 nanosheets as field-emission source. *Beilstein J. Nanotechnol.* **2018**, *9*, 1686–1694, doi:10.3762/bjnano.9.160.

11. Veeramalai, C.P.; Li, F.; Liu, Y.; Xu, Z.; Guo, T.; Kim, T.W. Enhanced field emission properties of molybdenum disulphide few layer nanosheets synthesized by hydrothermal method. *Appl. Surf. Sci.* **2016**, *389*, 1017–1022, doi:10.1016/j.apsusc.2016.08.031.

12. Gao, D.; Si, M.; Li, J.; Zhang, J.; Zhang, Z.; Yang, Z.; Xue, D. Ferromagnetism in freestanding MoS2 nanosheets. *Nanoscale Res. Lett.* **2013**, *8*, 1–8, doi:10.1186/1556-

276X-8-129.

13. Zhong, Y.; Shi, T.; Huang, Y.; Cheng, S.; Chen, C.; Liao, G.; Tang, Z. Three-dimensional MoS2/Graphene Aerogel as Binder-free Electrode for Li-ion Battery. *Nanoscale Res. Lett.* **2019**, *14*, doi:10.1186/s11671-019-2916-z.

14. Zhang, X.; Tang, H.; Xue, M.; Li, C. Facile synthesis and characterization of ultrathin MoS2 nanosheets. *Mater. Lett.* **2014**, *130*, 83–86, doi:10.1016/j.matlet.2014.05.078.

15. Wang, X.; Feng, H.; Wu, Y.; Jiao, L. Controlled synthesis of highly crystalline MoS2 flakes by chemical vapor deposition. *J. Am. Chem. Soc.* **2013**, *135*, 5304–5307, doi:10.1021/ja4013485.

16. Lee, C.; Yan, H.; Brus, L.E.; Heinz, T.F.; Hone, J.; Ryu, S. Anomalous lattice vibrations of single- and few-layer MoS2. *ACS Nano* **2010**, *4*, 2695–2700, doi:10.1021/nn1003937.

17. Li, H.; Zhang, Q.; Yap, C.C.R.; Tay, B.K.; Edwin, T.H.T.; Olivier, A.; Baillargeat, D. From bulk to monolayer MoS 2: Evolution of Raman scattering. *Adv. Funct. Mater.* **2012**, *22*, 1385–1390, doi:10.1002/adfm.201102111.

18. Perea-López, N.; Lin, Z.; Pradhan, N.R.; Iñiguez-Rábago, A.; Elías, A.L.; McCreary, A.; Lou, J.; Ajayan, P.M.; Terrones, H.; Balicas, L.; et al. CVD-grown monolayered MoS2 as an effective photosensor operating at low-voltage. *2D Mater.* **2014**, *1*, doi:10.1088/2053-1583/1/1/011004.

19. Ahmad, S.; Mukherjee, S. A Comparative Study of Electronic Properties of Bulk MoS2

and Its Monolayer Using DFT Technique: Application of Mechanical Strain on MoS2 Monolayer. **2014**, *03*, 52–59, doi:10.4236/graphene.2014.34008.

20. Splendiani, A.; Sun, L.; Zhang, Y.; Li, T.; Kim, J.; Chim, C.Y.; Galli, G.; Wang, F. Emerging photoluminescence in monolayer MoS2. *Nano Lett.* **2010**, *10*, 1271–1275, doi:10.1021/nl903868w.

21. Eda, G.; Yamaguchi, H.; Voiry, D.; Fujita, T.; Chen, M.; Chhowalla, M. Photoluminescence from Chemically Exfoliated MoS2. *Nano Lett.* **2011**, *11*, 5111–5116, doi:10.1021/nl201874w.

22. Namphung Peimyoo, Jingzhi Shang, Chunxiao Cong, Xiaonan Shen, Xiangyang Wu, E.K.L.Y. and T.Y. Nonblinking, Intense Two-Dimensional Light Emitter: Monolayer WS2 Triangles. *ACS Nano* **2013**, *7*, 10985–10994.

23. Carozo, V.; Wang, Y.; Fujisawa, K.; Carvalho, B.R.; McCreary, A.; Feng, S.; Lin, Z.; Zhou, C.; Perea-López, N.; Elías, A.L.; et al. Optical identification of sulfur vacancies: Bound excitons at the edges of monolayer tungsten disulfide. *Sci. Adv.* **2017**, *3*, 1–10, doi:10.1126/sciadv.1602813.

24. Nan, H.; Wang, Z.; Wang, W.; Liang, Z.; Lu, Y.; Chen, Q.; He, D.; Tan, P.; Miao, F.; Wang, X.; et al. Strong photoluminescence enhancement of MoS2 through defect engineering and oxygen bonding. *ACS Nano* **2014**, *8*, 5738–5745, doi:10.1021/nn500532f.

25. Liu, K.K.; Zhang, W.; Lee, Y.H.; Lin, Y.C.; Chang, M.T.; Su, C.Y.; Chang, C.S.; Li, H.; Shi, Y.; Zhang, H.; et al. Growth of large-area and highly crystalline MoS 2 thin layers on

insulating substrates. *Nano Lett.* **2012**, *12*, 1538–1544, doi:10.1021/nl2043612.

26. Spevack, P.A.; McIntyre, N.S. A Raman and XPS investigation of supported molybdenum oxide thin films. 2. Reactions with hydrogen sulfide. *J. Phys. Chem.* **1993**, *97*, 11031–11036, doi:10.1021/j100144a021.

27. Senthilkumar, V.; Tam, L.C.; Kim, Y.S.; Sim, Y.; Seong, M.J.; Jang, J.I. Direct vapor phase growth process and robust photoluminescence properties of large area MoS2 layers. *Nano Res.* **2014**, *7*, 1759–1768, doi:10.1007/s12274-014-0535-7.

28. Rout, C.S.; Joshi, P.D.; Kashid, R. V.; Joag, D.S.; More, M.A.; Simbeck, A.J.; Washington, M.; Nayak, S.K.; Late, D.J. Superior field emission properties of layered WS2-RGO nanocomposites. *Sci. Rep.* **2013**, *3*, doi:10.1038/srep03282.

29. Yang, W.; Wang, J.; Si, C.; Peng, Z.; Frenzel, J.; Eggeler, G.; Zhang, Z. [001] Preferentially-oriented 2D tungsten disulfide nanosheets as anode materials for superior lithium storage. *J. Mater. Chem. A* **2015**, *3*, 17811–17819, doi:10.1039/c5ta04176g.

30. Zhu, Y.Q.; Hsu, W.K.; Terrones, H.; Grobert, N.; Chang, B.H.; Terrones, M.; Wei, B.Q.; Kroto, H.W.; Walton, D.R.M.; Boothroyd, C.B.; et al. Morphology, structure and growth of WS2 nanotubes. *J. Mater. Chem.* **2000**, *10*, 2570–2577, doi:10.1039/b004433o.

31. Qin, Y.Q.; Peng, Y.Q.; Yang, W.F.; Wang, Y.; Cui, J.W.; Zhang, Y. Ultrathin exfoliated WS2 nanosheets in low-boiling-point solvents for high-efficiency hydrogen evolution reaction. *IOP Conf. Ser. Mater. Sci. Eng.* **2020**, *770*, doi:10.1088/1757-

899X/770/1/012079.

32. Zheng, D.; Wu, Y.P.; Li, Z.Y.; Cai, Z.B. Tribological properties of WS2/graphene nanocomposites as lubricating oil additives. *RSC Adv.* **2017**, *7*, 14060–14068, doi:10.1039/c6ra28028e.

33. Shi, W.; Lin, M.L.; Tan, Q.H.; Qiao, X.F.; Zhang, J.; Tan, P.H. Raman and photoluminescence spectra of two-dimensional nanocrystallites of monolayer WS2 and WSe2. *2D Mater.* **2016**, *3*, doi:10.1088/2053-1583/3/2/025016.

34. Yuan, L.; Huang, L. Exciton dynamics and annihilation in WS2 2D semiconductors. *Nanoscale* **2015**, *7*, 7402–7408, doi:10.1039/c5nr00383k.

35. Yuanzheng, L.; Xinshu, L.; Tong, Y.; Guochun, Y.; Heyu, C.; Cen, Z.; Qiushi, F.; Jiangang, M.; Weizhen, L.; Haiyang, X.; et al. Accurate identification of layer number for few-layer WS 2 and WSe 2 via spectroscopic study. *Nanotechnology* **2018**, *29*, 124001.

36. Zeng, H.; Liu, G. Bin; Dai, J.; Yan, Y.; Zhu, B.; He, R.; Xie, L.; Xu, S.; Chen, X.; Yao, W.; et al. Optical signature of symmetry variations and spin-valley coupling in atomically thin tungsten dichalcogenides. *Sci. Rep.* **2013**, *3*, doi:10.1038/srep01608.

37. Jha, R.; Guha, P.K. An effective liquid-phase exfoliation approach to fabricate tungsten disulfide into ultrathin two-dimensional semiconducting nanosheets. *J. Mater. Sci.* **2017**, *52*, 7256–7268, doi:10.1007/s10853-017-0962-4.

38. Escalera-López, D.; Griffin, R.; Isaacs, M.; Wilson, K.; Palmer, R.E.; Rees, N. V. MoS2 and WS2 nanocone arrays: Impact of surface topography on the hydrogen evolution

electrocatalytic activity and mass transport. *Appl. Mater. Today* **2018**, *11*, 70–81, doi:10.1016/j.apmt.2018.01.006.

39. Huang, J.; Wang, X.; Li, J.; Cao, L.; Xu, Z.; Wei, H. WS2-Super P nanocomposites anode material with enhanced cycling stability for lithium ion batteries. *J. Alloys Compd.* **2016**, *673*, 60–66, doi:10.1016/j.jallcom.2016.02.237.

40. Jian-Gan Wang, Huanhuan Sun, Huanyan Liu, Dandan Jin, R.Z. and B.W. Edge-oriented SnS2 nanosheet arrays on carbon paper as advanced binder-free anodes for Li-ion and Na-ion batteries. *J. Mater. Chem. A* **2014**, *5*, 23115–23122, doi:10.1039/...1.

41. Huang, Y., Deng, H. X., Xu, K., Wang, Z. X., Wang, Q. S., Wang, F. M., ... & He, J. Highly sensitive and fast phototransistor based on large size CVD-grown SnS2 nanosheets. *Nanoscale* **2015**, *7*, 14093–14099, doi:10.1039/x0xx00000x.

42. Jiang, Y.; Feng, Y.; Xi, B.; Kai, S.; Mi, K.; Feng, J.; Zhang, J.; Xiong, S. Ultrasmall SnS2 nanoparticles anchored on well-distributed nitrogen-doped graphene sheets for Li-ion and Na-ion batteries. *J. Mater. Chem. A* **2016**, *4*, 10719–10726, doi:10.1039/c6ta03580a.

43. Ou, J.Z.; Ge, W.; Carey, B.; Daeneke, T.; Rotbart, A.; Shan, W.; Wang, Y.; Fu, Z.; Chrimes, A.F.; Wlodarski, W.; et al. Physisorption-Based Charge Transfer in Two-Dimensional SnS2 for Selective and Reversible NO2 Gas Sensing. *ACS Nano* **2015**, *9*, 10313–10323, doi:10.1021/acsnano.5b04343.

44. Rout, C.S.; Joshi, P.D.; Kashid, R. V.; Joag, D.S.; More, M.A.; Simbeck, A.J.; Washington,

M.; Nayak, S.K.; Late, D.J. Enhanced field emission properties of doped graphene nanosheets with layered SnS2. *Appl. Phys. Lett.* **2014**, *105*, 043109, doi:10.1063/1.4892001.

45. Ahn, J.H.; Lee, M.J.; Heo, H.; Sung, J.H.; Kim, K.; Hwang, H.; Jo, M.H. Deterministic Two-Dimensional Polymorphism Growth of Hexagonal n-Type SnS2 and Orthorhombic p-Type SnS Crystals. *Nano Lett.* **2015**, *15*, 3703–3708, doi:10.1021/acs.nanolett.5b00079.

46. Deshpande, N.G.; Sagade, A.A.; Gudage, Y.G.; Lokhande, C.D.; Sharma, R. Growth and characterization of tin disulfide (SnS2) thin film deposited by successive ionic layer adsorption and reaction (SILAR) technique. *J. Alloys Compd.* **2007**, *436*, 421–426, doi:10.1016/j.jallcom.2006.12.108.

47. George, J.; Joseph, K.S. Absorption edge measurements in tin disulphide thin films. *J. Phys. D. Appl. Phys.* **1982**, *15*, 1109–1116, doi:10.1088/0022-3727/15/6/021.

48. Cao, M.; Yao, K.; Wu, C.; Huang, J.; Yang, W.; Zhang, L.; Lei, F.; Sun, Y.; Wang, L.; Shen, Y. Facile Synthesis of SnS and SnS2 Nanosheets for FTO/SnS/SnS2/Pt Photocathode. *ACS Appl. Energy Mater.* **2018**, *1*, 6497–6504, doi:10.1021/acsaem.8b01414.

49. Ham, G.; Shin, S.; Park, J.; Lee, J.; Choi, H.; Lee, S.; Jeon, H. Engineering the crystallinity of tin disulfide deposited at low temperatures. *RSC Adv.* **2016**, *6*, 54069–54075, doi:10.1039/c6ra08169j.

50. Qin, Z.; Xu, K.; Yue, H.; Wang, H.; Zhang, J.; Ouyang, C.; Xie, C.; Zeng, D. Enhanced room-temperature NH3 gas sensing by 2D SnS2 with sulfur vacancies synthesized by

chemical exfoliation. *Sensors Actuators, B Chem.* **2018**, *262*, 771–779, doi:10.1016/j.snb.2018.02.060.

51. McCreary, A.; Berkdemir, A.; Wang, J.; Nguyen, M.A.; Elías, A.L.; Perea-López, N.; Fujisawa, K.; Kabius, B.; Carozo, V.; Cullen, D.A.; et al. Distinct photoluminescence and Raman spectroscopy signatures for identifying highly crystalline WS2 monolayers produced by different growth methods. *J. Mater. Res.* **2016**, *31*, 931–944, doi:10.1557/jmr.2016.47.

52. Gutiérrez, H.R.; Perea-López, N.; Elías, A.L.; Berkdemir, A.; Wang, B.; Lv, R.; López-Urías, F.; Crespi, V.H.; Terrones, H.; Terrones, M. Extraordinary room-temperature photoluminescence in triangular WS 2 monolayers. *Nano Lett.* **2013**, *13*, 3447–3454, doi:10.1021/nl3026357.

53. Kim, M.S.; Yun, S.J.; Lee, Y.; Seo, C.; Han, G.H.; Kim, K.K.; Lee, Y.H.; Kim, J. Biexciton Emission from Edges and Grain Boundaries of Triangular WS2 Monolayers. *ACS Nano* **2016**, *10*, 2399–2405, doi:10.1021/acsnano.5b07214.

54. Jiang, Y.; Wei, M.; Feng, J.; Ma, Y.; Xiong, S. Enhancing the cycling stability of Na-ion batteries by bonding SnS2 ultrafine nanocrystals on amino-functionalized graphene hybrid nanosheets. *Energy Environ. Sci.* **2016**, *9*, 1430–1438, doi:10.1039/c5ee03262h.

55. Sun, W.; Rui, X.; Yang, D.; Sun, Z.; Li, B.; Zhang, W.; Zong, Y.; Madhavi, S.; Dou, S.; Yan, Q. Two-Dimensional Tin Disulfide Nanosheets for Enhanced Sodium Storage. *ACS Nano* **2015**, *9*, 11371–11381, doi:10.1021/acsnano.5b05229.

56. Zhai, C.; Du, N.; Zhang, H.; Yu, J.; Yang, D. Multiwalled carbon nanotubes anchored with SnS2 nanosheets as high-performance anode materials of lithium-ion batteries. *ACS Appl. Mater. Interfaces* **2011**, *3*, 4067–4074, doi:10.1021/am200933m.

57. Li, H.; Gao, D.; Li, K.; Pang, M.; Xie, S.; Liu, R.; Zou, J. Texture control and growth mechanism of WSe 2 film prepared by rapid selenization of W film. *Appl. Surf. Sci.* **2017**, *394*, 142–148, doi:10.1016/j.apsusc.2016.10.050.

58. Wu, C.R.; Chang, X.R.; Wu, C.H.; Lin, S.Y. The Growth Mechanism of Transition Metal Dichalcogenides by using Sulfurization of Pre-deposited Transition Metals and the 2D Crystal Hetero-structure Establishment. *Sci. Rep.* **2017**, *7*, 1–8, doi:10.1038/srep42146.

59. Kong, D.; Wang, H.; Cha, J.J.; Pasta, M.; Koski, K.J.; Yao, J.; Cui, Y. Synthesis of MoS2 and MoSe2 films with vertically aligned layers. *Nano Lett.* **2013**, *13*, 1341–1347, doi:10.1021/nl400258t.

60. Han, S.; Zhou, K.; Yu, Y.; Tan, C.; Chen, J.; Huang, Y.; Ma, Q.; Chen, Y.; Cheng, H.; Zhou, W.; et al. A General Method for the Synthesis of Hybrid Nanostructures Using MoSe 2 Nanosheet-Assembled Nanospheres as Templates . *Research* **2019**, *2019*, 1–10, doi:10.34133/2019/6439734.

61. Liu, Y.; Ren, L.; Zhang, Z.; Qi, X.; Li, H.; Zhong, J. 3D Binder-free MoSe2 Nanosheets/Carbon Cloth Electrodes for Efficient and Stable Hydrogen Evolution Prepared by Simple Electrophoresis Deposition Strategy. *Sci. Rep.* **2016**, *6*, 2–10, doi:10.1038/srep22516.

62. Liu, N.; Choi, W.; Kim, H.; Jung, C.; Kim, J.; Choo, S.H.; Kwon, Y.; An, B.S.; Hong, S.; So, S.; et al. Rapid and mass-producible synthesis of high-crystallinity MoSe2 nanosheets by ampoule-loaded chemical vapor deposition. *Nanoscale* **2020**, *12*, 6991–6999, doi:10.1039/c9nr10418f.

63. Wu, C.T.; Hu, S.Y.; Tiong, K.K.; Lee, Y.C. Anisotropic effects in the Raman scattering of Re-doped 2H-MoSe2 layered semiconductors. *Results Phys.* **2017**, *7*, 4096–4100, doi:10.1016/j.rinp.2017.10.033.

64. Larentis, S.; Fallahazad, B.; Tutuc, E. Field-effect transistors and intrinsic mobility in ultra-thin MoSe 2 layers. *Appl. Phys. Lett.* **2012**, *101*, doi:10.1063/1.4768218.

65. Zeng, H.; Liu, G. Bin; Dai, J.; Yan, Y.; Zhu, B.; He, R.; Xie, L.; Xu, S.; Chen, X.; Yao, W.; et al. Optical signature of symmetry variations and spin-valley coupling in atomically thin tungsten dichalcogenides. *Sci. Rep.* **2013**, *3*, 4908–4916, doi:10.1038/srep01608.

66. Tongay, S.; Zhou, J.; Ataca, C.; Lo, K.; Matthews, T.S.; Li, J.; Grossman, J.C.; Wu, J. Thermally driven crossover from indirect toward direct bandgap in 2D Semiconductors: MoSe2 versus MoS2. *Nano Lett.* **2012**, *12*, 5576–5580, doi:10.1021/nl302584w.

67. Niu, Y.; Gonzalez-Abad, S.; Frisenda, R.; Marauhn, P.; Drüppel, M.; Gant, P.; Schmidt, R.; Taghavi, N.S.; Barcons, D.; Molina-Mendoza, A.J.; et al. Thickness-dependent differential reflectance spectra of monolayer and few-layer MoS2, MoSe2, WS2 and WSe2. *Nanomaterials* **2018**, *8*, doi:10.3390/nano8090725.

68. Chang, Y.C.; Wang, Y.K.; Chen, Y.T.; Lin, D.Y. Facile and reliable thickness

identification of atomically thin dichalcogenide semiconductors using hyperspectral microscopy. *Nanomaterials* **2020**, *10*, 1–15, doi:10.3390/nano10030526.

69. Weijie Zhao, Zohreh Ghorannevis, Leiqiang Chu, Minglin Toh, Christian Kloc, Ping-Heng Tan, and G.E. Evolution of Electronic Structure in Atomically Thin Sheets of WS2 and WSe2. *ACS Nano* **2012**, *7*, 791–797.

70. Wei, H.; Xi, Q.; Chen, X.; Guo, D.; Ding, F.; Yang, Z.; Wang, S.; Li, J.; Huang, S. Molybdenum Carbide Nanoparticles Coated into the Graphene Wrapping N-Doped Porous Carbon Microspheres for Highly Efficient Electrocatalytic Hydrogen Evolution Both in Acidic and Alkaline Media. *Adv. Sci.* **2018**, *5*, 1–7, doi:10.1002/advs.201700733.

71. Qu, Y.; Medina, H.; Wang, S.W.; Wang, Y.C.; Chen, C.W.; Su, T.Y.; Manikandan, A.; Wang, K.; Shih, Y.C.; Chang, J.W.; et al. Wafer Scale Phase-Engineered 1T- and 2H-MoSe2/Mo Core–Shell 3D-Hierarchical Nanostructures toward Efficient Electrocatalytic Hydrogen Evolution Reaction. *Adv. Mater.* **2016**, *28*, 9831–9838, doi:10.1002/adma.201602697.

72. Hanson, E.D.; Lilley, L.M.; Cain, J.D.; Hao, S.; Palacios, E.; Aydin, K.; Wolverton, C.; Meade, T.; Dravid, V.P. Phase engineering and optical properties of 2D MoSe 2 : Promise and pitfalls. *Mater. Chem. Phys.* **2019**, *225*, 219–226, doi:10.1016/j.matchemphys.2018.11.069.

73. Habib, M.; Khalil, A.; Muhammad, Z.; Khan, R.; Wang, C.; Rehman, Z. ur; Masood, H.T.; Xu, W.; Liu, H.; Gan, W.; et al. WX2(X=S, Se) Single Crystals: A Highly Stable

Material for Supercapacitor Applications. *Electrochim. Acta* **2017**, *258*, 71–79, doi:10.1016/j.electacta.2017.10.083.

74. Salitra, G.; Hodes, G.; Klein, E.; Tenne, R. Highly oriented WSe2 thin films prepared by selenization of evaporated WO3. *Thin Solid Films* **1994**, *245*, 180–185, doi:10.1016/0040-6090(94)90896-6.

75. Philipp Tonndorf, Robert Schmidt, Philipp Böttger, Xiao Zhang, Janna Börner, Andreas Liebig, Manfred Albrecht, Christian Kloc, O.G.; Dietrich R. T. Zahn, Steffen Michaelis de Vasconcellos, and R.B. Photoluminescence emission and Raman response of monolayer MoS2, MoSe2, and WSe2. *Opt. Express* **2013**, *21*, 4908–4916, doi:10.1038/srep01608.

76. Huang, J.-K.; Pu, J.; Hsu, C.-L.; Chiu, M.-H.; Juang, Z.-Y.; Chang, Y.-H.; Chang, W.-H.; Iwasa, Y.; Takenobu, T.; Li, L.-J. Large-Area Synthesis of Highly Crystalline WSe2 Monolayers and Device Applications. *ACS Nano* **2014**, *8*, 923–930.

77. Liu, B.; Fathi, M.; Chen, L.; Abbas, A.; Ma, Y.; Zhou, C. Chemical Vapor Deposition Growth of Monolayer WSe2 with Tunable Device Characteristics and Growth Mechanism Study. *ACS Nano* **2015**, *9*, 6119–6127, doi:10.1021/acsnano.5b01301.

78. Weijie Zhao, Zohreh Ghorannevis, Leiqiang Chu, Minglin Toh, Christian Kloc, Ping-Heng Tan, and G.E. Evolution of Electronic Structure in Atomically Thin Sheets of WS2 and WSe2. *ACS Nano* **2013**, *7*, 791–797.

79. Beal, A.R.; Knights, J.C.; Liang, W.Y. Transmission spectra of some transition metal dichalcogenides. I. Group IVA: Octahedral coordination. *J. Phys. C Solid State Phys.*

1972, *5*, 3531–3539, doi:10.1088/0022-3719/5/24/015.

80. Sokolikova, M.S.; Sherrell, P.C.; Palczynski, P.; Bemmer, V.L.; Mattevi, C. Direct solution-phase synthesis of 1T' WSe 2 nanosheets. *Nat. Commun.* **2019**, *10*, doi:10.1038/s41467-019-08594-3.

81. Wu, P.C.; Yang, C.L.; Du, Y.; Lai, C.H. Scalable Epitaxial Growth of WSe2 Thin Films on SiO2/Si via a Self-Assembled PtSe2 Buffer Layer. *Sci. Rep.* **2019**, *9*, 1–10, doi:10.1038/s41598-019-44518-3.

82. Saha, S.; Banik, A.; Biswas, K. Few-Layer Nanosheets of n-Type SnSe2. *Chem. - A Eur. J.* **2016**, *22*, 15634–15638, doi:10.1002/chem.201604161.

83. Huang, Y.; Xu, K.; Wang, Z.; Shifa, T.A.; Wang, Q.; Wang, F.; Jiang, C.; He, J. Designing the shape evolution of SnSe2 nanosheets and their optoelectronic properties. *Nanoscale* **2015**, *7*, 17375–17380, doi:10.1039/c5nr05989e.

84. Boscher, N.D.; Carmalt, C.J.; Palgrave, R.G.; Parkin, I.P. Atmospheric pressure chemical vapour deposition of SnSe and SnSe2 thin films on glass. *Thin Solid Films* **2008**, *516*, 4750–4757, doi:10.1016/j.tsf.2007.08.100.

85. Zhang, Y.; Shi, Y.; Wu, M.; Zhang, K.; Man, B.; Liu, M. Synthesis and surface-enhanced raman scattering of ultrathin SnSe2 nanoflakes by chemical vapor deposition. *Nanomaterials* **2018**, *8*, 515, doi:10.3390/nano8070515.

86. Rai, R.K.; Islam, S.; Roy, A.; Agrawal, G.; Singh, A.K.; Ghosh, A.; Ravishankar, N. Morphology controlled synthesis of low bandgap SnSe 2 with high photodetectivity.

Nanoscale **2019**, *11*, 870–877, doi:10.1039/c8nr08138g.

87. Jang, D.M.; Jung, H.; Hoa, N.D.; Kim, D.; Hong, S.K.; Kim, H. Tin oxide-carbon nanotube composite for NO X sensing. *J. Nanosci. Nanotechnol.* **2012**, *12*, 1425–1428, doi:10.1166/jnn.2012.4656.

88. Xu, X.; Song, Q.; Wang, H.; Li, P.; Zhang, K.; Wang, Y.; Yuan, K.; Yang, Z.; Ye, Y.; Dai, L. In-Plane Anisotropies of Polarized Raman Response and Electrical Conductivity in Layered Tin Selenide. *ACS Appl. Mater. Interfaces* **2017**, *9*, 12601–12607, doi:10.1021/acsami.7b00782.

89. Luo, S.; Qi, X.; Yao, H.; Ren, X.; Chen, Q.; Zhong, J. Temperature-Dependent Raman Responses of the Vapor-Deposited Tin Selenide Ultrathin Flakes. *J. Phys. Chem. C* **2017**, *121*, 4674–4679, doi:10.1021/acs.jpcc.6b12059.

90. V. S. Minaev, S.P.T. and V.V.K. STRUCTURAL AND PHASE TRANSFORMATIONS IN CONDENSED SELENIUM. *J. Optoelectron. Adv. Mater.* **2005**, *7*, 1717–1741, doi:10.1243/09544119JEIM686.

91. Fernandes, P.A.; Sousa, M.G.; Salomé, P.M.P.; Leitão, J.P.; Da Cunha, A.F. Thermodynamic pathway for the formation of SnSe and SnSe2 polycrystalline thin films by selenization of metal precursors. *CrystEngComm* **2013**, *15*, 10278–10286, doi:10.1039/c3ce41537f.

92. El-Nahass, M.M. Optical properties of tin diselenide films. *J. Mater. Sci.* **1992**, *27*, 6597–6604, doi:10.1016/j.radphyschem.2013.11.020.

93. Mukhokosi, E.P.; Krupanidhi, S.B.; Nanda, K.K. Band gap engineering of hexagonal SnSe2 nanostructured thin films for infra-red photodetection. *Sci. Rep.* **2017**, *7*, 1–10, doi:10.1038/s41598-017-15519-x.

94. Nair, P.K.; Barrios-Salgado, E.; Nair, M.T.S. Cubic-structured tin selenide thin film as a novel solar cell absorber. *Phys. Status Solidi Appl. Mater. Sci.* **2016**, *213*, 2229–2236, doi:10.1002/pssa.201533040.

95. Yan, T.; Han, Y.; Fu, Q.; Xu, T.; Yin, S.; Wu, W.; Liu, W. Ultrafast carrier relaxation in SnSex (x=1, 2) thin films observed using femtosecond time-resolved transient absorption spectroscopy. *Opt. Mater. (Amst).* **2020**, *108*, 110440, doi:10.1016/j.optmat.2020.110440.

96. Pawar, M.; Kadam, S.; Late, D.J. High-Performance Sensing Behavior Using Electronic Ink of 2D SnSe2 Nanosheets. *ChemistrySelect* **2017**, *2*, 4068–4075, doi:10.1002/slct.201700261.

97. D'olimpio, G.; Genuzio, F.; Menteş, T.O.; Paolucci, V.; Kuo, C.N.; Al Taleb, A.; Lue, C.S.; Torelli, P.; Fariás, D.; Locatelli, A.; et al. Charge Redistribution Mechanisms in SnSe2Surfaces Exposed to Oxidative and Humid Environments and Their Related Influence on Chemical Sensing. *J. Phys. Chem. Lett.* **2020**, 9003–9011, doi:10.1021/acs.jpclett.0c02616.

98. Barreca, D.; Garon, S.; Tondello, E.; Zanella, P. SnO 2 Nanocrystalline Thin Films by XPS . *Surf. Sci. Spectra* **2000**, *7*, 81–85, doi:10.1116/1.1288177.

99. Stranick, M.A.; Moskwa, A. SnO 2 by XPS . *Surf. Sci. Spectra* **1993**, *2*, 50–54,

doi:10.1116/1.1247724.

100. Lu, D.; Yue, C.; Luo, S.; Li, Z.; Xue, W.; Qi, X.; Zhong, J. Phase controllable synthesis of SnSe and SnSe2 films with tunable photoresponse properties. *Appl. Surf. Sci.* **2021**, *541*, 148615, doi:10.1016/j.apsusc.2020.148615.

101. Fan, Y.; Zhuo, Y.; Li, L. SeO 2 adsorption on CaO surface: DFT and experimental study on the adsorption of multiple SeO 2 molecules. *Appl. Surf. Sci.* **2017**, *420*, 465–471, doi:10.1016/j.apsusc.2017.04.233.

102. Lee, L.; Chen, C.W.; Manikandan, A.; Lee, S.H.; Wang, Z.M.; Chueh, Y.L. Phase-engineered SnSex toward SnSe2/SnSe heterostructure with improved thermal conductance by a low-temperature plasma-assisted chemical vapor reaction. *Nano Energy* **2018**, *44*, 419–429, doi:10.1016/j.nanoen.2017.11.064.

103. Vishwanath, S.; Liu, X.; Rouvimov, S.; Basile, L.; Lu, N.; Azcatl, A.; Magno, K.; Wallace, R.M.; Kim, M.; Idrobo, J.C.; et al. Controllable growth of layered selenide and telluride heterostructures and superlattices using molecular beam epitaxy. *J. Mater. Res.* **2016**, *31*, 900–910, doi:10.1557/jmr.2015.374.

104. Jing-Kai Huang, Jiang Pu, Chang-Lung Hsu, Ming-Hui Chiu, Zhen-Yu Juang, Yung-Huang Chang, Wen-Hao Chang, Yoshihiro Iwasa, Taishi Takenobu, and L.-J.L. Large-Area Synthesis of Highly Crystalline WSe2 Monolayers and Device Applications. *ACS Nano* **2014**, *8*, 923–930.

105. McCreary, K.M.; Hanbicki, A.T.; Jernigan, G.G.; Culbertson, J.C.; Jonker, B.T. Synthesis of Large-Area WS 2 monolayers with Exceptional Photoluminescence. *Sci. Rep.* **2016**,

6, 1–7, doi:10.1038/srep19159.

106. Barreca, D.; Carta, G.; Gasparotto, A.; Rossetto, G.; Tondello, E.; Zanella, P. A Study of Nanophase Tungsten Oxides Thin Films by XPS. *Surf. Sci. Spectra* **2001**, *8*, 258–267, doi:10.1116/11.20020801.

107. Shallenberger, J.R. 2D tungsten diselenide analyzed by XPS. *Surf. Sci. Spectra* **2018**, *25*, 014001, doi:10.1116/1.5016189.

Chapter 5

Sensing properties of Metal Dichalcogenides

In this Chapter, it is reported the sensing properties of the sensors engineered using MDs. The starting point was the growth of WO_3 on Alumina substrates with interdigitated platinum electrodes. Growth conditions discussed in Chapter 4 were employed for the synthesis of MDs (WS_2 Nanoflakes, WS_2 Nanotriangles and WSe_2 Nanoflowers). The different morphology and chemical concentration were evaluated by SEM and XPS, respectively. The sensing performance to part per billion (ppb) of NO_2 and NH_3 under various experimental conditions, including variable humidity level and temperatures effects is reported.

5.1 Gas Sensors

Some of the most critical air pollutants, such as nitrogen oxides (NO_x) and carbon oxides (CO, CO_2), come from combustion or automotive emissions and can cause serious diseases even at low concentrations. Ammonia (NH_3) is another dangerous analyte that has both natural and industrial derivation. The prolonged exposure to these toxic vapors may cause problems in respiratory apparatus, skin and eyes damage and pulmonary edema. For that, chemical gas sensors have been developed to detect these types of gases [1], [2], [3]. Carbon-based materials have proven to be good candidates for sensing applications but they show poor selectivity [4], [5] and slow recovery [6]. Recently, transition metal dichalcogenides (TMD) materials have attracted huge scientific interest because of their immense potential for technological applications because they display versatile chemistry and tunable band gaps that are much more beneficial in the design of practical gas sensing devices [7]. As we said in the chapters 3 and 4, this thesis work focusses in the vertically-aligned (VA)-MDs nanosheets because they are very promising for sensing applications thanks to their active exposed edges because they have most of their atoms exposed to the medium, which makes them particularly interesting for the application of gas detection. It has been demonstrated that vertical MoS_2 grown using CVD have great potential for hydrogen evolution reaction [8] or gas sensor applications [9] if it is compare with horizontally films. This is due to higher adsorption energy on MoS_2 edge as compared to basal plane of the MoS_2 films. Indeed, in the past few years, it has been emphasized experimentally [9] and theoretically [10] that semi-conductive MoS_2 (prototype of MDs material) is an interesting material for gas sensing applications due to the structural defects, including point defects, grain boundaries, and edges [9]. Unlike the basal plane, the vertically aligned MoS_2

is composed of (002) plane of the MoS_2 crystal structure terminated with dominantly exposed molybdenum or sulfur atoms.

5.2 Working principle

Different types of gas sensors have been developed and can be classified depending on their transduction mechanism as: electrochemical, optical, resistive, gravimetric, calorimetric and field-effect transistor sensors. In this work, resistive sensors were investigated due to their low cost and easy fabrication. A great variety of materials can be used as active materials in this type of sensors, such as semiconducting metal oxides, carbon materials, transition metal dichalcogenides and so on [11–13]. In resistive gas sensors, the response observed due to the interaction between the analyte and the sensing layer can be transduced as an electric signal which corresponds to a change in the conductance, potential or capacitance of the active material [13]. The reversibility of the sensor is defined as the capability to return to its initial state after the interaction with the target gas is stopped: the recovery time has to be fast for an efficient sensor.

The resistive sensing devices present an operational principle where the variation of the electrical resistivity (or conductivity, inversely) is a consequence of the gas molecules absorbed on the sensor surface. The sensing experiments consist of the measurement of the resistance variation as a function of the gas molecules concentration for subsequent cycles (Figure 5.1). The measurement of the resistance is continuously running allowing a real-time acquisition of its variation from the initial value, R_0, during the complete exposure cycle. When the gas flow is shut, the recovery time of the baseline is measured allowing the evaluation of the speed and reliability

of the sensor. The sensor response is then defined as the normalized resistance variation, according to the following relation:

$$\left|\frac{\Delta \boldsymbol{R}}{\boldsymbol{R}_0}\right| (\%) = \left|\frac{\boldsymbol{R}_0 - \boldsymbol{R}_f}{\boldsymbol{R}_0}\right|$$

where R_f is generally the steady state value of the sensor resistance while exposed to a target gas and Ro is the baseline resistance (i.e. sensor resistance while in dry air). The sign of the resistance variation depends on the type of semiconducting layer (*n*- or *p*-type depending on the electron or hole doping) and on the donor/acceptor behavior of the detected molecule. The physical process is described in the following by considering the *p*-type character of the active layer and keeping in mind that the *n*-type sensor behaves inversely.

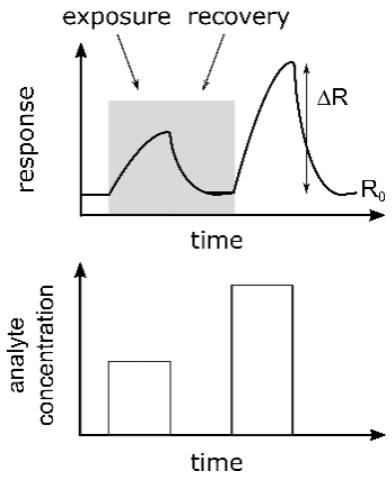

Figure 5.1 Measurement of the resistance variation as a function of the analyte concentration for subsequent cycles [14].

The physical process behind the resistance variation is the occurrence of charge transfer (Figure 5.2). In a p-type gas sensitive material the exposure to an oxidizing gas such as NO_2 leads to a depletion of the electron density in the as-prepared samples due to a charge transfer from the

layer to the target gas, and, as a result, the Fermi level of the sensing layer is downshifted in the valence band corresponding to an enrichment of hole carriers and enhanced sample conductance, hence reduced resistance (Figure 5.2 a). On the contrary, exposure to a reducing gas as NH_3 results in the release of electrons from the target gas to the sensor material, contributing to the increase of its electron density due to this inverted charge transfer direction. Consequently, the valence band of the as-prepared sample layer is shifted away from the Fermi level, resulting in hole depletion and reduced conductance, hence increased resistance (Figure 5.2 b).

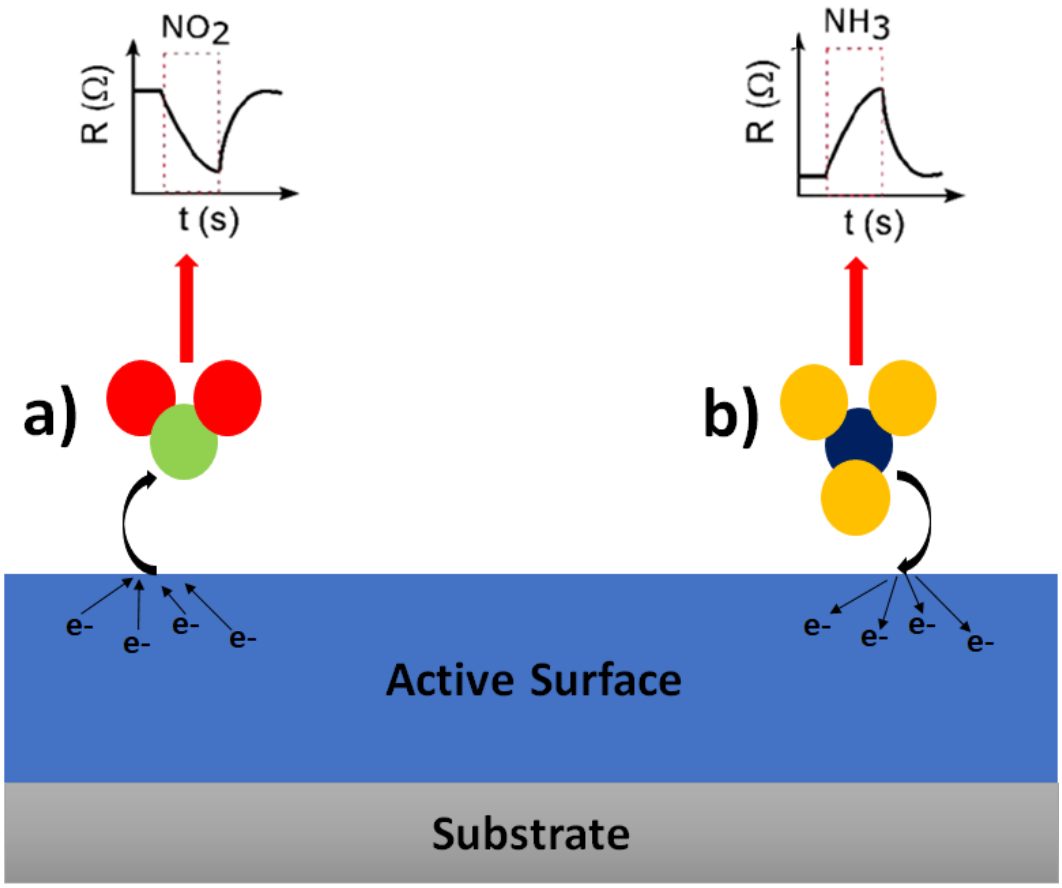

Figure 5.2 The charge transfer process and resistance variation are schematically illustrated upon exposure to NO_2 and NH_3 [14]. This is true for a p-type gas sensitive material.

5.3 Gas Sensing test

5.3.1 Experimental set-up

The sensing measurements are performed at the University Rovira i Virgili of Tarragona, in Spain, in collaboration with MINOS group, headed by Prof. Eduard Llobet. The gas sensing characteristics of the fabricated TMDs sensors were measured using a customized gas-sensing detection system. Alumina substrates with interdigitated platinum electrodes purchased from Ceram Tech GmbH (Figure 5.3) were used to grow the WO_3 nanofilms which were further sulfurized or selenized to synthesize WS_2 and WSe_2 films, respectively, at the University of Namur (see section 4.13 in Chapter 4).

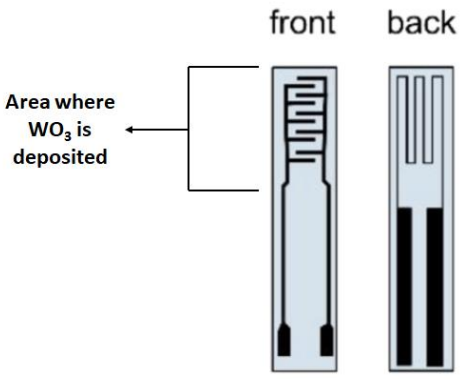

Figure 5.3 Schematic illustration of a commercial alumina sensor with Pt-electrodes from front side, where the sensing layer is deposited, and back side, where the heater is located.

For testing the as-fabricated MDs sensors are placed inside a teflon test chamber of 35 mL in volume. This testing chamber is connected to a fully automated, continuous gas flow measurement set-up able to supply diluted gas mixtures as well as humidified gas mixtures using

a mass flow controller. The gases employed for testing were used from calibrated gas cyclinders balanced in dry synthetic air. The electrical resistance was measured by using an Agilent-34972A multimeter. The operating temperature of the sensors was controlled by connecting its heater to an external power supply (Agilent, model 3492A). The measurement array comprises a set of computer-controlled mass flow meters and electro- valves systems to ensure reproducible concentrations of the gases that are delivered to a test chamber (Figure 5.4). The DC resistance of the sensors is continuously measured with an Agilent multimeter. The chamber consists of two main pieces: the bottom part (chamber base) where the sensors are connected for resistance measurement and the lid with the inlet and outlet gas connections, the lid and the chamber base are put together and closed with the help of screws.

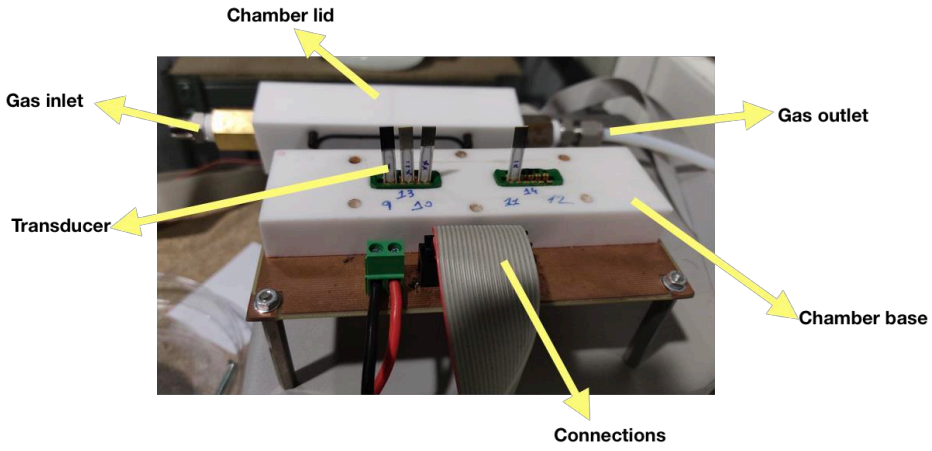

Figure 5.4 Test chamber used for commercial alumina substrates.

In a typical measurement cycle, pure dry air is flowed through the chamber until the sample resistance stabilizes, corresponding to a constant baseline R_0. Sequentially, a given concentration of the gas of interest is fed into the test chamber and kept flowing during the chosen exposure

time. A mixed flow of dry air and target gas is introduced to obtain the desired concentration (ppm down to ppb range) of the target gas. During the recovery phase, the flow is switched again to pure dry air. The measurements can be performed at room temperature (RT) or at certain working temperature or under different ambient moisture conditions as we will see in the section 5.4 of this chapter.

5.4 Gas sensing results

5.4.1 Gas sensing performances of WS_2 Nanoflakes and Nanotriangles

The gas sensing performances of WS_2 Nanoflakes (NFs) and WS_2 Nanotriangles (NTs) sensors were examined towards different concentrations of NO_2 and other species such as H_2S, H_2 and NH_3. For all direct-current resistance measurements, the target gas was injected for 10 min into the test chamber where sensors were placed, which was followed by 50 min purging with a dry air flow for sensors to regain their initial baseline resistances. The equation used to calculate sensor response is as follows:

$$R = \frac{(R_{air} - R_{gas})}{R_{air}} * 100$$

The effect of the operating temperature was studied with the performance of various NO_2 gas measurements at different temperatures (from 25 °C to 150 °C). Figure 5.5, in the graphs a) and b) we can observe the intensity of sensor responses as a function of the working temperature. The sensor response of WS_2 nanoflakes presents an almost linear increase with the increment of the operating temperature and we can see that both morphologies have a response. This can be

explained well by enhanced adsorption of gas molecules at higher temperatures [15]. The activation barrier is lowered which enhances the rate of gas adsorption on the surface, leading to a much higher response at an elevated temperature. The measurements were not performed at temperatures beyond 150 °C because the evaporation of sulfur would start and the formation process of WO_3 could initiate leading to a formation of a WO_3/WS_2 composite. Thus, for subsequent studies, 150 °C was considered as the optimal working temperature for this sensor.

The Figures 5.5 c) and d) show the evolution of the electrical resistance of the sensors operated at 150 °C under repeated exposure and recovery cycles of NO_2. As we can observe, WS_2 nanotriangles present a higher resistance than WS_2 nanoflakes, since the baseline resistances of nanotriangles is obviously bigger than nanoflakes.

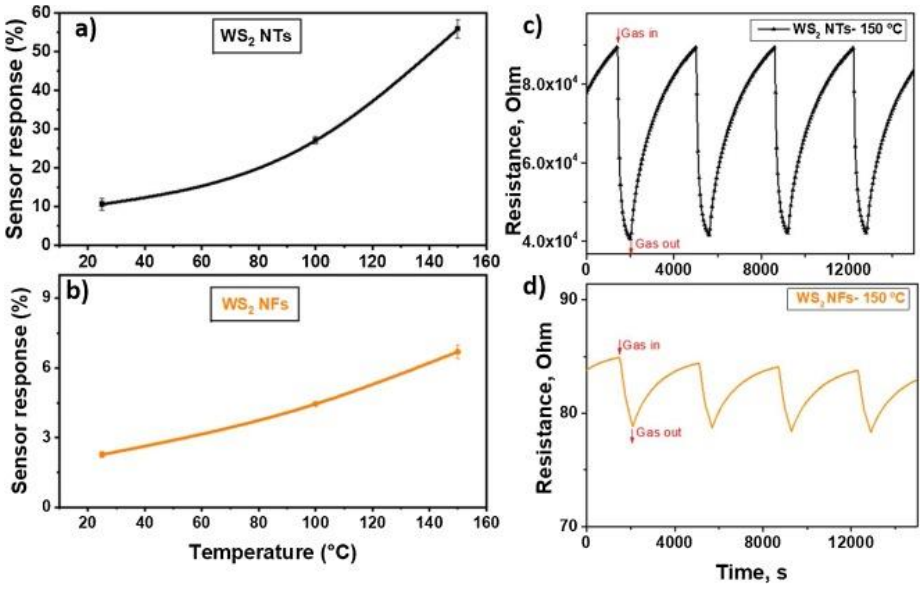

Figure 5.5 (a and b) gas sensor response of WS_2 NTs and WS_2 NFs as a function of temperature, towards NO_2 at 800 ppb and 300 ppb, respectively and (c and d) electrical resistance change of both sensors operated at 150 °C, toward these concentrations.

In the Figure 5.6 we can see the response of the sensor when it was exposed to consecutive concentration pulses of NO_2 that ranged from 50 to 300 ppb. In this case, the operating temperature was constant at 150 °C because it presented the best response. During these measurements, the two sensors were tested at five different concentrations of NO_2. A diluted mixture of NO_2 in dry air was injected for 10 min in steps of increasing concentrations of 50, 80, 100, 200 and 300 ppb. It is evident from the results obtained that there is an increase in response with each increment in analyte concentration. The WS_2 NFs sensor response was calculated to be 0.16%, 0.96%, 2.28%, 3.41%, and 6.69% for 50, 80, 100, 200 and 300 ppb of nitrogen dioxide, respectively. In contrast, the response increased to higher values (19.6%, 38.04%, 39.3%, 40.265, 41.75%) for the WS_2 NTs sensor. Hence, WS_2 NTs are significantly more sensitive to NO_2 than WS_2 NFs.

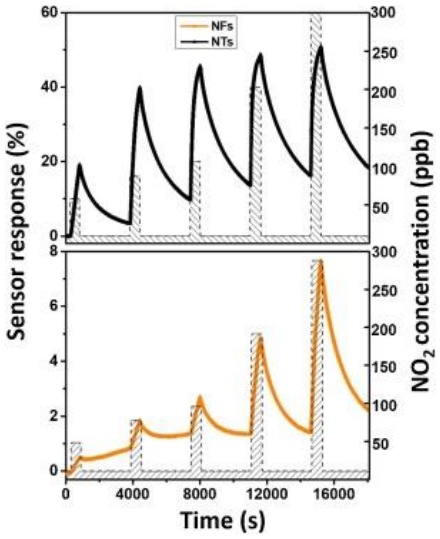

Figure 5.6 WS_2 nanotriangles (black), WS_2 nanoflakes (orange) sensor response and recovery towards pulses of increasing concentrations of NO_2 gas (from 50 to 300 ppb). Sensors were operated at 150 °C.

Figure 5.7 shows three replicate sensor response and recovery cycles towards 800 ppb of NO_2 for a WS_2 NT sensor operated at 150 °C in dry (~3% RH @ 25 °C) and humid (50% RH @ 25 °C) backgrounds. We can observe that under humid conditions, sensor remains fully functional with good and reproducible response. However, there is a tolerable decrease in response intensity, since response decreased from 56% to 30%. It is worth noting that most of the reported studies on layered MDs gas sensors have not studied the effect of ambient humidity on sensing performance, an essential aspect for the real application of gas sensors.

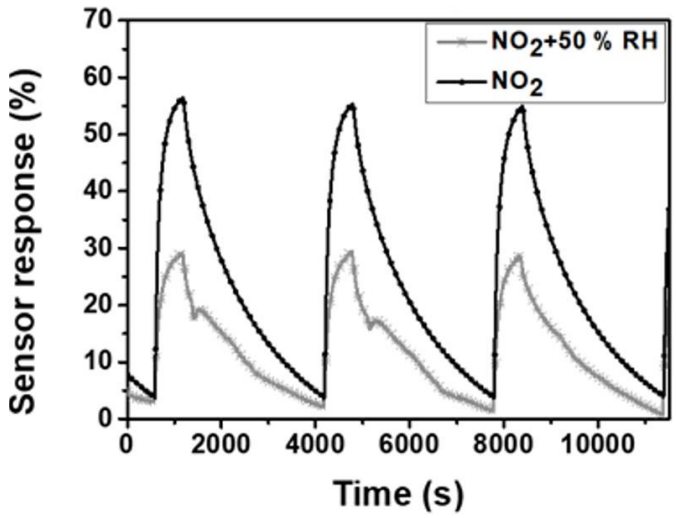

5.7 Three replicate measurements for 800 ppb in dry and 50% RH backgrounds.

The long-term stability of the sensors is presented in the Figure 5.8. NO_2 measurements were repeated at regular intervals over a long period and the evolution of the baseline resistance and sensor response was monitored. For WS_2 NFs, both baseline resistance and NO_2 response show a significant decreasing trend over time. The response towards 800 ppb of NO_2 decreases from 26.65% to 19.45% over a period of 19 weeks (Figure 5.8 a). The behavior for WS_2 NTs is different. While the baseline resistance shows a clear decreasing trend, sensor response towards NO_2

shows remarkable stability, as it varies from 55.95 % to 54.15% over a period of 35 weeks (Figure 5.8 b).

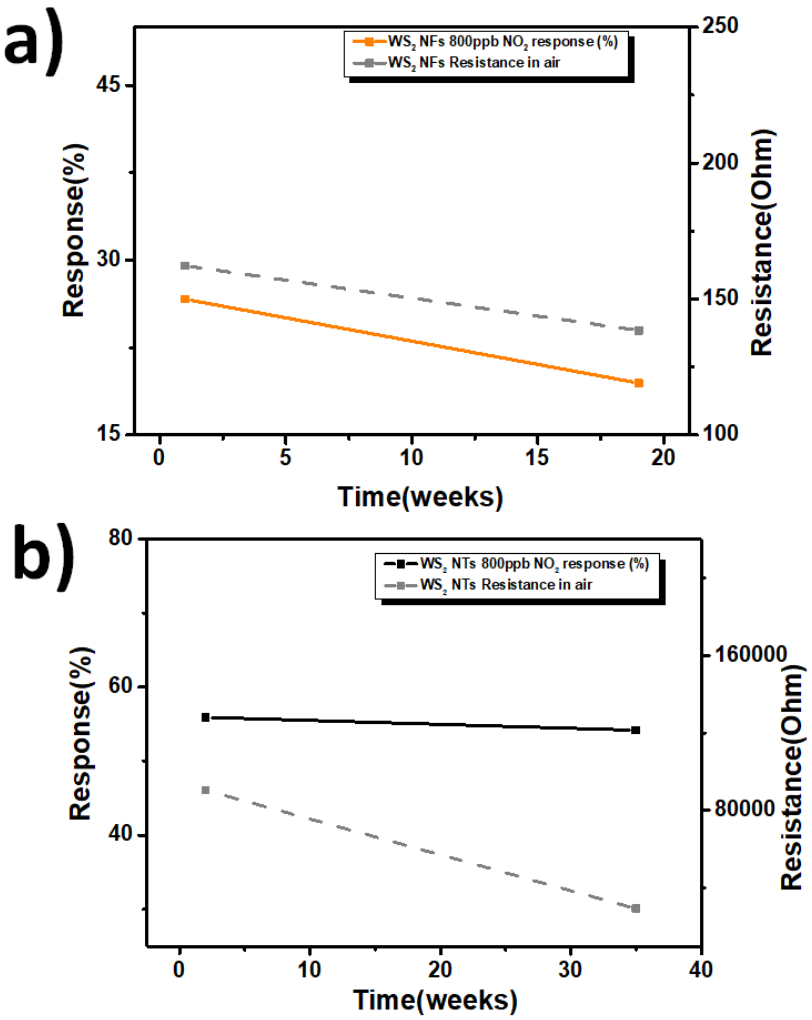

5.8 Long-term stability study. Evolution of the baseline resistance and sensor response to NO_2 over time. a) Stability study for WS_2 NFs and b) Stability study for WS_2-NTs.

Other gases such as NH_3, H_2S and H_2 were studied and the responses were compared with the ones that we obtained in the detection of NO_2. In the Figure 5.9 we can see these responses. The

results presented have negative values, because sensor resistance increases in the presence of these electron donor species, which further confirms the p-type behavior of our WS_2 nanomaterials. It is evident from the bar graph that the sensor is highly sensitive to NO_2. The response of NO_2 is significantly higher than the one recorded for any of the other species tested. These results are in line with previously reported theoretical studies indicating that the interaction of the NO_2 molecule with the surface of TMDs is characterized by higher adsorption energy and charge transfer than for other molecules such as NH_3 or H_2S [16]. These results indicate that WS_2 sensors show potential for the selective detection of NO_2 traces, provided some surface functionalization is conducted to decrease the current cross-sensitivity experienced.

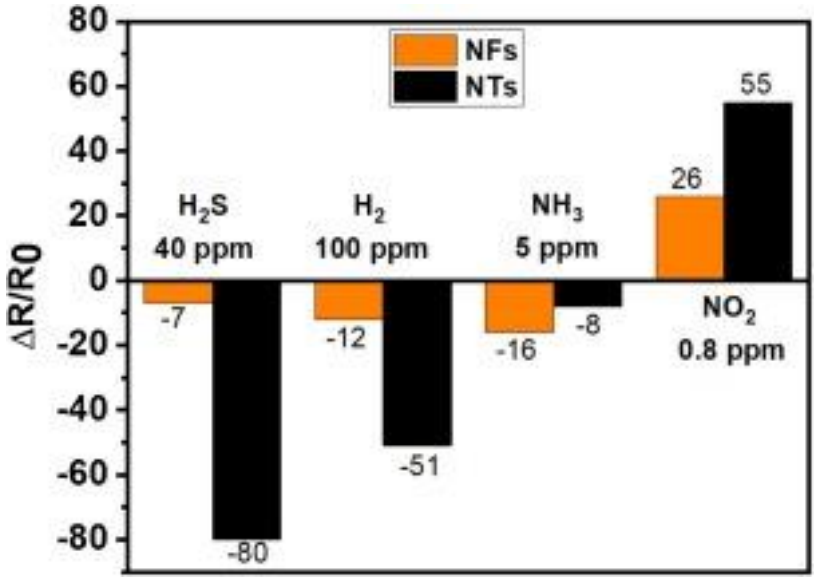

Figure 5.9 Response histogram of WS_2 NFs and WS_2 NTs sensors operated at 150 °C toward different gases.

Table 5.2 summarizes the main results obtained and puts them in context with the state of the art. In this table, the performance in the detection of NO_2 reported here are compared against

those in the literature NO_2 gas detection. From these results it is clear that sensors based on WS_2 NTs show very remarkable gas responses, if we make the comparison between the sensor response in all the materials presented, with high sensitivity an unprecedented detection limit below 5 ppb for NO_2 gas at 150 °C. Also, the working temperature is another aspect to consider, as we can see in the Table 5.2 different working temperatures are presented because each sensor has a better response at a given temperature. This may be due to the change in morphology of the synthesized material and in the way the sensor was prepared.

Table 5.2 Comparison of the sensing properties to NO_2 of resistive gas sensors based on different WS_2 sensing materials.

Structure	Working temp. (°C)	Studied conc.	Response (%)	Sensitivity (Response%/ppm)	Detection limit	Reference
Nanotriangles	150	800 ppb	55.9	70	<5 ppb (experim.)	[15]
Nanotriangles	25	800 ppb	10.6	13.2	N/A	[15]
Nanoflakes	150	800 ppb	26.6	33.2	~50 ppb (experim.)	[15]
Nanoflakes	25	300 ppb	0.5	1.7	N/A	[15]
Nanosheets	NA	25 ppm	8.7	0.3	N/A	[17]
Nanosheets	25	5 ppm	68.4	13.7	0.1 ppm (experim)	[18]
Nanostructure (aerogel)	180	2 ppm	3	1.5	10 ppb (theoret.)	[19]
Nanostructure	25	5 ppm	2.5	0.5	N/A	[20]
Nanosheets	160	5 ppm	121	242	< 200 ppb (experim.)	[21]

N/A: Not available; experim.: experimentally measured; theoret.: theoretically calculated.

5.4.2 Gas sensing performances of WSe_2 Nanoflowers

The gas sensing characteristics of as-fabricated WSe_2 nanosheet gas sensors were measured. To determine the performance of a gas sensor it is essential to select the optimal operating temperature. The WSe_2 nanosheet sensors were exposed towards 800 ppb of NO_2 in dry air balance and measured the corresponding responses at different operating temperatures but not beyond 150 °C. This is due to the thermal instability of 2H-WSe_2 at elevated temperatures and to avoid ambient oxidation [15]. As depicted in Figure 5.10, the sensor response first increases with increase in operating temperature from 25°C to 100°C, and then gradually decreases as the temperature is further increased. This could possibly be due to the physisorption of NO_2 molecules on the surface of WSe_2 nanoflowers. Initially, with an increase in operating temperature, the number of physiosorbed NO_2 molecules increases, thereby increasing sensor response but as the temperature is further increased beyond 100 °C there is a sharp drop in sensor response. The increase in sensor response at 100 °C is attributed to the presence of possible selenium vacancies (or defect sites). The presence of selenium vacancies promotes NO_2 molecule adsorption and hence interaction with the sensing surface. For instance, it has been reported in previous density functional studies that in the absence of disulfide vacancies there is negligible adsorption of N_2 molecules on MoS_2 surface [22].

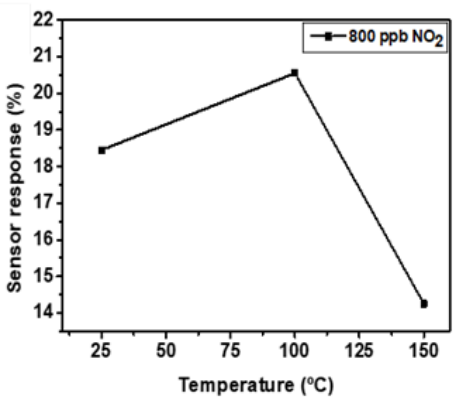

Figure 5.10 Gas sensor response of WSe_2 as a function of temperature, towards NO_2 at 800 ppb.

At room temperature, the sensor response is calculated to be 18.5 % which jumps to a value higher than 20.5 % at an operating temperature of 100°C to finally drop down to only 14.2 % at 150°C. Therefore, it can be concluded that 100°C is the optimal working temperature for the fabricated WSe_2 nanoflower sensors for NO_2 gas detection. Figure 5.11 displays the dynamic film resistance changes towards 800 ppb of NO_2 gas, at 100 °C. It is observed that WSe_2 sensors respond as a p-type semiconductor with decreasing resistance when exposed to an oxidizing type of a gas, such as NO_2 in this case. When a p-type material is exposed to an oxidizing gas there is an extraction of electrons from the material surface thereby increasing the hole density and decreasing the electrical resistance of the material. The higher temperature (100 °C) promotes faster desorption of gas molecules, thereby resulting in an improved recovery cycle. The response time of WSe_2 nanoflower sensors towards 800 ppb NO_2 did not change much with temperature, while the recovery time diminished sharply with increase in temperature.

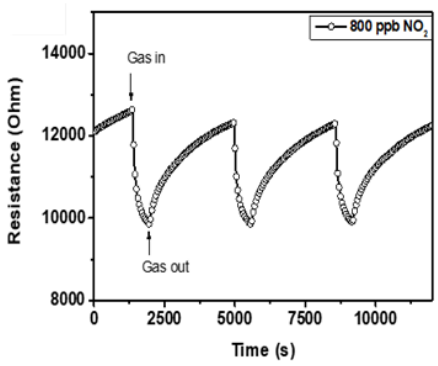

Figure 5.11 Electrical resistance change of WSe_2 sensor operated at 100 °C, towards NO_2 at 800 ppb.

Figure 5.12 shows the dynamic gas sensing response of the fabricated WSe_2 nanoflower sensors towards NO_2 at different concentrations from 0.1 - 0.8 ppm at an operating temperature of 100 °C. The high response along with response stability at 0.8 ppm of NO_2 reveals the ability of the sensor to detect NO_2 at ppb levels. The WSe_2 sensor can detect even 0.1 ppm of NO_2 gas, which is lower than the experimental detection limit as well as the threshold exposure limit of NO_2 recommended by American Conference of Government Industrial Hygienists [23].

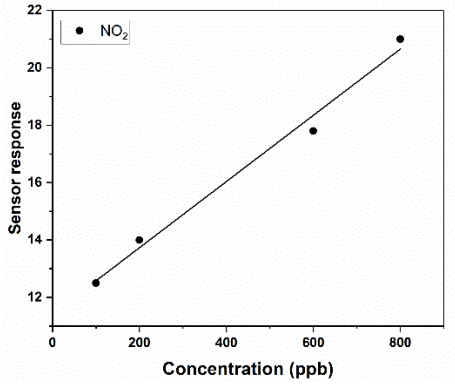

Figure 5.12 Linear fit of gas sensing response of the fabricated WSe_2 nanoflower sensors towards NO_2 at different concentrations from 0.1 - 0.8 ppm at an operating temperature of 100 °C.In

addition to NO_2 gas sensing studies, the performance of WSe_2 nanoflower sensor towards NH_3 gas was also studied. This gas is of particular interest due to its noxious effects on human health as well as the environment. For this we again investigated the optimal operating temperature for WSe_2 nanoflower sensors towards NH_3 gas. As depicted in Figure 5.13 a) a linear increase in sensor response with increase in temperature is observed with almost negligible response at room temperature, which can be expected due to rapid reaction rates at elevated temperatures. This behavior is more prominent when the concentration of target gas is increased from 10 ppm to 40 ppm. For instance, the gas response at 100 °C and 150 °C is 13% and 15.5% respectively towards 10 ppm of NH_3 gas. Furthermore, as the NH_3 gas concentration is further increased to 40 ppm the calculated response climbs up to a value of 20.5% and 24.5% at 100 °C and 150 °C respectively. This can be attributed to the hierarchical nanoflower structure resulting into a high surface area which in turn enhances the active sites for NH_3 gas adsorption and surface reactions. Considering a higher sensing response at 150 °C it has been considered as the optimal working temperature for subsequent measurements with NH_3 gas. As discussed before, being a p-type material, the sensor shows an increase in the electrical resistance when exposed to NH_3 (i.e., a reducing gas). Additionally, it is clearly seen that the sensor shows reproducible response at each concentration where the response and recovery time is much lower for higher concentrations of NH_3 (40ppm) (Figure 5.13 a and b).

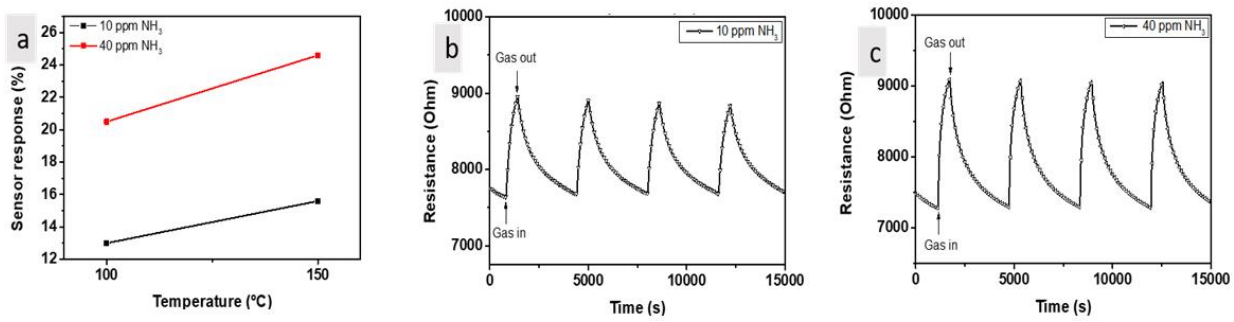

Figure 5.13 a) WSe_2 sensor response as a function of temperature towards NH_3 gas b) Film resistance change as a function of time, towards b) 10 ppm of NH_3 c) 40 ppm of NH_3, at 150 °C.

Figure 5.14 shows the response against different NH_3 concentrations at a constant operating temperature of 150 °C. During this measurement, the sensor was exposed to five consecutive concentration pulses of NH_3, that ranged from 2 to 10 ppm. The WSe_2 sensor response was calculated to be 8.2%, 10.3%, 12%, 13.4% and 14.5% for 2, 4, 6, 8 and 10 ppm of NH_3 respectively.

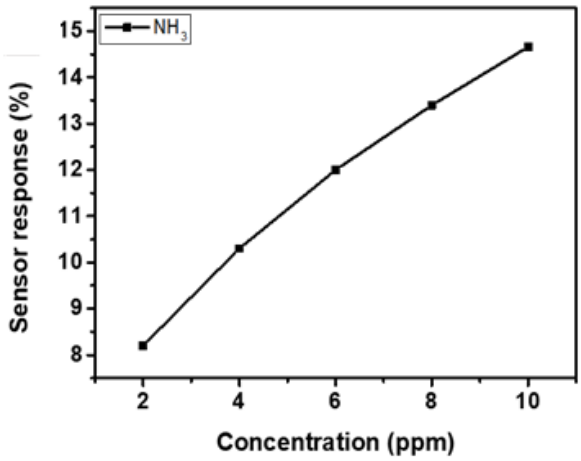

Figure 5.14 WSe_2 sensor response as a function of NH_3 concentrations at 150 °C.

Influence of humidity on the sensor response towards NH_3 and NO_2 gas has also been studied. The results are presented in Fig. 5.15 a) and b) where the sensor was tested towards 0.8 ppm NO_2 gas at 100°C and 40 ppm NH_3 gas at 150 °C in 50% humid background respectively. It was observed that when the sensor was exposed to 0.8 ppm NO_2 gas in presence of humidity the sensor response was enhanced from 20.5% to 26%. This slight increase in response could be assigned to the ionization of NO_2 molecules in presence of water molecules. However, no apparent decrease in sensor response is observed when exposed to NH_3 gas in presence of water vapor. The sensor response towards 40 ppm NH_3 in presence of 50% RH is calculated to be 24% which indicates negligible drop in its sensing response. This highlights a good reproducibility and stability of the WSe_2 nanoflower sensor towards NH_3 gas even in humid background.

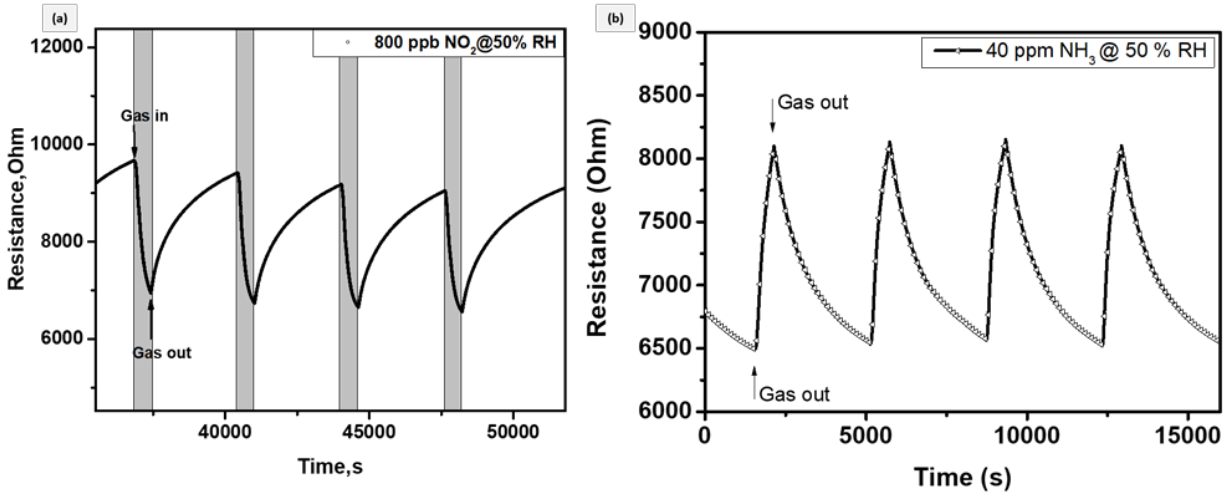

Figure 5.15 Relative humidity cross sensitivity to a) 0.8 ppm NO_2 at 100 °C and b) 40 ppm NH_3 at 150 °C.

The long-term stability of the sensors was studied and is presented in the Figure 5.16. NH_3 measurements were repeated at regular intervals over a considerable period and the evolution

of the baseline resistance and sensor response was monitored. For WSe_2 sensor, both baseline resistance and NH_3 response show a significant decreasing trend over time. The sensor response towards 40 ppm NH_3 shows steady results up to the first 15 days from the initial measurement but gradually starts decreasing after that and it fall off to a response of 15% after 4 weeks (Fig. 5.16 a). However, the baseline resistance of the sensor shows insignificant change and remains stable over the 4 weeks (Fig. 5.16 b).

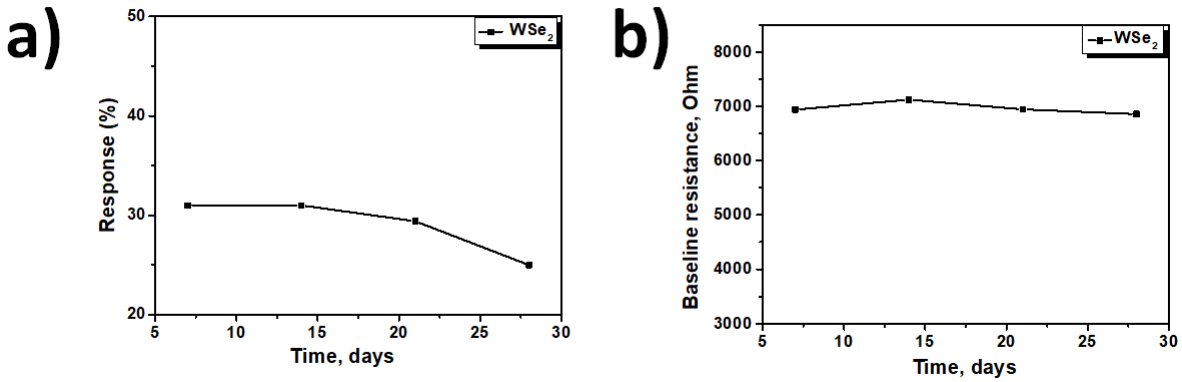

Figure 5.16 Long-term stability study. a) Stability study for WSe_2 sensor towards NH_3 gas over time and b) evolution of the baseline resistance with time.

Results presented in Figure 5.17 reveal the selectivity of the WSe_2 nanoflower sensor towards NH_3 gas with maximum response (25%) where the sensor shows negligible response towards benzene and carbon monoxide. Contrary to NH_3, the sensor shows some response (5%) towards hydrogen gas as well. However, it must be noticed that the concentration tested for hydrogen was 20 times higher than the one for NH_3. Additionally, the sensor also shows a moderate response (14%) towards 0.8 ppm of NO_2 gas at an operating temperature of 150 °C.

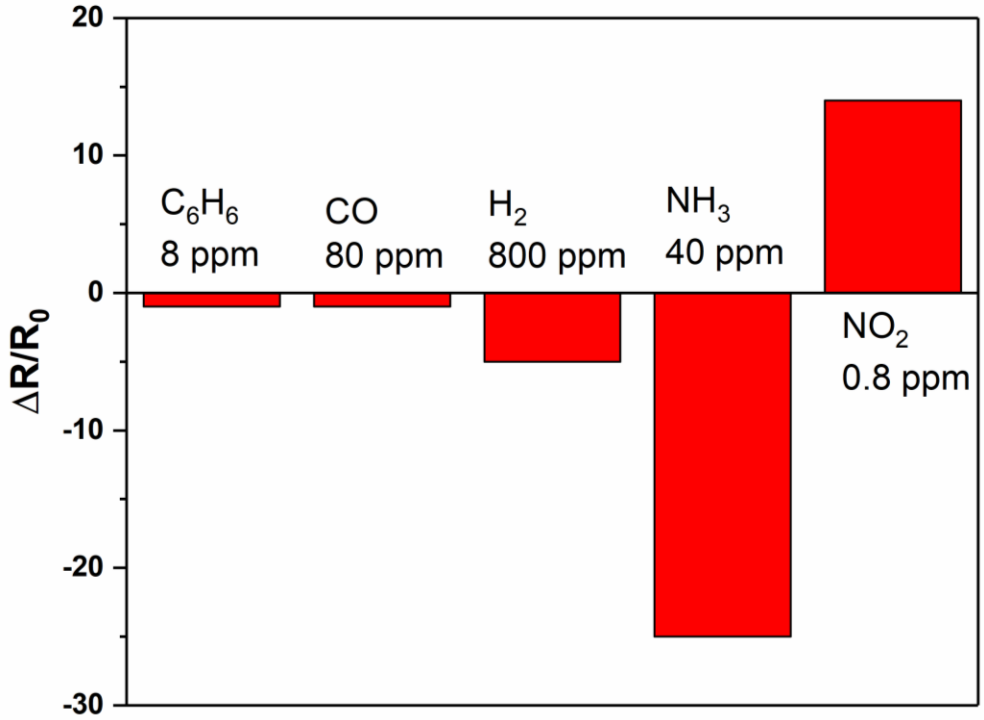

Figure 5.17 WSe_2 nanoflower sensor response based on exposure to 8 ppm C_6H_6, 80 ppm CO, 800 ppm H_2, 40 ppm NH_3, 0.8 ppm NO_2 gas at an operating temperature of 150 °C.

Table 5.3 summarizes the main results achieved and puts them in context with the state of the art. In this table, the performance in the detection of NO_2 and NH_3 reported here are compared against those in the literature gas detection. The aspects to be considered are the working temperature, the gases detected and the concentrations of these gases. As shown, depending on the morphology, the sensor detection may change.

Table 5.3 Comparison of the sensing properties to different gases of resistive gas sensors based on different WSe_2 sensing materials.

Structure	Working temp. (°C)	Studied conc.	Response (%)	Sensitivity (Response%/ppm)	Gas detected	Reference
Nanoflowers	100	0.8 ppm	20.5	14	NO_2	This work
Nanoflowers	150	40 ppm	24.5	25	NH_3	This work
Nanoscrews	RT	60 ppb	350	>40	NO	[24]
Monolayer	RT	25 ppb	20	20	NO_X	[25]
Vertical structure with exposing edges	RT	500 ppm	4.5	N/A	NO	[26]

5.4.3 Gas sensing mechanism

We can have two types of behaviors for these molecules, as electron acceptors (NO_2) and as electron donors (H_2S, H_2 or NH_3). For the first type, the resistance of the devices decreases in the presence of NO_2 (WS_2 Nanoflakes, WS_2 Nanotriangles and WSe_2 Nanoflowers sensors) and increases in the presence of NH_3 (WSe_2 Nanoflowers sensor), which is indicative that our multilayer tungsten disulfide and diselenide behaves as p-type semiconducting materials. While single layer WS_2 behaves usually as an n-type semiconductor, [27] The p-type behavior of WS_2 with exposed edges achieved via the sulfurization of WO_3 has been reported [15]. The nitrogen dioxide sensing mechanism in WS_2 and WSe_2 involves the adsorption of NO_2 or NH_3 molecules both on the edges of flakes and on their surface (or basal plane). Upon adsorption, electronic charge is injected from WS_2 towards the gas molecule, which generates a hole accumulation zone that results in a decrease in the resistance of the film. According to previously reported

computational chemistry studies in MoS_2, the edges are far more important than the basal plane for the adsorption of NO_2, because the adsorption energy of nitrogen dioxide at S edges is higher (∼−0.4 eV) than at the basal plane (∼−0.13 eV) and the associated electronic charge transfer is ∼0.5e and 0.1e, respectively [28]. These adsorption energies suggest that the interaction between WS_2 or WSe_2 with NO_2 would involve the physisorption of nitrogen dioxide. This is supported by the experimental results showing that sensor baseline resistance can be regained when flowing the sensor surface with clean air, even when sensors are operated at room temperature (i.e. 25 °C).

5.4.4 Conclusions

Gas sensing results showed that WS_2 and WSe_2 as a p-type semiconducting material. Furthermore, good stability and reproducibility of the responses were observed as well and these were related to the direct growth of the material on the sensor transducer. Henceforth this study paves a way to develop WS_2 gas sensors with improved quality with an unprecedented ultra-low detection limit under 5 ppb for NO_2. In the case of WSe_2, the detection limits are 0.1 and 2 ppm, for NO_2 and NH_3, respectively.

5.5 References

1. Panigrahi, P.; Hussain, T.; Karton, A.; Ahuja, R. Elemental Substitution of Two-Dimensional Transition Metal Dichalcogenides (MoSe2 and MoTe2): Implications for Enhanced Gas Sensing. *ACS Sensors* **2019**, *4*, 2646–2653, doi:10.1021/acssensors.9b01044.

2. Toda, K.; Furue, R.; Hayami, S. Recent progress in applications of graphene oxide for gas

sensing: A review. *Anal. Chim. Acta* **2015**, *878*, 43–53, doi:10.1016/j.aca.2015.02.002.

3. Yeow, J.T.W.; Wang, Y. A review of carbon nanotubes-based gas sensors. *J. Sensors* **2009**, *2009*, doi:10.1155/2009/493904.

4. Schedin, F.; Geim, A.K.; Morozov, S. V.; Hill, E.W.; Blake, P.; Katsnelson, M.I.; Novoselov, K.S. Detection of individual gas molecules adsorbed on graphene. *Nat. Mater.* **2007**, *6*, 652–655, doi:10.1038/nmat1967.

5. Choi, H.; Choi, J.S.; Kim, J.S.; Choe, J.H.; Chung, K.H.; Shin, J.W.; Kim, J.T.; Youn, D.H.; Kim, K.C.; Lee, J.I.; et al. Flexible and transparent gas molecule sensor integrated with sensing and heating graphene layers. *Small* **2014**, *10*, 3685–3691, doi:10.1002/smll.201400434.

6. Yu, K.; Wang, P.; Lu, G.; Chen, K.H.; Bo, Z.; Chen, J. Patterning vertically oriented graphene sheets for nanodevice applications. *J. Phys. Chem. Lett.* **2011**, *2*, 537–542, doi:10.1021/jz200087w.

7. Lee, E.; Yoon, Y.S.; Kim, D.J. Two-Dimensional Transition Metal Dichalcogenides and Metal Oxide Hybrids for Gas Sensing. *ACS Sensors* **2018**, *3*, 2045–2060, doi:10.1021/acssensors.8b01077.

8. Ma, C.B.; Qi, X.; Chen, B.; Bao, S.; Yin, Z.; Wu, X.J.; Luo, Z.; Wei, J.; Zhang, H.L.; Zhang, H. MoS2 nanoflower-decorated reduced graphene oxide paper for high-performance hydrogen evolution reaction. *Nanoscale* **2014**, *6*, 5624–5629, doi:10.1039/c3nr04975b.

9. Cho, S.Y.; Kim, S.J.; Lee, Y.; Kim, J.S.; Jung, W. Bin; Yoo, H.W.; Kim, J.; Jung, H.T. Highly Enhanced Gas Adsorption Properties in Vertically Aligned MoS2 Layers. *ACS Nano* **2015**, *9*, 9314–9321, doi:10.1021/acsnano.5b04504.

10. He, Q.; Zeng, Z.; Yin, Z.; Li, H.; Wu, S.; Huang, X.; Zhang, H. Fabrication of flexible MoS2 thin-film transistor arrays for practical gas-sensing applications. *Small* **2012**, *8*, 2994–2999, doi:10.1002/smll.201201224.

11. Pakapongpan, S.; Mensing, J.P.; Phokharatkul, D.; Lomas, T.; Tuantranont, A. Highly selective electrochemical sensor for ascorbic acid based on a novel hybrid graphene-copper phthalocyanine-polyaniline nanocomposites. *Electrochim. Acta* **2014**, *133*, 294–301, doi:10.1016/j.electacta.2014.03.167.

12. Tonezzer, M.; Le, D.T.T.; Iannotta, S.; Van Hieu, N. Selective discrimination of hazardous gases using one single metal oxide resistive sensor. *Sensors Actuators, B Chem.* **2018**, *277*, 121–128, doi:10.1016/j.snb.2018.08.103.

13. X. Zhang, V. S. Turkani, S. Hajian, A. K. Bose, D. Maddipatla, A. J. Hanson, B. B. Narakathu, M.Z.A. Novel Printed Carbon Nanotubes Based Resistive Humidity Sensors. *IEEE Int. Conf. Flex. Printable Sensors Syst.* **2019**, 1–3, doi:10.1201/b22370-11.

14. Struzzi, C. Spectromicroscopy investigation of plasma fluorinated carbon nanomaterials for gas sensing application. *Univ. Mons* **2017**.

15. Alagh, A.; Annanouch, F.E.; Umek, P.; Bittencourt, C.; Sierra-Castillo, A.; Haye, E.; Colomer, J.F.; Llobet, E. CVD growth of self-assembled 2D and 1D WS2 nanomaterials for the ultrasensitive detection of NO2. *Sensors Actuators, B Chem.* **2021**, *326*, 128813, doi:10.1016/j.snb.2020.128813.

16. Ou, J.Z.; Ge, W.; Carey, B.; Daeneke, T.; Rotbart, A.; Shan, W.; Wang, Y.; Fu, Z.; Chrimes, A.F.; Wlodarski, W.; et al. Physisorption-Based Charge Transfer in Two-Dimensional SnS2

for Selective and Reversible NO2 Gas Sensing. *ACS Nano* **2015**, *9*, 10313–10323, doi:10.1021/acsnano.5b04343.

17. Ko, K.Y.; Song, J.G.; Kim, Y.; Choi, T.; Shin, S.; Lee, C.W.; Lee, K.; Koo, J.; Lee, H.; Kim, J.; et al. Improvement of Gas-Sensing Performance of Large-Area Tungsten Disulfide Nanosheets by Surface Functionalization. *ACS Nano* **2016**, *10*, 9287–9296, doi:10.1021/acsnano.6b03631.

18. Xu, T.; Liu, Y.; Pei, Y.; Chen, Y.; Jiang, Z.; Shi, Z.; Xu, J.; Wu, D.; Tian, Y.; Li, X. The ultra-high NO2 response of ultra-thin WS2 nanosheets synthesized by hydrothermal and calcination processes. *Sensors Actuators, B Chem.* **2018**, *259*, 789–796, doi:10.1016/j.snb.2017.12.070.

19. Yan, W.; Worsley, M.A.; Pham, T.; Zettl, A.; Carraro, C.; Maboudian, R. Effects of ambient humidity and temperature on the NO 2 sensing characteristics of WS 2 /graphene aerogel. *Appl. Surf. Sci.* **2018**, *450*, 372–379, doi:10.1016/j.apsusc.2018.04.185.

20. Yan, W.; Harley-Trochimczyk, A.; Long, H.; Chan, L.; Pham, T.; Hu, M.; Qin, Y.; Zettl, A.; Carraro, C.; Worsley, M.A.; et al. Conductometric gas sensing behavior of WS2 aerogel. *FlatChem* **2017**, *5*, 1–8, doi:10.1016/j.flatc.2017.08.003.

21. Liu, D.; Tang, Z.; Zhang, Z. Comparative study on NO2 and H2S sensing mechanisms of gas sensors based on WS2 nanosheets. *Sensors Actuators, B Chem.* **2020**, *303*, 127114, doi:10.1016/j.snb.2019.127114.

22. Tongay, S.; Suh, J.; Ataca, C.; Fan, W.; Luce, A.; Kang, J.S.; Liu, J.; Ko, C.; Raghunathanan, R.; Zhou, J.; et al. Defects activated photoluminescence in two-dimensional semiconductors:

Interplay between bound, charged, and free excitons. *Sci. Rep.* **2013**, *3*, 1–5, doi:10.1038/srep02657.

23. Li, X.; Li, X.; Li, Z.; Wang, J.; Zhang, J. WS2 nanoflakes based selective ammonia sensors at room temperature. *Sensors Actuators, B Chem.* **2017**, *240*, 273–277, doi:10.1016/j.snb.2016.08.163.

24. Chen, Y.Z.; Lee, S.H.; Su, T.Y.; Wu, S.C.; Chen, P.J.; Chueh, Y.L. Phase-modulated 3D-hierarchical 1T/2H WSe2 nanoscrews by a plasma-assisted selenization process as high performance NO gas sensors with a ppb-level detection limit. *J. Mater. Chem. A* **2019**, *7*, 22314–22322, doi:10.1039/c9ta05348d.

25. Medina, H.; Li, J.G.; Su, T.Y.; Lan, Y.W.; Lee, S.H.; Chen, C.W.; Chen, Y.Z.; Manikandan, A.; Tsai, S.H.; Navabi, A.; et al. Wafer-Scale Growth of WSe2 Monolayers Toward Phase-Engineered Hybrid WOx/WSe2 Films with Sub-ppb NOx Gas Sensing by a Low-Temperature Plasma-Assisted Selenization Process. *Chem. Mater.* **2017**, *29*, 1587–1598, doi:10.1021/acs.chemmater.6b04467.

26. Chen, Y.Z.; Medina, H.; Wang, S.W.; Su, T.Y.; Li, J.G.; Yen, W.C.; Cheng, K.Y.; Kuo, H.C.; Shen, G.; Chueh, Y.L. Low-Temperature and Ultrafast Synthesis of Patternable Few-Layer Transition Metal Dichacogenides with Controllable Stacking Alignment by a Microwave-Assisted Selenization Process. *Chem. Mater.* **2016**, *28*, 1147–1154, doi:10.1021/acs.chemmater.5b04579.

27. Dmitry Ovchinnikov, Adrien Allain, Ying-Sheng Huang, Dumitru Dumcenco, and A.K. Electrical Transport Properties of Single-Layer WS2. *ACS Nano* **2014**, *8*, 8174–8181,

doi:10.1103/PhysRevB.90.155128.

28. Deokar, G.; Vancsó, P.; Arenal, R.; Ravaux, F.; Casanova-Cháfer, J.; Llobet, E.; Makarova, A.; Vyalikh, D.; Struzzi, C.; Lambin, P.; et al. MoS2–Carbon Nanotube Hybrid Material Growth and Gas Sensing. *Adv. Mater. Interfaces* **2017**, *4*, 1–10, doi:10.1002/admi.201700801.

Chapter 6

Conclusions and Perspectives

6.1 Conclusions

During this work, we synthesized large-area vertically aligned 2H-Metal Dichalcogenides nanosheets using atmospheric pressure chemical vapor deposition on magnetron sputtering pre-deposited metals on different substrates (such as such as Si/SiO_2, sapphire and Alumina substrate with interdigitated platinum electrodes). Many characterization techniques were used to analyze in depth the so-synthesized materials.

The strategy developed is to use the methodology of 2H-MoS_2 nanosheets from previous works made in our laboratory as starting point: this efficient and a simple route used for synthesizing a large area MoS_2 nanosheets can be applied as a general method for the synthesis of other metal dichalcogenides as we did in this thesis work with improvements in the synthesis process depending in the metal and chalcogen used. A two-step CVD technique was applied for the Transition Metal Dichalcogenides (MoS_2, WS_2, $MoSe_2$ and WSe_2), whereas a single step method was used for tin dichalgenides (SnS_2 and $SnSe_2$).

When Sulfur was used as chalcogenide, the reaction is made without the help of any additional chemical. This means that the sulfur is strong enough to perform the reduction and help the formation of the vertically aligned nanosheets. We have demonstrated the synthesis of vertically aligned and highly crystalline (2H phase) MoS_2 and WS_2 nanosheets. In the case of the last sulfured material, SnS_2, the methodology was fixed in a simple one-step CVD technique. The principal differences in comparison with the first two materials were the pre-oxidation of the tin film before the synthesis and the use of lower temperature (550 °C instead of 850 °C). With this, we evidence the formation of vertical, homogeneous and well-crystalline 2H-phase SnS_2 nanosheets. We showed that the nanosheets presented structural defaults at their exposed edges.

When Selenium is used instead of Sulfur, the use of another chemical is mandatory. Indeed, in addition to the presence of Se as a chalcogen, H_2 is necessary for the reactions to take place because Se is not a strong reductant like S. We have evidenced the CVD growth of vertically aligned 2H-$MoSe_2$ nanosheets. The resulting $MoSe_2$ is large in area, highly crystalline but not completely homogeneous. The MoS_2 synthesis process was taken as a starting point but it was modified in temperature (900 °C instead of 850 °C) and Ar flow to succeed with the synthesis, in addition to the presence of H_2. The same methodology of the first materials (MoS_2 and WS_2) was used for WSe_2, with the difference in the Ar flow and the presence of H_2 during the reaction. We have shown that the synthesized film is constituted of highly crystalline vertically and horizontally aligned WSe_2 nanosheets. The presence of another phase different to the 2H stable phase has also been shown, and could open a new route to tune the physical properties by phase engineering, as has already been done for similar materials, such as $MoTe_2$. The underlying

growth mechanism must be further studied in order to establish the best parameters so as to control the synthesis of the WSe_2 film with different phases. Also, we have demonstrated the synthesis of vertically aligned $SnSe_2$ nanosheets using a simple one-step CVD technique by direct selenization of a pre-oxidized tin film. $SnSe_2$ presents 2H-phase with vertically aligned and well crystalline nanosheets. $SnSe_2$ nanosheets also presents structural defects at their edges but in this case, the nanosheets have a bigger size, less homogeneity and the presence of other materials (SnSe as well as unreacted selenium). Due to the use of Se and H_2 during the synthesis process, the degree of nanosheet alignment with Selenium seems less than using Sulfur as a chalcogen because Se that is not enough reactive as Sulfur.

Our results provide a new direction to the synthesis of large-size Metal Dichalcogenides nanosheets on low-cost, and form the basis of a versatile approach for the synthesis of MDs for different applications such as gas sensors and hydrogen evolution reaction catalysis. For that, WS_2 and WSe_2 were synthesized on Alumina substrate with interdigitated platinum electrodes. These materials were tested as a gas sensor at the University Rovira i Virgili, Spain in the research group of the Prof. Llobet Valero. The results show good stability and reproducibility of the responses with toxic gases such as NO_2 and NH_3.

Gas sensing results showed that WS_2 and WSe_2 as a p-type semiconducting material. Furthermore, good stability and reproducibility of the responses were observed and we showed that the sensing results depended on the sensing material morphology (nanoflakes versus nanotriangles). So, the sensors based on WS_2 nanotriangles show very remarkable gas responses with high sensitivity an unprecedented detection limit below 5 ppb for NO_2 gas at 150 °C. In the case of WSe_2, we found the detection limits of 0.1 and 2 ppm, for NO_2 and NH_3, respectively.

6.2 Perspectives

Based on the results obtained in this thesis work and the improvements made in the CVD system for the synthesis of Metal Dichalcogenides, the next step will be the synthesis of other MDs such as $MoTe_2$, WTe_2 and $SnTe_2$ using Tellurium as a chalcogen. Also, thanks to the improvements in the system and the use of solid precursors proposed in this work, our attention can be focus in the synthesis of other materials. For example, hexagonal boron nitride (h-BN) that is a material with a structure comparable with graphene and has potential applications photonics, fuel cells and as a substrate for two-dimensional heterostructures.

MoS_2, WS_2 and WSe_2 nanosheets have been tested and published as a gas sensor in the previous reports and they have presented promising results for the detection of toxic gases. For that, SnS_2 nanosheets will be synthesized on Alumina substrate with interdigitated platinum electrodes to be tested as the mentioned materials due to their vertical orientation with exposed edges behavior. For that, SnS_2 nanosheets are proposed to be used as a gas sensor to make a comparison between the results obtained with MoS_2, WS_2 and WSe_2 in collaboration with Prof. Llobet Valero (University Rovira i Virgili, Spain).

Appendix I

Materials and Characterization Techniques

In this appendix materials and equipment used during the synthesis and characterization of MDs are described. In order to evaluate the quality of a material, we used different nevertheless complementary characterizations techniques. These techniques are extremely valuable as they represent the first step in quantifying and understanding the properties of a given material. Each technique will provide specific information on the structure or properties. The characterization of the synthesized nanomaterials, will allow evaluation of its quality and intrinsic properties.

A.1 Materials

A.1.1 Precursors

There is a variety of precursors available for MDs synthesis via CVD, we mainly focus in the use of metals such as Molybdenum (Mo), Tungsten (W) and Tin (Sn), and in the Sulfur (S) and Selenium (Se) commercial powders. The next sections show a basic presentation of these precursors.

All the materials used for this thesis for all the synthesis are presented in the Table A.1, with its grade of purity and the its provider.

A.1.1.1 Molybdenum

Molybdenum is a Group VI chemical element with the symbol Mo and atomic number 42. Mo display body centered cubic structure at room temperature [1]. Depending on the growth method, metal oxide powders can be used as the starting material to obtain Mo, from vaporized liquids or can be directly deposited in form on thin metallic or metal-oxide layer on the substrate. The use of powders leads to problem as reproducibility and large-scale homogeneity. It is often reported that the synthesis of mono or few-layers MoS_2 or $MoSe_2$ depends on the thickness and homogeneity of the initial Mo deposition [2].

A.1.1.2 Tungsten

Tungsten is a chemical element with the chemical symbol W and atomic number 74. W is a hard and rare metal under standard conditions and found naturally on Earth only in chemical compounds [3].

A.1.1.3 Tin

Tin is a chemical element with the chemical symbol Sn and atomic number 50. Sn is a silvery metal that characteristically has a faint yellow hue. For Sn, as Mo and W, the direct deposition onto SiO_2 or sapphire substrates is the best way to control their thickness via sulfurization or selenization.

The influence of the metal thickness in the resulting MD or TD nanostructure was not studied during this thesis. The same starting metal thickness, 50 nm was used.

A.1.1.4 Sulfur

Sulfur is a chemical element with the symbol S and atomic number 16. S powders are the most common precursors to deliver S to the substrate. S powders are available with high-purity (99.99%), they are not toxic, they can be used easily and for these reasons they are preferred than H_2S. Sulfur forms several polyatomic molecules. The best-known allotrope is octasulfur, cyclo-S_8. Octasulfur is a soft, bright-yellow solid that is odorless, however impure samples have an odor similar to that of matches. The melting temperature of the S powder is at 115 °C and evaporates to gaseous sulfur. At 95.2 °C, below its melting temperature, cyclo-octasulfur changes from α-octasulfur to the β-polymorph. The structure of the S_8 ring is virtually unchanged by this phase change, which affects the intermolecular interactions. Between its melting and boiling temperatures, octasulfur changes its allotrope again, turning from β-octasulfur to γ-sulfur, again accompanied by a lower density but increased viscosity due to the formation of polymers. At higher temperatures, the viscosity decreases as depolymerization occurs. Molten sulfur assumes a dark red color above 200 °C.

A.1.1.5 Selenium

Selenium is a chemical element with symbol Se and atomic number 34. Se powders are the precursors that are most used for the process of selenization of metal. As powders, they are easily handled as Sulfur with a purity up to 99.99%. Contrary to Sulfur, Se powders present toxicity if it's inhaled or swallowed. For these reasons it has to be handled with more precaution than S [4]. Selenium forms several allotropes that interconvert with temperature changes, depending somewhat on the rate of temperature change. When prepared in chemical reactions, selenium is usually an amorphous, brick-red powder. When rapidly melted, it forms the black, vitreous form, usually sold commercially as beads. The structure of black selenium is irregular and complex and consists of polymeric rings with up to 1000 atoms per ring. Black Se is a brittle.

The red α, β, and γ forms are produced from solutions of black selenium by varying the evaporation rate of the solvent. They all have relatively low, monoclinic crystal symmetries and contain nearly identical puckered Se_8 rings with different arrangements, as in sulfur. The packing is mostdense in the α form. Other selenium allotropes may contain Se_6 or Se_7 rings. Selenium melts at 217 °C and evaporates to gaseous selenium. Unlike Sulfur, the presence of a strong reducer is mandatory for the selenization reaction, compared with the sulfurization reaction [5]. For that, the use of H_2 to obtain a successful selenization is necessary.

Table A.1 Characteristics of the reagents used.

Reagent	Grade	Maker
Mo	99.95%	Micro to Nano
W	99.95%	Micro to Nano
Sn	99.95%	Micro to Nano
S	99%	Alfa Aesar
Se	99%	Alfa Aesar
H_2	99.9995%	ALPHAGAZ
Ar	99.9995%	ALPHAGAZ

A.2 Sample analysis

The characterization techniques used throughout this thesis are describe in this section. The techniques can be categorized in two areas: microscopy and spectroscopy. Microscopy measurements such as SEM and TEM provide information on the sample's structure with valuable direct imaging approaches. Spectroscopy measurements such as XPS, XRD, Raman spectroscopy, Photoluminescence and Uv-vis, provide information on the chemical composition, composition variation, crystallographic structure and optoelectronic properties of the materials.

A.2.1 Scanning Electron Microscopy (SEM)

Scanning electron microscopy (SEM) is a microscopic technique where a beam of electrons rasters over a sample, causing multiple interactions to occur. The different interactions are then analyzed by detectors in the SEM. Backscattered electrons are those which are produced by the

scattering of the incident electrons in the sample, and can be used to provide information on the chemical composition of a material by the contrast in the SEM image. Secondary electrons originate from the surface or a few nm into the sample. This means that secondary electron detection, using an InLens detector, can highlight topographical features. When analyzing topographical features, low voltages are used in order to only image the surface features. In the results presented in this work, SEM was used to examine the uniformity and topography of synthesized materials [6].

A focused electron beam is used to scan specimen in Scanning electron microscopy (SEM) from the optical to nanoscale range. Secondary electron backscattered electrons, generated from the specimen due to electron-specimen interaction, are collected by a detector to map out the local morphology and compositional information of the specimen, respectively. SEM was carried out by JEOL 7500F microscope operating at 15 kV (Figure A.1), at the microscope service of the University of Namur.

Figure A.1 JEOL 7500F microscope.

A.2.2 Transmission Electron Microscopy (TEM)

Electron microscopy is a powerful and versatile tool that allows us to obtain high-resolution images and provides structural information at a spatial resolution of 1 nm [7]. Due to its high resolution, the Transmission Electron Microscope (TEM) has been used for the visualization of nanostructures, since it allows its observation in dispersion and to obtain information about its degree of crystallinity, functionalization and morphology [8]. TEM is based on the interaction between electrons and matter; when an electron beam strikes the sample, part of these electrons passes through it. The diffracted electrons as they pass through the sample generate a diffractogram that can be directly transformed into an image. TEM analyses were conducted on a TECNAI T20 microscope (Figure A.2) working under 200 kV at the microscope service of the University of Namur.

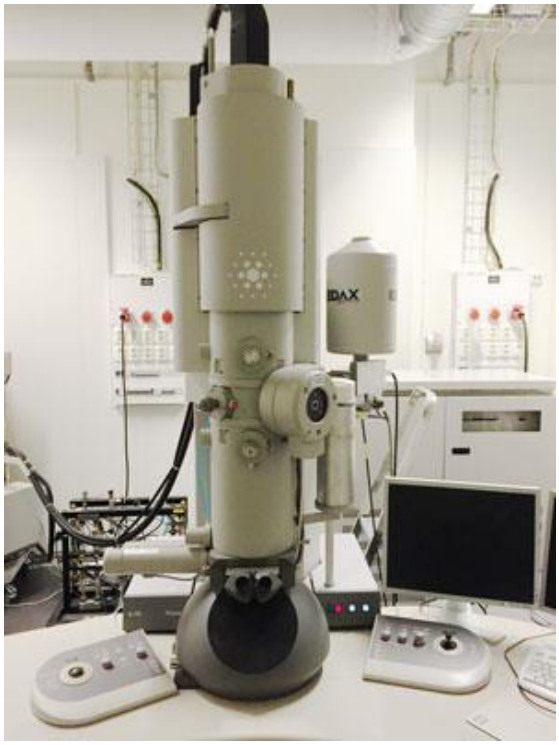

Figure A.2 TECNAI T20 microscope.

A.2.3 X-Ray diffraction analysis (XRD)

X-rays used for material studies are electromagnetic radiation of wavelength 0.2 to 2.5 Å, which is about the same size as an atom and comparable to lattice constants in crystals. X-rays enable to probe crystalline structure and chemical composition of materials and thin films. Each crystallized solid has a unique X-ray diffraction pattern representing its structure type and Laue symmetry, which can be used to determine the crystal structure. The unit cell of any compound can be determined by analyzing the diffracted X-ray intensities in accordance with the Bragg's law and the reflex conditions related to crystal system and Bravais lattice type. Equation 4.1 is Bragg's law, where 'd' is the interplanar distance, 'θ' is the angle of incidence with respect to the plane, 'λ' is the wavelength of the incident beam, and 'n' is the order of diffraction. As per Bragg's law, depending upon the path difference between the two reflected beams from two different planes, they either add up constructively or destructively resulting in an intensity pattern on detector plates [9].

$$n\lambda = 2d \sin(\theta) \qquad \text{A.1}$$

Diffraction is therefore essentially a scattering phenomenon. Atoms scatter incident radiation in all directions, and in some directions the scattered rays will be in phase and therefore present constructive interference to form diffracted rays (Figure A.4). Since atoms are periodically arranged in a lattice, destructive interference occurs in most directions however constructive interference occurs in a few directions and diffracted rays are formed.

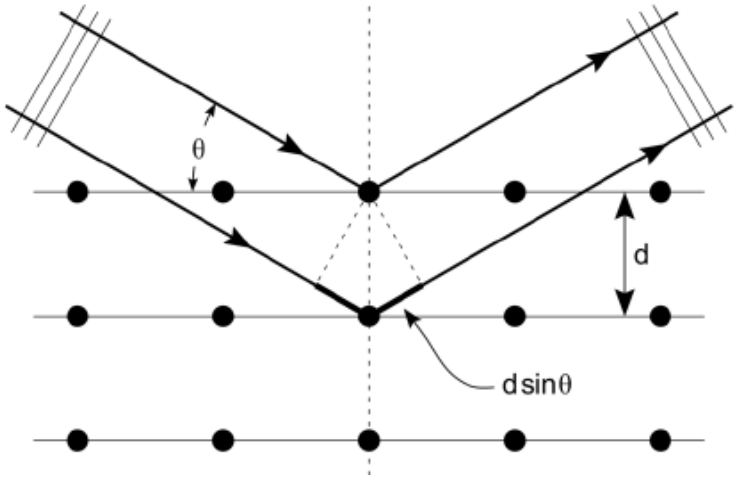

Figure A.4 Schematic representation of Bragg diffraction.

The peak intensities are determined by the atomic positions within the lattice planes. Consequently, the XRD pattern is the fingerprint of periodic atomic arrangements in a given material. An online search of a standard database for X-ray powder diffraction patterns enables quick phase identification for a large variety of crystalline samples. The unit of measurement of the X-Ray wavelength is in angstroms (Å), and the x-rays used in diffraction have wavelengths in the range 0.5-2.5 Å. Diffractometers consist of an X-Ray source, generally X-Ray tubes are used, and a detector to collect the diffracted X-Rays. Scintillation and semiconductors detectors are commonly used and they are based in the ability of X-Rays to ionize atoms.

XRD analyses were carried on a Panalytical X'Pert PRO diffractometer (comprising Cu Kα radiation, Bragg–Brentano geometry, a sealed tube operated at 45 mA 30 kV, and a X'Celerator linear detector in the University of Namur (Figure A.3).

Figure A.3 Panalytical X'Pert PRO diffractometer.

A.2.4 Raman spectroscopy

Raman spectroscopy is a powerful technique in the characterization of thin films as it is typically non-destructive and structure-sensitive. In the Raman analysis the sample is irradiated with a monochromatic light, normally from a laser in the visible light spectrum. A small part of energy from the light beam is storage by the chemical bonds in the sample, when relaxation occurs, the storage energy is irradiated and different scattering geometrics can be observed, the vast majority of the energy is irradiated at the same frequency as that of the incident light, known as Raleigh scattering. Nevertheless, a minor part of the storage energy is transferred to the sample and excites its vibrational modes, resulting in the energy from the light beam being shifted down, this phenomenon is named Stokes scattering. The contrary process can also occur, in the sample there are some vibrational states that are already excited by thermal processes, this exited vibrational states can add their energy to the beam light so the energy from the light beam being shifted up, this is known as anti-Stokes scattering. These three scattering geometrics are observed in the Raman spectrum of the samples. Rayleigh scattering is observed as a strong

central line in the spectrum, Stokes scattering lines are observed at lower frequencies that the incident beam with lower intensities than Rayleigh lines, the separation from Stokes and Rayleigh lines gives direct information about the vibrational frequencies of the samples. The anti-Stokes lines appear at higher frequencies that Rayleigh lines and are a mirror image from Stokes lines. [10].

The Raman analyses were conducted on a micro-Raman system (Senterra Bruker Optik GmbH) with a 3 cm^{-1} resolution, using a laser excitation laser source (532 nm wavelength), and a laser power of 2 mW (Figure A.4) at the Materia Nova in Mons, Belgium.

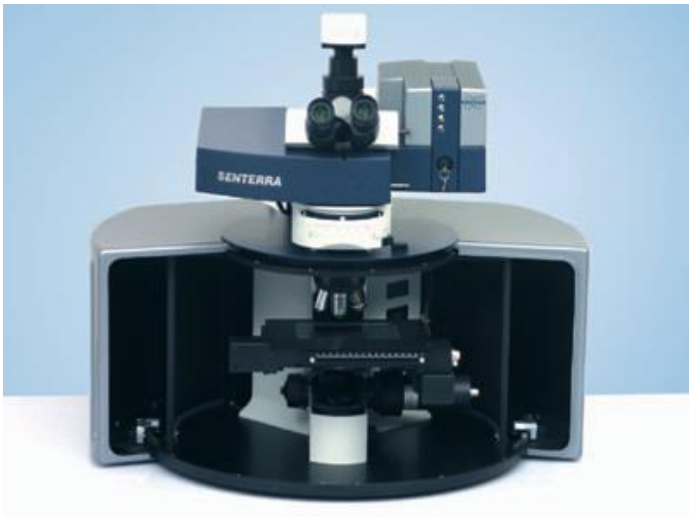

Figure A.4 Senterra Bruker Optik GmbH micro-Raman system**.**

A.2.5 Photoluminescence Spectroscopy

Luminescence is a phenomenon that involves the absorption of energy by a material, followed by the emission of light. In semiconductor research, a typical PL measurement involves the material being excited with a laser light of higher energy than its bandgap. The photons from the laser are absorbed into the material, and form electrons and holes in the conduction and valence bands. Following absorption, the electrons and holes undergo energy and momentum relaxation

towards the conduction and valence band minima respectively and eventually recombine and emit photons at the energy of the semiconductor bandgap [11].

The PL analyses were conducted on a micro-Raman system (Senterra Bruker Optik GmbH) with a 3 cm^{-1} resolution, using a laser excitation laser source (532 nm wavelength), and a laser power of 5 mW (Figure A.4) at the Materia Nova in Mons, Belgium.

A.2.6 Uv-vis Spectroscopy

Ultraviolet–visible spectroscopy or ultraviolet–visible spectrophotometry (UV–Vis or UV/Vis) refers to absorption spectroscopy or reflectance spectroscopy in part of the ultraviolet and the full, adjacent visible spectral regions. This means it uses light in the visible and adjacent ranges. The absorption or reflectance in the visible range directly affects the perceived color of the chemicals involved. In this region of the electromagnetic spectrum, atoms and molecules undergo electronic transitions. Ultraviolet-Visible spectroscopy (UV-Vis) is a good technique for characterizing MDs, since it provides information about their electronic structure, allows to know their monolayer or multilayer nature and their direct or indirect gap transitions [12].

UV-Vis analyses were conducted on a Perkin Elmer, LAMBDA 750 spectrophotometer at the University of Namur (Figure A.5).

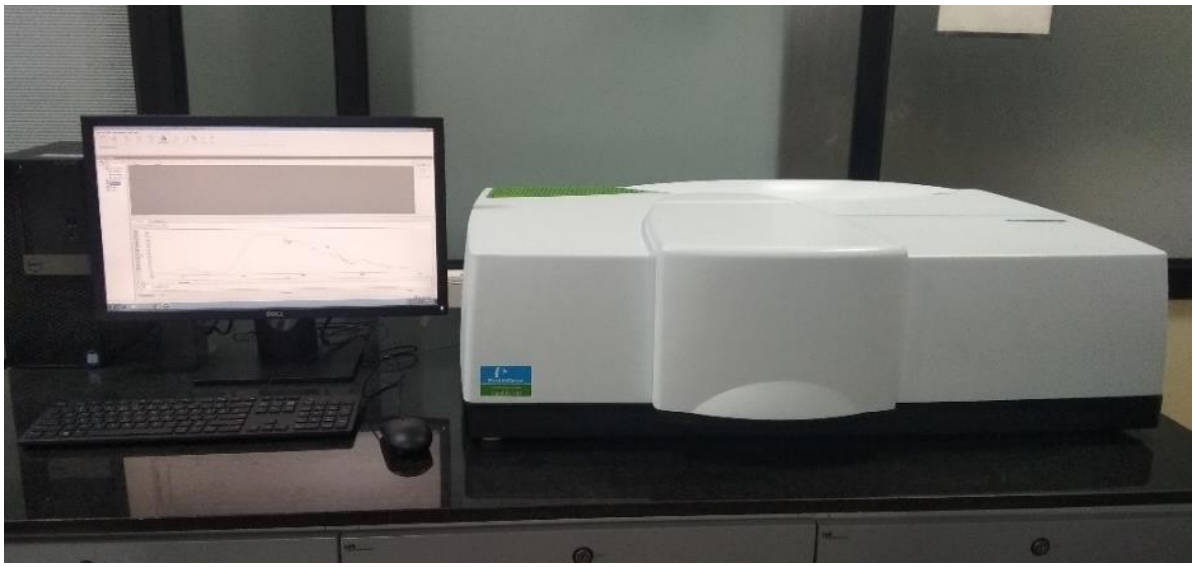

Figure A.5 LAMBDA 750 spectrophotometer.

A.2.7 X-Ray Photoelectron Spectroscopy (XPS)

Photoelectron spectroscopy is a technique that allows the chemical, elemental and quantitative characterization of a material surface. The sample is irradiated with X-Rays that transfer their energy to core electrons, so that characteristic photoelectrons are ejected from the material surface and their kinetic energy denoted Ek below, is measured by an analyzer. Knowing the energy of the initial photon (here, for the X-Ray from Al Kα Eph = 1486.7 eV), the electron binding energy, Eb, is simply deduced by the relation:

$$Eb = Eph - (Ek + \phi sp) \qquad A.2$$

Where ϕsp stands for the work function of the spectrometer. The binding energy of an electron from a specific orbital is characteristic of the chemical element and is also affected by the local bonding environment of the atom. The XPS survey spectrum consists of the number of electron counts detected as a function of the deduced binding energy. The number of electrons detected

can be related to the surface atomic composition, through the known atomic sensitivity factors, making XPS a quantitative technique (with ~1% accuracy).

The XPS signal is representative of the first 10 nm under the material surface (assumed homogeneous), however in the XPS analysis its ion beam sputtering can be coupled for depth profiling.

The XPS analyses were carried on an Escalab 250i Thermo Fisher Scientific™ instrument (consisting of a monochromatic Al Kα X-ray source and a hemispherical deflector analyzer working at a constant pass energy, Figure A.6) at the LISE in the University of Namur.

Figure A.6 Escalab 250i Thermo Fisher Scientific™.

A.3 References

[1] P. Jonmaire, "Molybdenum," *Hamilt. Hardy's Ind. Toxicol. Sixth Ed.*, vol. 37, no. 2, pp. 167–172, 2015, doi: 10.1002/9781118834015.ch24.

[2] Y. Niu *et al.*, "Thickness-dependent differential reflectance spectra of monolayer and few-layer MoS2, MoSe2, WS2 and WSe2," *Nanomaterials*, vol. 8, no. 9, 2018, doi: 10.3390/nano8090725.

[3] A. Kietzin and M. W. W. Adams, "Tungsten in biological systems," *FEMS Microbiol. Rev.*, vol. 18, no. 1, pp. 5–63, 1996, doi: 10.1016/0168-6445(95)00025-9.

[4] C. P. Yang, Y. X. Yin, and Y. G. Guo, "Elemental Selenium for Electrochemical Energy Storage," *J. Phys. Chem. Lett.*, vol. 6, no. 2, pp. 256–266, 2015, doi: 10.1021/jz502405h.

[5] Y. Li *et al.*, "Scalable Synthesis of Highly Crystalline MoSe2 and Its Ambipolar Behavior," *ACS Appl. Mater. Interfaces*, vol. 9, no. 41, pp. 36009–36016, 2017, doi: 10.1021/acsami.7b10693.

[6] K. C. A. Smith and C. W. Oatley, "The scanning electron microscope and its fields of application," *Br. J. Appl. Phys.*, vol. 6, no. 11, pp. 391–399, 1955, doi: 10.1088/0508-3443/6/11/304.

[7] Z. L. Wang, "Transmission electron microscopy of shape-controlled nanocrystals and their assemblies," *J. Phys. Chem. B*, vol. 104, no. 6, pp. 1153–1175, 2000, doi: 10.1021/jp993593c.

[8] J. H. Lehman, M. Terrones, E. Mansfield, K. E. Hurst, and V. Meunier, "Evaluating the characteristics of multiwall carbon nanotubes," *Carbon N. Y.*, vol. 49, no. 8, pp. 2581–2602, 2011, doi: 10.1016/j.carbon.2011.03.028.

[9] E. S. Ameh, “A review of basic crystallography and x-ray diffraction applications,” *Int. J. Adv. Manuf. Technol.*, vol. 105, no. 7–8, pp. 3289–3302, 2019, doi: 10.1007/s00170-019-04508-1.

[10] P. Rostron, S. Gaber, and D. Gaber, “Raman Spectroscopy , Review,” no. September, 2016.

[11] A. W. Adamson, “Photochemistry of transition metal coordination compounds,” *Pure Appl. Chem.*, vol. 20, no. 1, pp. 25–52, 1969, doi: 10.1351/pac196920010025.

[12] F. C. Jentoft, *Chapter 3 Ultraviolet-Visible-Near Infrared Spectroscopy in Catalysis. Theory, Experiment, Analysis, and Application Under Reaction Conditions*, 1st ed., vol. 52, no. C. Elsevier Inc., 2009.

Appendix II

Scientific Contributions

The papers published in peer-reviewed journals, including those strictly related to the research subject discussed in this PhD Thesis, and book chapters are listed below.

- **Sierra-Castillo, A.**, Haye, E., Acosta, S., Bittencourt, C., & Colomer, J. F. (2021). Atmospheric Pressure Chemical Vapor Deposition Growth of vertically aligned SnS_2 and $SnSe_2$ nanosheets. (*Submitted*)
- **Sierra-Castillo, A.**, Haye, E., Acosta, S., Arenal, R., Bittencourt, C., & Colomer, J. F. (2020). Synthesis and Characterization of Highly Crystalline Vertically Aligned WSe_2 Nanosheets. Applied Sciences, 10(3), 874.
- Acosta, S., Casanova Chafer, J., **Sierra Castillo, A.**, Llobet, E., Snyders, R., Colomer, J. F., Quintana, M., Ewels, C., & Bittencourt, C. (2019). Low Kinetic Energy Oxygen Ion Irradiation of Vertically Aligned Carbon Nanotubes. Applied Sciences, 9(24), 5342.
- Alagh, A., Annanouch, F. E., Umek, P., Bittencourt, C., **Sierra-Castillo, A.**, Haye, E., Colomer, J. F., & Llobet, E. (2021). CVD growth of self-assembled 2D and 1D WS_2

nanomaterials for the ultrasensitive detection of NO_2. Sensors and Actuators B: Chemical, 326, 128813.

- Primo, J. D. O., Bittencourt, C., Acosta, S., **Sierra-Castillo, A.**, Colomer, J. F., Jaerger, S., Teixeira, V. C., & Anaissi, F. J. (2020). Synthesis of Zinc Oxide Nanoparticles by Ecofriendly Routes: Adsorbent for Copper Removal from Wastewater. Frontiers in Chemistry, 8.
- Acosta, S., **Sierra-Castillo, A.**, Colomer, J. F., Snyders, R., Quintana, M., Ewels, C., & Bittencourt, C. (2021). Thermal stability of oxygen functionalization in v-CNTs by low kinetic energy ion irradiation. Vacuum, 110423.
- Selene Acosta, **Ayrton Sierra**, J. F. Colomer, Juan Casanova Chafer, Eduard Llobet, Polona Umek, Axel Hemberg, Carla Bittencourt. Decoration of CNTs with Pd-Ni nanoparticles. (In preparation).
- Direct CVD growth of large-area vertically aligned MoS_2 nano-plates on conducting graphite films. (In preparation).
- An ultrasensisitive two dimensional WSe_2 nanoflower based gas sensor. (In preparation).